

Molybdenum disulphide nanoporous membranes as nanofluidic platforms - large-area engineering and study

Présentée le 10 juin 2022

Faculté des sciences et techniques de l'ingénieur
Laboratoire de biologie à l'échelle nanométrique
Programme doctoral en science et génie des matériaux

pour l'obtention du grade de Docteur ès Sciences

par

Michal Daniel MACHA

Acceptée sur proposition du jury

Dr A. Hessler-Wyser, présidente du jury
Prof. A. Radenovic, directrice de thèse
Prof. M. Mayer, rapporteur
Prof. M. Drndic, rapporteuse
Prof. A. Fontcuberta i Morral, rapporteuse

If we knew what we were doing, it wouldn't be called "research".

— Albert Einstein

Acknowledgements

Research is not easy. It may sound like an obvious and trivial truth but nonetheless, it is impossible to prepare and be ready for all of the challenges ahead. I would like to sincerely thank here everyone who supported me during this time of my life. Science is hard. But with a great support and guidance it can also be an exciting, satisfying and meaningful experience.

First and foremost, I want to thank Aleksandra Radenovic for allowing my PhD to happen. With her constant guidance and enthusiasm everything is possible and a beginner scientist such as myself could never dream about a better advisor. She has created an extremely supportive and inspiring environment where ideas can grow and blossom into exciting discoveries. Aleksandra is passionate, patient and always ready to share her wisdom, knowledge and advice. I am proud that she gave me a chance, I am proud to be a member of the Laboratory of Nanoscale Biology and I am proud I could learn and work with her.

Secondly, a thank you to Sanjin Marion. My closest collaborator and a dear friend. We have struggled through countless scientific and life obstacles together with the help of enormous coffee intake and honest work. A guide, a mentor and practically a brother. With his help, dedication and inspiration ideas became reality. It was truly a pleasure and an honor to work and binge-drink coffee together.

I want to thank all of my project collaborators and office mates. Path to PhD thesis is not a lonely road and nothing can be done without sharing daily life and work burdens with others. Thank you for all of the discussions, coffee breaks, brainstorming sessions and beers we drunk. There are too many names to list but you guys are all the best.

Finally, to all of my friends and family. For never-ending love and support. I am happy to have you all in my life.

And Dani. Thank you. Life is not pain with you by my side.

Lausanne, 19 April 2022

M. M.

Abstract

The work demonstrated in this thesis represents the path towards developing the large-scale fabrication of two-dimensional nanoporous membrane devices and use of thereof as platforms to study nanoscale physics of water and ion flow through confined channels. Methods developed here are used to fabricate molybdenum disulfide (MoS_2) membrane devices and investigate the fundamental physics of nanopore systems and thin films in aqueous solutions. In particular, the first chapter introduces the fundamental aspects of these systems and brings forth the motivation behind academic study and development in this field.

The second chapter presents the accomplishments in the **large-area MoS_2 synthesis via chemical vapor deposition**. Process modifications such as the use of spin-coated precursors/growth promoters and addition of active gases such as H_2O vapor or moderate amount of O_2 enable to scale up the growth reaction into the synthesis of a continuous monolayer films on 2-, 3- and 4-inch substrates.

The third chapter shows the **application of focused ion beam irradiation for engineering, imaging and studying optically active defects in MoS_2 and hexagonal boron nitride films**. On top of that, the ion irradiation protocol was used for establishing the tunable and high-throughout nanopore drilling process on suspended MoS_2 membranes. With the high-resolution, scanning electron transmission microscopy, nanopores were investigated with an analysis script and classified based on the pore geometries and edge composition. Coupled with molecular dynamics simulations the membranes populated with $\approx 1\text{nm}$ nanopores were assessed in the context of emerging ion- and water- permeation properties.

The last, fourth chapter presents the **application of nanoporous membranes** discussed in previous chapters in the nanofluidics study. A particular emphasis is put on the application of hydrostatic pressure in nanopore experiments as an additional measurement probe. Experimental results shown in this chapter uncover the non-linear signals originating from nanobubbles pinning, improper wetting and membrane adhesion issues. With the assistance of hydrostatic pressure, the nanoporous MoS_2 suspended membranes are then further investigated to explore the ion transport properties and nanopores behaviour under applied strain

in the context of artificial mechanosensing as well as osmotic power generation in salinity gradients.

The ion irradiated, atomically thin films proved to be a highly attractive membrane materials and demonstrated a great promise in broad nanofluidic applications. Insights acquired during the thesis study were used to advance the state-of-art knowledge in field of the synthesis and application of 2D membranes in the nanofluidics research.

Key words: 2D-materials, transition-metal dichalcogenide, molybdenum disulfide, MoS₂, nanofluidics, solid-state nanopore, osmotic power generation, monolayer, membrane, defect engineering, ion irradiation, focused ion beam, FIB, blue energy, reverse electrodialysis, transmission electron microscopy, metallorganic chemical vapor deposition, MOCVD

Résumé

Le travail démontré dans cette thèse représente le chemin vers le développement d'une méthodologie de fabrication à grande échelle de dispositifs de membranes nanoporeuses bidimensionnelles et leur utilisation comme plateforme nanofluidique. Les méthodes développées sont utilisées pour la fabrication de dispositifs en disulfure de molybdène (MoS_2) et l'étude de la physique fondamentale des systèmes de nanopores et des films minces en solutions aqueuses. En particulier, le deuxième chapitre présente les résultats de la synthèse de MoS_2 sur une grande surface par dépôt chimique en phase vapeur. Des modifications du procédé telles que l'utilisation de précurseurs enrobés par centrifugation et l'ajout d'oxydants faibles tels que H_2O ou de faibles quantités de O_2 permettent d'augmenter la croissance jusqu'à la synthèse d'un film monocouche continu sur des substrats de 2, 3 et 4 pouces. Le troisième chapitre montre l'application de l'irradiation focalisée par faisceau d'ions pour l'ingénierie, l'imagerie et l'étude de défauts optiquement actifs dans le MoS_2 et le hBN. En outre, le protocole d'irradiation ionique a été établi pour démontrer la méthode de forage de nanopores réglables et à grande profondeur sur des membranes de MoS_2 en suspension. Couplés à la microscopie électronique à transmission haute résolution, les nanopores ont été étudiés à l'aide d'un script d'analyse dédié et classés en fonction de la géométrie des pores et de la composition des bords. Le dernier et quatrième chapitre présente l'application des membranes nanoporeuses dans le domaine de la nanofluidique. Les mesures sont effectuées dans une cellule d'écoulement spécialement conçue pour appliquer une pression hydrostatique sur la membrane. Les résultats expérimentaux présentés dans ce chapitre révèlent les événements correspondants à des artefacts fondamentaux des membranes 2D dans les solutions aqueuses, tels que les problèmes de pincement des nanobulles, de mouillage et d'adhésion de la membrane. Avec l'aide de la pression hydrostatique, les membranes suspendues nanoporeuses en MoS_2 sont ensuite étudiées plus en détail afin d'explorer les propriétés de transport ionique et le comportement des nanopores sous des contraintes appliquées dans le contexte de la mécanosensibilité artificielle ainsi que de la génération d'énergie osmotique dans les gradients de salinité.

Les films atomiquement minces et irradiés par des ions se sont avérés être des matériaux membranaires très attrayants et se sont donc révélés très prometteurs pour de larges applications en nano fluidiques. Les connaissances acquises au cours de cette thèse ont été utilisées

pour faire progresser l'état de l'art dans le domaine de la synthèse et de l'application des membranes 2D à la recherche en nanofluidique.

Mots clefs : Matériaux 2D, dichalcogénure de métal de transition, fabrication, bisulfure de molybdène, MoS_2 , nanofluidique, nanopore à l'état solide, production d'énergie osmotique, monocouche, membrane, ingénierie des défauts, irradiation ionique, faisceau d'ions focalisé, FIB, PFIB, énergie bleue, électrodialyse inverse, microscopie électronique à transmission.

Contents

Acknowledgements	i
Abstract (English/Français)	iii
List of figures	xi
List of tables	xv
1 Introduction	1
1.1 Nanopores	1
1.2 Osmotic power generation	2
1.2.1 Understanding power generation	4
1.2.2 Materials for osmotic power generation	9
1.2.3 Selectivity and surface charges	14
1.2.4 Osmotic conductance	15
1.2.5 Optimal materials parameters	16
1.2.6 Fabrication of 2D materials and pores	16
1.2.7 Outlook	19
1.3 Molybdenum disulphide (MoS ₂) - properties	24
1.3.1 Monolayer MoS ₂ Synthesis methods	25
1.3.2 MoS ₂ as a nanoporous membrane	28
1.4 Motivation	28
1.5 Thesis Structure	28
2 Large-area synthesis of MoS₂ monolayer film	31
2.1 MoS ₂ CVD synthesis on location-specific area	31
2.1.1 Overview of the approach and motivation	31
2.1.2 Location-specific synthesis with lithographic mask	31
2.1.3 Stencil lithography of MoO ₃ and location-specific growth	32
2.1.4 Conclusions	33
2.1.5 Methods	34
2.1.6 Acknowledgements	35
2.2 Wafer-scale MOCVD growth of monolayer MoS ₂ on sapphire and SiO ₂	36
2.2.1 Abstract	36
2.2.2 Introduction	36
2.2.3 Results and Discussion	37
2.2.4 Conclusion	44
2.2.5 Methods	45
2.2.6 Supplementary Information	48

2.3	Wafer-Scale Fabrication of Nanopore Devices for Single-Molecule DNA Biosensing using MoS ₂	51
2.3.1	Abstract	51
2.3.2	Introduction	52
2.3.3	Results and Discussion	53
2.3.4	Conclusion	60
2.3.5	Methods	61
2.3.6	Supplementary Information	62
2.4	Wafer-scale MoS ₂ with water-vapor assisted showerhead MOCVD	72
2.4.1	Introduction	72
2.5	Experimental Results and Discussion	73
2.6	Conclusion	81
2.7	Authors contribution	81
2.8	Methods	81
2.8.1	Supplementary Information	83
2.9	Conclusions	87
3	Pore and defect engineering with Focused Ion Beam	89
3.1	Introduction to Focused Ion Beam nanofabrication	89
3.2	Ion-beam nanopore fabrication and pore-edge classification	92
3.2.1	Introduction	92
3.2.2	Experimental Section	93
3.2.3	Focused Ion Beam Irradiation	93
3.2.4	Pore-edge detection	94
3.2.5	Conclusion	103
3.2.6	Acknowledgements	104
3.2.7	Methods	104
3.2.8	Supplementary information	105
3.3	Patterning vdW materials	113
3.4	PFIB irradiation of MoS ₂	113
3.4.1	Motivation	113
3.4.2	Results	114
3.4.3	Conclusions	115
3.5	PFIB irradiation of hBN	117
3.5.1	Introduction	117
3.5.2	Results and discussion	118
3.5.3	Conclusion	125
3.5.4	Methods	125
3.6	Conclusion	134
4	Study of fundamental ionic transport properties of nanoporous membranes	135
4.1	Experimental setup	136
4.2	Wetting artifacts	138
4.2.1	Wetting of MoS ₂	140
4.2.2	Microfluidics chamber	144
4.2.3	Measurements	144
4.2.4	Supplementary information	146
4.3	Artificial mechanosensing with MoS ₂ nanoporous membranes	154

4.3.1	Mechanosensing mechanism	154
4.3.2	Results	155
4.3.3	Conclusion	160
4.3.4	Supplementary information	161
4.4	Osmotic Power Generation with FIB-irradiated MoS ₂	163
4.4.1	Experiment and measurements protocol	163
4.4.2	Results	164
4.4.3	Conclusions	167
4.5	Challenges of using FIB-irradiated thin films	167
4.5.1	Outline	169
4.6	Delamination and wrinkling phenomena of suspended MoS ₂ under applied pressure . .	171
4.6.1	Introduction	171
4.6.2	Results and Discussion	172
4.6.3	Conclusion	177
4.6.4	Methods	178
4.6.5	Supplementary Information	179
4.7	Conclusion	181
5	Conclusion and Outlook	183
A	An appendix	187
	Bibliography	232
	Curriculum Vitae	233

List of Figures

1.1	Typical solid-state nanopore devices.	5
1.2	Power densities per membrane area for different materials	9
1.3	Different materials used for nanopore power generation	13
1.4	Scaling properties of 2D nanoporous membranes	14
1.5	Nanopore drilling techniques	17
1.6	Osmotic conductance per single pore as a function of pore size for different materials	20
1.7	Influence of pore density and size	21
1.8	MoS ₂ in micro- and nanoscale	25
1.9	CVD and MOCVD synthesis of MoS ₂	26
1.10	CVD coverage limitations	27
2.1	Location-specific synthesis - concept	32
2.2	Stencil MoS ₂ synthesis - concept	33
2.3	Stencil MoS ₂ synthesis - results	34
2.4	Schematic illustration of 2-inch wafer-scale MoS ₂ film growth process	38
2.5	Basic characterization of as-grown MoS ₂ on SiO ₂	39
2.6	Raman, PL and XPS characterizations of MoS ₂ films.	41
2.7	Atomic structure of monolayer MoS ₂ films	43
2.8	Electrical transport measurement of the monolayer MoS ₂ device	44
2.9	Dependency of MoS ₂ growth on H ₂ supply	48
2.10	SEM images of as-grown MoS ₂ on sapphire and on SiO ₂	49
2.11	Reproduced growth of monolayer MoS ₂ on the same sapphire substrate	50
2.12	Growth of tungsten disulfide (WS ₂) with the same method	50
2.13	PDMS-transfer of MoS ₂	54
2.14	Characterization of large-area MoS ₂ films	57
2.15	Wafer-scale transfer efficiency map	59
2.16	Schematic of the homemade MocVD setup and MoS ₂ synthesis	63
2.17	Optical images of a MoS ₂ film under different growth conditions	64
2.18	Microfabrication steps involved in wafer-scale substrate fabrication	65
2.19	Substrate aperture variability and quality characterization	66
2.20	Optical images of a MoS ₂ monolayer film grown over a large area	66
2.21	Photoluminescence measurements	67
2.22	STEM imaging and large-field of view (FOV) of continuous MoS ₂ after transfer	68
2.23	Unsuccessful transfer of MoS ₂ on SiN _x membrane	69
2.24	Post-transfer TEM images of MoS ₂	70
2.25	I-V measurement for Device A	71
2.26	A schematic of the experimental MOCVD setup	74

2.27 Post-growth nucleation density and crystal size	75
2.28 H ₂ O assisted growth method	77
2.29 Raman, PL and XPS spectra analysis of showerhead MOCVD grown MoS ₂	79
2.30 STEM images of MoS ₂	80
2.31 MoS ₂ optical microscope images	83
2.32 Detailed Raman spectra analysis of showerhead-grown MoS ₂	83
2.33 Carbon Raman spectra	84
2.34 Mo 3d and S2p XPS peaks	85
2.35 E-beam dose test and defect concentration	86
3.1 FIB principle and schematic	90
3.2 Focused ion beam irradiation of 2D films	94
3.3 Pore edge detection algorithm outline	95
3.4 Pore edge analysis and statistical indicators obtained from pore edge detection	97
3.5 Pore edge shape distribution in Xe irradiated nanopores	100
3.6 Simulated pore properties	102
3.7 Porosity and pore-size distribution	105
3.8 Pore size histograms for 100pa FIB	106
3.9 Pore size histograms for 30pa FIB	107
3.10 Pore size histograms for 10pa FIB	108
3.11 Pore shape library	111
3.12 Patterned MoS ₂ imaged with 2D-PAINT	114
3.13 AFM height images of two FIB patterned MoS ₂ flakes	116
3.14 Generation of FIB-induced optically active defects in exfoliated hBN flakes	119
3.15 Exploring mechanical effects of FIB irradiation using TEM	120
3.16 Optical and morphological characterization of irradiated defect sites	121
3.17 Water-assisted etching of irradiated defect sites	123
3.18 Correlated super-resolution and atomic force microscopy of FIB-induced defects in hBN	124
3.19 TEM micrographs of FIB-cut hBN lamella	128
3.20 Analysis of FIB-induced line patterns of structural and optically active defects	129
3.21 Spectral dependence of fluorescence from induced defects on irradiation dose.	130
3.22 Confocal spectral mapping of produced defects with varying irradiation dose	131
3.23 Widefield image of the irradiated flake in air and in liquid.	131
3.24 AFM analysis of FIB-irradiated hBN flakes	131
3.25 AFM timelapse of the same irradiated hBN flake immersed in water	132
3.26 Dependence of hole size on irradiation dose (dwell time)	132
3.27 AFM analysis of suspended FIB-irradiated hBN flakes	133
4.1 Applying pressure to solid-state nanopores	137
4.2 Pressure and voltage wetting of a nanopore	139
4.3 Wetting of nanopores in single layer MoS ₂ membranes	141
4.4 Dependence of a MoS ₂ nanopore resistance R versus diameter d	146
4.5 Sample S _{MoS₂} 1	147
4.6 Sample S _{MoS₂} 2	149
4.7 Sample S _{MoS₂} 3	150
4.8 Sample S _{MoS₂} 4	151
4.9 Sample S _{MoS₂} 5	152
4.10 Pressure measurement time trace	153

4.11	Mechanosensitivity principle	155
4.12	Mechanosensing measurements	156
4.13	Mechanosensing obtained with MoS ₂ nanopores	158
4.14	Anomalous pressure-induced ionic transport on solid state chips	159
4.15	Anomalous pressure-induced ionic transport on solid state chips - current sweep	161
4.16	Anomalous pressure-induced ionic transport on solid state chips - dependence on time	162
4.17	Osmotic power generation with PFIB-irradiated MoS ₂	163
4.18	Non-linear ionic currents in gradient conditions	165
4.19	PFIB-created nanopores and MoS ₂ structure.	168
4.20	HRTEM images of MoS ₂ device prior and post irradiation	169
4.21	Temporary delamination of MoS ₂ during nanofluidic measurements	172
4.22	Delamination of suspended MoS ₂ due to surface indentation	175
4.23	Streaming current measurements on suspended MoS ₂ during delamination	176
4.24	Streaming potential measurements on suspended MoS ₂ during delamination	177
4.25	Non-linear IV of delaminated MoS ₂	179
4.26	TEM images of pressure-induced delaminated MoS ₂	180
4.27	TEM images of pressure-induced wrinkled MoS ₂	180
A.1	Location-specific synthesis - coverage map	189
A.2	Location-specific synthesis - coverage map, unmarked	189
A.3	Overgrowth of MoS ₂ on apertures	190
A.4	Pressure gassing of nanobubbles in hydrophilic nanopores	191
A.5	Elastic response and strain enlargement of Si/SiN _x membranes	192
A.6	Asymmetric mechanosensitivity with MoS ₂	192
A.7	FIB-induced surface contamination	193

List of Tables

2.1	Comparison of wafer-scale transfer efficiency	69
2.2	XPS atomic ratios table	86
3.1	Ion dose calculation	129
4.1	Measured osmotic power	166
A.1	Compilation of reported osmotic power generation up to date	188

1 Introduction

The rapid development of nanotechnology in past years have opened an exciting avenue to study new materials in a novel, extraordinary way. Indeed, at the nanoscale almost everything do exhibit abnormal behaviours as compared to their macro counterparts. That includes also fluids, such as water or water solutions flowing through confined, nanometric channels or structures with at least one dimensions below 100 nm. The very small ratio between nanochannel dimensions and the size of fluid particles (e.g. water molecules or ions) leads to the emergence of unique behaviors; properties such as electrical double-layer (EDL) overlap and surface charge influence significantly ion transport, ion separation and ion selectivity and lead to non-linear and asymmetric mechanisms^{1,2} unseen before. Nanofluidics - an emerging field dedicated to studying water and ion transport through confined nanochannels presents an unique opportunity to discover and study these exotic physical phenomena but also to exploit and engineer new materials and technologies, especially in the fields of desalination membranes³ biosensing⁴⁻⁶ and energy harvesting⁷⁻⁹.

1.1 Nanopores

A fundamental representative of a confined nanochannel is a nanopore. Defined as a hole (or a pore) of a nanometric size, typically in a thin material separating water or salt solutions. Nature's example of such structures are biological pores, created by folded proteins. They are the key to the proper function of living cells as they regulate the water, ion and nutrient flow through cell membrane. Nanostructural constructs using biological nanopores such as alpha-hemolysin (of precise 1.5 nm diameter) embedded in synthetic or biological membranes (e.g. lipid bilayers) are widely studied and used as biosensors as the DNA or RNA (or other protein) may pass through such a nanopore interrupting the open ionic current passing through the membrane allowing, in principle, to fully sequence such a molecule^{10,11}.

Fabricating completely synthetic nanopores however presents an opportunity to control and tune the porous membrane parameters on a different scales (specifically its thickness, pore size and density). Fundamental nanofluidic membrane properties such as thickness and pore diameters are in principle tunable but also pose a technological challenge, especially on membrane areas larger than millimeter-size chip-scales used in academic studies. Achieving such a control and precision however does bring the benefits of properties surpassing their biological-pore cousins (e.g. in study of artificial mechanosensing¹²). The synthetic nanopores are also somewhat more versatile. Depending on the pore dimensions, substrate geometry and salt solution conditions they can exhibit high ion-selectivity, water permeation or rejection, ionic current rectification or diode-like behaviour^{9,13}. Such a tunability

enables applications such as water desalination, and salinity gradient energy harvesting thus making nanoporous membranes a great platform to study general nanoscale physics in aqueous solutions.

This thesis focuses on a large-area, controllable synthesis of atomically thin membranes and large-scale fabrication of nanopores and study thereof. The initial, main goal and motivation to developing these was upscaling nanopore-based osmotic power generation, therefore, next sections of the **Introduction** discuss in details the fundamental principles and mechanism, choice and properties of membrane materials and synthesis processes as well as challenges, opportunities and outlook with this particular application in mind. As the work progressed however, the motivation evolved to also provide a robust 2D material platforms for applications of fundamental ion transport studies, DNA translocation and defect engineering: applications which are further discussed in the next chapters.

1.2 Osmotic power generation

The following section is based verbatim on the following publication:

Michal Macha^I, Sanjin Marion^I, Vishal V. R. Nandigana^{II} and Aleksandra Radenovic^I

2D materials as an emerging platform for nanopore-based power generation, *Nature Reviews Materials*, 2019.

Michal Macha and Sanjin Marion contributed equally to the manuscript. M.M. and S.M. wrote the manuscript; M.M., S.M. and A.R. researched the data for the article. V.N. contributed to the theory section. All authors discussed the contents and provided important contributions to the manuscript.

Modern society, industry and research require ever increasing amounts of electrical power. With fossil fuel supplies shrinking^{14,15} and nuclear power facing negative public opinion^{16–18} researchers are turning their attention to the establishment of efficient and sustainable energy sources that could be both safe and ecological.

Besides solar and wind power, another type of energy is especially attractive^{19–21}: that generated from water. Beside well-known hydropower generated by hydroelectric power plants (dams), scientists and engineers are exploring tidal energy, which exploits ocean waves friction to generate electricity (with triboelectric networks^{22–24}), and blue energy²⁵, which takes advantage of salinity gradients to harvest so-called osmotic energy. Blue energy (also known as osmotic or salinity gradient energy) — the extractable free energy of mixing of a concentrated salt solution with pure water — is promising, because the energy harvesting yield from mixing freshwater and seawater is estimated to be 3 kJ per litre mixed, which is equivalent to 0.8 kWhm⁻³, that could be harvested by prospective power generators²⁶. The general estimate for the global potential of this energy source reaches up to thousands of terawatt hours^{3,27–30} with the possible added benefit of the integration of water desalination plants and, in certain cases, of mineral harvesting processes. Given the amount of freshwater and saltwater mixing sites on our planet (both natural and manmade, such as brines and wastewater), there is a huge potential to develop a new, ecological and abundant source of energy. However, current prototypical implementations of osmotic energy generation give an energy production in the range of 1–5 W*m^{-231–35}, which is not enough to power real-world devices³⁶.

^IInstitute of Bioengineering, Laboratory of Nanoscale Biology, Ecole Polytechnique Federale de Lausanne CH-1015 Lausanne, Switzerland

^{II}Department of Mechanical Engineering, Indian Institute of Technology Madras, Chennai – 600036, Tamilnadu, India.

There are two general approaches to harvesting energy with membranes. Pressure-retarded osmosis (PRO)^{37–41} uses a membrane permeable only to water to move water between a salty and a freshwater reservoir to decrease the concentration of salt (and increase the entropy), producing osmotic pressure that drives a turbine and, thus, generates power. Several implementations of PRO power plants were tested, but none had sufficient profit margins, giving a maximum of $5 \text{ W} \cdot \text{m}^{-2}$ of generated power^{31–33}. The second, more promising approach for power generation upscaling is osmotic energy harvesting using reverse electrodialysis (RED)^{42–48}. In this concept, an ion-selective membrane is used between the salty and freshwater reservoir with minimal water flow. Owing to the ion selectivity of the membrane, the current of one type of ion is larger, producing a charge non-neutrality between the reservoirs that can be harnessed as a battery. The main bottleneck of both PRO and RED technologies lies in the low achievable power density³⁶ and high energy costs related to water pretreatment (to remove bulk particles and contamination that might clog the membrane) and pumping, as well as the intrinsic trade-off between energy harvesting efficiency and achievable power output^{49,50}. Making these technologies practically useful requires producing novel, highly efficient membrane materials, which, ideally, should be semi-permeable and ion selective (for RED), allow good water fluxes (for PRO), not be susceptible to fouling or clogging (thus lowering the energy cost of water pretreatment) and have good mechanical stability and durability to endure the working environment^{49–53}.

Several challenges face the field of membrane technologies for desalination and power generation^{54–57}. Issues such as selectivity, material durability in aqueous conditions and fouling were taken into consideration to test and develop new membrane structures based on advanced materials, including novel ceramics^{58–64}, polymers^{65–69}, composites^{70–74} and porous nanomaterials, such as nanotubes^{75–79}, metal–organic frameworks (MOFs)^{74,80,81}, stacked nanoflakes^{82–86} and, finally, thin suspended films^{4,8,51,87–92}. These materials were developed and tested in various configurations, including bulk intrinsically porous structures, precisely microfabricated nanochannels or nanopores on membranes (solid-state nanopores), stacked nanotubes and atomically thin, freestanding 2D materials (2D nanopores), which are now in the spotlight for blue energy harvesting.

The most substantial increase in generated power density was obtained by using nanotubes and then atomically thin materials. In 2013, the well-defined geometry of boron nitride nanotubes (BNNTs) was exploited to demonstrate power densities that could reach up to $4 \text{ W} \cdot \text{m}^{-2}$ in a RED configuration in laboratory conditions⁷. Then, in 2016, the 2D material MoS_2 was used to fabricate three-atom-thick membranes⁸ that reached a power of $\approx 1 \text{ MW} \cdot \text{m}^{-2}$. These results demonstrate improvements of orders of magnitude as compared with previously reported, ‘thick’ solid-state membranes, making thin nanomaterials (particularly 2D materials) especially promising for osmotic energy harvesting applications¹³. It remains to be clarified what are the underlying physical phenomena that make 2D materials so efficient in osmotic power generation, and how the material properties can be tuned to optimize efficiency and tackle practical issues with in-lab membranes.

To explore the role of 2D materials and their properties in osmotic power generation using RED, we first introduce the fundamental underlying phenomena and concepts, and then review relevant materials, starting with thick membrane materials before focusing on nanotubes and 2D materials and their properties. After surveying fabrication methods and important results on single-pore systems, we expand on avenues for the wafer-scale production of porous membranes for RED. Finally, the current challenges are discussed, including manufacturing methods, chemical and mechanical robustness, and upscaling to whole membranes.

1.2.1 Understanding power generation

Most research on 2D materials as a platform for power generation membranes has focused, so far, on single pores under so-called laboratory conditions, with the aim to understand and characterize the important materials parameters. In laboratory conditions, one is constantly working at a fixed gradient, as the real total energy density per unit area is low, implying that the two solutions do not have the opportunity to significantly mix, unlike in large-scale applications⁹³.

Efficient power generation using ion-selective membranes demands optimizing three parameters⁹³: the resistivity of the membrane, which must be reduced under gradient conditions; the selectivity of the membrane to anions or cations, which must be maximized; and the molar water permeation, which must be low so that there is minimal water flux from the high-concentration to the low-concentration chamber. In this section, we discuss the role of single-pore parameters in making efficient RED membranes, with an emphasis on selectivity and membrane resistance.

A typical design of an osmotic power generator involves a salinity difference between two reservoirs separated by a membrane, with a single pore providing a pathway for ions between the reservoirs (Fig. 1.1a,b). Assuming a linear response, an internal electromotive force ϵ_{osm} (the osmotic potential) produces a driving force through the pore with conductance G_{osm} , which generates an osmotic current I_{osm} ^{62,94,95}. When taking electrical measurements to characterize the system, one usually obtains current–voltage characteristics (Fig. 1.1c) with a distinct offset: a non-zero, open-circuit voltage ϵ_{osm} and a non-zero, closed-circuit current I_{osm} . The two electrodes have an inherent potential difference due to redox potentials that we ignore here; it is usually subtracted from measurement values⁶² or experimentally eliminated using salt bridges on the electrodes⁹⁶. What remains are the driving electromotive force ϵ_{osm} and the response function to this force, which we call osmotic conductance, G_{osm} (which is different from the membrane conductance G_m in the absence of a salt gradient between the reservoirs). In a naive picture, the resistance of a porous membrane comes from the parallel connection of pores with individual resistances G_m^{-1} . The higher the individual osmotic conductance of the pores, the more osmotic power is produced by the membrane under the same driving concentration gradient.

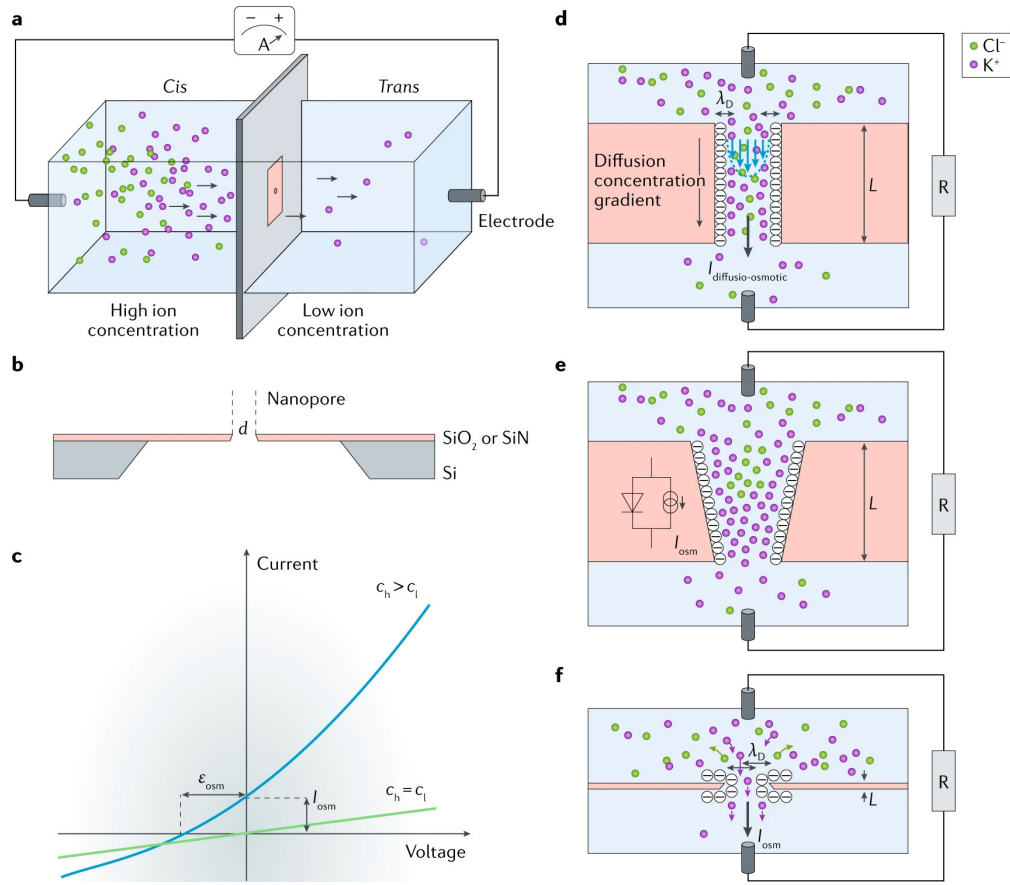


Figure 1.1:

Typical solid-state nanopore devices. a | A thin membrane is placed between two reservoirs with a salt gradient that are connected via Ag/AgCl electrodes. b | The most commonly used design consists of etched, freestanding porous membranes of either SiN or SiO_2 , which can also act, in more complex experiments, as a supporting window for suspending monoatomic layers of flat materials with nanopores. c | Typical measured current–voltage curves under no osmotic gradient (green curve) and under an osmotic gradient (blue curve). d–f | Different ways to obtain power generation: a regime with salinity gradient (panel d), which causes a diffusio-osmotic flow, with the velocity profile inside the channel dragging the charges; an asymmetric nanopore cross section (panel e), which can result in an ionic current rectification behaviour; and a flat 2D membrane (panel f). ϵ_{osm} , osmotic potential; c_h , concentration of the more salty solution; c_l , concentration of the less salty solution; I_{osm} , osmotic current; L , membrane thickness.

The driving force for osmotic power generation comes from the mixing of two solutions, one with a high concentration of salts c_h (salty water) and one with a low concentration of salts c_l (freshwater). In ideal solutions, the net flux of an ion species of valence z_i and diffusion constant D_i is given by the Nernst–Planck equation:

$$J_i = -D_i \left[\nabla C_i + \frac{z_i e c_i}{k_B T} \right] (\nabla \phi) + c_i v_i \quad (1.1)$$

where the first term comes from the concentration gradient (diffusion), the second term from an electric field gradient (drift) and the last term is related to convection. In this section, we ignore liquid flow effects, leaving this discussion for the sections on nanotubes and 2D materials, and focus on symmetric salt solutions of valence $\pm z$. In a membrane with a pore (or channel) between the two sides, a net ion flux flows owing to the concentration gradient (Fig. 1.1d–f). Neglecting fluid flow and requiring charge neutrality, we find that a local electric field proportional to the logarithm of the local ion concentration $E \approx (c(r))$ is produced to counteract the ion flux⁹⁷. If we calculate the electric potential difference between the two sides of the membrane as measured by the electrodes, neglecting any fine effects related to the pore and differences in ion activities, we find that the osmotic electrostatic potential difference can be approximated as⁶²:

$$\epsilon_{osm} = \frac{k_B T}{ze} S \ln \frac{c_h}{c_l} \quad (1.2)$$

where $S = (D_+ - D_-)/(D_+ + D_-)$ describes the ion selectivity of the system; D_{\pm} is an effective diffusion constant, and $k_B T/e \approx 25.7$ mV at 25 C. We note that, if the effective diffusion constants of the cation and anion are the same, and there is no significant deviation from the ideal behaviour (which is usually manifested by a difference in the activity coefficients of different ions), there is no driving force for osmotic power and all the Gibbs free energy of mixing dissipates into heat. If the pore is ion selective, then the flux of one charged ion species is larger than that of the other and produces a non-zero, short-circuit electrical potential difference, thus converting some of the Gibbs free energy of mixing into harvestable power^{94,98}. A more general, model-independent way of defining the ion selectivity of channels is via the electrical current I_{\pm} carried by the two different ion species⁹⁹, or via ion permeability, P_{\pm} , as:

$$S = \frac{I_+ - I_-}{I_+ + I_-} = \frac{S_+ - S_-}{S_+ + S_-} \quad (1.3)$$

which gives $S = 1$ for a completely cation-selective channel, $S = -1$ for an anion-selective channel and $S = 0$ in case of no selectivity.

Eq. 1.2 provides insight, but it overestimates the osmotic potential at high salt gradients and selectivity, so care should be taken when comparing it with experimental results. A better model is based on the Goldman–Hodgkin–Katz (GHK) voltage equation (here written for symmetric, monovalent salt solutions), which is valid for a constant electric field inside the pore¹⁰⁰:

$$\varepsilon_{osm} = \frac{P_+ c_h - P_- c_l}{P_+ c_l + P_- c_h} \quad (1.4)$$

with $P_{\pm} = K_{\pm} D_{\pm} / L$ the permeability and K_{\pm} the partitioning coefficient in the pore¹⁰⁰. The GHK voltage equation reduces to the Nernst equation for a perfectly selective pore. The Nernst potential in this case represents the maximal driving potential for osmotic power. In nature, water solutions contain a mix of different ions (Cl^- , Na^+ , Mg^{2+} , SO_4^{2-} , Ca^{2+} , K^+ , ...) that can adversely influence RED performance; for example, multivalent ions have a low osmotic driving potential and can produce adverse effects such as uphill charge transport¹⁰¹.

Ion Selectivity

Ion selectivity under a salt gradient and its response to the driving force G_{osm} define the extracted osmotic current and, thus, power. Both are related to the characteristic length scales of the electrostatic screening and surface charges. The electrostatic screening length λ_D , also called the Debye length, determines the effective range of electrostatic interactions in the solution and is larger at smaller local salt concentrations. Owing to surface chemistry effects, all interfaces between solid materials and water have a certain surface charge density, which is usually also dependent on the local salt concentration and pH¹. Aqueous salt solution tends to screen out these surface charges, forming a double layer on the surface with an increased local salt concentration. Charged ions in the solution will be repelled from the surface, producing local variations in the total charge. These local variations of ion concentration, coupled with the sample geometry, are responsible for selectivity and partially for osmotic conductance. Good selectivity is achieved when the characteristic length scale of the screened surface charge is comparable to the physical dimensions of the pore or if there is such a high level of confinement that the size of the ion hydration layer becomes relevant^{102–105}. In general, selectivity increases with smaller pore sizes, longer pore or channel lengths and higher densities of surface charges on the pore walls^{94,99}. Selectivity directly influences one important performance parameter, the energy conversion efficiency ϕ . ϕ is defined as the ratio between the Gibbs entropy of mixing and the extracted power, and is proportional to the square of the selectivity ($\phi = S^2/2$)^{62,98}. Thus, one of the design strategies for 2D nanopore power generators is to maximize their ionic selectivity by decreasing the pore size and increasing the surface charge, although the atom-sized thickness would be expected to reduce the selectivity.

Osmotic Conductance

Maximizing the osmotic conductance is another design requirement, as this determines the extracted power density. The maximal power density of a membrane is defined as the maximal power divided by the surface area of the membrane; thus, to calculate it, single pore values have to be extrapolated to the membrane scale assuming a certain maximal achievable pore density. The maximal power that can be extracted is $P_{max} = 1/4 G_{osm} \varepsilon_{osm}^2$ when the power is transmitted to an external load with the same resistance as the power generator, $G_{osm}^{-1} = RL$, and depends on both the osmotic conductivity and osmotic driving potential (selectivity)^{62,95}. Even if the energy of mixing is efficiently converted, the power still needs to be transferred to an external load or it will dissipate within the system, for example, through current backflow through the pore. The ideal pore does not allow current backflow, behaving as an electrical diode with no resistance in the forward direction and infinite resistance in the

backward direction. Such an ideal rectifying ionic power generator might be made to generate power depending only on the load¹³ $P_{max} \approx R_L I_{osm}^2$. A high level of ionic current rectification r , defined as the ratio of the current at forward bias V to the current at reverse bias $-V$, $r = |I(V)|/I(-V)$, is needed, particularly as the porosity of membranes for power generation is increased, thus decreasing their resistance to backflow. Ionic current rectification can be achieved in systems with an asymmetric geometry (Fig. 1.1e) or surface charge distribution¹⁰⁶, and has been demonstrated in conditions of concentration gradients^{107,108}. It is known that, in some conditions, ionic current rectification can be destroyed by hydraulic pressure^{109,110}, but the influence of osmotic pressure is not yet completely understood. Importantly, ionic current rectification is accompanied by ion selectivity¹¹¹ and could be used to further enhance osmotic power generation using RED with 2D materials¹¹².

Little systematic modelling has been done on the values of osmotic conductance and on its dependence on different parameters. It is known that, in long channels, the osmotic conductance is independent of the concentration gradient for pore sizes smaller than the Debye length, whereas for larger pores, it increases with increasing concentration gradients^{94,95}. In the case of 2D materials, there are, to our knowledge, no detailed studies of these effects, so we have to relate the osmotic conductance to the conductance under no salinity gradients. Neglecting finite-size effects of ions, the conductance of a pore under symmetric salt concentrations can be approximated^{113–116} as a combination of bulk surface conductance G_{bulk} and pore surface conductance G_s so that the total conductance is $G_{bulk} + G_s = \kappa \pi d^2 / 4L + \kappa_s \pi d / L$, with κ the bulk conductivity, κ_s the surface conductivity and d and L the diameter and length of the pore, respectively. G_{bulk} and G_s are connected in series with two access resistances $G_{ac}^{-1} = (d\kappa)^{-1}$, leading to a total resistance of the pore $G^{-1} = (G_{bulk} + G_s)^{-1} + G_{ac}^{-1}$. The access resistance is determined by the conductance of the region where the current converges towards the pore (which can be approximated as a hemisphere of diameter d). The contribution of the surface conductivity with respect to the bulk conductivity is defined through the so-called Dukhin length, $l_{Du} = \kappa_s / \kappa$, which can be approximated as $l_{Du} \approx |\Sigma| / 2ec$, where Σ is the surface charge density. In case of small salt concentrations, the surface charge can dominate and even modify the access resistance, as the semi-spherical cupola is influenced by the spatial extent of the double layer, which leads to the following equation, which includes both effects¹¹⁷:

$$G = \kappa \left(\frac{4L}{\pi d^2} \frac{1}{1 + 4l_{Du}/d} + \frac{2}{\alpha d + \beta l_{Du}} \right) \quad (1.5)$$

with $\alpha \approx \beta \approx 2$. This equation correctly accounts for the pore conductivity for a salt concentration of interest, but was never extended to salt gradient conditions. For nanopores in 2D materials, the access resistance is the most important contribution to the osmotic conductance, especially as the pore size decreases. In nanopores with diameters smaller than 2 nm, ion hydration effects and pore edge interactions can also contribute and provide strong nonlinear effects^{102–105,118}, invalidating this simplified analytical model. Special care needs to be taken when extrapolating finite-element models to model 2D materials with pores in the nanometre range, as continuum modelling is expected to fail at these length scales¹. We can conclude that larger pores in thinner materials increase the osmotic conductance, a competing requirement with that for small and long pores needed for high selectivity. In both cases, high levels of surface charge increase the energy extraction efficiency and power density.

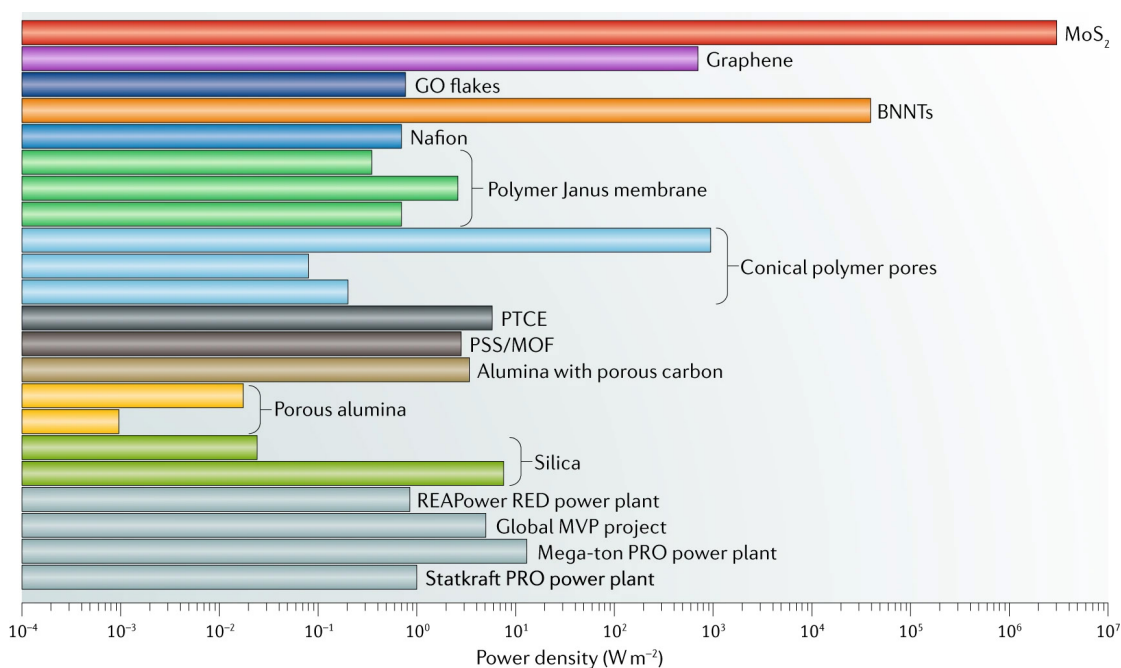


Figure 1.2:

Power densities per membrane area for different materials. Reported and/or extrapolated values of power generation density for MoS₂⁸, graphene^{96,119}, graphene oxide (GO) flakes¹²⁰, boron nitride nanotubes (BNNTs)⁷, polymers with conical pores^{68,98,121,122}, Janus membranes^{71,123,124}, poly(4-styrenesulfonic acid) (PSS) on a metal–organic framework (MOF)⁷⁴, phenol-tetrachloroethane (PTCE)^{125,244}, Nafion¹²⁶, silica^{62,127}, alumina^{61,63,128,129} and for commercial projects^{31–33,35,130}. The values for MoS₂, graphene and BNNTs are estimates based on measurements in laboratory conditions.

1.2.2 Materials for osmotic power generation

Most research on nanopore devices for blue energy harvesting emerged indirectly from research on membrane-based desalination devices^{3,43,55} and solid-state nanopore biosensors^{4–6,131–136}. The similarities in core concepts such as water permeability, ion selectivity, general stability and performance in aqueous solution lead to similar design across these devices. When considering osmotic power generators, one has to take into account general material properties such as mechanical durability under water pressure, pore edge termination, surface charges and fabrication protocols, which dictate the potential of practical usability and scalability. As opposed to conventional membrane technologies for power generation, 2D nanopore generators are still in the initial stages of research; hence, experiments are usually performed in a controlled, laboratory environment, and mostly with cation-selective membranes.

Typical nanopore devices are tested with either intrinsically porous materials, which directly yields the power density per membrane area, or with artificially made single or multiple nanopores or nanochannels. Because the power density is often used as a benchmark, single-pore measurements are usually parallelized and the results extrapolated to the theoretically achievable power density for a pore array with a certain porosity. The parameters and performance of different membranes, including commercial, solid-state and 2D membranes, are compared in Appendix Table 1. Their power densities are summarized in Fig. 1.2.

Solid-state nanopores

Before the advent of 2D materials, most of the reported osmotic energy harvesting devices were based on nanofluidic channels and solid-state pores. Solid-state porous membranes are made of various materials, such as stacked graphene oxide (GO)^{91,92,96,119,138} flakes, zeolites^{139–141} and single or aligned nanotubes^{7,119,142–145}. Most of the solid-state nanopore devices for which power generation was reported are based on polymer^{69–71,74,121,146,147}, silica and alumina membranes^{61–63,128,148–151} (Fig. 1.3).

Polymer-based devices are typically obtained via ion irradiation, ion track etching of polyamide membranes or by using commercially available perfluorinated ion-exchange membranes⁶⁷ (Nafion 117; Fig. 1.3a). These fabrication methods often yield pores with asymmetric cross-sections^{69,121,152}, which can lead to ionic diode behaviour, significantly enhancing energy harvesting. Furthermore, polymer membranes can show rich chemistry and enable unique designs, such as two-sided Janus membranes made of two different materials (such as polymer–polymer^{70,71,74} or porous alumina–polymer¹²⁸), often with different pore geometries and ion selectivity. So far, reported power densities of single polymeric membranes were in the range $2\text{--}20\text{ W m}^{-2}$, with pores of diameters from 10 nm to 50 nm^{68,69,98,147}. The downside of this approach lies in its material limitations: the membrane thickness (directly linked to harvestable power) is usually in the range of micrometres^{67–69} and can rarely be lower than 500 nm¹⁵³, which limits the osmotic conductivity. Pore-etching techniques enable vast ranges of pore densities but also yield a pore size distribution, thus resulting in a lack of precise control over the device geometry. Other often investigated materials for power generation are porous alumina and silica^{61–63,128,148–151} (Fig. 1.3b). Membranes made of these materials are intrinsically porous and have charged surfaces in solution. With present fabrication methods, it is possible to create columnar, uniform pore structures ranging from 4 nm to 200 nm in diameter, with an intrinsic porosity of up to 10^{11} pores cm^{-2} . However, the minimal thickness of these membranes is limited, ranging from 100 nm¹²⁷ to tens or hundreds of microns^{61,64}, leading to a bulk regime rather than a 2D regime. Reported power densities do not exceed 10 W m^{-2} . A significant power increase, up to 94 W m^{-2} , can be achieved by deliberately combining pores with a conical cross section with high surface charges¹²¹ (for example, using polymer coatings inside pores). Such membranes exhibit extremely high power densities but are inherently limited by the base diameter of the conical pores (often in the range of a few microns^{69,121,152}, which limits the effective pore density) and membrane thickness (limiting base osmotic conductance). All these findings indicate that, to improve the energy yield, it is necessary to increase the power density, as the energy conversion efficiency φ is already approaching the theoretical maximum of 50%. Clearly, the osmotic conductance in such systems is small. Assuming that the non-gradient nanopore conductance scaling is valid in the osmotic gradient condition, the thickness of the membrane becomes an important factor for increasing the osmotic conductance, as the bulk conductance dominates in solid-state systems, $G_{osm} \approx G_{bulk} = \kappa \pi^2 / 4L$. A good strategy could be to reduce the channel length or harness alternative conductance mechanisms, for example, by harnessing an increase of conductance from fluid flow in gradient conditions.

Nanotubes

The first real step towards high-power-density membrane materials was reported using BNNTs in 2013⁷. The device comprised a single-micron-long nanotube of 15–40 nm in diameter embedded by micromanipulation and sealed under a scanning electron microscope into a silicon nitride membrane separating two reservoirs with varying concentrations of a KCl solution (Fig. 1.3c). Power generation densities reaching the record high value (for the time) of 4 kW m^{-2} per single BNNT⁷ cross-sectional

area were reported. By applying hydraulic pressure, under no salinity gradient, the authors proved via zeta potential measurements (which probe the magnitude of the surface charge) and independent surface conductance measurements at low salt concentrations that there is an extremely large surface charge density of up to $\Sigma = 1 \text{ C m}^{-2}$ at alkaline pH. Such a high surface charge density corresponds to about six elementary charges per nm^2 , implying hydroxilation of all possible surface sites. This surface charge is responsible for an enhanced double layer inside the BNNT, which varies considerably in width between the salty and fresh reservoir. Such variation in the double layer produces local charge non-neutrality, which varies along the tube length. Because there is a potential difference between the salty and the fresh reservoir, an electric field is produced, which exerts a net volume force on the liquid. This fluid flow is called diffusio-osmotic flow and forms a plug-like velocity profile (Fig. 1.1d) that scales as $v_{DO} \approx \nabla \log(c(r))^{7,97}$ and then drags the excess cations in the channel, producing a current proportional to the surface charge⁷:

$$I_{osm} \approx \frac{2\pi R \Sigma}{L} \frac{k_B T}{\eta \lambda_B} \Delta \log(C_S) \quad (1.6)$$

that is three orders of magnitude larger than the streaming current induced by hydraulic pressure. The term $\Delta \log(C_S)/L$ can be considered as an integral of the driving force over the membrane and η is the dynamic viscosity of the fluid.

Although the extracted power density is considerably larger than in solid-state pores (on the order of 1 kW m^{-2}), the power generation demonstrated using BNNTs has a low energy conversion efficiency of $\phi \approx 10\text{--}20\%$ ⁷. We interpret this low efficiency as coming from the large opening radii of the BNNTs, a critical parameter for selectivity^{94,99} along with the high surface charge density⁹⁹. In a linear model of power generation, the osmotic conductance scales as $G_{osm} \approx R \Sigma / L \eta$ in the case of high surface charge densities and as $G_{osm} \approx \Sigma^3$ for small values of the surface charge. The main conductance mechanism is fluid flow, which is usually neglected in the case of nanochannels and bulkier nanopores, and can be enhanced by the low surface friction of certain types of nanotubes (which results in large slip lengths)⁹⁵. The diffusio-osmotic fluid flow goes in the opposite direction to the osmotic water flow and improves the water permeation of the membrane by reducing uncontrolled mixing⁹³. The diffusio-osmotic current model predicts an increase in the generated osmotic power as the ‘membrane’ thickness L is reduced, but the exact value cannot be predicted for 2D materials, in which pore access resistance is expected to strongly influence conductance^{114,116} and liquid flow¹⁵⁴. Although nanotube systems can provide high levels of power generation, the complexity of the fabrication of aligned and stacked nanotube membrane^{7,155}, along with their low energy conversion efficiency, makes upscaling unrealistic.

2D nanopores

Power density is higher for thinner membranes (Fig. 1.2). By following this trend, eventually one encounters the final limit: atomic thickness. Synthesized or exfoliated single layers of van der Waals materials used as suspended porous membranes are especially interesting for osmotic power conversion, as they are expected to be more energy dense than other membrane materials (they support a higher power generation at the same level of porosity) and can be fabricated using well-established protocols⁹⁰. In 2D materials, the dominant contribution to the osmotic conductance comes from the access resistance, whereas bulk contributions are negligible, thus the osmotic conductance (and

osmotic power density) is larger than in typical solid-state nanochannels. From nanochannels, we know that selectivity and, thus, energy extraction efficiency, reduces as the thickness of the membrane tends to zero⁹⁹. Yet, the selectivity and osmotic conductance of 2D materials such as MoS₂, graphene and hexagonal boron nitride (hBN) can match or exceed that of BNNTs. In this section, we discuss why nanopore osmotic power generators based on 2D materials can be so efficient and power dense.

The highest reported power density — two orders of magnitude higher than that obtained with BNNTs — was measured in a nanopore power generator based on monolayer MoS₂, showing an energy conversion efficiency of up to $\phi = 20\%$ ⁸. MoS₂ is a van der Waals material actively researched for general nanopore applications^{6,53,90,156–158}. A single-layer MoS₂ sheet is a semi-conducting, three-atom-thick film consisting of molybdenum atoms sandwiched by two sulfur atoms each¹⁵⁹, similar to other transition metal dichalcogenide materials. MoS₂ with nanopores in the range 2–20 nm (Fig. 1.3d) displayed the maximal generated power at a pore size of ≈ 10 nm, which, assuming a 30% porosity (roughly corresponding to 10^{12} pores cm⁻²), translates to a generated power density of $\approx 10^6$ W m⁻²⁸. The strong influence of membrane thickness on generated power in MoS₂ was confirmed by molecular dynamics simulations⁸ (Fig. 1.4a). Another candidate for 2D nanopore-based osmotic generators is graphene (Fig. 1.3e). Graphene is superior to solid-state membranes for water desalination and purification owing to its mechanical properties and high fluid permeability^{51,91,92,138,159–161}, but does not perform as well in 2D pore-based power generators, as it is estimated, based on single-pore measurements, that the power density reaches only ≈ 700 W m⁻²¹¹⁹, although with possible energy extraction efficiencies of up to $\phi = 50\%$ ^{96,119}. Tests on single-layer hBN indicate a similar level of selectivity as in graphene¹¹⁹. Clearly, there are still unexplained differences between the performances of different 2D materials, which will need to be understood to identify the optimal 2D membrane.

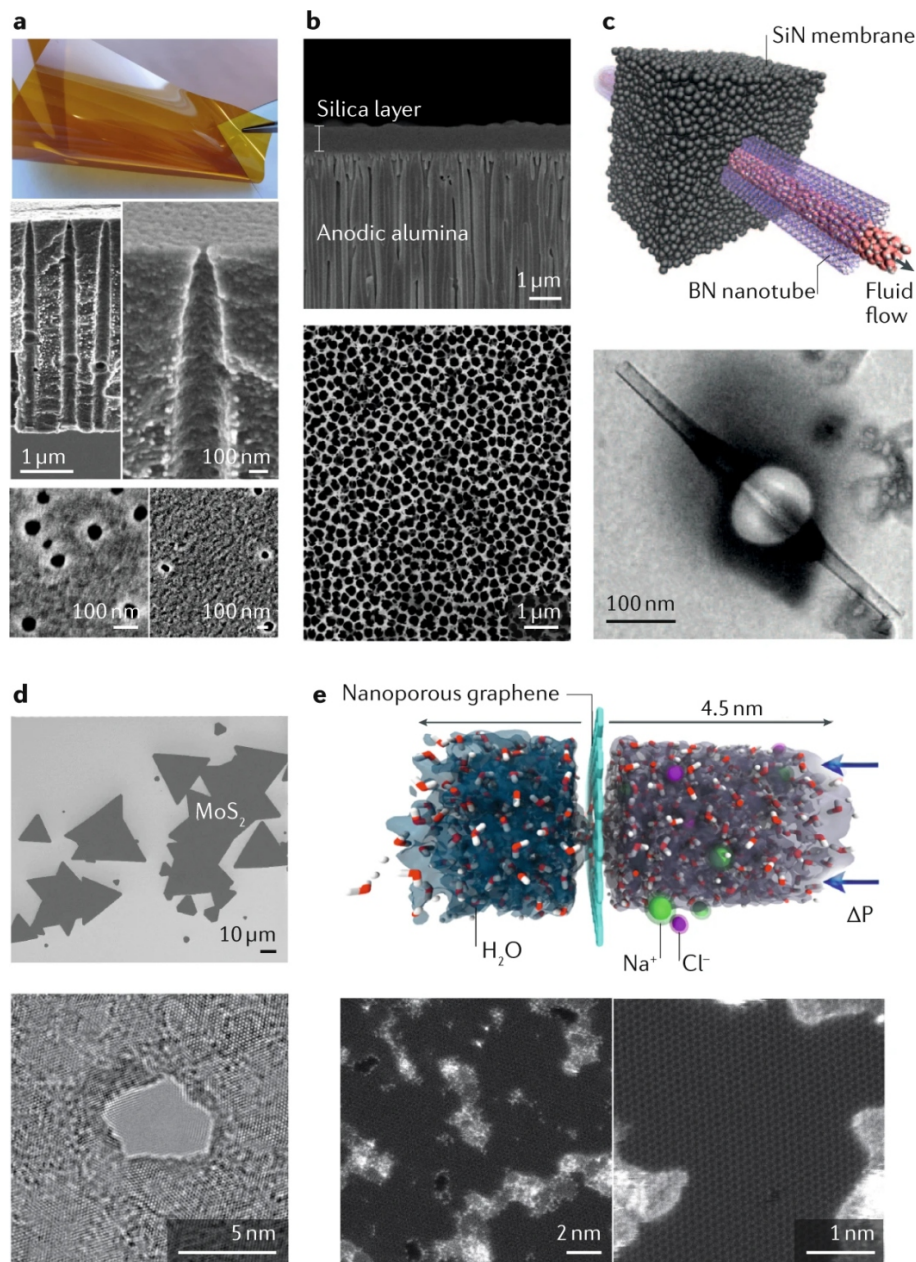


Figure 1.3:

Different materials used for nanopore power generation. a | Polymer-based thin films made of polyimide, Nafion or polyethylene terephthalate (PET) allow large-area, inexpensive membrane synthesis. Nanopores are either intrinsically and densely packed during synthesis or defined later by ion beam techniques, as shown on the scanning electron microscopy images¹³⁷. b | Scanning electron microscopy images of a cross-section and top view of highly porous membranes made of silica and anodic alumina⁶¹. c | Osmotic power generator based on a hexagonal boron nitride (hBN) nanotube embedded in silicon nitride with schematic water flow; a transmission electron microscope (TEM) image of the actual device is also shown⁷. d | Freestanding MoS₂; the magnification shows a nanopore made by TEM irradiation⁸. e | A model of a porous graphene membrane and TEM images of a freestanding graphene membrane with nanopores made using Ar⁺ irradiation^{92,138}.

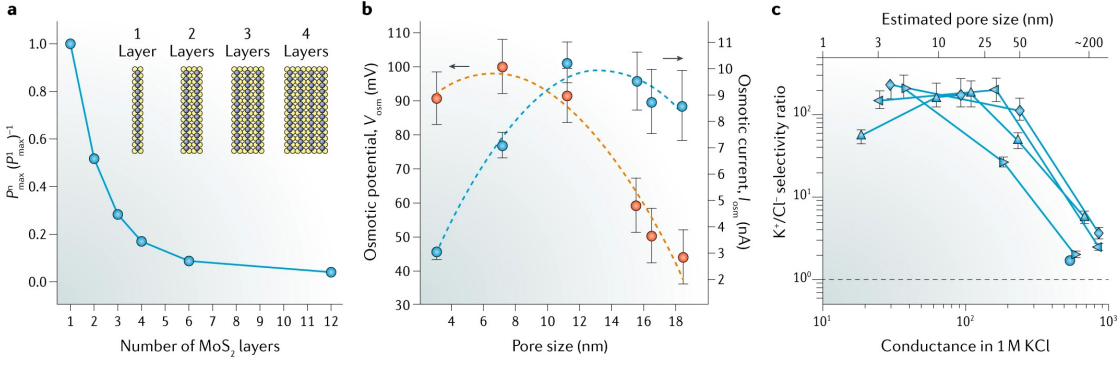


Figure 1.4:

Scaling properties of 2D nanoporous membranes. a | Ratio of the maximum power obtained from multilayer membranes (P_{max}^n) to the maximum power obtained from a single-layer material (P_{max}^1) as a function of thickness, as obtained from molecular dynamics simulations⁸. b | MoS_2 osmotic potential and current versus pore size. c | Pore-size dependence of the ion selectivity (permeability) ratio P_K/P_{Cl} in graphene⁹⁶. The selectivity can then be calculated from this ratio using Eq. 3. Each curve corresponds to one device. The conductance was measured for one pore size, then the pore was enlarged in situ and conductance was measured again. Thus, the pore diameter is not measured directly but estimated based on the current conductance.

1.2.3 Selectivity and surface charges

The selectivity of nanopores in 2D materials can be increased by reducing the pore size (Fig. 1.4b,c). The difference in pore radius is sufficient to explain the contrast in the energy extraction efficiency between 2D materials and BNNTs, because BNNTs have a pore diameter several times larger than the optimal diameter found in MoS_2 or graphene. This simple method for tuning selectivity provides an important advantage for 2D materials. From work on nanochannels and similar systems^{94,99}, we know that the surface charge is a critical factor for selectivity and that its sign determines if the pore is cation or anion selective. The pore surface charge depends strongly on the aqueous environment (pH) and steadily increases with increasing pH, with the highest surface charges obtained at alkaline pH values, well above the pH expected in natural water reserves (pH 7–8)¹⁶². It is a problem common to 2D materials and BNNTs that their surface chemistry does not support high charge densities at moderate pH. Graphene has a relatively low surface charge, as, in its pristine form, there are no chemically active surface groups. However, in the presence of externally attached surface groups (as in GO) or defects produced by plasma treatments, higher surface charges can be obtained (around 0.25 C m^{-2} at pH 7)¹⁶³, comparable to those in BNNTs (up to 1 C m^{-2} at pH 11)⁷. This increased surface charge in graphene is expected to be highly sensitive to environmental conditions and unstable. The surface charge of MoS_2 at pH 5 was calculated to be in the range of -0.024 C m^{-2} to -0.088 C m^{-2} for 2–25 nm pores⁸⁹, which is comparable to values for graphene ($\approx -0.2 \text{ C m}^{-2}$ at pH 7)¹⁶³ and nanotubes (≈ -0.1 at pH 5.5)⁷ at similar pH values. The surface charge can be enhanced by light irradiation, as was demonstrated for MoS_2 ; thus, both selectivity and power generation are boosted in natural light conditions¹⁶⁴. The surface charge, through the overlap of Dukhin lengths on the freshwater side of the membrane, is expected to provide the most significant contribution to selectivity^{99,112}. Differences in surface charges and nanopore sizes might help to explain the differences in selectivity of MoS_2 and graphene, yet one must be careful in examining these values owing to variations in sample quality and measurement conditions. The values of surface charges are usually obtained using a fit to Eq. 5 for solutions of different salinity, and the same formula is often used to determine or confirm the size of nanopores produced in 2D

materials. New approaches need to be developed to measure the surface charges of 2D materials and to reliably determine pore sizes, as well as to develop anion-selective membrane materials⁹³, which would enable the creation of stackable RED cells and further upscaling of 2D nanopore power generators.

1.2.4 Osmotic conductance

Although selectivity is known to come from surface charges, the factors influencing the osmotic conductance in 2D materials are unclear, and materials with seemingly comparable surface charges (MoS₂ and graphene) show drastic differences in osmotic conductance. The osmotic conductance is $\approx 10 \text{ nA V}^{-1}$ for graphene⁹⁶ and $\approx 100 \text{ nA V}^{-1}$ for MoS₂⁸ for 3 nm pores (at pH 11 with $c_h = 1 \text{ M}$ and $c_l = 1 \text{ mM KCl}$), which is at the base of the high power density of MoS₂. For comparison, BNNTs have an osmotic conductance of $\approx 10 \text{ nA V}^{-1}$ for much larger pores (40 nm) in the same salt conditions⁷. Standard models for 2D pore conductance in graphene and MoS₂, based on a combination of surface, bulk and access conductance contributions, cannot explain these differences between 2D materials unless there is a significant difference in surface charges and surface conductivity, something which is seemingly not supported by the observed similar selectivities. A possible explanation could be found in diffusio-osmotic flow^{7,97}, the main reason why nanotubes can compete with thin 2D membrane materials despite their micron lengths. It is known that adding flow effects increases the selectivity of nanochannels without salt gradients, with more pronounced effects in short and small channels⁹⁹. In the case of extremely highly charged BNNTs with a surface charge of up to $\approx 1 \text{ C m}^{-2}$, this diffusio-osmotic flow is the major contribution to conductance and is responsible for high osmotic currents. For 2D materials, the flow through nanopores is dominated by hydrodynamic access resistance¹⁵⁴, similar to the conductance, and, for small pore sizes, a large pressure drop between the membrane sides can build up due to electro-osmotic flow¹⁶⁵. Recent work on diffusio-osmotic flow in 2D materials indicates that, apart from surface charges, any charge on pore walls can influence osmotic conductance; the same work calculated how solute and solution fluxes scale with pore parameters¹⁶⁶. The graphene pore edge termination is charge neutral⁹⁶, so it does not induce any surface charges that could boost osmotic current for small pores, in which edge effects are more relevant. By contrast, the pore edge of monolayer MoS₂ can be terminated with either Mo or S atoms. Such termination could, in theory, be tuned^{167,168} and might allow attachment of functional groups to increase the hydrophilicity of the pore interior. The character of pore-edge chemistry (for example, attached or adsorbed hydroxyl groups) can influence the electrostatic interactions inside the pore and, thus, additionally enhance ion selectivity^{92,119,167–169}. We can even speculate that the nature of the material surface might help diffusio-osmotic flow in a similar way that hydrodynamic slip can boost osmotic power generation in nanochannels and nanotubes^{95,170}, albeit care needs to be taken to include the effects of mobile surface charges¹⁷⁰. Recent ab initio modelling indicates that there are differences in surface charge mobilities between 2D materials (graphene and hBN)¹⁷¹. In addition, if fluid flow has a major role in the osmotic conductance, graphene's high level of water permeability⁹² might become problematic, as, owing to osmosis, it would allow water to move in the opposite direction through the membrane, reducing the nanopore performance⁹³. Differences in pore edge termination and surface charge mobilities might explain the much higher power output of MoS₂ compared with graphene, especially if the effects of flow are included.

1.2.5 Optimal materials parameters

Understanding the selectivity and osmotic conductance of pores in 2D materials is critical for choosing the right material and pore size for power generation purposes. To achieve maximal power densities in MoS₂, the optimal pore size is $\approx 6\text{--}10\text{ nm}$ ⁸. We propose that this is because the osmotic conductance grows with pore size as $G_{osm} \approx d$, based on experiments⁸ on MoS₂ and modelling in related systems⁹⁵, and the selectivity (as seen from the osmotic potential) saturates with pore sizes below 10 nm (Fig. 1.4a). Recent theoretical work on the influence of access effects on diffusio-osmotic flow of uncharged solutes seems to corroborate these conclusions¹⁶⁶. Yet, as the access resistance implies a similar scaling with pore parameters as with fluid flow, it is not clear how much of the osmotic conductance comes from diffusio-osmotic flow effects. Untangling the role of diffusio-osmotic flow in the osmotic conductance of 2D membranes requires careful study of flow effects through 2D membranes, which calls for large porous membranes with well-defined pore size distributions or new, precise measurement techniques applicable to single nanopores (such as minuscule flow rate sensors¹⁷²).

1.2.6 Fabrication of 2D materials and pores

To achieve power generation using 2D or solid-state pores, it is important to take into account the role of device fabrication protocols and their influence on membrane and nanopore properties. The membrane material (typically, Si/SiN_x, Si/SiO₂, Al₂O₃, HfO₂, TiO₂, ...) has to be resistant to the working environment of the power generator, and either provide a stable support for porous 2D layers transferred on top or be thinned and processed to create pores. Generally, the fabrication processes are well established owing to the extensive and long-term use of 2D materials for solid-state nanopore sensing devices^{4–6,53,131,133–136,157,173–182} and are based on photolithography followed by 2D material transfer and pore drilling.

Membrane preparation

For solid-state pores, a typical fabrication process consists of membrane preparation (such as track etching of polymer films^{122,124,137,183,184}), chemical synthesis of the porous material (such as alumina or silica with intrinsic pores^{61,63}) or photolithography followed by wet and dry etching to obtain a substrate (such as Si, SiO₂ or SiN_x) with defined porous membranes^{59,148–151} (Fig. 1.5a–c). Such devices act either as a standalone solid-state pore system or host a monolayer material (or other porous material, such as Janus membranes) transferred on top. To host a suspended 2D film, a support membrane should ideally be mechanically and chemically stable under working conditions, exhibit good adhesion to the supported 2D layer and be easily fabricated, to allow potential upscaling (as is the case for low-stress SiN_x membranes on Si chips)⁹⁰.

2D layers synthesis and transfer

Usually, 2D layers are grown by chemical vapour deposition (CVD) or metalorganic CVD (MOCVD)^{199–212}. Both approaches have good process scalability with high material quality and crystallinity. After growth, the 2D material is transferred onto a designated substrate (the supporting membrane) via wet or dry transfer methods^{199,210,213–215}. Transfers are commonly performed by coating or dry stamping the as-grown material with a polymer (such as poly(methyl methacrylate), PMMA or polydimethylsiloxane, PDMS). As-grown 2D materials adhere to the polymer and can be separated from their growth

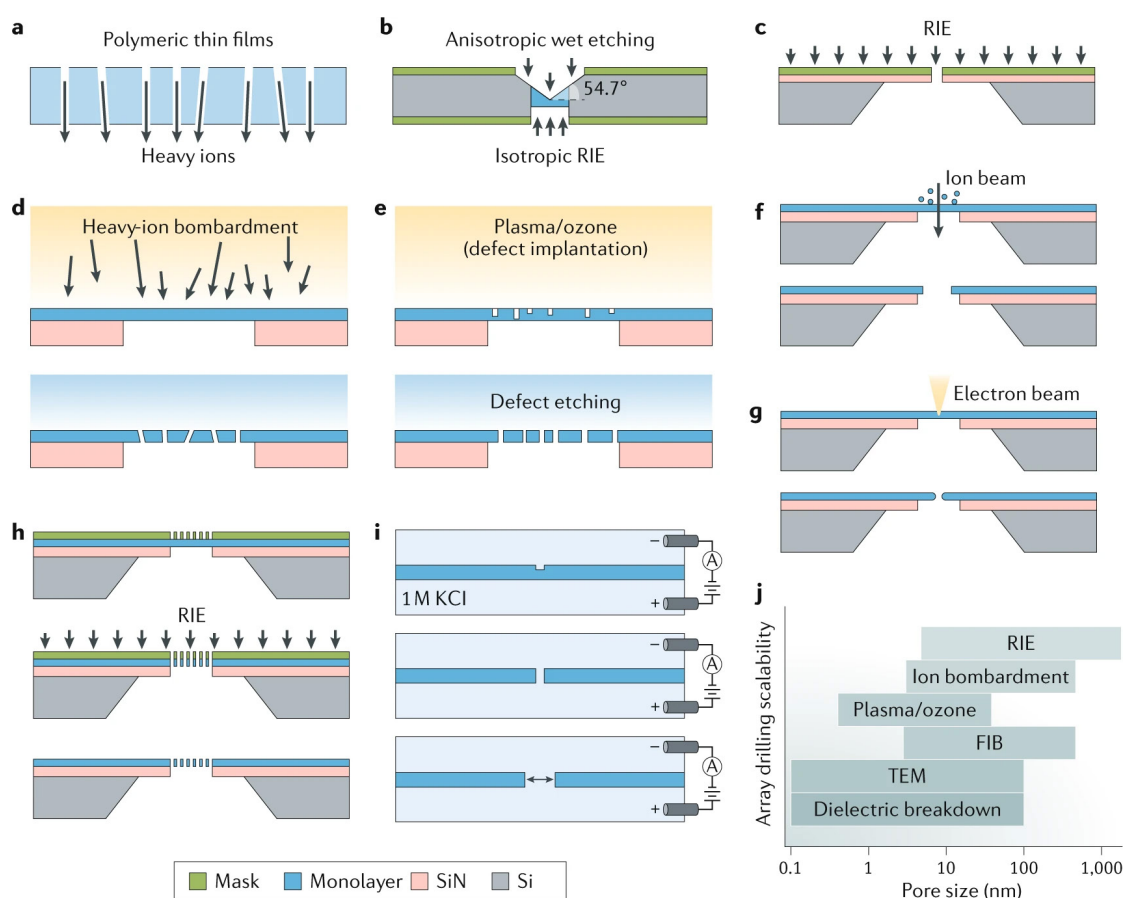


Figure 1.5:

Nanopore drilling techniques. a–c | Different nanopore drilling techniques for solid-state pores: ion track etching (panel a), based on using heavy-ion irradiation to perforate (mostly) polymeric membranes^{122,124,137,183,184}; selective wet etching (panel b), based on photolithographic processing to define pore-to-be locations and taking advantage of anisotropic etching of Si by wet etchants to precisely obtain porous structures on a Si wafer¹⁸⁵; and lithographic reactive-ion etching (RIE) on a masked membrane area of a Si/SiO₂ or Si/SiN_x wafer^{148–150,186} (panel c). d–i | Nanopore drilling techniques for 2D nanopores: heavy-ion irradiation^{187,188} (panel d); plasma or ozone irradiation (panel e), which leads to the implantation of defects that can be further etched to obtain pores^{189–191}; focused ion beam (FIB; panel f), based on heavy ions that mill through suspended thin films^{59,186,187,192–196}; the focused electron beam of a transmission electron microscope (TEM) tuned to use local irradiation damage to sputter away single atoms^{8,53,90,133,197} (panel g); e-beam lithography combined with RIE to obtain pore arrays¹⁵¹ (panel h); and dielectric breakdown or electrochemical reaction (panel i), based on applying a critical voltage to a thin layer submerged in an electrolyte that creates a nanopore due to oxidation and expansion of intrinsic defect edges^{6,198}. j | Overall obtainable pore sizes and process upscaling capabilities (going from dielectric breakdown techniques that only enable the drilling of one precise nanopore to RIE with ion bombardment, which enable theoretically unlimited and/or well-defined pore array sizes).

substrate either by wet lift-off or by slow, careful peeling. The 2D material is then transferred on the final substrate, and the polymer is dissolved (PMMA) or peeled off (PDMS); this works even on the large scale of whole Si/SiN_x wafers^{199,204,210,213,216,217}. This process is relatively quick and robust; however, because the polymer and pristine monolayer are in contact, contamination of the monolayer

is inevitable²¹⁸, often lowering the fabrication yield and limiting the usable material area. To address this problem, a lab-scale CVD growth process allowing the growth of pristine monolayers over the supporting porous membrane was proposed²¹⁹, allowing the transfer step to be skipped and achieving clean, suspended films. However, for large-scale processing and upscaling, 2D material transfer might be inevitable. Fortunately, with recent developments in CVD and MOCVD growth of various types of nanotubes^{206,220–223}, hBN²⁰², graphene^{224,225}, MoS₂^{199–212} and other 2D materials as well as new, cleaner transfer methods²²⁶, both the growth and transfer steps are no longer a bottleneck.

Nanopore drilling

The nanopore size is one of the most important factors in determining the efficiency of the generator and, ideally, should be around 7–15 nm^{8,96}. Drilling methods for solid-state pores and suspended thin films can be used to create 2D nanopores (on the lab scale); these include heavy-ion bombardment (Fig. 1.5d), plasma etching or ozone treatments (Fig. 1.5e) that produce randomly distributed pores with various diameters, and more precise techniques such as focused ion beam^{186–188,192–195} (FIB; Fig. 1.5f) or transmission electron microscope (TEM) drilling^{8,90,148,149,197} (Fig. 1.5g), in which highly focused electron or ion beams are used to create a hole through a suspended atomic membrane. Amongst these methods, TEM drilling, which exploits the controlled energy dose and a finely tuned spot size of the electron beam, offers the highest precision and enables the operator to open pores atom by atom and, more importantly, observe and measure them in situ. The downside of this technique is the susceptibility of monolayers to irradiation damage and carbon deposition^{227,228}. This phenomenon might be interesting for graphene membranes, in which, with proper heating and tuning of the beam parameters, the nanopore size can be fine tuned, exploiting the competing processes of electron-beam-induced sputtering along nanopore edges and carbon adatoms generation^{229,230}. For other materials, especially those sensitive to the electron beam, this process can be considered as contamination and might negatively influence membrane thickness and surface charges.

TEM drilling is time consuming and cost ineffective, and cannot be upscaled and automatized; thus, in principle, it is not the perfect tool for the mass fabrication of devices for experimental and potential industrial purposes. A compromise between scalability and pore size can be achieved by ion bombardment^{187,189,190}. However, this method does not offer good control over pore location and size. The pore density, interpore distance and geometrical arrangement are crucial parameters for increasing the efficiency of the generator^{231,232} 221,222, thus it is important to be able to control them. Ion techniques affording a higher precision, such as milling or low-energy ion irradiation using Ga⁺, Ar⁺ or He⁺ FIBs, might be effective in terms of batch fabrication of pore arrays or high pore densities^{59,186,187,192–195,233}. Ion irradiation works in the low-energy regime, as opposed to electron beam irradiation, thus it does not cause direct knock-on or radiation damage but, rather, atomic displacements induced by the ion collision process. The size of the pores directly depends on the ion energy and its size. For solid-state (SiN_x or SiO₂) nanopores, an initial large hole can be shrunk effectively from dozens of nanometres to a subnanometric diameter, a phenomenon attributed to the local fluidization of amorphous SiN_x or SiO₂ molecules under the ion beam, which directly leads to pore shrinking¹⁴⁸. For a monoatomic layer, however, the pore size depends directly on the beam parameters, which have to be precisely tuned to achieve the smallest pore sizes.

Graphene nanopores were fabricated¹⁹² using a helium ion microscope to precisely drill arrays of pores of 5–30 nm in diameter. The capability of the helium ion microscope for nanopore fabrication was further tested on other suspended 2D materials²³³ and, by careful tuning of focus, irradiation time and ion dose, a precise and reproducible pore formation technique was obtained. With the

achievement of 1.5 nm pores in graphene and pores smaller than 5 nm in MoS₂ and boron nitride, this semi-automatic drilling process shows great promise for batch production of lab-scale nanopore power generator devices. Another interesting approach is using lithographic processing on suspended 2D materials. By extremely careful processing and process control, it is possible to use polymer mask, e-beam lithography and dry etching to obtain precise porous arrays in graphene (Fig. 1.5h), with pore diameters down to 16 nm¹⁵¹. Alternatively, one can use defocused ion irradiation, plasma or ozone^{96,119} treatment to nucleate defects that can be further enlarged to the desired diameter by sputtering or chemical etching^{189–191} to obtain the desired pore density. However, one has to be aware that increasing the fine defects density may significantly influence the surface charges as well as compromise the membrane's mechanical stability. Finally, dielectric breakdown can be used on an untreated material to enlarge already existing point defects^{6,198} (Fig. 1.5i). This method is based on applying a specific critical voltage to a thin membrane in an electrolyte solution. Its ability to create a precise sub-nanometre pore is a considerable advantage for lab-scale experiments, but this technique inherently lacks scalability and control over the pore position and geometry. In the end, the choice of drilling method should be based on the type of 2D material and desired batch scale (Fig. 1.5j). Because all as-grown 2D materials exhibit intrinsic defects, it is important to use a technique that does not deteriorate the film further (for example, most 2D layers are fragile to electron and ion beams, and excessive irradiation can render them useless) and allows controllable nanopore fabrication. Note that film deterioration is a problem only in suspended monolayer materials. In slightly thicker layered or stacked films, it is not necessarily an issue but can decrease the osmotic power generation performance.

1.2.7 Outlook

Upscaling of osmotic power generation

The viability of 2D nanopore-based osmotic power generators as power sources largely depends on the possibility of producing large-scale membranes with high power densities and high energy conversion efficiencies. In the previous sections, we have focused on single-nanopore power generators, because 2D materials are still an emerging technology without demonstrated large-scale applications. Platforms that can lead to high generated power per single pore include membranes with conical pores, nanotubes and 2D membranes. Yet, not all of these pores can be made of equal size (Fig. 1.6) and 2D materials have the smallest possible individual pores at the same osmotic conductance. For example, conical pores have a large cone base diameter, which can be in the micron range, and, as such, are not good candidates for achieving a high power density.

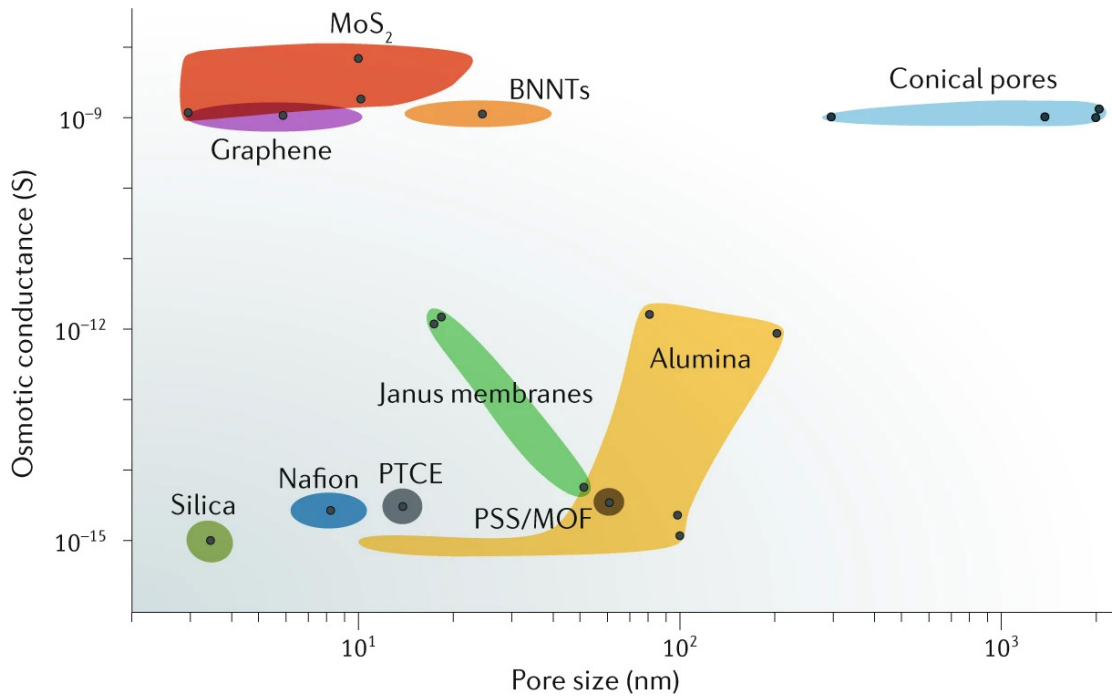


Figure 1.6: **Osmotic conductance per single pore as a function of pore size for different materials.**

The pore size is interpreted here as the largest obtained diameter in a given experiment (that is, for conical pores, it is the base diameter that effectively limits the available pore density on membrane area). The values of the osmotic conductance are calculated from the following references: MoS₂^{8,164}, graphene^{96,119}, boron nitride nanotubes (BNNTs)⁷, conical pores^{68,98,121,122}, Janus membranes^{70,71,124}, poly(4-styrenesulfonic acid) (PSS) on a metal–organic framework (MOF)⁷⁴, phenol-tetrachloroethane (PTCE)¹²⁵, Nafion¹²⁶, silica^{62,127} and alumina^{61,63,128,129}.

To achieve a large osmotic power density, an array of nanopores scalable up to industrial sizes is needed, with a high density of pores per unit area. One could naively imagine that the ionic conductance scales linearly with the number of pores N and as $N \rightarrow \infty$, $G \approx N G_{osm}$. But for thin membranes with small aspect ratios, the pore conductance is predicted²³² to scale not linearly with the array size but sub-linearly with the number of pores N , and to depend on the topology of the network. The conductance is expected to scale like $G \approx N / \log N$ for a 1D line of pores and like $G \sqrt{N}$ for a 2D array of pores (Fig. 1.7a). Such a reduction of osmotic power with increasing pore densities was also corroborated using numerical simulations for high pore densities while also including different pore sizes²³⁴ (Fig. 1.7b). The physical mechanism is related to the interactions between neighbouring pore access resistances, which effectively reduce the cross-sectional area of individual pores in the array. This effect is expected to influence the hydrodynamic flow²³² but it is not yet clear if it influences the diffusio-osmotic flow, which originates from the local concentration gradient in the pore.

Numerical simulations of pore arrays in thick membranes²³⁴ showed that osmotic power generation reaches a peak at a certain pore density (10^9 pores cm^{-2}) and then drastically decreases with increasing porosity due to the impairing of charge selectivity and strong ion concentration polarization. A nonlinear growth of diffusion current density with increasing pore density was also shown, suggesting that, with interpore distances shorter than 3,000 nm, the pore–pore interactions become important²³¹.

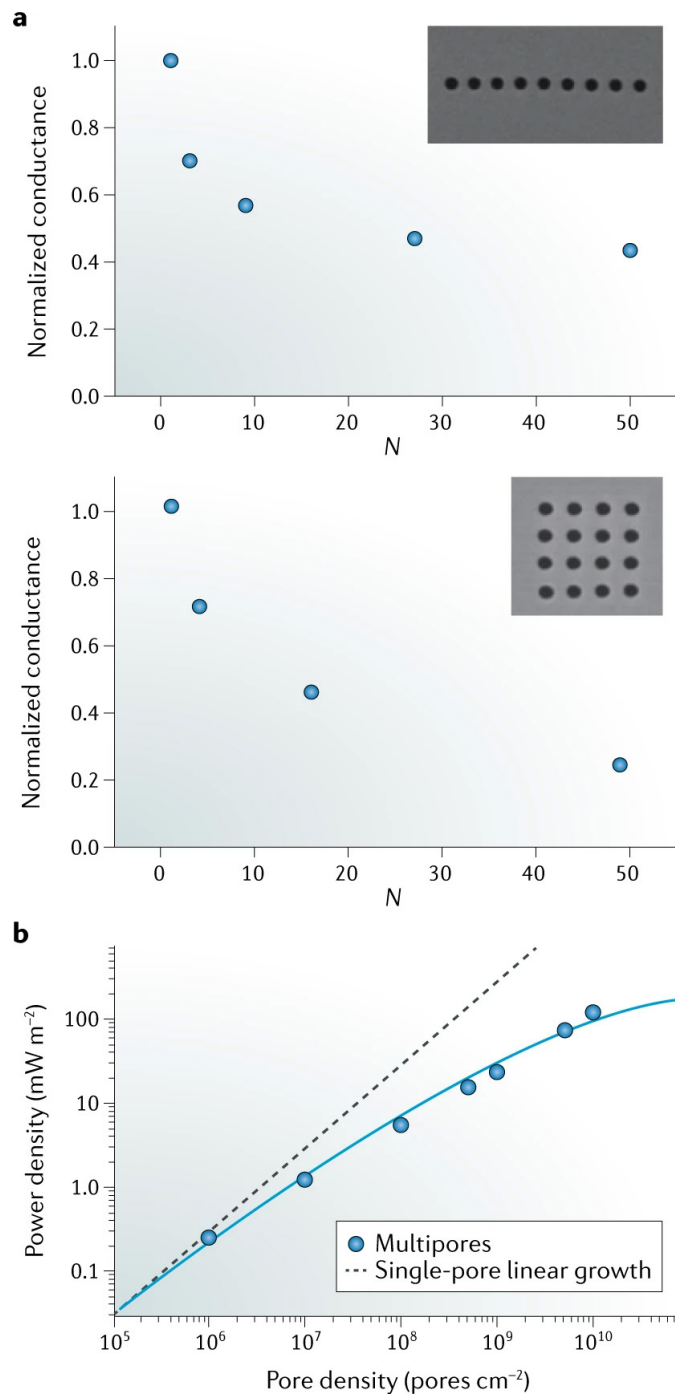


Figure 1.7:

Influence of pore density and size. a | Normalized conductance in a 1D and 2D array as a function of the number of pores, N . These results show that pore–pore interactions influence pore array scalability. b | Power density as a function of pore density for small nanopores, showing a deviation from the ideal linear growth²³⁴. Panel a is adapted with permission from ref.²³², AIP Publishing.

These simulations were confirmed by an experimental study carried out on 10 nm pores in a 1 μm thick polyethylene terephthalate (PET) film, and it was finally concluded that single-pore models for predicting power generation scaling are not valid for high pore densities (above 10^7 pores cm^{-2}). These interaction effects originate from the overlap of charge concentration clouds of nanopores in the array, which reduces selectivity and osmotic current²³⁴. Consequently, care has to be taken when extrapolating single-pore power generator values to macroscopic membranes. Notably, these simulations did not include fluid flow effects and peculiarities of 2D materials. The effect of pore density on power generation has not yet been tested experimentally in 2D systems, but it is clear that there is interplay between the interpore distance, the Dukhin length of the system and pore entrance effects, and that individual pore osmotic generation is compromised at high pore densities. A conservative estimate for MoS_2 with a porosity of 10^7 pores cm^{-2} gives a power generation density of $\approx 1 \text{ kW m}^{-2}$, which is still a considerable improvement on the best membrane materials in use today. The most cost-effective way to produce such high pore densities in 2D membranes would most likely involve using chemical etching or ion bombardment techniques, which are both currently under active development^{153,188,192,196}.

Pore functionalization

Another interesting topic related to osmotic energy harvesting and its practical use is the exploration of the ionic diode behaviour of the nanopores to ensure efficient transmission of power to external loads and to enhance osmotic power generation performance. Substituting cylindrical for asymmetric conical pore shapes enhances the ion current flow in one direction, causes ionic current rectification due to geometry-induced concentration polarization¹¹⁰ and can produce high power density and energy conversion efficiency^{121,122}. With the ionic diode behaviour due to a preferential direction for ion flow, any back current is effectively suppressed. This kind of geometrical functionalization is typically explored in thicker, solid-state pores made of glass, SiN_x or PET due to fabrication feasibility. The ionic diode behaviour can be further upscaled and adjusted by using various functionalization approaches to modify the pore walls, such as polyelectrolyte brushes^{121,122,235}. PET conical pores were functionalized with polyelectrolytes¹²¹, which resulted in an osmotic energy yield of 120 pW (the same order of magnitude as the yield of a boron nitride nanotube) and an energy density of 945 W m^{-2} . Other studies^{124,128,236} also demonstrated the potential of using ionic current rectification in energy harvesting from desalination. In theory, this effect could be coupled with 2D materials by constructing a large array of conical pores acting as an access channel over which a 2D material with a large pore density would be placed. In addition to acting as a mechanical support for the membrane, such an array could boost the performance of osmotic power generators based on 2D materials.

Although pore-wall functionalization can be used in thick materials for tuning and enhancing ion selectivity, as well as producing ionic current rectification, its influence on atomically thin materials is limited. What can be done on this scale is to chemically modify the surface around the pore. Such functionalization is especially viable for graphene, which has relatively low surface charges, but, in principle, could also be implemented for MoS_2 and other materials to increase or induce specific positive or negative ion selectivity in the system. This was observed in graphene, in which surface functionalization using N or F atoms made the pores cation selective²³⁷. Such selectivity can be achieved by proper tuning of any neutrally charged pores. Cation selectivity in sub-nanometre neutral graphene, for example, was studied in connection with partial dehydration of K^+ ions and pore edge modifications²³⁸. Another functionalization approach is to dope the 2D layers with certain molecules to change or tune the surface charges, boosting the efficiency of the device²³⁹. Because the surface charge seems to have an enormous impact on osmotic energy generation, doped 2D materials might

open up new ways to increase performance.

Challenges of 2D porous materials

When considering the potential application of membrane-based energy harvesting systems in the river–seawater environment, one has to pay special attention to fouling. Nanometric pores tend to attract large particles and become clogged when exposed to volatile contamination. In such cases, cleaning 2D nanoporous membranes either chemically or mechanically is, at least to say, problematic or even impossible. Besides that, monoatomic membranes (especially if they are porous and pretreated during fabrication) are fragile both on the micro and macro scale (at which unwanted defects can lead to lower power output and even to a material tear), which makes the whole device delicate and problematic to use in real environments. A compromise might be achieved with thicker nanopore membranes, with which the power output is traded for better mechanical and chemical stability and more feasible fabrication cost efficiency. A different pathway would be to engineer a design of conical channels supporting a highly selective 2D material to further increase the energy density. Interestingly, some 2D materials may exhibit anti-biofouling properties, which can be activated by material functionalization or light irradiation (for example, photocatalysis in MoS_2)^{169,240,241}. Light irradiation might additionally boost the power generation performance, especially for small pore sizes¹⁶⁴ 154. However, learning from solid-state PRO/RED research, without significant energy output, the power generator will not be efficient enough to either be commercially viable or to sustain itself, since defouling or (if necessary) water pretreatment processes usually require a massive amount of energy^{49,50,54}. It is still unclear what requirements for water treatment 2D materials will have, but their successful use in desalinization research is encouraging for developing practical applications.

There are techniques to remove larger particles from water sources, but the presence of multivalent ions constitutes a problem. Multivalent ions like Ca^{2+} or Mg^{2+} have been shown to reduce the power output of systems by up to 50%¹⁰¹, yet this simple fact is often ignored by the membrane community. The power output reduction happens because of several interconnected phenomena^{101,242}: the osmotic potential is lowered because it is inversely proportional to the valence of the ion; there is ‘uphill transport’ of multivalent ions against the concentration gradient; and there is an affinity of the membrane to different ion charges. 2D materials can provide interesting solutions to these problems. The variation of pore size and surface charge can produce membranes with varying degrees of selectivity to monovalent or multivalent ions⁹⁶, which can be stacked to first repel multivalent ions and then proceed to harvest the salinity gradient with monovalent ions²⁴². The degree to which technical solutions can tackle fouling and the presence of multivalent species will determine the membrane’s practical applicability. As this emerging technology starts to be implemented, its applicability might be limited to working with hypersaline solutions and brines, which are expected to provide better energy yields with smaller power consumption for water pretreatment⁵⁰.

There is a huge scale gap between the research and development of solid-state membranes for PRO/RED technologies and that of 2D materials, due to the almost half a century of prior research on current membrane technologies. Although there are phenomena that we still do not fully understand or know how to exploit, we can learn lessons from 2D materials such as MoS_2 and apply them to other systems. With thousands of possible monolayer van der Waals materials²⁴³, only a few have been explored in terms of osmotic energy harvesting^{244–247}. A major step would be performing more detailed computational studies of important material properties (such as surface charge in solutions and pore edge terminations) of other monolayer materials. Other functional materials that have not yet been fully examined for osmotic energy harvesting applications might also be very promising as flat

membranes. MOFs, made of a metal oxide cluster within an organic matrix, might be a candidate, as they offer outstanding functionalization possibilities and control over pore density and spacing, and have nanometric thickness and mechanical stability. MOFs are proven to perform as well as porous membranes⁷⁴, with the strong advantages of tuneable ion selectivity, extremely high possible porosity (up to 90%) and thickness as low as a few nanometres (for MFI zeolite nanosheets^{182,248}). Another promising material group might be stacked monolayer materials. Such heterostructures are attractive because they allow yet another level of functionalization and material properties control. Proper composition of stacked 2D layers could hypothetically boost the efficiency of osmotic energy harvesting even beyond the best reported values. Yet, obtaining such stacks in a controllable, repeatable and contamination-free way to achieve pristine interlayer interfaces is still a challenge.

Conclusions

2D membranes are an emerging technology that could be crucial for tapping into blue energy. Efficient membranes for osmotic power generation require high power densities and energy extraction efficiencies. 2D materials excel in both of these categories, providing power densities that are several orders of magnitude higher than those of current membrane materials that are undergoing large-scale testing. However, there are issues that still need to be addressed to fully understand the physics of osmotic power generation in these systems and, more importantly, to enable a wider and more practical usage of this technology. The nature of ion selectivity needs to be addressed with more systematic experimental studies of surface charge and pore size effects, particularly with the aim of obtaining also efficient anion-selective membranes via surface functionalization. A better understanding of the mechanisms for the generation of the osmotic conductance, and especially of the role of fluid flow in 2D materials, will enable the design of better membranes. Extensive experimental studies on the fabrication and upscaling of 2D pore arrays along with a diligent investigation of multipore systems will show how close we can get to the outstanding extrapolated estimations of power densities. 2D membranes would be best utilized in combination with other materials to remedy their inherent weaknesses, for example, materials with asymmetric pore geometries or supporting membranes with asymmetric cross sections. By learning from the fast advancement of graphene from discovery to practical applications in the past 15 years, we believe that 2D materials could find their place in real-world RED applications within a similar timescale.

1.3 Molybdenum disulphide (MoS₂) - properties

Classified as a transition metal dichalcogenide MoS₂ in its bulk form is a silver solid exhibiting semiconductor properties with indirect bandgap of 1.23 eV²⁴⁹, similar to silicon. Structurally, MoS₂ is a Van der Waals (VdW) material: a crystalline material composed of atomically thin atomic layers held together by weak Van der Waals forces, composed of molybdenum atom plane sandwiched between two sulfur atom planes (Fig. 1.8D). These three hexagonal planes are covalently bonded and form a single MoS₂ monolayer of 0.65 nm of thickness (0.317 nm distance between sulfur atoms plus the distance of VdW gap). Such a three-atom thick 2D film is not only a prime candidate for efficient nanoporous membranes as discussed in previous section but also a direct-gap (1.8 eV²⁵⁰ in a monolayer form) semiconductor with unique electronic properties²⁵¹, widely studied in micro- and nanoelectronics field. MoS₂ naturally occurs in either of two semiconducting phases: the hexagonal 2H-MoS₂ and rhombohedral 3R-MoS₂, sharing similar physical properties and trigonal prismatic coordination with lattice constant of $a = 0.316$ nm. A third known phase, tetragonal 1T-MoS₂ with octohedral coordination

exhibits metallic properties, however, is only obtainable synthetically through alkali metal intercalation, electron beam irradiation or mechanical stress²⁵², and is metastable, converting back to 2H phase spontaneously with time or by microwave radiation²⁵³. Various examples of monolayer MoS₂ (forming truncated triangles), imaged by optical and electron microscopy are presented on Fig. 1.8.

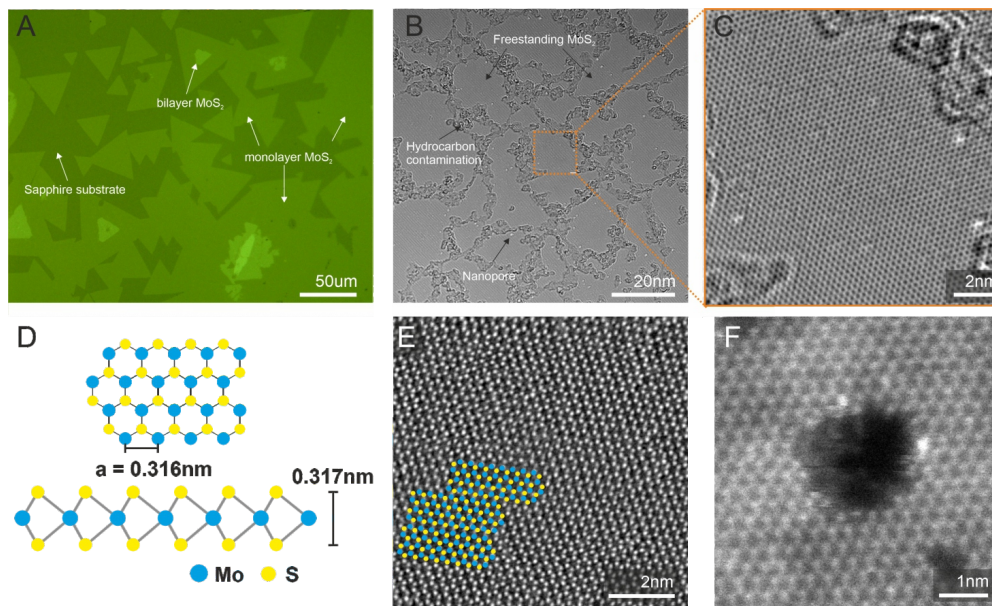


Figure 1.8:

MoS₂ in micro- and nanoscale. A showcase of typical MoS₂ features as imaged by optical microscope (A), a suspended film imaged by HRTEM (B) with local hydrocarbon residues with closer look at the best achievable lattice contrast (C). Atomic structure of the MoS₂ monolayer (2H-phase) with lattice constant and S-Mo-S distance (D) is visible only with using scanning transmission electron microscopy (STEM), here overlaid on the STEM image (E). An example of an e-beam drilled nanopore imaged by STEM is presented on panel (F).

1.3.1 Monolayer MoS₂ Synthesis methods

There are several approaches towards synthesizing monolayer materials²⁵⁴. Most common top-down one is the mechanical exfoliation, known as scotch-tape method, widely used for peeling apart practically all VdW, layered crystals such as graphene, hBN, MoS₂ and other transition metal dichalcogenides. Similarly, a liquid-phase exfoliation with alkali (e.g. lithium) metals can be used to produce mono- and multilayer MoS₂ flakes in large batches. These methods however do not yield a continuous atomically thin film which can be turned into a nanofluidic membrane, especially not on large-area substrates. For this application, a bottom-up approach such as Chemical Vapor Deposition (CVD) or Metallorganic Chemical Vapor Deposition (MOCVD) can be utilized. Here, one can directly synthesize monolayer material on the target substrate. Due to its hexagonal lattice symmetry, MoS₂ forms triangular single crystals (Fig. 1.8A) which shape can range from truncated triangles to hexagons, star-shapes or tree-like dendrites, depending on the growth conditions²⁵⁵. The main vision of this thesis is to develop, research and apply suspended nanoporous membranes, therefore the main focus from here on will remain on CVD and MOCVD synthesis methods.

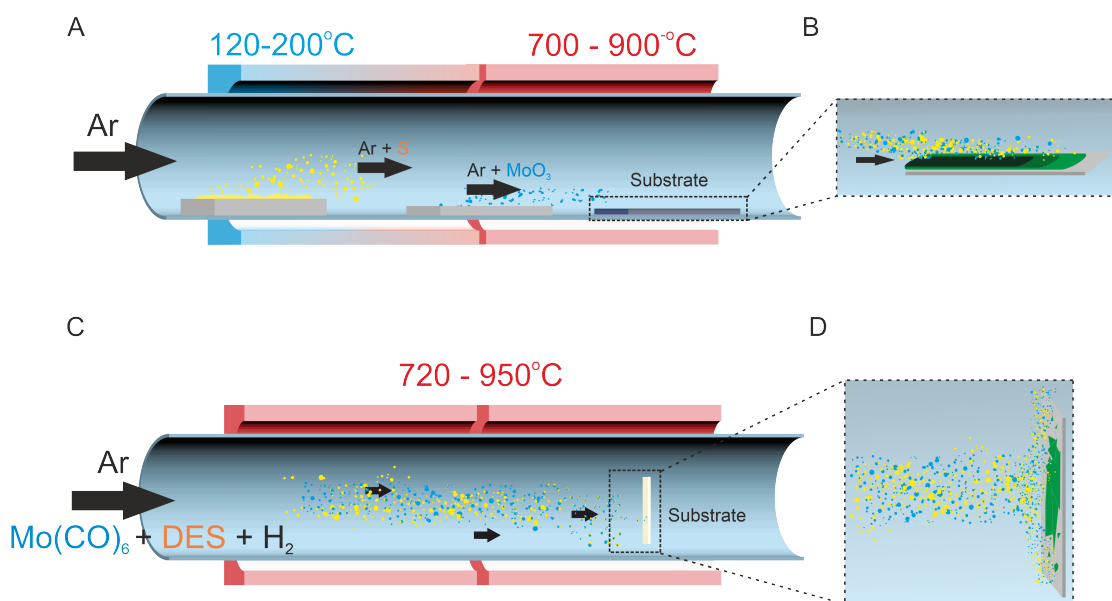


Figure 1.9:

CVD and MOCVD synthesis of MoS₂. In CVD approach (A), a sulfur is placed upstream, by the colder part of the furnace and its vapor is carried by carrier gas (Ar in this example) to the substrate area. Similarly MoO₃ which should be located at higher temperature zone, around its volatilization point ($\approx 700^\circ\text{C}$). Growth result consists of gradient-areas of various thickness, depending on the distance between quartz boats with precursors (B). MOCVD approach rely on using only gaseous precursors (C) such as H₂S or diethyl sulfide (DES) and Mo(CO)₆ thus it is much more versatile and repeatable in reaching the uniform and constant Mo:S ratio all over growth substrate area (D).

Chemical Vapor Deposition (CVD)

Chemical vapor deposition is a process which allows to deposit thin crystalline films on substrates from volatile, vapor-phase precursors, typically at high temperatures allowing precursor reaction or decomposition. For MoS₂, the most conventional CVD synthesis uses a tube furnace setup with solid sulfur and molybdenum trioxide (MoO₃) as precursors. Sulfur is kept in a quartz boat in the colder part of the furnace (typically downstream), at around its melting temperature (120-200°C). The MoO₃ boat is placed at higher temperature zone of the furnace, closer to the growth substrate. Volatile S and molybdenum oxide particles are carried by the ambient flow of inert gas (argon or nitrogen) and react at the substrate surface forming MoS₂ crystals. Growth temperature at the substrate location ranges from 700 to 900 °C to allow thermal reduction and disulphide formation (Fig. 1.9A). MoS₂ can be synthesized on amorphous substrates such as SiO₂ or Si₃N₄, although best reported results are obtained using EPI-polished, c-cut sapphire (Al₂O₃), which surface after annealing in 1000°C in air form atomically flat terraces. The commensurability of the sapphire and MoS₂ lattice allow to control MoS₂ lattice orientation thus enabling epitaxial growth on centimeter scale²⁵⁶. Over years, various modifications of CVD process were reported, making the CVD synthesis more facile and obtained material more uniform and reproducible^{257,258}. Use of alkaline salts such as sodium chloride impacts the MoS₂ nucleation density and increases the surface reaction rate leading to large monolayer crystal formation^{259,260}. Various studies using seeded growth promoters²⁶¹ or localized, pre-deposited, stencil-templated MoO₃²⁶²⁻²⁶⁴ were performed to improve growth location controllability. Early MoO₃ sulfurization (sulfur poisoning) is commonly occurring problem limiting the reaction output. To prevent that, attempts were made to shield molybdenum precursor from direct sulfur

exposure before its volatile particles can reach the substrate surface²¹⁰. The addition of active gases such as hydrogen²⁶⁵ or oxygen^{210,266} was practiced to activate the surface, controllable etch thick, multilayer crystals. Another modifications of the CVD process include use of molybdenum foil instead of oxide powder²⁶⁷ for slow and continuous Mo- supply and use of gaseous H₂S as a sulfur source²⁶⁸ to further improve the material quality and growth uniformity.

Albeit rapid and relatively cheap method of high-quality monolayer synthesis, CVD has significant limitations. Reproducibility and growth uniformity are far from perfect. Reliance on vaporization of solid precursors inside the furnace lead to significant variations of the precursor supply during the growth. These depend on the precursors quartz boat locations in relation to the growth substrate^{269,270}, a parameter which is notoriously hard to replicate from growth to growth. This also leads to uneven crystallization due to the gradient of precursor mass flow. Shape, size and thickness of the MoS₂ depends on the local ratio of Mo:S species able to react and form the crystal^{255,271}. Therefore, material tends to grow thicker in the center of the substrate, on areas closer to the evaporating precursor boats, and thinner on the less exposed to Mo and S edges (Fig. 1.10). This alone, makes the CVD process, commonly used for small-size substrates, challenging to adapt for large-area growth.

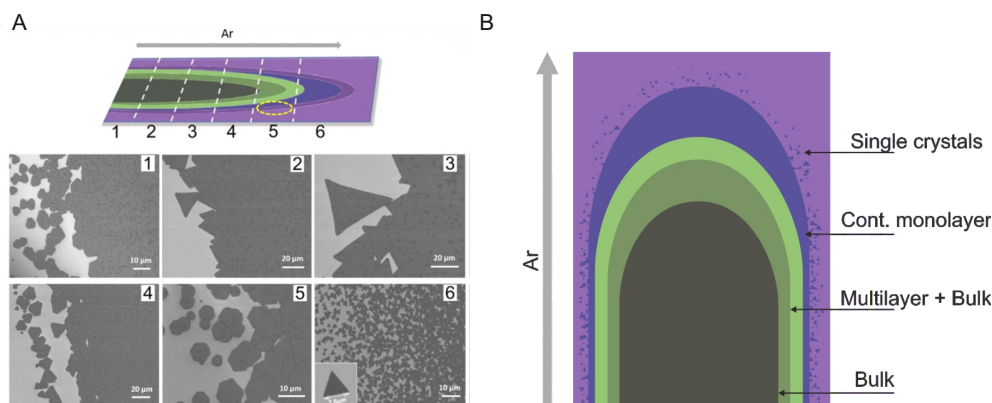


Figure 1.10:

CVD coverage limitations Crystal size variability (A) depending on the substrate area and distance from the Mo and S source²⁵⁵. Center of the substrate is usually unusable, due to large bulk overgrowth with single crystals occurring at the edge area (B).

Metalloorganic Chemical Vapor Deposition (MOCVD)

A use of metalloorganic precursor instead of solid powder metal source was the key to unlock the scalability needed for the MoS₂ synthesis on a scale larger than a toenail (or what is considered in nomenclature as a "chip" or a "lab" scale). In general, MOCVD can be conducted in the exact same CVD setup with the exception of using only gaseous precursor materials. All metalloorganic sources should consist of a metal (molybdenum in this case) with organic ligand, able to thermally decompose or reduce under the high-temperature growth conditions. Molybdenum hexacarbonyl (Mo(CO)₆) is an example of this material and is commonly used as a metal source in MoS₂ growth synthesis along with sulfur gas in the form of either vaporized diethyl or dimethyl sulfide (DES and DMS) or pure gaseous chalcogen hydroxide (H₂S). Following the most common example and setup used in this thesis: Mo(CO)₆, DES/DMS are kept in separate bubblers placed in thermal baths for these materials partial pressure highly depend on their temperature. A carrier, inert gas (Ar) is used to flow through bubblers and transfer the material to the growth reactor. A precise control over the amount of the

precursor is possible by fine tuning their pressure and temperature while keeping ambient, carrier gas flow constant. Moreover, additional process modifications such as use of active gases to aid in ligand decomposition or reaction rate (e.g. H_2 or O_2) during the process are possible and often employed to improve the growth yield. All while maintaining uniform precursor distribution, necessary for precise and repeatable process control. Use of gas-phase only sources is highly promising as it, in principle, due to gas-flow uniformity allows to grow monolayer material on any substrate size that fits in the MOCVD furnace⁶⁴. Including standard for the semiconductor industry 4-inch wafers. It is however a challenging task, as the following chapters of this thesis will further discuss.

1.3.2 MoS₂ as a nanoporous membrane

Fabrication steps towards nanoporous membrane and its desired parameters are discussed in previous section 1.2.6. Solid state porous Si/SiN_x membranes are used as a support for freestanding MoS₂ (Fig. 1.1). The most important aspects of the porous device are the thickness of the MoS₂ film - ideally atomically thin, and pore diameter as most of the important ion-transport physics scale with these dimensions. Fine-tuning these properties dictates whether the device will be suitable for osmotic power generation, water filtration, biosensing or gas-flow sensing applications²⁷². Typical nanopore diameter should be below 10 nm in order to maintain ion-selectivity necessary for energy harvesting⁶ and below 2-3 nm to study DNA translocation²⁷³ or nanoscale ion transport phenomena such as hydration shell shredding^{102,274}, gas permeation²⁷² or artificial mechanosensing¹². Therefore, to progress general nanofluidic research using nanopores a nanometric precision is highly anticipated.

1.4 Motivation

It is clear, that the key to advancing the status quo of applied single-pore devices and chip-scale membranes is large-area synthesis and fabrication. As discussed in previous section, most of the nanoporous membrane devices investigating energy harvesting lack scalability. Providing a solution to make atomically thin membranes in batches with controllable nanopores will not only enable to scale up the potential power generation and experimentally demonstrate the viability of this technology but also might open up the path towards commercial applications. These especially are needed now, in the times of emerging global energy crisis. In addition to that, with large pore arrays and high device fabrication yield the ion-transport phenomena in nanoscale can be thoroughly examined and probed on multi-pore systems as opposed to single-pore ones. To achieve all of that, a facile and reproducible MoS₂ large-area synthesis method is necessary. MoS₂ transfer methods need to be revised and tuned to match large-area substrates. Finally a methodology to create precise nanopores on a large scale has to be engineered. All of these process steps have to be devised with not only "uniformity" and "precision" as highest characteristics but also with "reproducibility". Characteristics, which are sometimes mutually exclusive and notoriously lacking in nanotechnology and nanofabrication.

1.5 Thesis Structure

The following chapters of this thesis present the path towards establishing the large-scale fabrication methodology of 2D nanoporous membrane devices. Developed methods are used for MoS₂ device fabrication and investigation of the fundamental physics of nanopore systems and thin films in aqueous solutions. In particular, chapter no. 2 presents the chronological efforts and progress in large-area, con-

tinuous, monolayer MoS₂ synthesis via CVD and MOCVD processes. Chapter no. 3 shows the approach of using FIB irradiation for engineering and studying optically active defects in MoS₂ and hBN as well as nanopore drilling on suspended MoS₂ membranes. The automatic computational script is used to analyze and classify nanopores based on high resolution electron micrographs and gather the statistical data on pore geometries and edge composition. Finally, Chapter no. 4 presents the application of nanoporous membranes in the nanofluidics study. The measurements are performed in the flowcell setup specifically designed to apply a hydrostatic pressure on the membrane. Experiments shown in Chapter 4 investigate the very fundamental aspects of the 2D membranes in aqueous solutions such as nanobubbles pinning, wetting and membrane adhesion artifacts. Insights and gained knowledge is used to further investigate the ion transport properties and nanopore behaviour under applied strain in the context of mechanosensing ion channels and osmotic power generation in salinity gradients.

An important note is that most of the projects presented here were done with collaborative efforts of the Laboratory of Nanoscale Biology members. In particular, the nanofluidics study discussed in Chapter 4 was performed in close collaboration with Dr. Sanjin Marion, who designed the hydrostatic-pressure experiments and worked on numerous improvements on the measurement setup and data analysis.

2 Large-area synthesis of MoS₂ monolayer film

Following sections discuss the experiments and accomplishments leading towards large-area synthesis. Chronologically, first concepts revolved around improving and modifying CVD recipes which soon shifted towards the use of gas-precursor MOCVD growth methodology. Experiments were performed at tube-reactor furnace with all gas connections initially designed and constructed by me and dr. *H. Cun* and later, accompanying instruments such as mass flow controllers, valves, line heating and vent lines adapted solely by me. The same setup (explained in details in each section, along with recipe details) was used for both CVD and MOCVD experiments.

2.1 MoS₂ CVD synthesis on location-specific area

2.1.1 Overview of the approach and motivation

The initial experiments were inspired by the work of Waduge et al.²¹⁹ who demonstrated monolayer growth directly on the membrane with apertures. Such an approach allow to eliminate the need to transfer the material from growth substrate onto the device and make nanopore-device fabrication faster and relatively easier. As discussed in Section 1.2.6 Fabrication of 2D materials and pores, currently used transfer methods introduce a potentially **highly contaminating step** to the device fabrication pipeline. Avoiding it would in principle improve general fabrication yield significantly. All location-specific growth attempts discussed below were done with powder-precursor CVD approach.

2.1.2 Location-specific synthesis with lithographic mask

To tackle that challenge with a large-scale processing in mind, instead of demonstrated chip-scale²¹⁹, an approach of using a large-scale chip holder was conceived. A holder was made of thin alumina plates which was design to hold multiple devices, each with size typically of 5x5mm(2.1A and B). Placed on top of the boat containing MoO₃ and NaCl and subjected to sulfur vapors in a CVD reactor it was meant to enable direct material synthesis on the

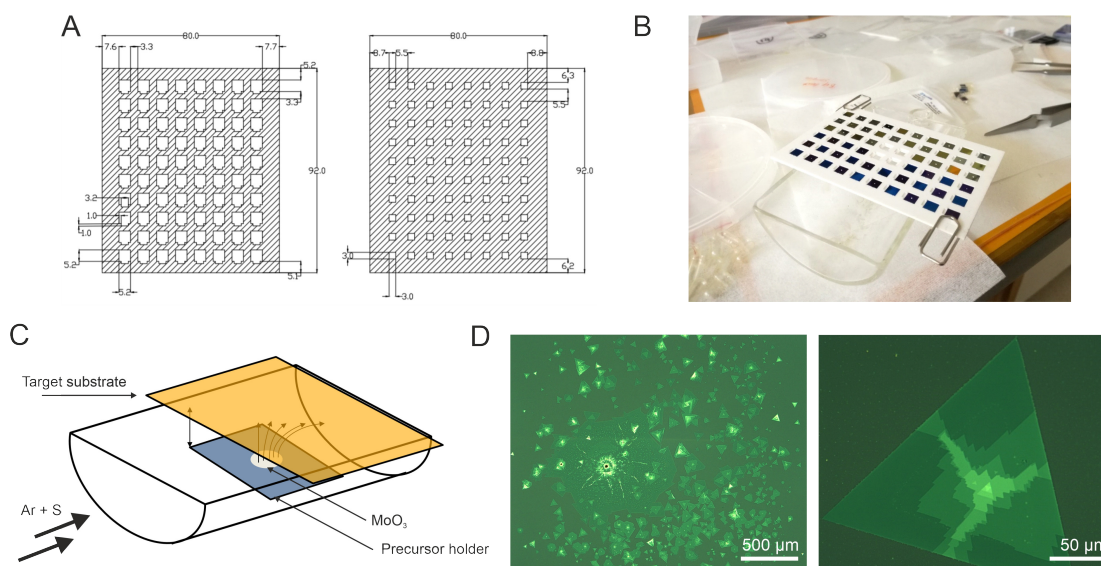


Figure 2.1: **Location-specific synthesis.** A) alumina chip holder allowing to hold 80 devices (B) during the CVD process. C) a schematic of the precursor and substrate placement during the growth and D) optical images of growth localized in holder's square localized area.

apertures (Fig. 2.1C). The results were however not satisfactory. Albeit locally producing good quality monolayer crystals (Fig. 2.1D), significant portion of devices were either not exposed to Mo and S vapors enough to promote large crystals forming or were rendered unusable due to bulk MoS₂ growth on the areas closest to the powder precursor source. Optical images and detailed map of MoS₂ coverage is presented in Appendix, figure A.1 and A.2. Unfortunately, even if devices were placed in the "green", monolayer zone of the holder the crystal growth was too unpredictable and not location-specific enough. Even the smallest variances in the precursor-substrate distance and amounts of MoO₃ and NaCl and their placement in the quartz boat are significantly impacting the results. It quickly became obvious, that using powder precursor is not a repeatable nor reliable way of synthesizing thin films directly on devices.

2.1.3 Stencil lithography of MoO₃ and location-specific growth

To improve the specificity of the growth area it was clear, that one has to control the location of Mo precursor. The use of powder MoO₃ in a quartz boat does produce large-area results however resulting, synthesized material's uniformity is far from desired uniformity. A solution was to use stencil lithography to evaporate arrays of MoO₃ spots on sacrificial substrate which would be placed face-to-face with target device, as depicted on Fig. 2.2.

The established lithographic techniques allowed to create wafer-scale masks and thermal evaporation methods enabled large-area MoO₃ deposition with precise thickness. Various masks designs were fabricated on SiN_x/Si wafers and tested (Fig. 2.3A). Arrays from 20x20

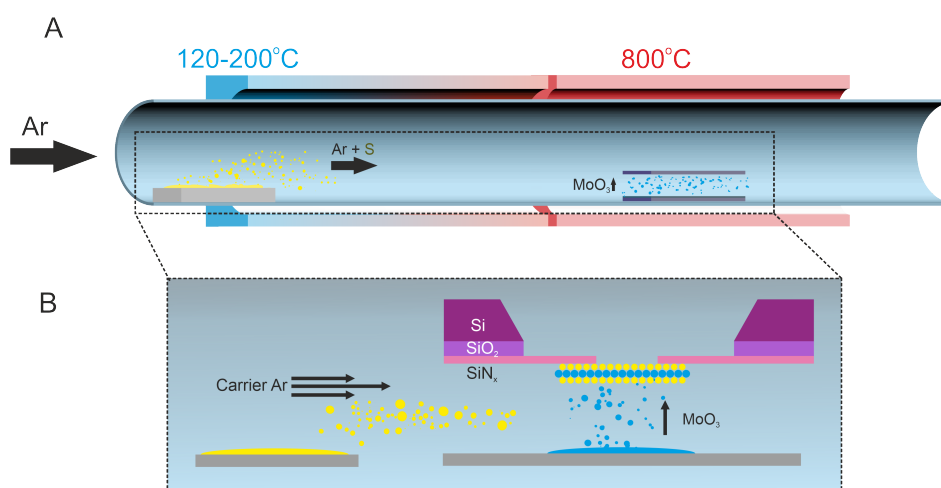


Figure 2.2: **Stencil MoS₂ synthesis schematic.** Concept of stencil assisted synthesis using conventional CVD setup (A). Stencil-evaporated MoO₃ is evaporating and form MoS₂ directly on the target substrate (membrane device) (B).

up to 100x100 spots, 20 μm in diameter, were used to deposit Mo precursor with various thicknesses ranging from 1 to 50 nm (Fig. 2.3B). All of that to explore and probe best possible conditions to achieve a repeatable monolayer growth using this new synthesis method. Our findings were following: distance between the sacrificial MoO₃ array-holding chip and target substrate should be precisely controlled and minimized to limit sulfur vapor flow and too fast sulfurization (sulfur poisoning) which leads to premature reaction stopping. Therefore, stencil mask fabrication, thermal evaporation and chip positioning had to be precisely maintained to enable results.

Optimal MoO₃ thickness was set to 5 nm with x-y array distance of 100 μm . Target substrate had to be either coated or placed in the vicinity of NaCl for large-crystal growth. Growth results varied, best ones yielded localized near the evaporated arrays MoS₂ crystals (Fig. 2.3C) which would merge to form continuous film (Fig. 2.3D: bright green circles are the remnants of the evaporated array). Signature characteristic of stencil-assisted MoS₂ growth is the presence of bulk, unreacted molybdenum oxysulfide spots where the MoO₃ array was deposited - both at the sacrificial chip as well as target substrate.

2.1.4 Conclusions

Even with precisely localized synthesis with MoO₃ arrays, experiments soon stumbled across an immovable obstacle. During the experiments with Si/SiN_x solid state porous devices we found that membrane aperture acts as a nucleation site of MoS₂ crystal. This in turns made the aperture hopelessly clogged and thus rendered this growth approach non viable. Examples of overgrown MoS₂ on membrane chips are presented in Appendix figure A.3. Therefore further attempts to grow the material in-situ on devices were stopped.

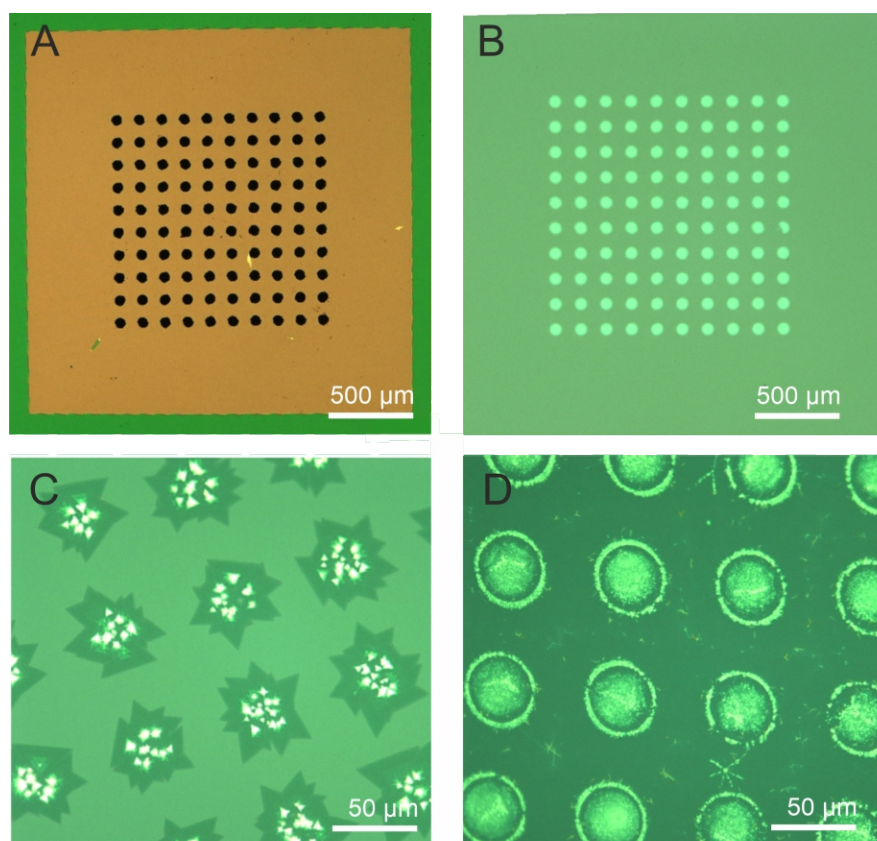


Figure 2.3: **Stencil MoS₂ synthesis.** Optical images of a membrane with etched holes (A) which was used to thermally evaporate MoO₃ with precise thickness on sacrificial SiN_x chip. Results were ranging from localized single crystal domains (C) to fully covered, continuous areas (D) with bulkier MoO₃ reaction remnants (bright spots).

Moreover, we reached a conclusion that the use of powder-CVD to grow anything on large areas reproducible is virtually impossible. All attention was shifted to develop the recipe using gaseous Mo(CO)₆ and diethyl sulfide as precursors instead of solid powder.

2.1.5 Methods

CVD furnace All experiments were performed in a 4-inch hot-wall tube furnace (MTI OTF-1200X-II). Substrates were either SiN_x/Si, SiO₂/Si chips cleaned in IPA and acetone or SiN_x/SiO₂/Si membrane devices with an aperture of 50-100 nm in the nitride window. Typical process involved keeping sulfur in a quartz boat at low temp. zone and using carrier argon flow when the substrate zone reached reaction temperature (700-800 °C). Furnace was then vented and cooled down naturally.

Stencil masks fabrication Stencil masks for MoO₃ evaporation were done from scratch on SiN_x/Si wafers using Heidelberg VPG200 laser lithography system and etched with SPTS APS

dielectric plasma etcher. Arrays were design in formats of 20x20, 30x30, 50x50 and 100x100. Holes were kept at 20 μm in diameter with 70-100 μm distance between each.

Thermal evaporation Thermal evaporation of MoO₃ was done at Leybold Optics LAB 600H and at Alcatel EVA600. Thickness of evaporated MoO₃ was kept at 5nm.

2.1.6 Acknowledgements

I want to acknowledge Davor Capeta from Center for Excellence for Advanced Materials and Sensing Devices, Institute of Physics, Bijenička 46, 10000, Zagreb, Croatia, for help and assistance with stencil-growth attempts. Part of the work was done on his small-scale CVD setup with in-situ camera that enabled to observe live the crystal growth during the process.

2.2 Wafer-scale MOCVD growth of monolayer MoS₂ on sapphire and SiO₂

The following section is based verbatim on the following publication:

Huanyao Cun^I, **Michal Macha^I**, HoKwon Kim^{II}, Ke Liu^I, Yanfei Zhao^{II}, Thomas LaGrange^{III}, Andras Kis^{II} and Aleksandra Radenovic^I

Wafer-scale MOCVD growth of monolayer MoS₂ on sapphire and SiO₂, Nano Research, 2019.

H.C. wrote the manuscript; H.C. and M.M. build the setup, research data for the article and performed MOCVD experiments, M.M. performed AFM and SEM imaging, H.K performed XPS measurements, Y.Z. performed electrical transport measurements, T.L. performed STEM imaging. All authors discussed the contents and provided important contributions to the manuscript.

Full manuscript and supplementary information is available online.

2.2.1 Abstract

High-quality and large-scale growth of monolayer molybdenum disulfide (MoS₂) has caught intensive attention because of its potential in many applications due to unique electronic properties. Here, we report the wafer-scale growth of high-quality monolayer MoS₂ on singlecrystalline sapphire and also on SiO₂ substrates by a facile metal-organic chemical vapor deposition (MOCVD) method. Prior to growth, an aqueous solution of sodium molybdate (Na₂MoO₄) is spun onto the substrates as the molybdenum precursor and diethyl sulfide ((C₂H₅)₂S) is used as the sulfur precursor during the growth. The grown MoS₂ films exhibit crystallinity, good electrical performance (electron mobility of 22 cm² V⁻¹ s⁻¹) and structural continuity maintained over the entire wafer. The sapphire substrates are reusable for subsequent growth. The same method is applied for the synthesis of tungsten disulfide (WS₂). Our work provides a facile, reproducible and cost-efficient method for the scalable fabrication of high-quality monolayer MoS₂ for versatile applications, such as electronic and optoelectronic devices as well as the membranes for desalination and power generation.

2.2.2 Introduction

The transition metal dichalcogenides (TMDs) are an emerging class of two-dimensional (2D) materials with unique properties, which lead to wide applications in novel electronic and optoelectronic devices^{275,276}. Monolayer molybdenum disulfide (MoS₂) is a representative TMD with excellent chemical stability, promising electronic and optical properties. Thus MoS₂ has been used to realize field effect transistors (FETs) with the high current on/off ratios²⁷⁷,

^ILaboratory of Nanoscale Biology, Institute of Bioengineering, EPFL, Lausanne, Switzerland

^{II}Nanoscale Electronics and Structures, Institute of Materials Science and Engineering, EPFL, Lausanne, Switzerland

^{III}Interdisciplinary Center for Electron Microscopy (CIME), EPFL, Lausanne, Switzerland

photodetectors²⁷⁸, valley devices²⁷⁹, energy harvesting⁸ and catalysis^{280,281} etc. In order to realize the full potential for harnessing its attractive properties, a crucial bottleneck is how to synthesize uniform monolayer MoS₂ with high-quality on a large scale with low-cost and in a reproducible manner. Recently, various approaches have been developed to obtain monolayer MoS₂, such as mechanical exfoliation²⁸², liquid exfoliation²⁸³, sulfur annealing of dip-coated ammonium thiomolybdate layer⁵³, sulfurization of molybdenum oxides^{217,284}, chemical vapor deposition (CVD)^{22,256,285–287} and metal-organic CVD (MOCVD)^{64,288,289}. However, the conventional CVD method typically involves vaporization of molybdenum trioxide (MoO₃) and sulfur inside a heated zone of the growth chamber^{22,256,285,286}, which limits control of the vapor phase composition, nucleation density, deposition rate and coverage, thus leading to poor reproducibility. The MOCVD method allows more reliable control of the evaporation rates of the solid precursor such as molybdenum hexacarbonyl (Mo(CO)₆). In addition, the role of alkali metal promoter in enhancing the lateral growth of monolayer MoS₂ has been intensively discussed in different processes including CVD and MOCVD methods^{64,200,259,289–291}. However, the MoS₂ domain size is limited to a few micrometers either with a growth period of time up to 26 h⁶⁴, or by employing highly toxic and flammable compound H₂S as sulfur precursor with an acceptable ceiling concentration of only 20 ppm²⁹², which might not be attractive for industrial applications due to the relatively long growth time and limitations of the practical settings of using toxic H₂S gas. Here, we report a facile and improved approach to synthesize high-quality large-area monolayer MoS₂ film on silicon dioxide (SiO₂) and sapphire substrates at 2-inch wafer scale in a MOCVD chamber. The molybdenum (Mo) precursor is provided with a spin-coated aqueous solution of sodium molybdate (Na₂MoO₄) on the substrates prior to the growth, where the amount of Mo is controlled with appropriate concentration of the Na₂MoO₄ and the rotation speed. The Na₂MoO₄ solution also provides alkali metal promoter (Na) for the monolayer MoS₂ growth. The amount of sulfur is regulated precisely by controlling the flow rate of non-toxic organic compound diethyl sulphide (DES, (C₂H₅)₂S) during the growth. 10 sccm H₂ is introduced into the growth chamber to assist the synthesis process. The grown monolayer MoS₂ films not only show structural continuity maintained uniformly over the entire wafer, but FETs fabricated with transferred MoS₂ achieve electron mobility of 22 cm² V⁻¹ s⁻¹ at room temperature. This is a significant improvement over the growth morphology obtained without using additional alkali metal halides and allows a reproducible and cost-effective way to synthesize 2D TMDs.

2.2.3 Results and Discussion

To synthesize monolayer MoS₂, molybdenum and sulfur precursors were prepared separately. The preparation process is illustrated in the Fig. 1(a). Prior to the growth process, sapphire substrates are annealed in a quartz tube in the air at 1100 °C for 1 h to achieve clean and atomically flat surfaces. In the first process step, the substrates (sapphire and SiO₂/Si) are treated with 25 wt.% potassium hydroxide (KOH) solution to increase their hydrophilicity for better wetting. Afterward, an aqueous solution of Na₂MoO₄ is dropped and then spin-coated with certain speed on the surface to achieve a uniform layer of Mo precursor. Subsequently,

the spin-coated substrates are introduced into a quartz tube with a 2-zone MOCVD hot-wall furnace setup as depicted in Fig.2.4(a). Previous work of Boandoh et al.²⁰⁹ involved two stages of two types molybdenum precursors of Na₂MoO₄ and Mo(CO)₆. In addition, the Mo and S precursors are mixed in the same bubbler at the second stage. In this work, we apply spin-coated Na₂MoO₄ exclusively as the sole Mo precursor, and the single sulfur precursor is supplied by liquid (C₂H₅)₂S, which is stored in a stainless steel bubbler and connected to the quartz tube with a mass flow controller (MFC) to precisely control the amount of the required sulfur precursor.

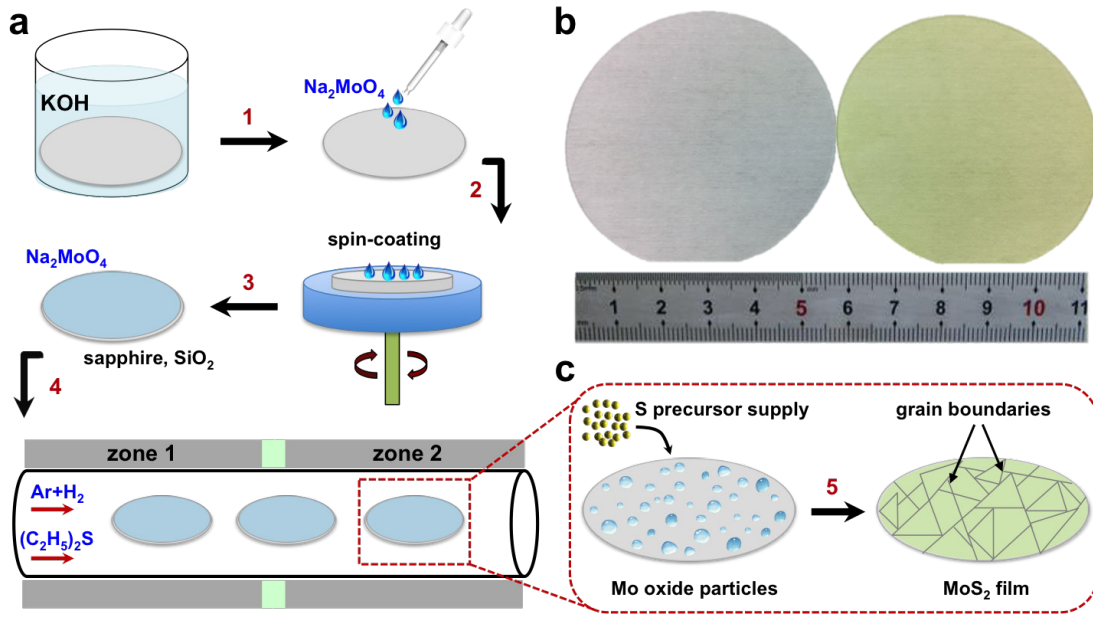


Figure 2.4: Schematic illustration of wafer-scale MoS₂ film growth process. (a) Growth procedure: (1) KOH treatment to increase the hydrophilicity of growth substrates; (2) drops of Na₂MoO₄ is applied on the surfaces; (3) spin-coating of Mo precursors; (4) forming sodium molybdate layer on the surfaces; (5) placing the spin-coated substrates in the MOCVD quartz tube, and introducing (C₂H₅)₂S while using Ar and H₂ as carrier gases. (b) Photos of the 2-inch wafers of clean sapphire substrate (left) and as-grown MoS₂/sapphire (right). (c) Proposed mechanism for MoS₂ growth on the substrates.

Typical growth involves carrier gases with the flow rate of 350 sccm of Ar, 10 sccm of H₂ and 8 sccm of DES at the growth temperature of 850 °C for ≈ 20 min (details see Experimental section). The reaction mechanism of the growth process, which obeys a typical surface-limited growth mode, is schematically illustrated in Fig. 2.4(c). Initially, sulfur precursor (C₂H₅)₂S decomposes into various hydrocarbon sulphides (C_xH_yS) at high temperature⁶⁴ and reacts with the spin-coated Mo precursor sodium molybdate at a growth temperature of 850 °C, inducing nucleation of MoS₂ grains with Ar and H₂ flow. The hydrogen is proposed to play double roles during the synthesis process: (1) as a reduction agent for molybdenum oxide [28] to form MoS₂; (2) as a chemical etchant, which promotes chemical etching effect (desulfurization of MoS₂)²⁹³. That is, excess concentration of H₂ promotes rapid decomposition of precursors (leading to growing) and desulfurization (etching) of MoS₂ flakes, respectively. The

combination of the two effects results in the eventual MoS₂ film. Therefore, a moderate H₂ gas flow is important to synthesize large-area and continuous monolayer MoS₂. Figure S2.9 in the Supplementary Material displays the effect of various H₂ flow rates on the quality of MoS₂ film on SiO₂. Based on the experimental results, the optimal H₂ flow rate is 10 sccm, which can substantially decrease the nucleation density of MoS₂ (Fig. S2.9(e)). The grains grow larger gradually and merge to form a continuous film with optimal growth time of \approx 20 min. Figure 2.4(b) displays the photographs of the clean sapphire wafer (left, transparent) and typical as-grown MoS₂ film (right, greenish yellow) at the 2-inch wafer scale.

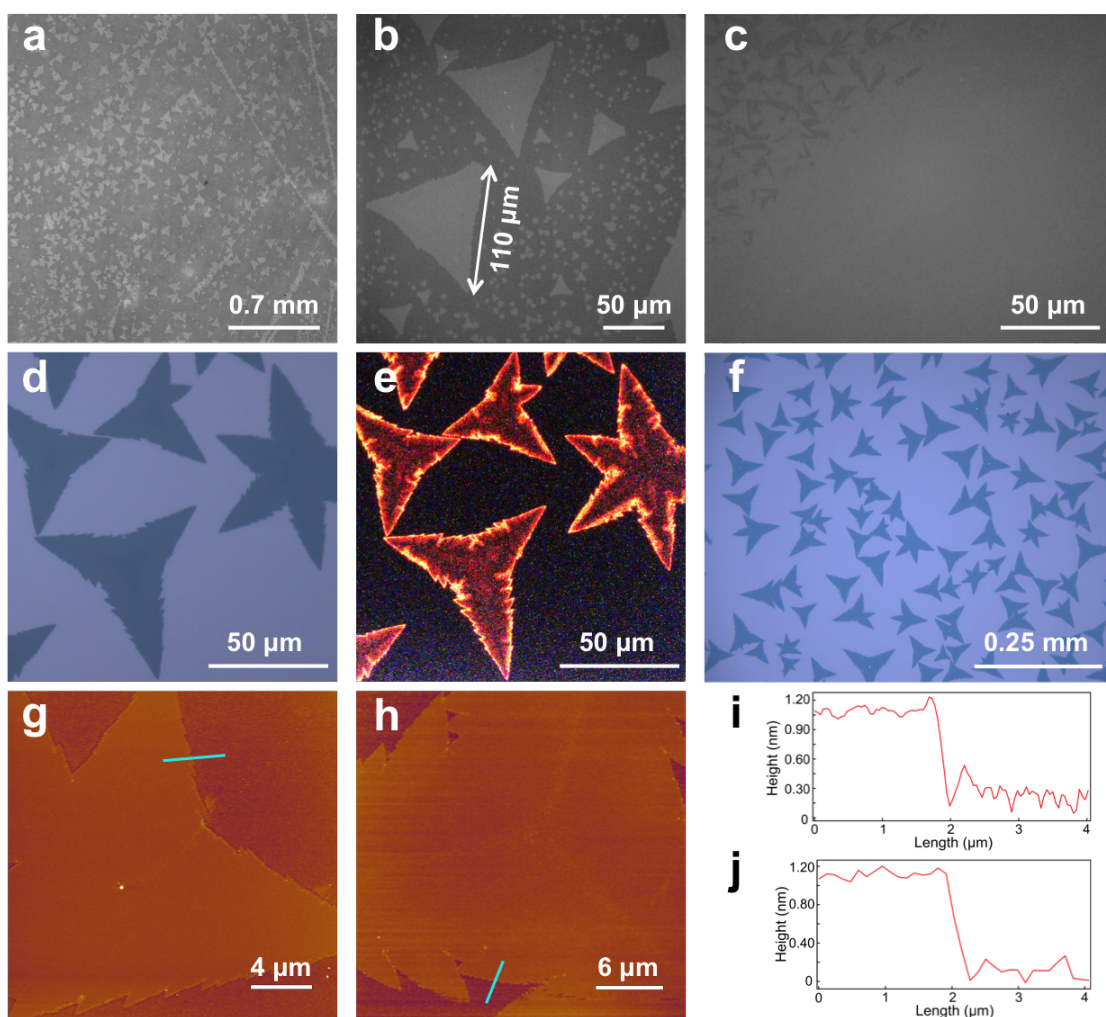


Figure 2.5: Characterizations of as-grown MoS₂ films on sapphire and SiO₂. (a)–(d) and (f) Typical optical images of as-grown MoS₂ on sapphire (a)–(c) and on SiO₂ (d) and (f). (a) Large-area image of MoS₂ partial-coverage at low magnification. (b) Zoom-in image shows big MoS₂ flakes larger than 100 μ m. (c) MoS₂ flakes merge to form a continuous film at high coverage. (e) PL image of the same area as in (d). The red flakes are monolayer MoS₂. (f) Large-scale optical images of MoS₂ on SiO₂. (g) and (h) AFM images of as-grown monolayer MoS₂ on sapphire (g) and on SiO₂ (h). (i) and (j) Line profiles showing the thickness along the two light-blue lines in (g) and (h).

Figure 2.5 shows a series of optical microscope images of as-grown MoS₂ on sapphire (Figs. 2(a)–2(c)) and on SiO₂ (Figs. 2.5(d) and 2.5(f)). A typical large-area of as-grown MoS₂ is demonstrated in Fig. 2.5(a), in which the contrast of the triangular MoS₂ flakes is lighter than the bare sapphire substrate (white-gray). The zoomed-in optical image in Fig. 2.5(b) of a partial-coverage wafer shows big triangular MoS₂ flakes up to 110 μm . Figure 2.5(c) displays an almost-completed continuous monolayer merged with many triangles of MoS₂. Figures 2.5(d) and 2.5(e) are the same area of typical as-grown MoS₂ on 270 nm of SiO₂/Si substrate. Figure 2.5(d) shows the optical contrast of MoS₂ domains and bare SiO₂ for a zoom-in area, while the photoluminescence (PL) of the same area is displayed in Fig. 2.5(e), where the MoS₂ flakes are excited with a red laser. A larger area of typical as-grown MoS₂ on SiO₂/Si substrate is shown in the Fig. 2.5(f), which exhibits the homogeneous distribution of MoS₂ flakes on the SiO₂ surface. Better views of scanning electron microscopy (SEM) imaging of as-grown MoS₂ on sapphire and on SiO₂ are displayed in the Fig. S2.10 in the Supplementary Information. The detailed morphology of further zoomed-in flakes of as-grown MoS₂ monolayers on sapphire (Fig. 2.5(g)) and on SiO₂/Si substrate (Fig. 2.5(h)) are measured with atomic force microscope (AFM). The flakes are flat and are stitched together from different triangles (domains) with a film thickness of ≈ 0.7 nm. The cross-sectional line profiles from the MoS₂ flakes in Figs. 2.5(g) and 2.5(h) are displayed in the Figs. 2.5(i) and 2.5(j), individually.

Raman and PL measurements of multiple MoS₂ grains on sapphire and on SiO₂ indicate the monolayer character of MoS₂ films. Figures 2.6(a)–2.6(c) are the optical images of as-grown MoS₂ on SiO₂ (Fig. 2.6(a)), transferred MoS₂ on SiO₂ (Fig. 2.6(b)) and as-grown MoS₂ on sapphire (Fig. 2.6(c)) while Raman and PL spectra were measured. Figures 2.6(d) and 2.6(e) show representative Raman and PL spectra for as-grown MoS₂ on SiO₂ (red), transferred MoS₂ on SiO₂ (blue), as-grown MoS₂ on sapphire (green) and bare sapphire (black). Raman characteristic peaks of in-plane vibrational mode E'_{2g} and out-of-plane mode A_{1g} are at 384 and 403 cm⁻¹ respectively for as-grown MoS₂ on sapphire. The E'_{2g} and A_{1g} peaks show no split, and the distance between the two peaks is 19 cm⁻¹, indicating the monolayer nature of as-grown MoS₂²⁹⁴. The full width at half-maximum (FWHM) of the E'_{2g} and A_{1g} peaks are 5.1 and 6.6 cm⁻¹, suggesting that the density of defects of as-grown MoS₂ film is very low²¹⁰. The positions of peaks shift slightly for as-grown MoS₂ on SiO₂ (383.1 and 404.2 cm⁻¹) and for transferred MoS₂ on SiO₂ (384.1 and 401.9 cm⁻¹) because of different adhesion force, which does not affect the monolayer feature due to narrow FWHM of the peaks (21.1 and 17.8 cm⁻¹). The FWHM of few-layer MoS₂ is broader (e.g., 25.7 cm⁻¹). Room temperature PL spectrum of as-grown MoS₂ on sapphire (green) in Fig. 2.6(e) exhibits a strong emission from the A exciton at 1.83 eV with a narrow FWHM, which is the characteristic of the direct band gap of monolayer MoS₂^{250,295}. The variations of PL peaks of monolayer MoS₂ grown on sapphire (green) and on SiO₂ (red) can be attributed to nonuniform strain fields within different MoS₂ flakes grown on different growth substrates (SiO₂ and sapphire). This may be caused by the sample cooling procedure, where some parts of MoS₂ flakes pinned to the substrate while some parts are relaxed due to difference in the thermal expansion coefficient of the different substrates. After the transfer of MoS₂ on 270 nm SiO₂/Si substrate, the maximum

peak position of the PL spectrum (blue) shifts 9 meV, which is expected from the thermal expansion coefficient mismatch between bulk MoS₂ and SiO₂. These features are in good agreement with the high-quality monolayer MoS₂^{250,294,295}.

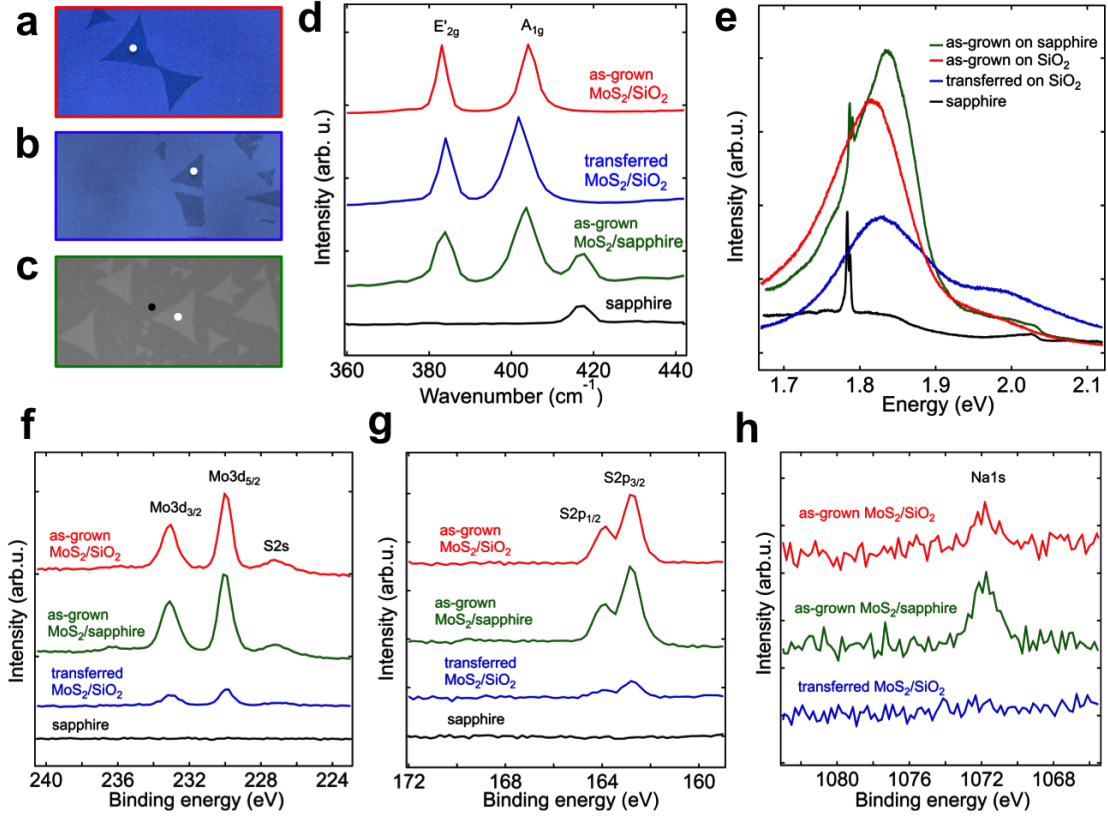


Figure 2.6: Raman, PL and XPS characterizations of MoS₂ films. (a)–(c) Optical images of as-grown MoS₂ on SiO₂ (a), transferred MoS₂ on SiO₂ (b), and as-grown MoS₂ on sapphire (c) while taking Raman and PL measurements. The white spots represent the positions of the Raman and PL spectra measured in (d) and (e), and the black spot is the bare sapphire substrate. The scale bar length is 50 μm . (d) and (e) Representative Raman and PL spectra at room temperature for as-grown MoS₂ on SiO₂ (red), transferred MoS₂ on SiO₂ (blue), as-grown MoS₂ on sapphire (green) and bare sapphire (black). (f)–(h) XPS (Al K α with an energy of $h\nu = 1,486.6$ eV) core-level spectra of the Mo3d (f), S2p (g) and Na1s (h) for as-grown MoS₂ on SiO₂ (red), as-grown MoS₂ on sapphire (green), transferred MoS₂ on SiO₂ (blue) and bare sapphire (black).

In order to analyze the chemical element compositions of the grown MoS₂ films, X-ray photoelectron spectroscopy (XPS) (Al K α with an energy of $h\nu = 1,486.6$ eV) measurements were carried out before and after transferring the entire film onto SiO₂/Si and Si₃N₄ substrates. The typical survey spectra indicate that as-grown MoS₂ samples (both on sapphire and on SiO₂) contain a small amount of sodium originating from the Mo precursor sodium molybdate. Figures 2.6(f) and 2.6(h) display the XPS spectra of Mo3d (Fig. 2.6(f)), S2p (Fig. 2.6(g)) and Na1s (Fig. 2.6(h)) of as-grown MoS₂ on SiO₂ (red), as-grown MoS₂ on sapphire (green) and transferred MoS₂ on SiO₂/Si (blue). For direct visibility of the elemental ratios, the intensi-

ties of the individual elements are normalized with the corresponding photoemission cross sections.

The spectra of Mo3d orbit in Fig. 2.6(f) show two peaks at 229.9 and 233.1 eV, respectively, which are attributed to the doublet of Mo3d_{5/2} and Mo3d_{3/2}. The core-level of S2p_{3/2} and S2p_{1/2} are 162.8 and 163.9 eV (Fig. 2.6(g)). According to the previously reported results of MoS₂ crystal, the binding energy of Mo3d_{5/2} and Mo3d_{3/2} are 229.2 and 232.3 eV, while core-level of S2p_{3/2} and S2p_{1/2} are 162.0 and 163.3 eV, respectively^{283,296,297}. We noticed that there are an overall of ≈ 0.7 eV shift towards higher binding energy for the measured binding energies of Mo3d and S2p peaks because of applied compressive strain on insulating substrates²⁹⁸. The element ratio Mo:S of the monolayer MoS₂ films is 1:2. After transferring MoS₂ onto SiO₂/Si substrate, sodium can no longer be detected. Obviously, sodium is rinsed in the KOH solvent and deionized (DI) water during the wet-transfer process. Indeed, the Na1s signal from transferred MoS₂ on SiO₂ in the plot of Fig. 2.6(h) (blue curve) clearly shows the disappearance of the Na1s peak compared with as-grown MoS₂ on SiO₂ and also on sapphire. This indicates that sodium only interacts weakly with the substrate. However, the alkali metal, i.e., sodium, plays an important role during the growth process, that it, acting as a promotor in enhancing the lateral growth of monolayer MoS₂^{200,259,290,291}.

To take a closer look at the atomic structure, as-grown MoS₂ monolayer films on sapphire were transferred onto transmission electron microscopy (TEM) grid, and high-resolution TEM (HRTEM) and aberration-corrected scanning TEM (STEM) measurements were carried out on freestanding MoS₂. Figure 2.7(a) displays a low-magnification optical image of transferred MoS₂ on Si₃N₄ TEM grid. The dark-brown triangles are transferred MoS₂ flakes. Figure 2.7(b) is the TEM image of the area marked with a white square in Fig. 2.7(a). The size of the empty holes is 2 μ m. The further zoom-in TEM image in Fig. 2.7(c) shows large-area of freestanding MoS₂, with little traces of polymethylmethacrylate (PMMA) remaining on the surface. Atomically clean monolayer MoS₂ (Fig. 2.7(d)) can easily be observed at room temperature. The diffraction pattern displayed in Fig. 2.7(e) shows MoS₂ monolayer feature with discernible hexagonal symmetry. In order to better demonstrate the atomic structure with visibility of single Mo and S atoms, high-resolution integrated differential phase contrast scanning transmission electron microscopy (IDPC-STEM) imaging was carried out on the same sample, and Fig. 2.7(f) illustrates a well-ordered MoS₂ atomic lattice clearly exhibiting an ideal 2H-phase lattice structure with no Mo vacancies or other point/line defects and impurities. A few S vacancies are detected, but we can not unambiguously attribute them to as-grown defects or due to electron beam induced damage. The use of the IDPC technique has the distinct advantage imaging at low electron doses yet maintaining high spatial resolution, while limiting the number of knock-on damage events. For better visualization, the regular atomic structure is illustrated in the up-right corner of the Fig. 2.7(f) with blue circles representing molybdenum atoms and yellow dots corresponding to sulfur atoms.

Although the “wet-transfer” method is used to delaminate the MoS₂ film from arbitrary substrates, no damage of the sapphire substrates occurs. Therefore, the sapphire substrates after

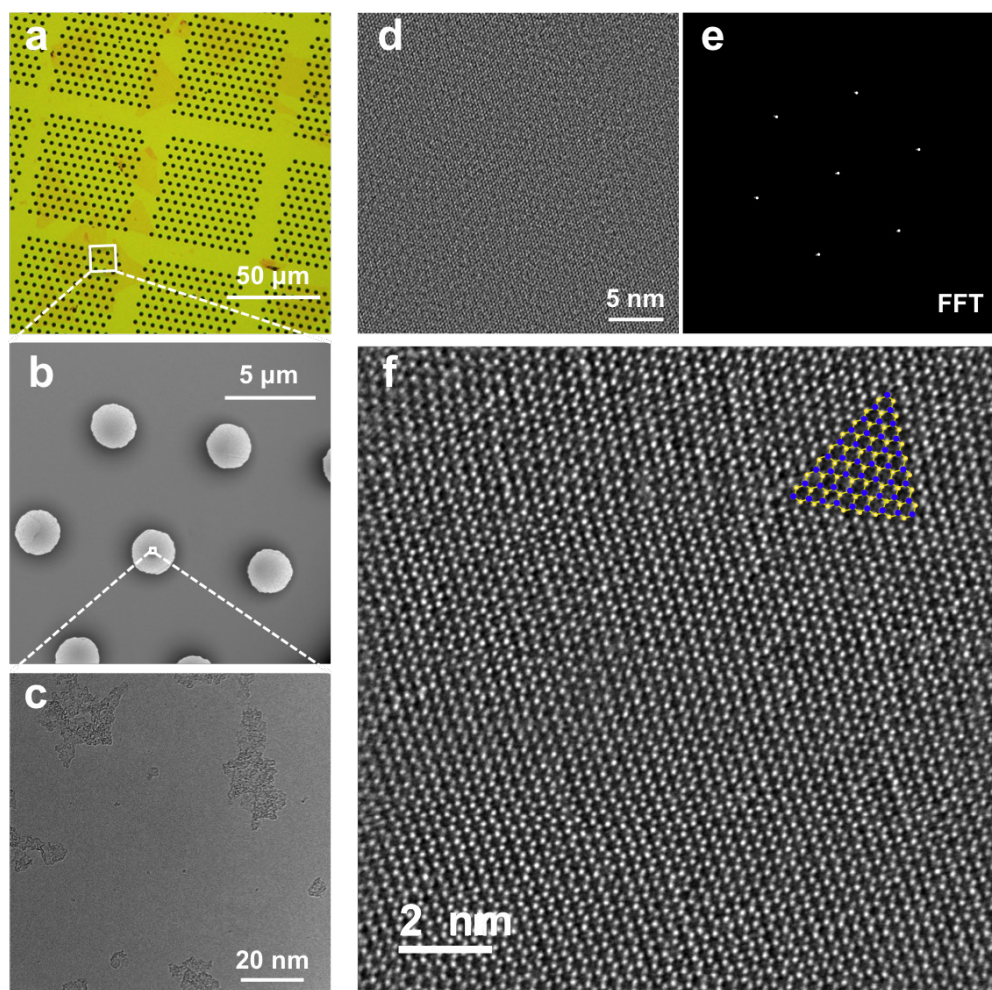


Figure 2.7: Atomic structure of monolayer MoS₂ films. (a) A representative large-area optical image of transferred MoS₂ onto a Si₃N₄ TEM grid. (b) Low- magnification TEM image of the transferred MoS₂ film covering multiple holes on a TEM grid. (c) Zoom-in TEM image of the white square in (b) shows freestanding MoS₂ with little PMMA residue traces. (d) HRTEM image of an atomically clean monolayer MoS₂. (e) The diffraction pattern of the freestanding MoS₂ monolayer. (f) IDPC-STEM image clearly shows Mo and S atoms, which are overlaid with a structural model where blue dots are Mo atoms and yellow dots represent S atoms. The intensity of the image is linear with atomic numbers, e.g., 1 Mo atom = 2.625 S atoms.

transfer of MoS₂ films can be repeatedly used after cleaning. This is favorable given the high cost of sapphire wafers. Figure S2.11 in the ESM shows multiple growths on the same sapphire substrate. It is noticed that the growth of MoS₂ shows no apparent degradation.

For electrical measurements, the as-grown MOCVD MoS₂ was transferred onto degenerately doped n++ silicon covered with 270 nm thermally-grown SiO₂ layer. Before measurements, the device was annealed in-situ at 140 °C for 12 h in a high vacuum chamber to reduce contact resistance and remove surface adsorptions. The measurement was performed at room

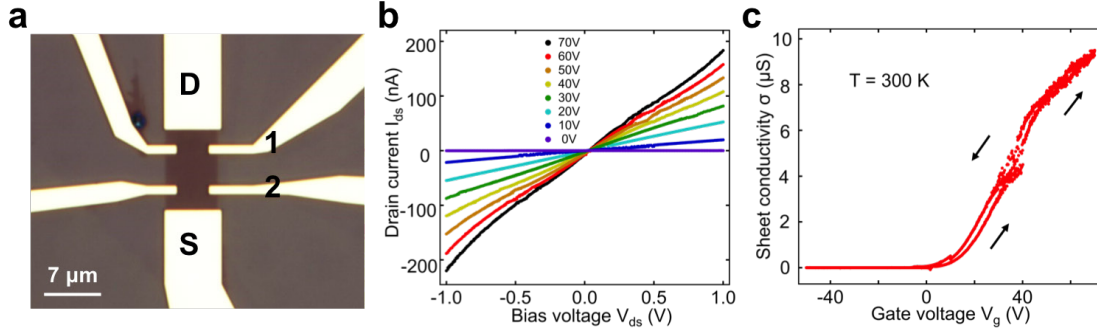


Figure 2.8: Electrical transport measurement of the device based on the monolayer MOCVD MoS₂ film. (a) Optical microscope image of the device structure for four-probe measurements. (b) I_{ds} - V_{ds} characteristics recorded for different values of V_g from 0 to 70 V at room temperature. (c) Four probe sheet conductivity as a function of V_g measured at room temperature. The black arrows show the direction of the gate voltage sweep.

temperature in vacuum (2×10^{-7} mbar). Drain-source current (I_{ds}) as a function of bias voltage (V_{ds}) is shown in Fig. 2.8(b). At different values of back gate voltage (V_g) from 0 to 70 V, the I_{ds} - V_{ds} curves show approximately linear and symmetric behaviors, which indicate an ohmic contact between the top electrode (Au) and the monolayer MoS₂ after in-situ annealing.

In order to further eliminate the influence of contact resistance and obtain the intrinsic performance of the channel materials, we performed four-probe measurements. The Hall bar geometry of the device is shown in the Fig. 2.8(a) (the device is fabricated from MoS₂ flakes transferred onto SiO₂, with channel length $L = 10 \mu\text{m}$, channel width $W = 6.5 \mu\text{m}$, and the distance between the two probes $L_{12} = 5 \mu\text{m}$). Figure 2.8(c) shows the measured sheet conductivity of the channel materials as a function of V_g , where the influence of channel geometry (L_{12}/W) has been removed. No hysteresis is observed from the curve, which proves the existence of a contamination-free surface achieved by high-vacuum annealing before the measurements. The black arrows show the direction of gate voltage sweep. The device shows obvious n-type behavior, with a low intrinsic doping level in the MOCVD monolayer MoS₂. The linear region of the transfer curve is used for calculation of field effect mobility, which gives a value of $21.6 \text{ cm}^2 \text{ V}^{-1} \text{ s}^{-1}$ at room temperature, comparable to previous high-quality CVD grown films^{299,300,299,300}.

This straightforward, efficient and cost-effective method is quite practical and general, and it can be easily applied for the synthesis of other TMDs by changing the precursors. For instance, employing same sulfur precursor of diethyl sulfide, but using Na₂WO₄ instead of sodium molybdate to grow WS₂ film on sapphire (see the Fig. S2.12).

2.2.4 Conclusion

In conclusion, we present the wafer-scale synthesis with monolayer MoS₂ continuous films on sapphire and SiO₂ by a facile and controllable method with spin-coated Mo precursor and

non-toxic S precursor DES. By introducing fairly moderate H₂ gas flow, the nucleation density of MoS₂ can be substantially decreased. The high electron mobility at room temperature and atomic structure of as-transferred MoS₂ demonstrate the high quality with a relatively low density of defects, as confirmed by our electrical, optical and HRTEM characterization. The MoS₂ films can be transferred onto arbitrary substrates, while the sapphire substrates can be repeatably used. We also show the same method for the growth of WS₂ on sapphire. The presented synthesis method is simple, reproducible, low-cost and highly scalable, and opens the way to wafer-scale production of TMDs for practical applications.

2.2.5 Methods

Materials

Na₂MoO₄ (powder, 98.0%) and DES liquid (98%) were purchased from Sigma-Aldrich. DI water was used to prepare aqueous solutions of sodium molybdate as the molybdenum source.

Substrate preparation

Prior to the growth process, sapphire and SiO₂/Si substrates were first rinsed in acetone, isopropanol and DI water with ultrasonic bath. Next, sapphire substrates were annealed in a quartz tube in the air at 1,100 °C for 1 h. Subsequently, the sapphire and SiO₂ substrates were treated with 25 wt.% KOH solution for minimum 1 h. Afterwards the sapphire and SiO₂ substrates were rinsed with significant amounts of DI water and dried with the N₂ gun.

Preparation of the molybdenum precursor

0.1 M aqueous solution of sodium molybdate dihydrate was prepared in distilled water. Several dilute solutions were then prepared from the 0.1 M solution. Sodium molybdate was spin-coated onto the KOH-treated sapphire and SiO₂ substrates with a speed of 2,000– 6,000 rpm. A good combination of the Na₂MoO₄ concentration and spin-coating speed for a good synthesis we used is 0.006 M and 3,500 rpm.

Controlled synthesis of high-quality MoS₂ film

The 2-zone MOCVD hot-wall furnace setup (MTI Corporation, USA) consists of a 4-inch quartz tube (outer diameter of 100 mm) connected to a stainless bubbler containing liquid sulfur precursor DES. The growth substrate spin-coated with sodium molybdate was placed at the center of the quartz tube, with 350 sccm Ar used in purging the system at a pressure of 700 mbar. The quartz tube was ramped slowly (2 h) up to 850 °C for 10 min in a preheated furnace. The growth of MoS₂ was carried out at 850 °C with 350 sccm Ar, 10 sccm of H₂ and 8 sccm of DES as the sulfur source for 20 min. After growth, the quartz tube was rapidly cooled down with the supply of 5 sccm of DES until a temperature of 150 °C. DES source and Ar flow were

then switched off.

Sample characterization

Raman and PL measurements were performed using a Renishaw inVia confocal Raman microscope with objective lens of $\times 50$ and $\times 100$ and the laser wavelength of 532 nm with a laser power (< 0.3 mW) carefully adjusted for a minimal damage by checking to ensure that there are no peak shifts in the sample over repeated number of measurements. Diffraction gratings of 1,200 and 600 g mm⁻¹ were used for Raman and PL measurements, respectively, for suitable spectral ranges and resolution. For XPS survey and core-level XPS analysis, ULVC-PHI Versa Probe II equipped with laboratory Al K α X-ray source ($h\nu = 1,486.6$ eV) was used with a typical beam size of 200 μm for a survey and average-area analysis while a beam size of 20 μm was used for single-island analysis. A dual-beam charge neutralizer (low energy electron and He ion) was used on the insulating samples. The C1s peak at the binding energy of 284.8 eV was taken as a reference for offsetting the raw spectra. AFM and SEM imaging: AFM topographical imaging was performed with the Cypher Asylum Research atomic force microscope in amplitude modulation mode. SEM images were obtained by a field emission SEM Zeiss Merlin microscope equipped with a charge neutralizer device to image the as-grown sample on sapphire and on SiO₂ directly. The samples for the TEM and STEM investigation were transferred on Si₃N₄ TEM windows (Norcada, Canada) with arrays of 2 μm diameter holes. TEM and STEM images were measured on an aberration-corrected (with double Cs corrector) Thermo Fisher Scientific Titan Themis TEM (60–300 kV) with a high brightness Schottky X-FEG electron source and a monochromator operated at an 80 kV acceleration voltage and low electron beam current values (< 10 pA). To resolve the structure of monolayer MoS₂ films, minimal dose was used to reduce electron beam damage in high-resolution STEM (HRSTEM), images were taken by using IDPC technique^{301,302}. The IDPC-STEM images were taken by using the priority software plugin contained within the Thermo-scientific VeloxTM software package and by using C2 aperture size of 70 μm and a camera length of 115 mm, which provided the proper diffraction conditions for imaging with the segmented DF4 detector of the Titan Themis. The STEM images were processed by Wiener filtering in Gatan Digital Micrograph software.

Transfer method

To measure electrical properties, the as-grown MoS₂ films were transferred from the sapphire substrate onto degenerately doped n++ silicon covered with 270 nm thermally grown SiO₂ layer. A thin layer of PMMA A2 was spin-coated as the supporting film. The film was then detached in 30 wt.% of KOH solution and transferred onto SiO₂/silicon substrate and Si₃N₄ TEM grids in DI water after raising several times. The PMMA film was then dissolved in hot acetone (70 °C) for a few minutes. To further remove PMMA residues, the transferred samples were immersed in acetone for overnight and then annealed in Ar/H₂ atmosphere at 340 °C for 8 h.

Device characterization

A single MoS₂ film was chosen and fabricated into a Hall bar like FET for four-terminal measurements. The contact electrodes were patterned by e-beam lithography, followed by e-beam evaporation of 2 nm of Ti and 90 nm of Au where titanium was used as an adhesion layer. To achieve a rectangular shape of MoS₂ for uniform current flow, e-beam lithography was again used for patterning followed by oxygen plasma etching with PMMA A4 serving as the mask. The device was then annealed in vacuum (2×10^{-7} mbar) at 250 °C for 6 h to reduce the contact resistance. The electrical measurements were performed in a Janis closed-cycle cryogen free cryostat. Before the measurement, the device was annealed in-situ at 140 °C for 12 h at a vacuum level better than 10^{-7} mbar to remove absorption and contamination on the surface. FET measurement was performed at room temperature immediately after annealing using Keithley 2400 SMU and Keithley 2000 DMM.

2.2.6 Supplementary Information

Influence of H₂ flow during the MoS₂ growth

The typical growth of MoS₂ involves carrier gases of 350 sccm Ar, 10 sccm of H₂ and 8 sccm of diethyl sulphide at the growth temperature of 850° C for ≈20 min. The hydrogen flow plays double roles during the synthesis process: Vaporization of precursors and desulfurization of MoS₂ flakes, which lead to growing and etching of MoS₂ flakes, individually.^{1,2} Thus, it is important to apply the appropriate amount of H₂ during the synthesis of the MoS₂. To optimize the H₂ flow, different flows of H₂ were applied during the growth procedures. Figure S2.9 shows the effect of various H₂ flow rates on the quality of the MoS₂ film on SiO₂ at the sodium molybdate (Na₂MoO₄) concentration of 0.006 M. Clearly, the nucleation density of MoS₂ can be substantially decreased at the optimal H₂ flow rate of 10 sccm.

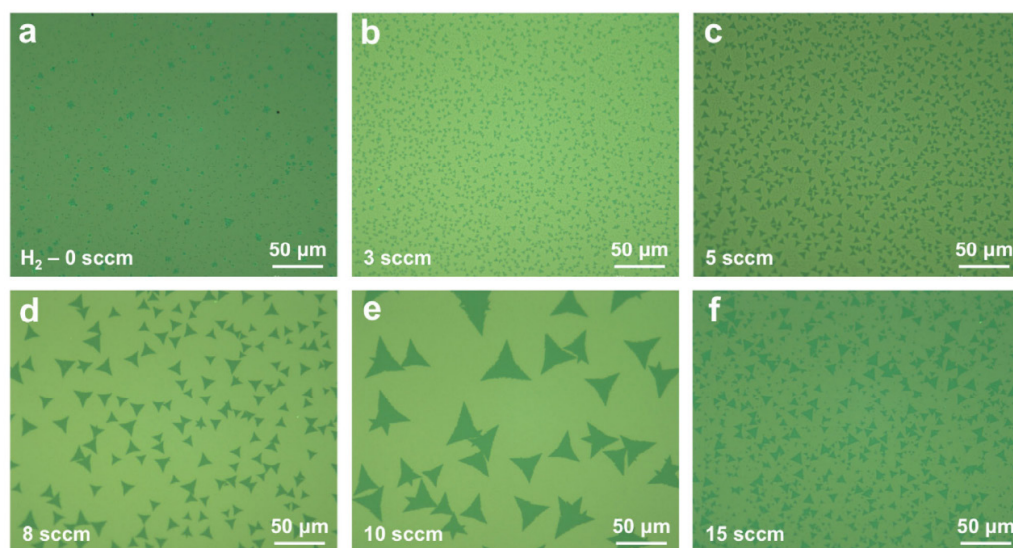


Figure 2.9: Dependency of MoS₂ growth on H₂ supply. (a-f) A series of optical images of as-grown MoS₂ on SiO₂/Si substrates depending on the H₂ flow rate. (a) MoS₂ flakes are barely observed without H₂ flow. (b) Tiny triangles of MoS₂ formed with 3 sccm of H₂ flow. (c) Slightly bigger flakes with 5 sccm of H₂ flow. (d) Nucleation density is decreased, and bigger MoS₂ flakes are observed at H₂ flow rate of 8 sccm. (e) Large MoS₂ flakes form on the SiO₂ surface with low nucleation density at H₂ flow rate of 10 sccm. (f) The excess H₂ flow of 15 sccm etches some MoS₂ flakes.

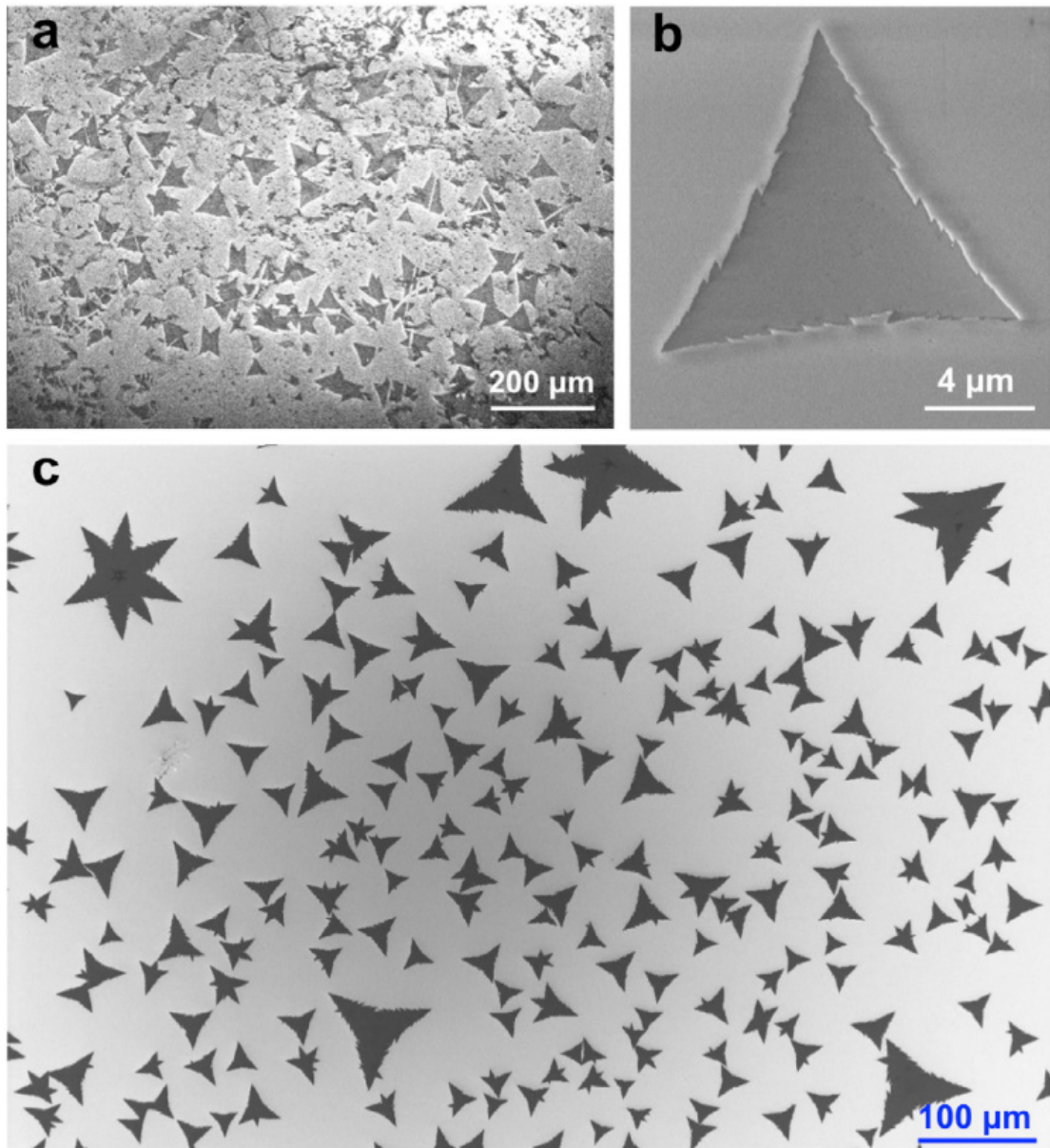
SEM imaging of as-grown MoS₂ on sapphire and on SiO₂

Figure 2.10: **Scanning electron microscope (SEM) imaging of as-grown MoS₂ on sapphire and on SiO₂.** (a) large-area SEM image of as-grown MoS₂ on sapphire. The darker contrast flakes are MoS₂. (b) Zoom-in SEM image of a representative MoS₂ flake. (c) Typical SEM image of as-grown MoS₂ on SiO₂/Si at large scale.

Repeated growth of monolayer MoS₂ on the same sapphire substrate

After transferring as-grown MoS₂ onto SiO₂ or TEM grids, the remained sapphire substrates were cleaned in an ultrasonic bath with acetone, isopropanol and deionized (DI) water. Subsequently, the cleaned sapphire substrates were annealed in the quartz tube in air at 1100° C for 1 h. Afterward, these sapphire substrates were treated with KOH, spin-coated with sodium molybdate, and then placed in the quartz tube for the second time of growth. After finishing growth, the MoS₂ film was transferred, and the sapphire substrate is again used for the third time of growth after the cleaning cycle. The repeated growth samples were checked with an optical microscope, as displayed in the Figure S2.11.

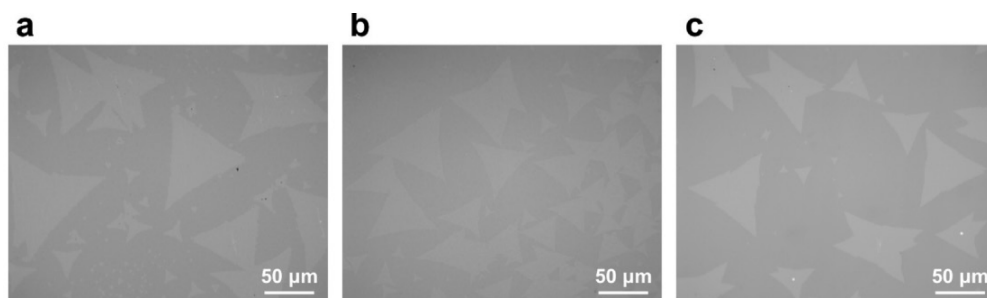


Figure 2.11: **Reproduced growth of monolayer MoS₂ on the same sapphire substrate.** (a-c) Optical microscopy images of the first (a), the second (b) and the third (c) growth on the same sapphire substrate. The quality of MoS₂ growth shows no obvious degradation.

Growth of WS₂ with the same method

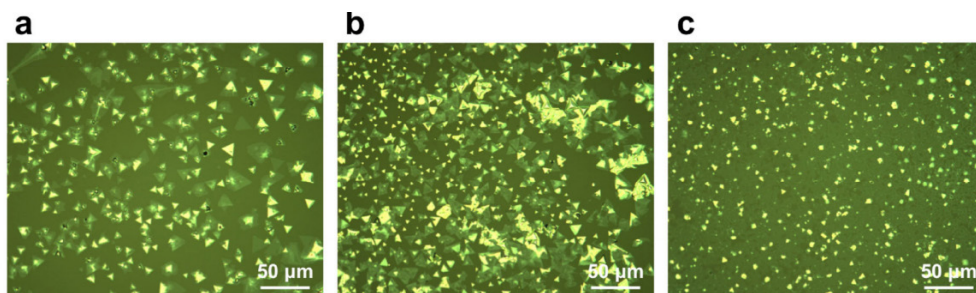


Figure 2.12: **Growth of tungsten disulfide (WS₂) with the same method.** (a-c) Optical images of as-grown WS₂ on sapphire substrate with different coverage applying the same MOCVD method for MoS₂ synthesis. The WS₂ films are grown with 350 sccm of Ar, 10 sccm H₂ and 7.5 sccm of diethyl sulphide at 850° C for 20 min with concentration of sodium tungstate (Na₂WO₄) 0.05 M with spin-coating speed of 6000 rpm (a), 5000 rpm (b) and 4000 rpm (c), individually. Obviously, the lower rotation speed leads to higher coverage of WS₂. (c) displays a fully-covered monolayer WS₂ with a few thicker flakes (brighter contrast) on top.

2.3 Wafer-Scale Fabrication of Nanopore Devices for Single-Molecule DNA Biosensing using MoS₂

The following section is based verbatim on the following publication:

Mukeshchand Thakur^{IV}, Michal Macha^{IV}, Andrey Chernev^{IV}, Michael Graf^{IV}, Martina Lihter^{IV}, Jochem Deen^{IV}, Mukesh Tripathi^V, Andras Kis^V, Aleksandra Radenovic^{IV}

Wafer-Scale Fabrication of Nanopore Devices for Single-Molecule DNA Biosensing using MoS₂, *Small Methods*, 2012.

Mukeshchand Thakur and Michal Macha contributed equally to this work. M.M. developed the large-scale growth method and performed the Raman, AFM, SEM and optical characterization. Mukeshchand Thakur transferred the MoS₂ and performed biosensing experiments. Mukesh Tripathi performed STEM imaging, Jochem Deen developed nanopore-sensing software.

Parts of the publication related to DNA translocation experiments were not included here, as they were the contribution of M.T. and are not relevant for the thesis.

2.3.1 Abstract

Atomically thin (two-dimensional - 2D) nanoporous membranes are an excellent platform for a broad scope of academic research. Their thickness and intrinsic ion selectivity (demonstrated for example in molybdenum disulfide – MoS₂) make them particularly attractive for single-molecule biosensing experiments and osmotic energy harvesting membranes. Currently, one of the major challenges associated with the research progress and industrial development of 2D nanopore membrane devices is small scale thin-film growth and small-area transfer methods. To address these issues, we demonstrate a large-area protocol including a wafer-scale monolayer MoS₂ synthesis, Si / SiN_x substrate fabrication and wafer-scale material transfer. Firstly, we introduce the 3-inch wafer scale MOCVD growth yielding homogenous monolayer MoS₂ films. Secondly, we fabricate a large number of devices in one batch by employing the wafer-scale thin-film transfer method with high transfer efficiency (>70% device yield). The growth, the transfer quality and cleanliness were investigated using transmission electron microscopy, atomic force microscopy and Raman spectroscopy. Finally, the applicability and robustness of our large-area protocol was demonstrated by performing a set of double-stranded DNA translocation experiments through as-fabricated MoS₂ nanopore devices. We believe that the shown approach will pave the way towards wafer-scale, high-throughput use of 2D nanopores in various applications

^{IV}Laboratory of Nanoscale Biology, , EPFL ,Lausanne, Switzerland

^VNanoscale Electronics and Structures, Institute of Materials Science and Engineering, , EPFL ,Lausanne, Switzerland

2.3.2 Introduction

Nanopore-based sensing is attractive in the field of single-molecule detection as it offers low-cost, label-free and high-throughput analysis. In general, a nanopore device is a small nanometric aperture separating two compartments filled with ionic solutions. When a bias voltage is applied, an electrically charged molecule (e.g. DNA) electrophoretically threads through the nanopore. This process generates a transient resistive pulse in the ion current, which can be used to study the translocation of a single molecule. Based on their composition, nanopores are categorized as biological, silicon- or polymer-based solid-state pores or DNA-origami pores^{175,303–305}. One of the promising applications of nanopore devices is DNA sequencing, often regarded as the fourth-generation sequencing technology. So far, only biological nanopores have been used for commercial sequencing applications^{306,307}. Since the functional unit of these biological nanopores are protein channels, their stability in the lipid-bilayer is limited by the ionic strength of the electrolyte, the voltage that can be applied, chemical, mechanical and thermal stability. In contrast, solid-state nanopores are more mechanically and chemically robust, providing flexibility in working with higher voltages, ionic concentrations and temperatures. Their size can be precisely tuned for a desired application and on top of that, they can be fabricated in sizable arrays, potentially improving the sensing efficiency. To improve the spatial and temporal resolution of detection, for biopolymers such as DNA, the thickness and the pore diameter of the sensing membrane needs to be comparable with the lateral diameter of the biopolymer. In this regard, two-dimensional (2D) materials such as graphene^{5,177}, hexagonal boron nitride³⁰⁸, and transition metal dichalcogenides (TMDs) materials such as tungsten disulfide (WS₂)¹⁷⁶ and molybdenum disulfide (MoS₂)^{6,90,219,309,310} were explored as 2D solid-state nanopores. MoS₂, in particular, is interesting since it is composed of three-atoms (≈ 0.65 Å)²⁷⁷. In addition to the thickness, the presence of hydrophilic molybdenum atoms at the pore facilitates the base differentiation. Furthermore, DNA tends to interact less with the membrane surface when compared to graphene¹⁵⁶. And lastly, the signal-to-noise ratio in MoS₂ is higher than in other 2D materials^{156,309}. All these reasons make MoS₂ an attractive and widely studied 2D material for DNA biosensing application. Experimentally, using a gradient of room temperature ionic liquids and KCl solution, monolayer MoS₂ nanopore devices have achieved single-nucleotide differentiation⁶. Furthermore, monolayer MoS₂ nanopore devices are becoming promising tools for emerging scientific applications in defect-engineering research^{153,188,311–313} and highly-efficient blue energy harvesting^{8,9,164}.

One of the most crucial bottlenecks of monolayer device fabrication is the thin film synthesis and its processing scale. Most reported applications rely on a relatively small monolayer substrate size which enforces a single-chip transfer and fabrication of a single device a time^{6,90,176,309,314}. This approach is highly time consuming and cost ineffective, especially if the application requires a significant number of devices. Likewise, even if a uniform thin film growth is performed on a large substrate area, without an easy and repeatable large-scale transfer method the same problem remains. Hence, a large-scale approach towards the production of robust, low-cost and scalable nanopore devices is paramount to ensure high research yield

and scientific progress in this field. Currently, the major challenges associated with 2D MoS₂ nanopore devices are their high-quality and defect-free synthesis, sensing noise associated with device architecture, and variability in the fabricated devices in terms of pore size, pore geometry and thickness. These problems, usually occurring with applications requiring 2D materials requiring a clean large-scale microfabrication process.

In this work, we address these challenges by growing large-area continuous MoS₂ films on a 3-inch sapphire substrate with subsequent wafer-scale transfer using polydimethylsiloxane (PDMS). The growth process is based on metalorganic chemical vapor deposition (MocVD). By using the c-plane sapphire substrates, high-purity gaseous phase precursors and an alkaline salt as a growth catalyst, we obtain the reproducible and highly efficient synthesis of continuous mono- to few-layer MoS₂ films. For the transfer of MoS₂ films, we use PDMS as a supporting polymer along with water, avoiding any hazardous etchants (e.g. KOH) or additional etching steps during transfer. The transfer process is less labour intensive and does not need any additional expensive instruments usually used in existing deterministic transfer methods^{90,315}. Furthermore, the MoS₂ growth substrate is recyclable thereby reducing the substrate costs. In combination with PDMS transfer, we demonstrate cost-effective and time-efficient method for large-scale nanopore-device fabrication (a total of 128 devices per batch) with successful transfer yield (>70%). The 2D material quality and cleanliness of the wafer-scale transferred MoS₂ was evaluated with high-resolution transmission electron microscopy (HRTEM) and aberration-corrected scanning transmission electron microscopy (STEM) imaging. We have found that transfer quality is comparable to the well established, small-scale PMMA-based techniques and can be adapted to other polymer materials.

2.3.3 Results and Discussion

Wafer-Scale MoS₂ Growth and Transfer

For the 2D material synthesis, we have used a modified and upscaled methodology based on a combination of two different approaches. The first one uses the metalorganic precursor (molybdenum hexacarbonyl Mo(CO)₆) and diethyl sulfide (DES) as molybdenum and sulfur sources⁶⁴, respectively. The second one relies on the addition of spin-coated liquid-phase growth promoters, sodium molybdate (Na₂MoO₄) and alkaline salt, prior to the growth phase^{209,316}. Using a spin-coated Na₂MoO₄ solution both to ensure uniform seeding and as an additional molybdenum source during growth step yields highly homogenous, large 2D crystals of MoS₂, leading to continuous monolayer formation under proper process parameters. The use of alkaline salts as a crystal growth catalyst is a common practice in the MoS₂ synthesis protocols^{200,207,256}, which lowers the density of nucleation sites and the melting point of the solid-state precursors. This results in an increase of the final crystal size by orders of magnitude. In particular, NaCl is an advantageous addition to the growth. Under elevated temperature, it can form intermediate ternary species with molybdenum acting as planar, cyclic seeding promoters both suppressing the nucleation and increasing lateral crystal growth rate on the target substrate²⁰⁷.

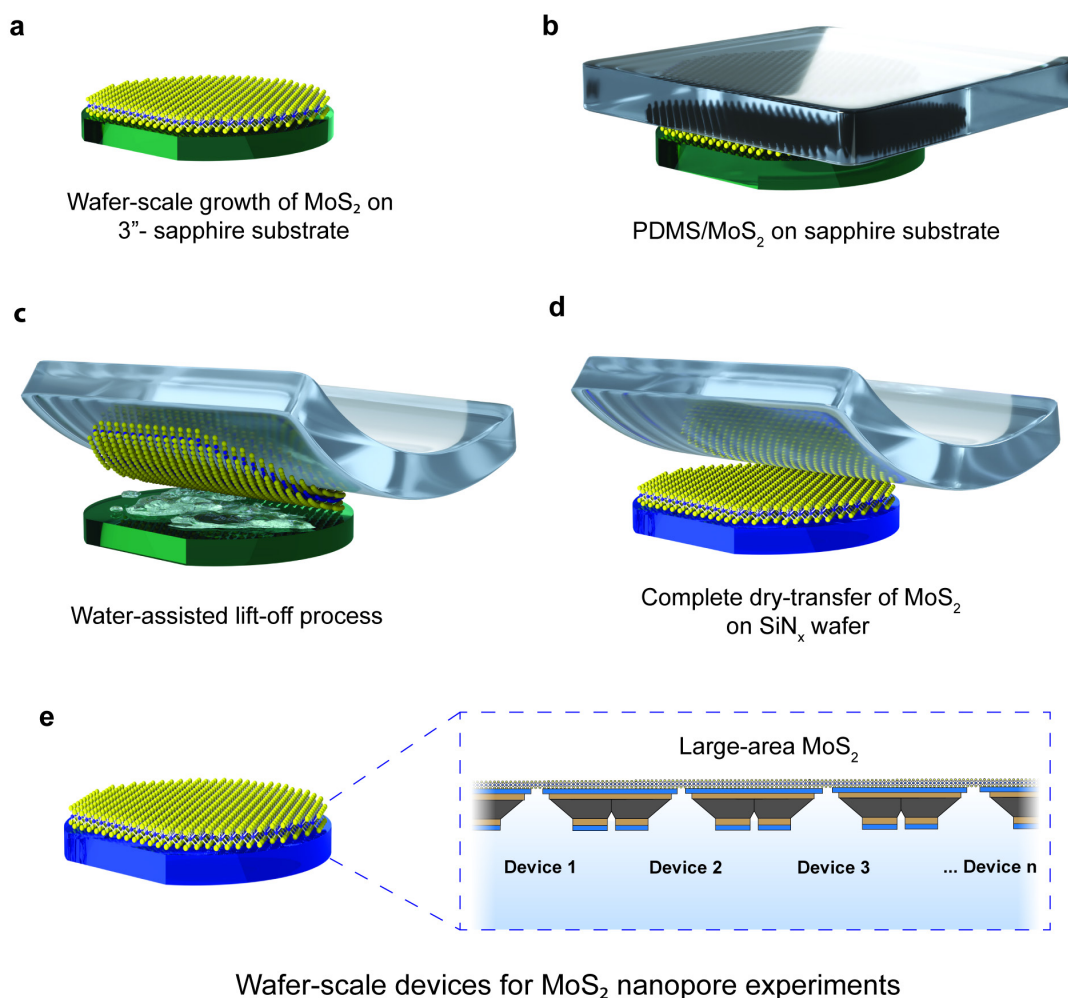


Figure 2.13: Illustration showing **the wafer-scale PDMS-transfer of MoS₂** from a 3-inch sapphire wafer to a silicon substrate containing an array of SiN_x membranes with apertures. The objects are not to scale. (a) Large-area MoS₂ on the growth substrate. (b) The PDMS stamp is aligned to the MoS₂/sapphire substrate. (c) Lift-off process where the water penetrates the interface between sapphire and MoS₂, while using a step-motor the PDMS/MoS₂ is lifted off. (d) Dry transfer of large-area MoS₂ on the SiN_x wafer achieved by stamping using PDMS. (e) Large-area MoS₂ transferred to the target substrate now containing devices that can be used for the nanopore experiments.

Taking advantage of both of these approaches, we have used a spin-coated mixture of both Na₂MoO₄ and NaCl as a continuous growth promoter. Prior to the growth, annealed and hydrophilized (see Experimental methods section) c-plane sapphire wafers (3-inch) were coated with promoter solution to achieve a uniform layer. Typical growth step is performed in a homemade MocVD, hot-wall, vertical furnace for 30 min at 850°c under the flow of 210 sccm of Ar, 1 sccm of O₂, 4 sccm of H₂ (Figure S2.16 S1). In contrast to previous publications^{207,209,316}, we are adding several new elements and improvements to our process. First, we use separate bubblers for Mo(CO)₆ and DES, which increases the control in delivering the gases into the

chamber, and 12 sccm of Ar is flowing through a bubbler filled with, Mo(CO)₆, and 3 sccm of Ar through separate DES bubbler. Second, the sapphire substrate is placed vertically to achieve uniform exposure to the gases and homogeneous reaction conditions. The combination of the metal-organic gaseous precursor, the sulfur-rich atmosphere, and the Na₂MoO₄ solution uniformly coated on the substrate, ensures a uniform seeding of MoS₂ across the whole substrate and a steady supply of Mo mass, promoting large-scale, continuous film formation with a high degree of control. The addition of NaCl to the spin-coating solution ensures a high reaction rate and a low nucleation density, which as a result increases the overall grain size, visible through merged, extruded grain boundaries, and single crystals on the edges of the substrate. A moderate amount of hydrogen is necessary to help decomposing the DES and Mo(CO)₆ ligands and to prohibit carbon containing reaction products from depositing on the substrate. Lastly, we are introducing small amounts of oxygen to the process, which ensures smooth grain mergers, decreases the probability of a secondary layer formation, and further limits the nucleation density due to local etching of unsteady nuclei²⁰⁹. The thickness of the continuous MoS₂ film can be controlled both with the concentration ratio of Na₂MoO₄ / NaCl and the flow of O₂ (Figure S2.17), and can range from single flakes to continuous multilayer. As a result, this method allows to repeatedly and efficiently produce large area mono- and multilayer MoS₂ alike.

The substrate fabrication process is detailed in the Experimental methods section and Figure S2.18. Each fabricated silicon wafer results in >120 devices where each device has one single aperture in a thin SiN_x membrane. In order to assess the variability of these apertures, we have characterized the apertures from different parts of the wafer using TEM. The size of the aperture is ≈75 nm within 5% error (Figure S2.19).

The next step is the large-scale transfer of MoS₂ to the Si / SiN_x wafer. Figure 2.13 depicts the steps involved in this process. The lift-off step is based on a surface-energy assisted transfer of MoS₂ using water^{213,309,317,318} with a step-controlled translating stage (See Experimental methods section). The material transfer is performed by aligning the PDMS onto the as-grown MoS₂ growth substrate (Figure 2.13 a-b). The next step comprises of manually placing of MoS₂/PDMS layer in a container with water and lifting-off as water penetrates at the interface between the MoS₂ and the sapphire substrate (Figure 2.13c). Due to the surface interaction between MoS₂/PDMS (hydrophobic) and sapphire (hydrophilic), the water preferentially penetrates between MoS₂ and the sapphire substrate enabling the surface-energy based lift-off of MoS₂^{317,319}. In the absence of water, the MoS₂ does not attach to the PDMS completely. Subsequently, MoS₂ is manually stamped on the SiN_x surface completing the large-area transfer^{317,320}. It must be noted that during the transfer steps, we used the lift-off and stamping speed in the range of 5-10 μm/s (Figure 2.13 c-d). One of the advantages of wafer-scale transfer is that unlike deterministic transfer methods^{90,321}, this approach is simple and does not require any precise optical alignment setup. While wet-etching based wafer-scale transfer using polymers such as poly(methyl methacrylate) (PMMA) was recently demonstrated for MoS₂³²¹, it requires surface modification of the growth substrate and an additional substrate etching step which may deteriorate the thin 2D material due to the harsh etchants used (e.g.

KOH). In addition, PMMA coating was shown to have a time-dependant corrosive effect on the coated 2D materials, which can lead to poor device performance³²². Furthermore, due to the thickness of thin PMMA films (several hundreds of nanometers), the wet transfer processes are prone to unwanted crumbling of the material, decreasing the transfer efficiency²¹⁶. The PDMS, being significantly thicker (1-2 mm), but still flexible and optically transparent, provides a better mechanical stability, increasing transfer efficiency^{315,317,323}. Previous reports have demonstrated small-scale deterministic transfer of TMDs using a micromanipulator stage using both PDMS and PMMA^{90,317,321,323}.

Characterization of MoS₂ Films

Optical images of as-grown MoS₂ (Figure S2.20) show a uniform layer of film with rare secondary nucleation spots. Using sapphire as a substrate ensures epitaxial connection on the MoS₂/sapphire interface due to crystal lattice match³⁰⁰. However, Na-based compounds assisting the MoS₂ growth were reported to diminish such an epitaxial interface due to Na intercalation under the grown film Large-Area Epitaxial Monolayer³²⁴. Indeed, optical images (Figure S2.20) reveal rare spots of extruded grain boundaries, which suggests imperfect grain stitching. Nonetheless, for our application, we have not observed any odd grain boundaries nor low-quality suspended areas on fabricated membrane devices. In our case, the sapphire substrate was (depending on the batch) ≈ 90 -100% covered with continuous monolayer to few-layer films (Figure 2.14a) which were transferred to the SiN_x substrates (Figure 2.14b).

To further inspect the large-scale growth quality and uniformity, Raman spectroscopy was performed across the whole wafer pre- and post-transfer (Figure 2.14c-d). The relative distance between in-plane E_{12g} and out-of-plane acoustic phonon modes is an indicator of MoS₂ thickness^{321,322,325}. In our case, the average separation between E_{12g} and A_{1g} peaks remains in the range of 19.5 cm⁻¹ - 20.5 cm⁻¹, suggesting a uniform monolayer character of the film across the entire substrate. The absence of a peak separation difference between the spectra before and after the transfer is an indication of the non-destructive character of the transfer method. We observe, however, a small increase in E_{12g}/A_{1g} intensity ratios after the transfer, which can be due to changes in exciton-phonon interaction with the supporting substrate¹⁰⁴ or doping by charge transfer³²⁵. Additionally, to analyse the uniformity or the quality of the MoS₂ films, photoluminescence (PL) measurements were performed at the similar regions (labelled in Figure 2.14a-b) before and after the transfer (Figure S2.21). The PL peaks did not show any significant shift (< 5 nm) before and after transfer process indicating that the crystal quality of the layers did not deteriorate after the transfer^{321,326}. These results are in corroboration with the Raman measurements. This may be attributed to the mild conditions used in the water-assisted transfer process that avoids the use of any harsh etchants, preserving the quality of the MoS₂ films³²¹. The AFM surface characterization reveals ≈ 0.7 nm thick layers after the transfer, corresponding to the thickness of monolayer MoS₂ (Figure 2.14e)²⁷⁷. Aberration-corrected STEM is a well-established method to characterize the structural uniformity at atomic scale in low-dimensional materials including MoS₂, h-BN and graphene^{324,327,328}. The

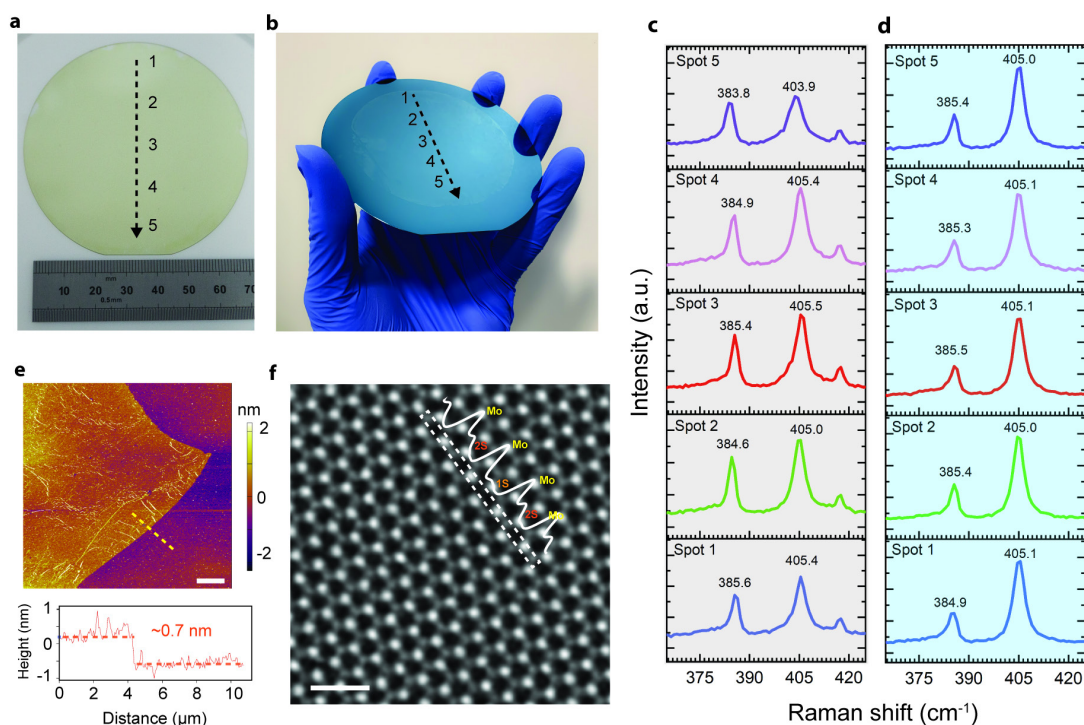


Figure 2.14: Characterization of large-area MoS₂ films. (a) Continuous MoS₂ film grown on a sapphire substrate. (b) Large-area wafer-scale transfer of MoS₂ over a silicon wafer with 128 SiN_x membranes containing apertures. The blue contrast of the MoS₂ transferred from the growth substrate is visible on the SiN_x surface. (c-d) Raman spectroscopy from the same region of the wafer before (gray panel) and after the transfer (blue panel) of the MoS₂ films (unmarked peak around 420 cm⁻¹ on a before-transfer spectra is a signature peak of the Al₂O₃ substrate used for the MoS₂ synthesis). (e) AFM analysis showing monolayer MoS₂ post-transfer with ≈ 0.7 nm height profile. Scale bar is 6 μ m. (f) Double Gaussian filtered STEM image after transfer showing a clean MoS₂ lattice structure. Due to its Z-contrast dependency, the lattice structure can be directly inferred from the molybdenum atom (brighter) and the sulfur atom (darker) contrasts. A few intrinsic sulfur-vacancies can be directly observed in the image (inset: Intensity peak profile along the line for selected atoms showing one sulfur vacancy). Scale bar is 1 nm.

STEM image (Figure 2.14f) shows the crystal lattice structure of a monolayer MoS₂ film. Due to the annular dark field contrast dependency, the intensity of the atomic columns can be directly interpreted since it is directly proportional to $Z^{1.6-2.0}$ (where Z is the atomic number)³²⁴. Thus, Mo-atomic sites appear brighter in intensity than the sites where two sulfur atoms are on top of each other. The intensity profile along the line shows the peak positions of the Mo-atoms and S-atoms, respectively. To avoid electron-beam induced knock-on damage, a low acceleration voltage (80 kV) was used during the imaging³²⁴. A few intrinsic S-vacancies can be observed in the image³²⁷, further confirming the high-quality growth of our MoS₂ films (also shown in the line profile in Figure 2.14f). Furthermore, to assess the cleanliness of the suspended transferred MoS₂ regions, larger areas were analysed where large-area clean regions with MoS₂ films can be observed with some polymer contamination (see Figure S2.22).

Due to advancements of aberration-correction, a smaller sized electron-beam probe (full width half maximum, FWHM, ≈ 1 Å) in STEM can be intentionally placed on the clean MoS₂ regions to create nanopores with tunable sizes in a controlled way by sputtering the atoms, for instance Panel 4 in Figure S2.22 shows a nanopore (≈ 2 nm²) formed by the electron-probe.

Wafer-Scale Transfer Efficiency

The wafer-scale MoS₂ transfer efficiency of >70% device yield was calculated as the percentage of devices that have an aperture fully covered with MoS₂ (2.15a). Variation from batch to batch is shown in a Table S2.1. Two optical images of devices without MoS₂ (2.15b) and with MoS₂ (2.15c) show large-area MoS₂ transferred over the SiN_x membrane. Representative devices analysed by TEM imaging are shown in 2.15d. For devices, where the transfer process was unsuccessful, it is possible to use a chip-scale deterministic transfer method⁹⁰ to increase the device yield. The transfer efficiency can be enhanced by a slow lift-off process and a high monolayer coverage of the MoS₂ on the growth substrate.

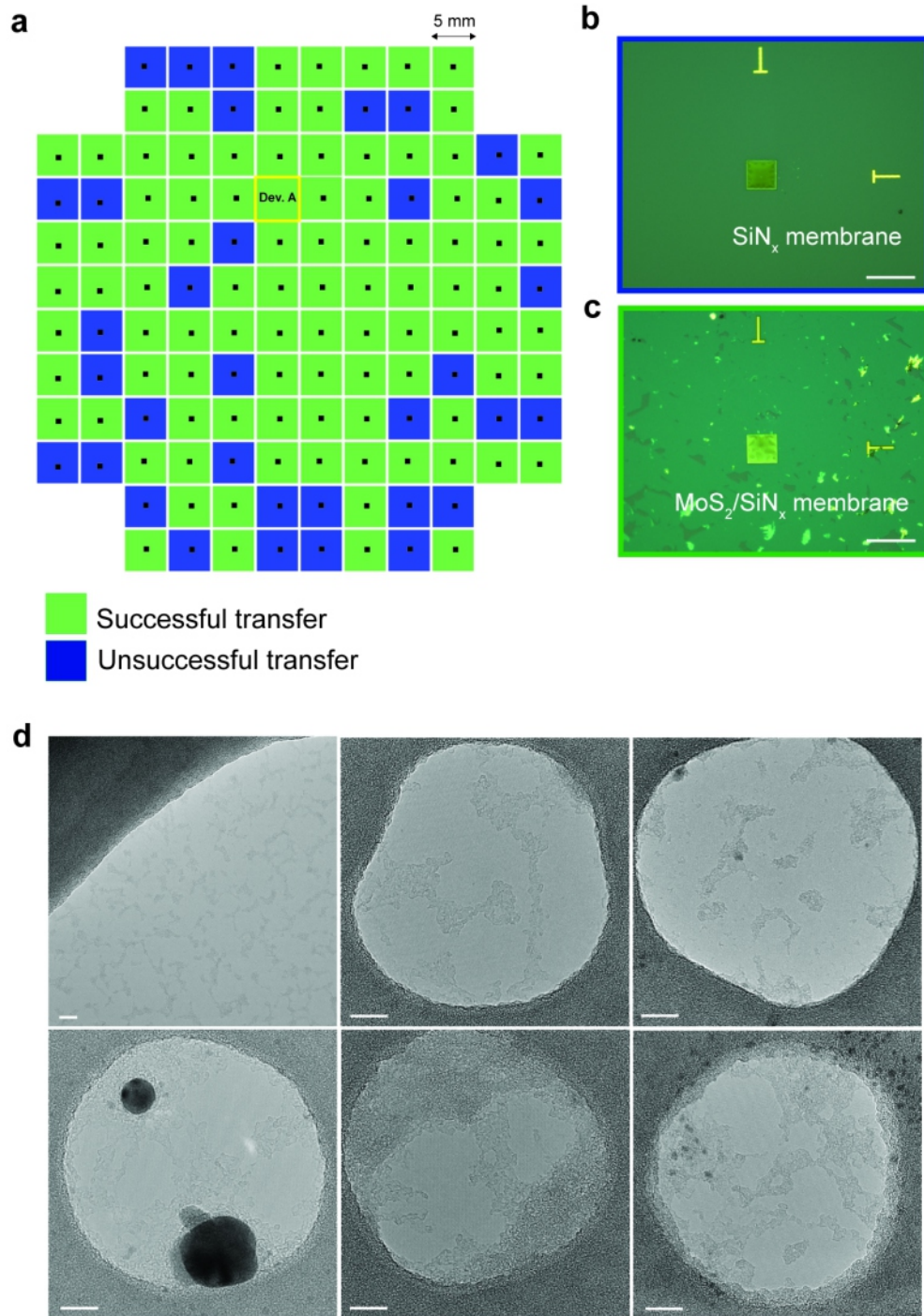


Figure 2.15: (a) Color-map showing the **wafer-scale transfer efficiency of MoS₂** over the SiN_x membrane using PDMS. The devices and their transfer is represented as complete (n = 94, green) or unsuccessful transfer (n = 34, blue). (b) A representative substrate before transfer and (c) after transfer to the SiN_x membrane. All scale bars are 50 μm. (d) TEM imaging of suspended MoS₂ after transfer. The devices show MoS₂ regions with few polymer residues after transfer. All scale bars are 10 nm.

One of the biggest challenges is to obtain residue-free transfer, since it affects the electronic properties of 2D materials. This surface contamination originates from the transfer methods using sacrificial polymer coatings (e.g. PDMS or PMMA)^{90,329}. During the transfer, polymer layer is in direct contact with the MoS₂ which inevitably leads to residual surface contamination on the monolayer film³³⁰. Additional contamination sources are airborne hydrocarbon contaminants adsorbing on the MoS₂ layers when exposed to air^{331,332}. The device cleanliness can be improved by transfer strategies, which avoid the use of polymers³²⁸. However, such methods are not compatible with the large-area transfer because the thin 2D material films without polymer support can cause uncontrolled transfer, leading to large cracks or folding in the transferred material. Another approach is to develop strategies that allow the direct growth of MoS₂ over the SiN_x aperture, as demonstrated by Waduge et al.²¹⁹ where the approach indeed promises scalability and avoids any further contamination with polymer arising from the transfer step. However, growing over apertures is not trivial and typically yields a mix of single and multilayer MoS₂ films. Thus, currently, polymer-based wafer-scale transfer for device fabrication is preferred³²¹.

Another challenge is the lack of an efficient nanopore fabrication method that could be employed for wafer scale fabrication while maintaining pore size reproducibility and distribution. Among all the state-of-art techniques, ion beam irradiation³¹² and lithography-based fabrication^{332,333} are the most promising. However, they are still facing a number of technical problems which make them not suitable for batch fabrication of single nanopore devices. Ion beam methods are generally used for pore fabrication at a large scale and lack precise pore definition. The lithographic approach on the other hand requires additional steps involving polymer coatings, leading to further, otherwise avoidable, surface contamination. For these reasons, we have used an ECR-based pore drilling method³³⁴.

2.3.4 Conclusion

In conclusion, we demonstrated large-area manufacturing of MoS₂ nanopore devices by wafer-scale growth, fabrication and transfer of MoS₂ films. We show that the fabrication of 128 devices on a single 4-inch wafer can be performed with >70% efficiency. With the current technique, it is possible to further scale-up by using higher density of devices and transfer of large-area 2D materials. The MoS₂ quality and the nanopore devices were clean at the atomic scale as confirmed by TEM and STEM imaging. The single-nanopores were created by the ECR method. Unlike TEM-based nanopore drilling, by electrically isolating each device from each other, this method has the potential for simultaneous creation of nanopores in-situ making it a scalable method of single nanopores production on the same wafer. We believe that further integration and parallelization of nanopore based membrane devices will lead to high-throughput usage and in turn will encourage new, emerging, commercial applications of this technology.

This work concludes the achievements of tube-furnace, large-area synthesis. After developing a robust and reproducible recipe, this approach was commonly used to supply MoS₂ for all

experiments. Further efforts on the large-area synthesis were shifted towards the cold-wall, 4-inch showerhead system, where one has access to many more in-depth process parameters. The complexity, both technical and physical, as well as the accomplishments of this project is described in the next section.

2.3.5 Methods

Wafer-scale growth of MoS₂

Prior to the growth, 3-inch c-plane sapphire wafers (MTI) were cleaned with IPA, acetone and DI, annealed in 1000 °C for 6 h to obtain an atomically smooth surface, treated with potassium hydroxide solution (Sigma Aldrich, 99.0%) for 30 min, rinsed with DI water, dried, and finally spin-coated with a growth promoter in aqueous solution of 0.03 M Na₂MoO₄ (Sigma Aldrich, 98.0%) and 0.1 M NaCl (Sigma Aldrich, 99.5%). MoS₂ film synthesis was performed in a 4-inch hot-wall tube furnace (MTI OTF-1200X-II). For carrier and process gases we used ultra high purity Ar (Carbagas, 99.999%), H₂ (Vici DBS NM Plus 100 Hydrogen Generator, purity 99.999%), and O₂ (Carbagas, 99.9%). Molybdenum hexacarbonyl (M(CO)₆, Sigma Aldrich, 99.9%) and diethyl sulphide (C₂H₆S₂, Sigma Aldrich, 98.0%) were used for metalorganic precursor and reaction gas respectively, and were kept in separate bubblers maintained at stable 17 °C and room pressure. Spin-coated sapphire substrates were then loaded vertically in a quartz boat placed inside the reactor tube. This position ensures perpendicular exposure to the gas flow, thus ensuring axial growth uniformity. Furnace was then filled with Ar, ramped up to 120 °C and held under carrier Ar flow of 210 sccm for 30 min to dry the reactor walls of adsorbed water molecules. After this step, the reactor was ramped to 850 °C at a rate of 20 °C/min. The growth step was initiated by injecting 4 sccm of H₂, 1 sccm of O₂ and precursor gases. With an argon flow of 12 sccm for Mo(CO)₆ and 3 sccm for DES through both bubblers, the actual mass flow of Mo(CO)₆ and DES at 17 °C and at ambient pressure was 4.40*10⁻⁴ sccm and 2.50*10⁻¹ sccm, respectively. After the growth step, the furnace was cooled down to room temperature naturally. To avoid MoS₂ deterioration, samples were kept in a dry atmosphere between all of the subsequent transfer and characterization steps.

Nanopore substrate fabrication

Double-side polished 100 mm (100) undoped Si-wafers (produced by Active Business Company) were covered with 60 nm of SiO₂ and 20 nm low-stress SiN_x from both sides (done by supplier). Photolithography and dry etching were done to open apertures in the back side SiN_x layer for the subsequent wet etching process required for SiN_x membrane formation on the front-side. Front-side e-beam lithography and dry etching were performed to form 80 nm-diameter apertures in SiN_x membranes with the following parameters: 100kV e-beam voltage, polymethyl methacrylate (PMMA, molecular weight 495K, 4% in anisole) as e-beam resist (EBR) and CHF₃/O₂ gas mixture for dry etching. As a final step acid piranha cleaning was done to achieve clean surface of the target nanopore substrate prepared for the further

MoS₂ transfer.

MoS₂ transfer

We used PDMS-assisted transfer of 3-inch MoS₂ films from the sapphire wafer to the SiN_x wafer assisted by water³¹⁸. The PDMS base reagent and curing agent were mixed in a 10:1 ratio and cured on a 4-inch Si-wafer for 4 h at 80°C. The PDMS was then cut, peeled off, and attached to a custom-made translation stage (MTS25A-Z8, Thorlabs) motorized by a DC Servo. For the complete lift-off process, one edge of the PDMS is attached to the translation stage while the PDMS is carefully placed on MoS₂/sapphire substrate. During this step a special care should be taken to avoid any air gaps or dust on the polymer/substrate interface. The PDMS/MoS₂/sapphire is then placed in a clean container and filled with Pre-filtered (20 nm) DI-water. To preserve an entire 3-inch area of MoS₂ and ensure complete delamination we have used a slow, controlled lift-off speed of 5-10 $\mu\text{m/s}$. As a result, the PDMS slowly lifts off MoS₂ from the sapphire as the water penetrates below the MoS₂, enabling the attachment of MoS₂ to the PDMS surface. Further, we manually place PDMS/MoS₂ onto the SiN_x wafer in an all dry-transfer stamping technique. The PDMS is then peeled off with the translation motor to complete the transfer of MoS₂ on SiN_x wafer. After the transfer process is complete, the SiN_x wafer is annealed at 250°C (8 h) in argon and hydrogen (100 sccm and 10 sccm, respectively) environment.

Characterization

Atomic force microscopy was performed on the Asylum Research Cypher AFM system with tapping mode. Raman and PL spectroscopy were done with a Renishaw inVia Confocal Raman Microscope with a 532 nm laser beam at a low power (<0.3 mW) to avoid defect nucleation and substrate damage. A diffraction grating of 3000 mm^{-1} was used for good spatial resolution. Transmission electron microscopy was performed on a FEI TEM Talos at 80 kV acceleration voltage in high-resolution TEM (HRTEM) mode. Prior to imaging, we performed moderate substrate heating in air (160°C for 30min) to minimize contamination and unwanted electron beam induced deposition of hydrocarbons. Scanning transmission electron microscopy imaging experiments were conducted using an aberration-corrected (with double Cs corrector) FEI Titan Themis TEM 60-300 kV, equipped with Schottky X-FEG electron source and a monochromator to reduce the effect of chromatic aberrations. To avoid sample damage, a low acceleration voltage (80 kV) was used for all the experiments, which is below the electron-beam induced knock-on damage of MoS₂. The typical electron probe current was 18 pA. Images were acquired with a Gatan high angle annular dark field (HAADF) detector with angular range (49.5-198 mrad) using 185 mm camera length. To highlight the relevant detail, the image was processed using the “double-Gaussian filtering” method³³⁵.

2.3.6 Supplementary Information

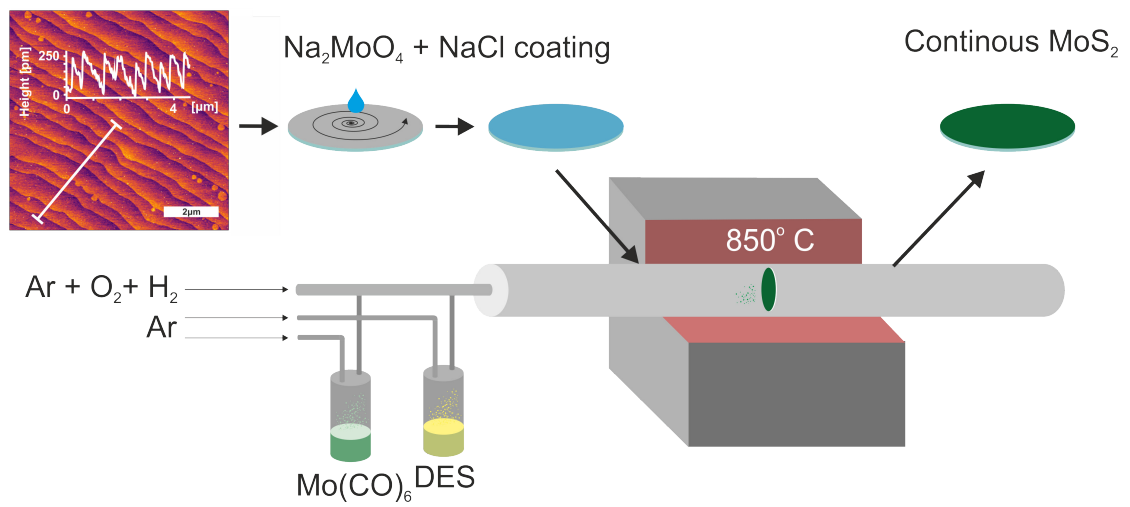


Figure 2.16: Schematic of the custom-made MocVD setup for the MoS₂ monolayer synthesis. The annealed c-plane sapphire 3-inch wafer is spin-coated with growth promoter (mixture of Na₂MoO₄ and NaCl) and placed in a tube furnace. Growth step is performed in ambient pressure and at 850°C.

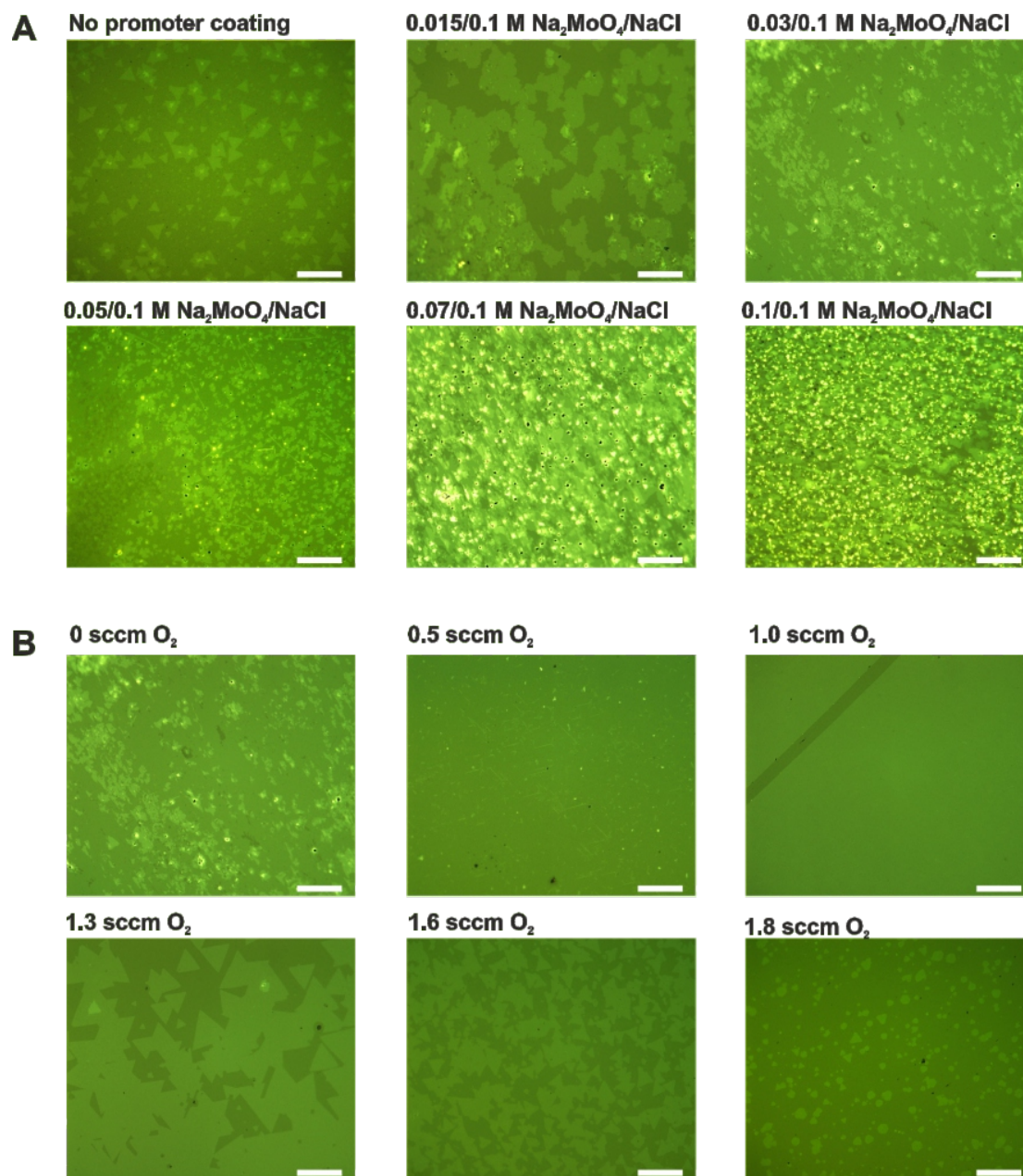


Figure 2.17: Optical images of a MoS₂ grown under different process conditions showing (a) an impact of precursor solution concentration ratio over a growth thickness. The growth process was done at 210 sccm of Ar, 3 sccm of diethyl sulphide, 12 sccm of Mo(CO)₆, 4 sccm of H₂ and 0 sccm off O₂ at 850°C for 30min. (b) a growth results influenced by the addition of slight O₂ flow to the reaction. The growth conditions were the same as in (a) with a constant precursor concentration of 0.03 M / 0.1 M and varying oxygen flow. All scale bars are 50 μm.

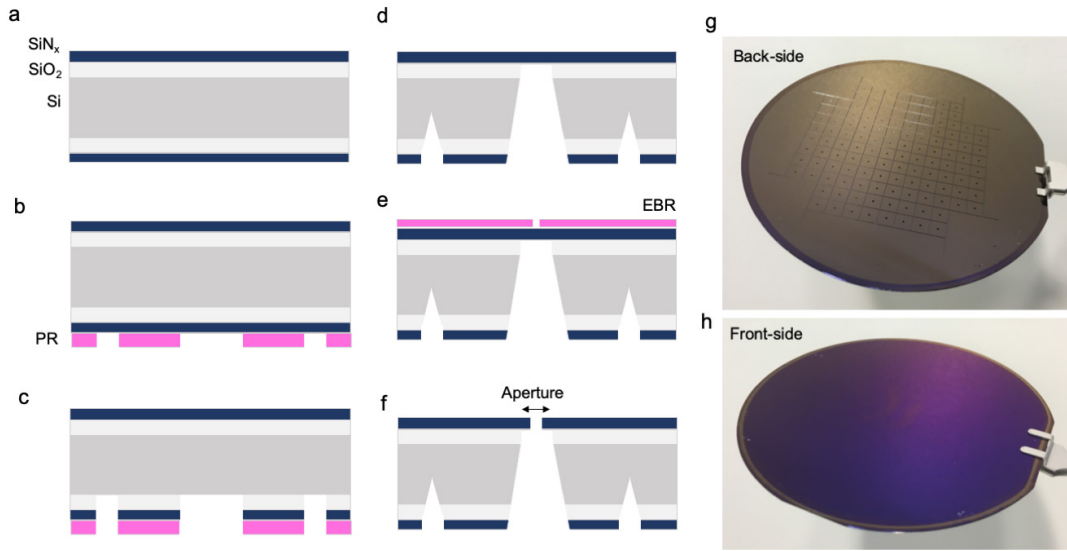


Figure 2.18: Substrate fabrication. Wafer-scale process of the supporting SiN_x chips preparation is explained step by step: double side polished 380 μm thick Si (100) 100 mm diameter wafer (darker grey) with 60 nm of SiO₂ (lighter grey) and 20 nm of SiN_x (dark blue) on each side (a) is being processed with back-side photolithography, pink for photoresist (PR) layer (b) and the pattern is transferred using dry etching (c). The aperture is exposed to 25% wt KOH to form the SiN_x membranes and dicing lines (d). The ≈ 80 nm apertures in the middle of each membrane are being formed using e-beam lithography, pink for e-beam resist (EBR) layer (e) and a consequent dry etching (f). The resulting wafer design is shown from the back side (g) and the front side (h).

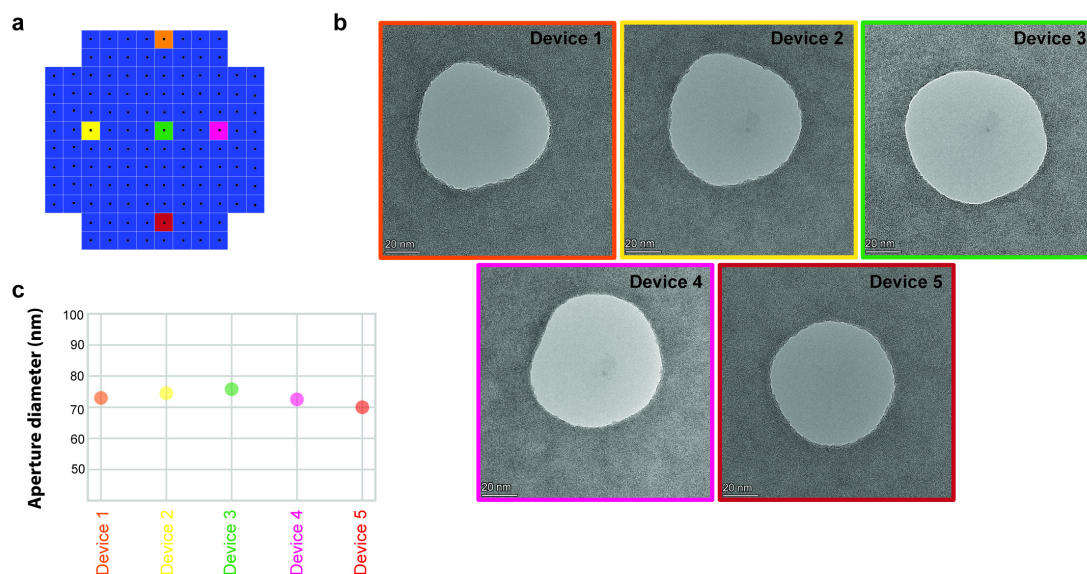


Figure 2.19: Substrate aperture variability and quality characterization. (a) Representative sites on the wafer from where five devices are used to characterize their aperture size and cleanliness before transfer. Presence of bulky residues around the aperture causes blister formation after the transfer of MoS₂. (b) TEM images of respective devices show the aperture openings and showed clean surface. (c) The aperture diameter was ≈ 75 nm showing similar sizes and very low substrate variation ($< 5\%$ error), estimated using Image J.

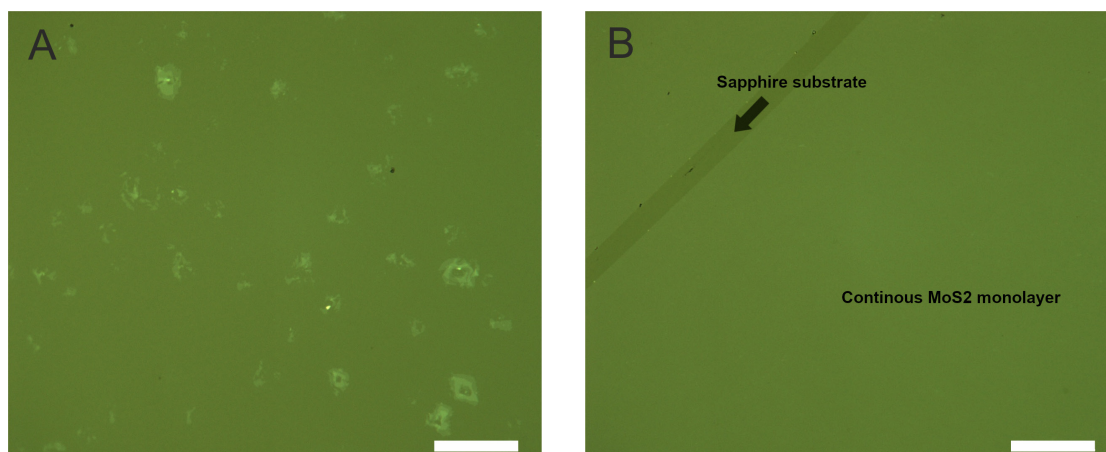


Figure 2.20: Optical images of a MoS₂ monolayer film grown over a large area from the same batch. (a) with visible extruded grain boundaries and secondary nucleation sites where the spin-coated solution was the thickest (around the edges of the substrate) representing roughly $\approx 10\%$ of the substrate area, and (b) with a clean, continuous monolayer surface visible on the remaining area. Scale bars are 50 μm .

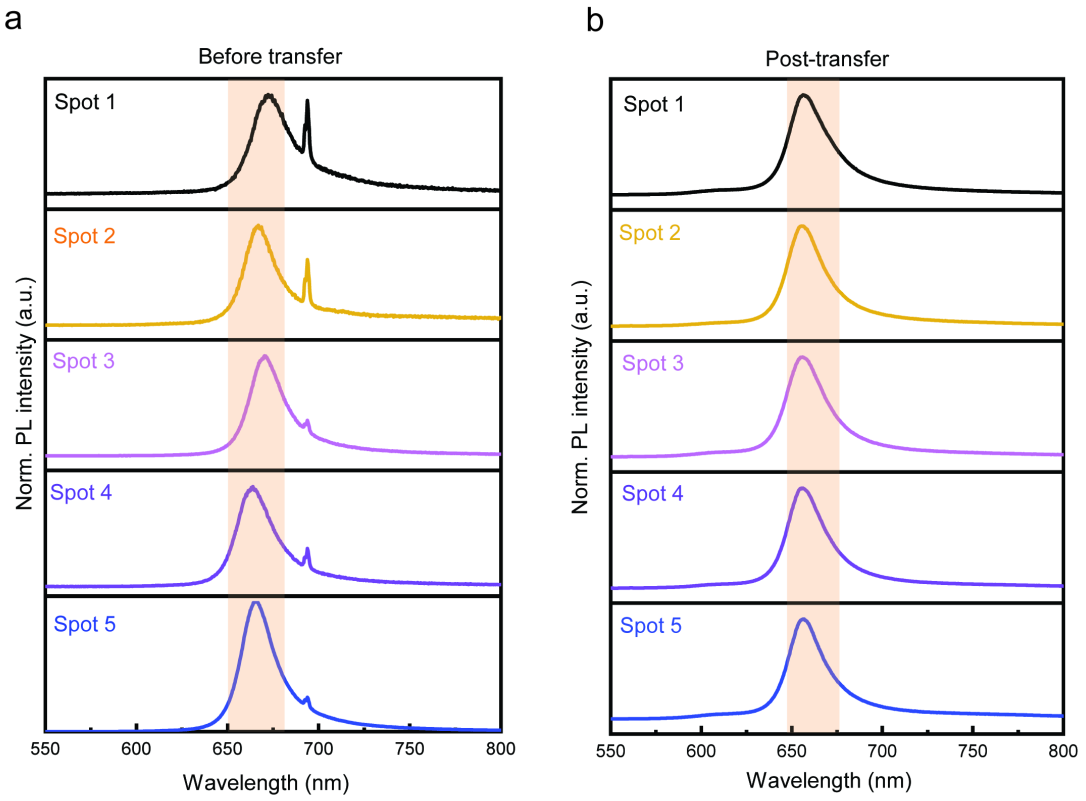


Figure 2.21: Photoluminescence measurements. (a) As-grown MoS₂ on the sapphire substrate from five different spots (shown in Figure 2a-b in the manuscript) before and (b) after the transfer on SiN_x surface. The shaded region in the graphs is a guide to the eye showing the peaks corresponding to the MoS₂.

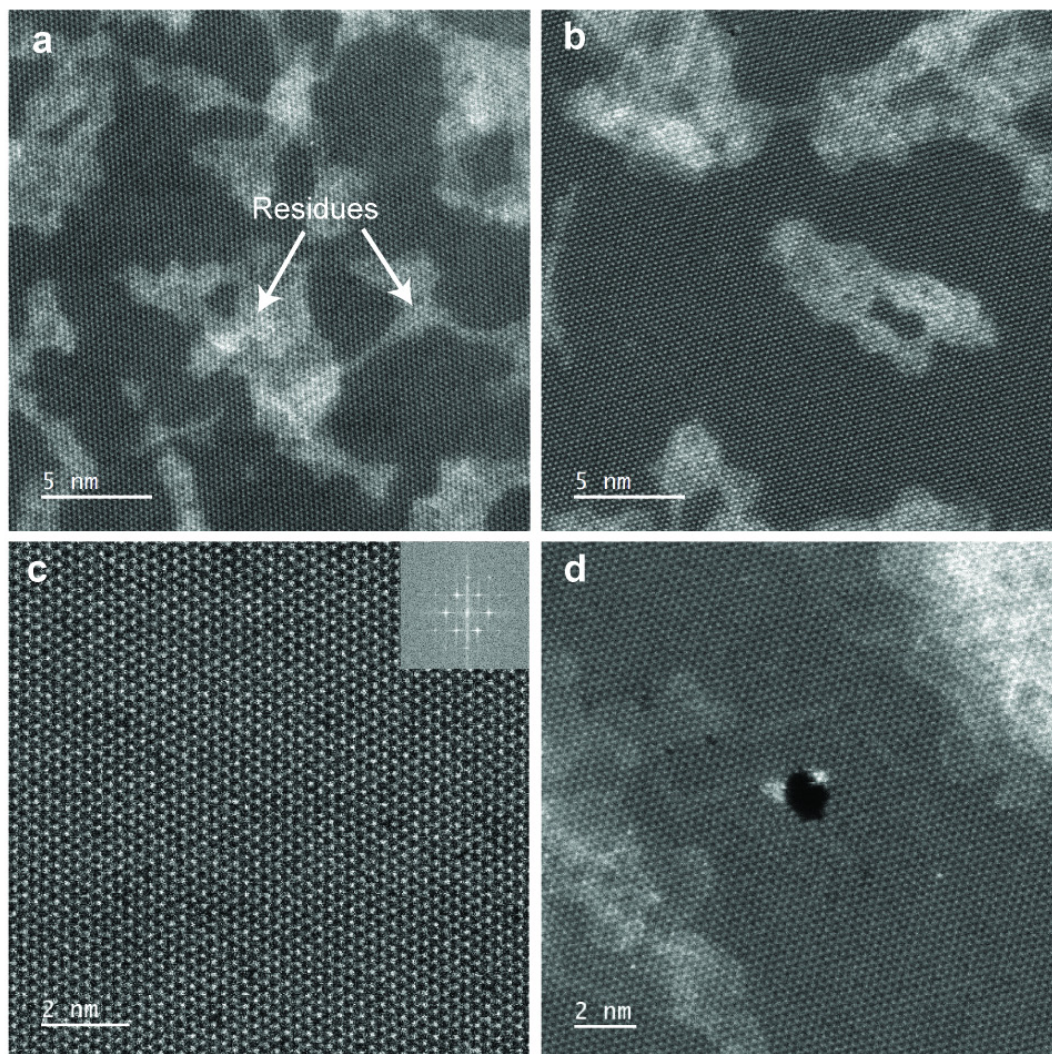


Figure 2.22: Raw STEM/HAADF images show a large-field of view (FOV) of continuous MoS₂ lattice transferred by PDMS. (a, b) Representative MoS₂ areas with residues (brighter contrast on the panels). (c) High magnification STEM image shows the perfect lattice structure of monolayer MoS₂. The inset image shows the Fast Fourier transform, which further confirms the monolayer structure. (d) A nanopore (≈2 nm²) in the center of the image, formed by the electron-beam probe in STEM.

Batch	Total chips	Successful transfer	Unsuccessful transfer	Broken SiN _x membrane post-transfer	Transfer efficiency (%)
Batch S	120	83	36	1	69.1
Batch B	128	87	41	0	67.9
Batch C (shown in Figure 32.15)	128	94	34	0	73.4

Table 2.1: Comparison of wafer-scale transfer efficiency of MoS₂ using PDMS among different batches of substrates. From these wafer-scale transfer, the average transfer efficiency is 70.13 ± 2.4 %.

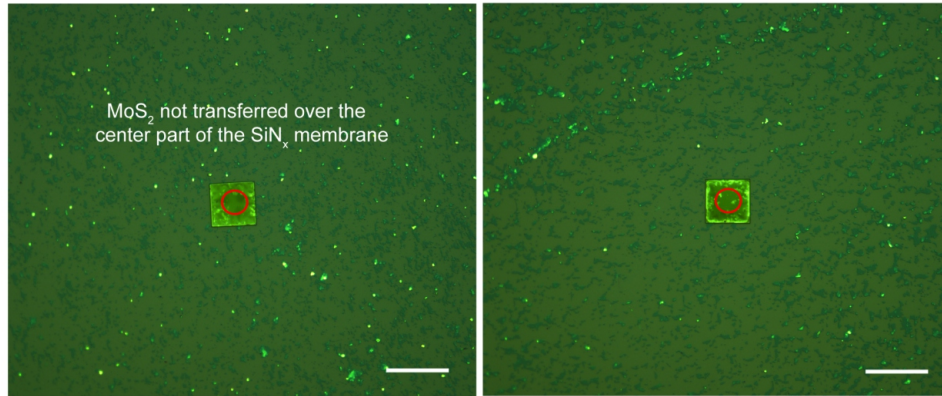


Figure 2.23: Optical images showing examples of unsuccessful transfer of MoS₂ over the highlighted region where the aperture is located. All scale bars are 50 μm .

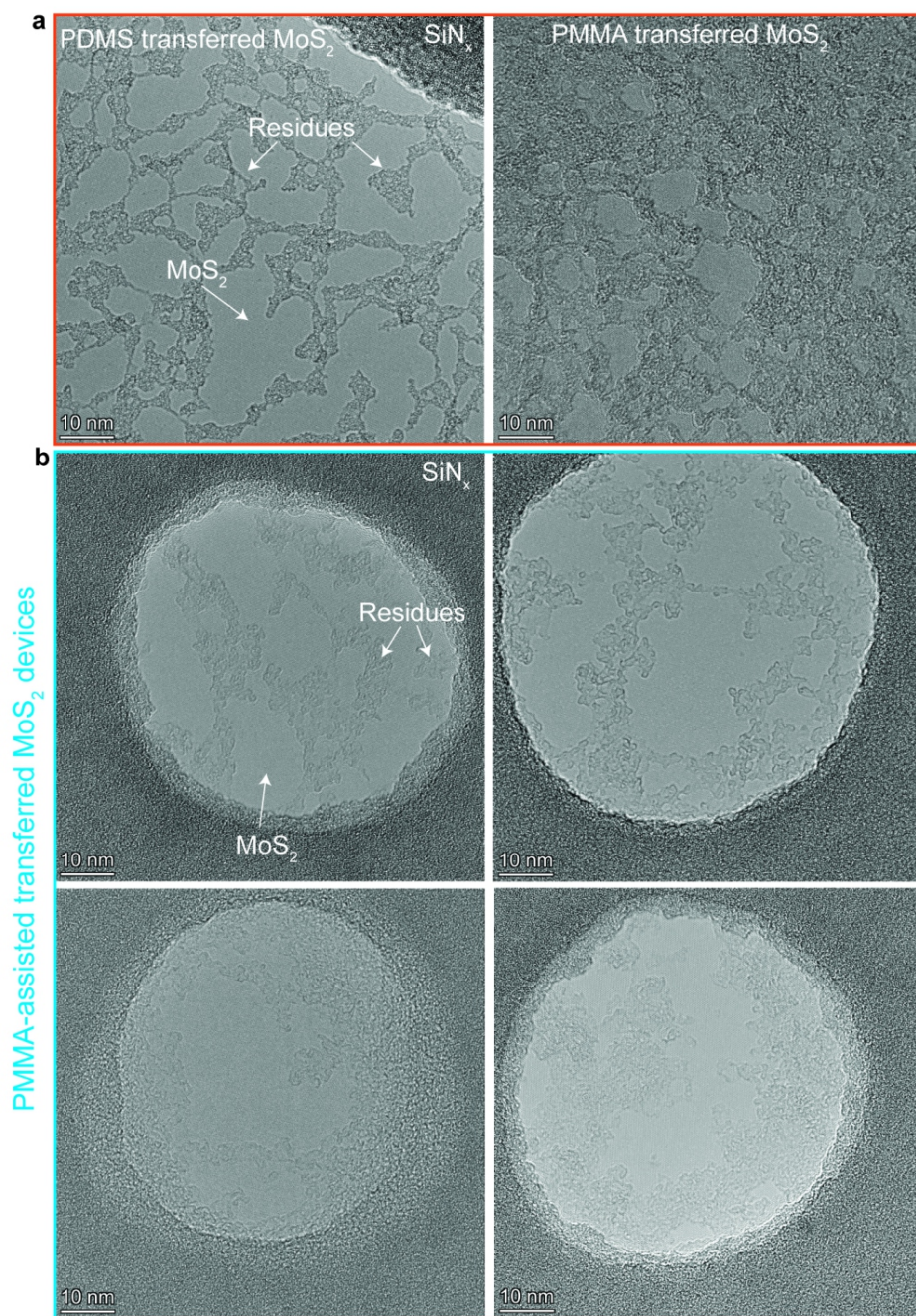


Figure 2.24: Comparison and cleanliness variation among samples of MoS₂ imaged using TEM. (a) TEM images showing suspended MoS₂ post-transfer using PDMS and PMMA polymers on SiN_x TEM grids. The calculated clean area MoS₂ (without residues) with traditional PMMA was $\approx 20\%$ while with PDMS (current method) was $\approx 50\%$ clean area on the respective MoS₂ samples. The clean regions were calculated using Image J1. (b) Representative devices with MoS₂ transferred using traditional PMMA polymer showing variation in cleanliness. These devices show comparable cleanliness with MoS₂ devices transferred using PDMS polymer (2.15b in main text).

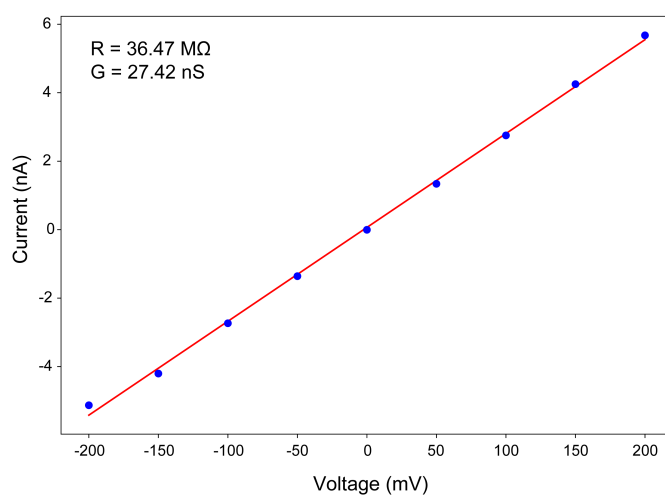


Figure 2.25: I-V characteristics (Device A). The location of Device A is highlighted in 2.15a in the manuscript. The I-V response for the MoS₂ nanopore was measured in 1M KCl by sweeping the voltage in the range between -200 mV and +200 mV.

2.4 Wafer-scale MoS₂ with water-vapor assisted showerhead MOCVD

The following section is based verbatim on the following publication:

Michal Macha^{VI}, Hyun Goo Ji^{VII}, Mukesh Tripathi^{VII}, Yanfei Zhao^{VII}, Mukeshchand Thakur^{VI}, Jing Zhang^{VII}, Andras Kis^{VII} and Aleksandra Radenovic^{VI}

Wafer-scale MoS₂ with water-vapor assisted showerhead MOCVD, In preparation, 2022.

A.R, A.K. and M.M. conceived and designed the experiments; M.M. synthesized samples and optimized the process, M.M., H.G.J., Y.Z. and J.Z. developed the process parameters, M.M. performed optical, SEM, HRTEM, Raman and PL measurements, H.G.J. and M.M. analyzed the data, M.Thakur transferred the substrates on TEM grids, M.Tripathi performed and analyzed STEM images. M.M. wrote the paper, with inputs from all authors; A.K. and A.R. supervised the project; All authors discussed the results and commented on the manuscript.

2.4.1 Introduction

From the broad family of atomically thin, two-dimensional (2D) materials the molybdenum disulphide (MoS₂) has been found particularly interesting in recent years. Being a member of the transition metal dichalcogenides (TMD)³³⁶, MoS₂ unique electronic^{277,333} and optical properties²⁵⁰ combined with high mechanical flexibility^{317,337} make it an attractive candidate for a potential new generation of wearable devices³³⁸, flexible sensors^{339–341} or nanoelectronics^{277,342} as well as heterostructure research and development^{343–351}. Therefore, after years of extensive study the shift of academic focus from small, lab-scale synthesis methods towards the prototype applications and scalable processes is inevitable^{352–354}.

One of the most vigorously investigated aspect of scaling up the research and application of MoS₂ is the large-scale, uniform and high quality material synthesis^{199,291,299,320,355–359}. Over the years, numerous efforts to understand, optimize and grow large-area 2D films have been reported^{353,360}. The most researched, and versatile approaches are the chemical vapor deposition (CVD)^{320,357,358,361} and metallorganic chemical vapor deposition (MOCVD) processes^{199,273,316,359}, both allowing the atomic thickness-controlled growth. While CVD is considered the most common and straightforward synthesis method due to the use of commonly available powder precursors of sulfur and molybdenum its metallorganic MOCVD variant is considered to be crucial to achieve best results and highest reported material quality¹⁹⁹.

The most important feature of MOCVD is its high level of repeatability due to the use of gaseous precursors and wide array of tunable process parameters. Recent research showed the potential of MOCVD to obtain the high quality monolayer TMD films using hexacarbonyls (e.g. molybdenum hexacarbonyl - Mo(CO)₆) as a metal source^{199,289,316,359} and either diethyl^{273,316}, dimethyl³⁵⁵ or chalcogenide hydrides as the chalcogen precursor (e.g. hydrogen

^{VI}Laboratory of Nanoscale Biology, , EPFL ,Lausanne, Switzerland

^{VII}Nanoscale Electronics and Structures, Institute of Materials Science and Engineering, , EPFL ,Lausanne, Switzerland

disulphide H₂S^{199,289}). This, combined with a thorough study of the precursor reactions and thermodynamics, gaseous parameters^{288,362} and added growth promoters using liquid salt solutions^{289,290,355} proved to be the key to obtaining superior material properties, large crystal size and uniform substrate coverage on large scale substrates.

However, most of the results in the field are obtained using the hot-wall, tube furnace setup. Albeit robust and relatively cheap method of 2D material synthesis, tube furnaces do have a significant size limitation prohibiting further fabrication upscaling and industrial adaptation of monolayer MoS₂. Promising studies using much more versatile showerhead systems, typically used in modern semiconductor's industry³⁶³ for repeatable, large-scale manufacturing, has demonstrated the capability of MoS₂ and other TMDs synthesis on a 4-inch wafer scale. The atomic layer deposition (ALD)^{364,365}, molecular beam epitaxy (MBE)^{366,367} and MOCVD approaches^{359,368} to synthesize TMD monolayers were reported. Material made in such a process however lacks the qualities of tube-furnace monolayers. Due to different furnace geometry (lamellar gas flow, shorter distance between the gas inlet and substrate, heating directly at the substrate susceptor), most successful tube-furnace recipes cannot be directly used. Thin films reported up to date show much smaller domain size (in the order of tens of nanometers^{359,364,365,368}) which significantly impact the material properties. The high-temperature decomposition products of organic gaseous precursors tend to contaminate the material with carbonaceous impurities³⁶⁹ and might lead to growth limiting or suppressing phenomena^{288,362}, thus need to be precisely controlled. On top of that, typical process suffers from long deposition times, often reaching tens of hours which renders grown material expensive to obtain.

In this study we compare and combine the state-of-art tube-furnace methods of large-scale monolayer MoS₂ synthesis using salt solutions as growth and seeding promoters with gas-phase and liquid-phase precursors in the industrial showerhead system. We further optimize the best synthesis approach to achieve an uniform, continuous wafer-scale monolayer MoS₂ with largest reported grain sizes up to date (>100 μ m) using the showerhead MOCVD. Finally, we show and discuss how the material quality, uniformity and coverage can be dramatically improved by adding the water vapor to the process gas mixture to eradicate growth-limiting factors such as carbonaceous and organic gas decomposition products. The results are supported by systematic Raman and photoluminescence (PL) analysis as well as X-ray photoelectron spectroscopy (XPS) and defect density calculations based on scanning transmission electron microscope (STEM) study. This work provides direct methodology to widely adapt large-area, monolayer MoS₂ synthesis to industrial showerhead systems.

2.5 Experimental Results and Discussion

All experiments were performed on the commercial Aixtron BM Novo MOCVD system. The coldwall, showerhead reactor is designed to separate the chalcogen and metal precursor sources enabling the MOVCD reactions to occur only at the substrate surface (Fig. 2.26A)

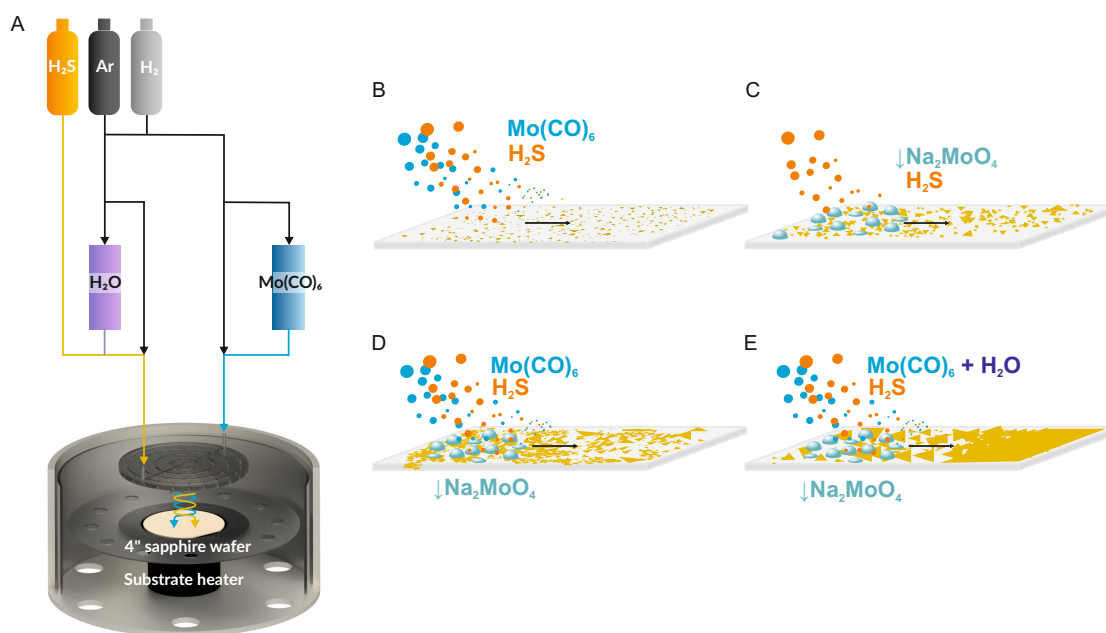


Figure 2.26: (A) A schematic of the experimental MOCVD setup with showerhead designed to prevent the chalcogen and metal precursor sources from mixing before reaching the substrate. With gas-phase only approach (B), A liquid-phase-sulfurization approach, hybrid gasliquid growth method (D) and a H₂O assisted growth method with a controlled supply of the moderate amount of H₂O vapor (E).

minimizing potential unwanted processes and reactor contamination. Such an adaptation is vital for controlled and clean process reaction since the decomposition temperature of gaseous molybdenum precursor used here (Mo(CO)₆) is relatively low (250°C³⁷⁰) and may lead to gas lines and showerhead contamination. All MOCVD growth variations are schematically shown on Fig. 2.26B-E and are discussed in details in the following sections. All growth experiments are performed under constant parameters of 960°C, 830mbar of pressure, 150min of growth step time and by using 4-inch c-cut sapphire wafer as a growth substrate. Argon is used as an ambient gas and precursor carrier whereas H₂ is used as an active gas and carbonyl reduction agent. Flow parameters are detailed in Methods section and remain constant for all growth approaches.

MoS₂ growth with gas-phase precursors. The first investigated MOCVD process pathway for MoS₂ growth is the gas-phase synthesis (Fig. 2.26B). It is considered as a benchmark process as it does exploit all tube-furnace recipe adaptations discussed further. During gas-phase MOCVD growth, all of the precursors are fed into the reactor chamber through the showerhead along with the carrier gas (argon) and additional process gases (hydrogen) necessary for efficient synthesis of monolayer film. Albeit fundamentally scalable and clean synthesis approach, achieving large lateral MoS₂ domains in the showerhead system is challenging due to large nucleation density and low reaction rate²⁰⁰. Typical crystal size reported in literature reaches up to 100nm^{359,365,368}. In addition, only material thickness (and not single grain size) scales with the process time. In our optimized recipe we have surpassed that limit reaching the

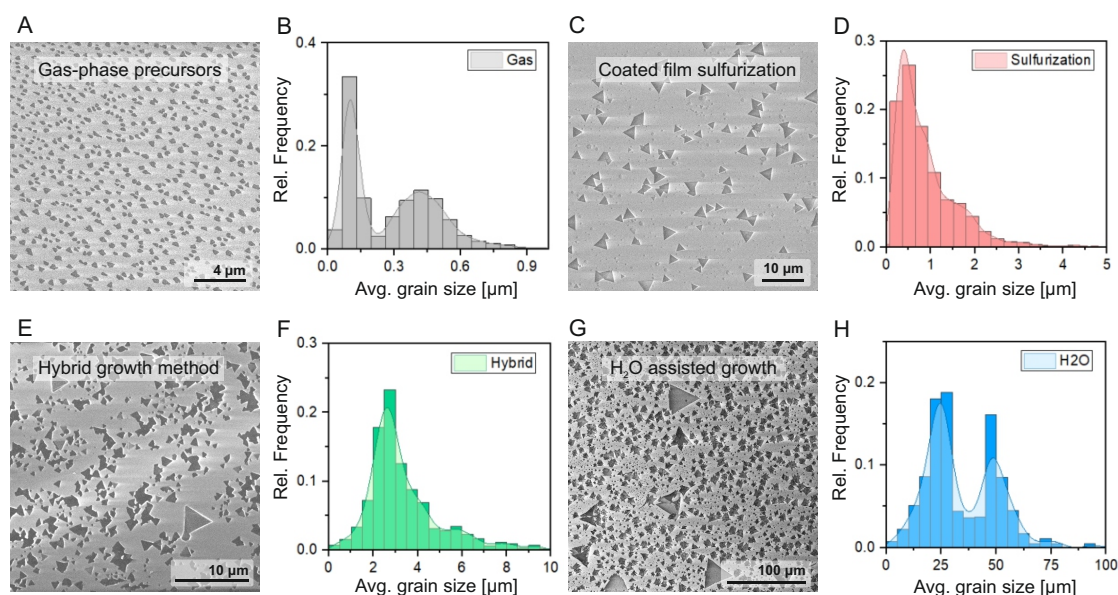


Figure 2.27: A comparison of MoS₂ growth yield obtained through different growth approaches. The SEM image analysis of gas-phase only approach (A) shows small, densely nucleated grain clusters with an average size of 500nm and large contribution from unripened nuclei (D). A coated-film sulfurization approach yield large, 1 μ m crystals which locally reach up to 3-4 μ m (C-D). The hybrid growth method results in an average of 3 μ m single crystals (E,F). Finally, with a controlled supply of the moderate amount of H₂O vapor lateral crystal size increases by order of magnitude (G-H) with evident separation between two combined growth regimes (liquid and gas-phase) visible in grain size distribution (H). The presented SEM images were chosen from the substrates' edge to show an av. grain size. Histograms were calculated from 20 separate SEM images from each growth method.

size of 500nm of single crystal monolayer material (Fig. 2.27A-B) with gas-phase precursors only. It is evident that crystal size is limited by the reaction byproducts^{199,288,362} causing high temperature etching effects as well as high nucleation rate prohibiting the lateral crystal growth. The average substrate surface is thus composed of large crystals mixed with much smaller MoS₂ nuclei, constantly formed and etched during the process (Fig. 2.27B) by gaseous products of Mo(CO)₆/H₂S/H₂ chemical reaction³⁶⁸. On top of that, since the process requires a steady ratio of Mo:S along the entire substrate area, even the smallest flaws or imbalances in the gas feed or showerhead design may cause nonuniform growth conditions leading to uneven crystallization and local growth anomalies. Therefore, achieving stable coverage and substrate-wide uniformity, using this approach is still challenging and far from the results reported in hotwall MOCVD systems¹⁹⁹.

MoS₂ growth with coated film sulfurization. Another way of controlling the precursors coverage is to use a liquid source of molybdenum. In this approach we are spin-coating the substrate with sodium molybdate (Na₂MoO₄) and sodium chloride (NaCl) water solution (Fig. 2.26C). Such a combination allows to pre-seed^{316,355} the surface with controlled amount of molybdenum as well as enables the use of catalytic NaCl, widely used in tube furnace MOCVD MoS₂ recipes for increasing the reaction rate and decreasing nucleation density

leading to large single crystal formation^{316,355}. Coated wafer is then sulfurized under H₂S gas flow without an external, gaseous source of molybdenum. The material tends to form large single crystals and continuous films, whose thickness and coverage depend on the spincoated mixture concentration which controls the local Mo saturation during growth. Na₂MoO₄/NaCl sulfurization approach is highly scalable however the use of the alkali salt solution is heavily impacting the final material quality. Intermediary NaCl+MoS₂ reaction products³²⁴ lead to the fast crystal growth rate but also have been found to remain underneath MoS₂ films. This phenomenon, driven by excessive use of NaCl, negatively impacts the epitaxial connection between crystal and sapphire substrate and may lead to grain boundary defects and uneven grain stitching inherently deteriorating large-area continuous films cohesion and its electronic parameters³²⁴. To avoid this unwanted effect we have limited the Na₂MoO₄/NaCl molar concentration to 0.03M and 0.1M respectively. This allowed to preserve the MoS₂/sapphire epitaxy and maintain high material coverage. In our coldwall, showerhead regime we note lateral crystal size varying from 0.7 up to 3-4 μm (Fig. 2.27C and D) with sporadic events of >100 μm single crystals forming continuous films locally. This growth method has an intrinsic self-limiting character due to a fixed amount of Mo coated on the substrate. Tuning the precursor solution molar concentration allows the control over the coverage and nucleation density, however uniformity is problematic on large area substrates. The inherent to spincoating process uneven film thickness (especially emphasized at large-scale growth areas) lead to different local Mo:S concentrations during the process. Such a coverage issue manifest in bilayer, multilayer or blank areas with the presence of unreacted, bulk molybdenum oxide particles on different substrate areas. Sulfurization of spincoated Na₂MoO₄/NaCl film is therefore not perfectly adjustable in the case of 4-inch substrates and requires careful molar concentration to balance between preserving epitaxy and promoting continuous film growth to be usable.

MoS₂ growth with hybrid process. Increasing the control over the material's coverage, crystal density and uniformity even further requires fine-tuning the precursor flux i.e. by combining two precursor sources: adding a gas phase Mo(CO)₆ flow to the process with spincoated mixture of Na₂MoO₄/NaCl (Fig. 2.26D) on the substrate. Combined, hybrid method in principle allows to compensate individual limitations of small grain size present in gas phase method and self-limiting Mo supply of spincoated film sulfurization approach. In this case, we consider Na₂MoO₄/NaCl as a Mo seeding/catalytic agent, leading to the formation of molybdenum oxychlorides, oxysulfides and suboxides³⁵⁵ kickstarting and promoting the film growth under the constant supply of Mo from the Mo(CO)₆ gas phase. Indeed, in our experiments the hybrid method yields single crystals of 3 μm in average lateral size (Fig. 2.27E and F) with largest exceeding 100 μm locally. Adding Mo(CO)₆ however reintroduces the carbonyl reaction byproducts from the $Mo(CO)_6 + H_2S + H_2$ reaction. Further optimization of the process (to improve single crystal size, uniformity and monolayer coverage) does not intuitively scale with the Mo(CO)₆ nor Na₂MoO₄/NaCl concentration during the growth. Local imbalances of Na₂MoO₄ and Mo(CO)₆ lead to multilayer islands formation. We have found that reducing the molar concentration of Na₂MoO₄ to as low as 0.005M is enough to effectively pre-seed and nucleate Mo₂ and crucial to minimize the multilayer growth under the constant

Mo(CO)₆ mass flux. As discussed later, in our experiments carbonaceous reaction products (CO₂, CH₄, C) do not seem to dope MoS₂ nor contaminate the substrate however they do contaminate the showerhead and MOCVD reactor heavily, significantly suppressing the growth process by releasing carbonaceous products to the gas phase growth environment limiting the reproducibility. Thus further increase of MoCO₆ concentration is unwelcome and counter productive for obtaining high-quality, large-area films. Scalability of hybrid approach offers more process parameters and better coverage control, however it still requires a significant optimization to be viable on industrial scale.

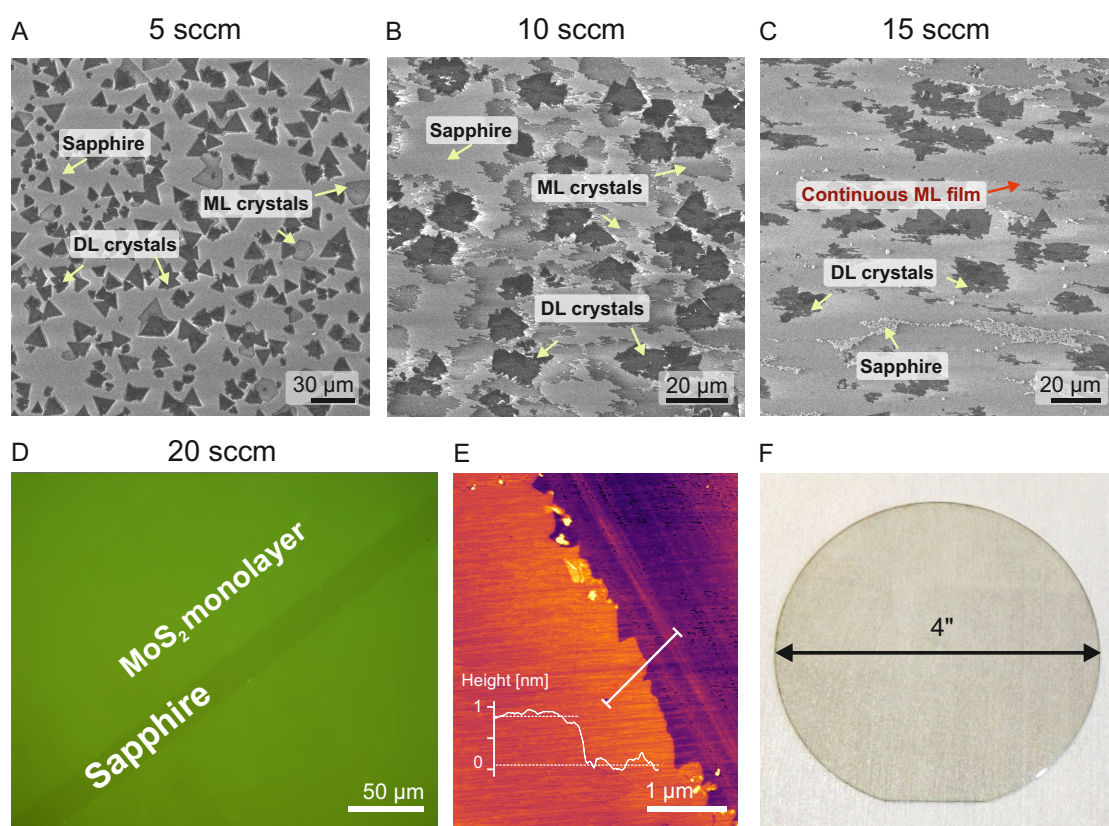
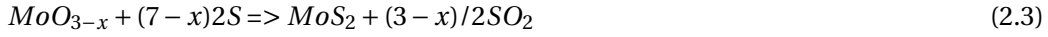


Figure 2.28: SEM images of MoS₂ coverage with increasing H₂O vapor concentration during the growth process. Coverage of the continuous monolayer film improves gradually with the increase in the water vapor supply (A-C) and peaks at 20 sccm where continuous monolayer film is observed as shown on a panel D (optical microscope image of deliberately scratched MoS₂ film). Local AFM analysis confirms the monolayer thickness. Material uniformity is maintained over the 4-inch substrate area (F).

Water-assisted large grain growth. The presence of water vapor during the MOCVD reaction is widely considered as unwanted. Uncontrollable moisture can lead to significant decrease of material quality due to water-induced oxidation and reduction during growth process²⁰⁹. However, a controlled addition of small amounts of water vapor (Fig. 2.26E) was found to be beneficial due to low oxidizing effects which assist in the removal of carbonaceous reaction products³⁷¹ and assists in reduction of molybdenum oxides into suboxides and hydrogen

promoting the lateral growth (formula 1-3)



In our case, a flow of 5 sccm of Argon through a room-temperature H₂O filled bubbler was sufficient to significantly remove impurities and promote monolayer crystals to reach an average lateral size of 25-50 μm (Fig. 2.27G and H) with largest locally exceeding 100 μm (Fig. 2.28) and with the significant increase in continuous film coverage with further increase in water vapor flow. Monolayer coverage peaked at 20 sccm of H₂O vapor flow (Fig. 2.28D-E) and it's continuity was maintained across 4-inch substrate area (Fig. 2.28D). We attribute this dramatic improvement of crystal size and monolayer coverage to the self-regulating effect of H₂O. Due to gas-flow imbalances coming from subtle showerhead and gas-line imperfections and coated film non-uniformity (amplified by large-area substrate), different $Mo(CO)_6 + H_2S + H_2$ reaction pathways may occur locally leading to the formation of volatile CH₄, C, CO, CO₂, COS, CS₂ species in different concentrations^{362,368}. Water vapor may react with and suppress the formation of the excess carbon oxides and sulfides negating the effects of local differences in reaction paths and their negative impact on MoS₂ grains lateral growth leading to overall better coverage as shown in figure 2.28D and E.

Spectroscopic characterization. A detailed material characterization was performed to compare the uniformity and crystallinity of MoS₂ synthesized from each growth approach. Analysis of the shape of characteristic E₂g and A₁g Raman peaks from monolayer areas from each method (Fig. S2.32A) shows $\Delta_{E_2g-A_1g}$ to be 20.9, 20.8 and 19.5 for sulfurization, hybrid and H₂O consecutively. Gas-phase growth method proved to be difficult to analyze due to small grain size and low Raman signal. The full width at half maximum (FWHM) of E₂g and A₁g of each method is shown in Fig. S2.32B and it was found to be narrowest for H₂O assisted approach of 2.6 and 3.4 for E₂g and A₁g, indicating higher crystallinity and good uniformity. In case of all substrates, spectra taken from the 1000 - 1700 cm⁻¹ range showed no distinguishable carbon peaks (Fig. S2.33). Raman spectra taken radially from 50 spots on each wafer confirm the self-regulating effect of H₂O (Fig. 2.29A-B). The separation between E₂g and A₁g peaks smaller than 20 cm⁻¹ is regarded as a proof of a high-quality monolayer³⁷² film. The positions of Raman peaks in case of water-assisted growth remain constant which indicates uniformity in thickness and strain compared with other growth methods. Water vapor can promote further oxidation of thick particles from residual Mo oxides and etching of emerging multilayers during the growth process due to local H₂ generation (as presented in formulas 1-3). Result is formation of continuous monolayer film without thicker, seed particles on wide area of the 4-inch substrate. Panel 2.29C shows PL spectra of MoS₂ synthesized with sulfurization(red), hybrid(green) and H₂O assisted(blue) method. Significantly higher PL emission from water assisted growth indicates that water improves crystal quality by removing carbon contamination which is known to quench PL³⁷¹) as well as enhance the efficiency of precursor

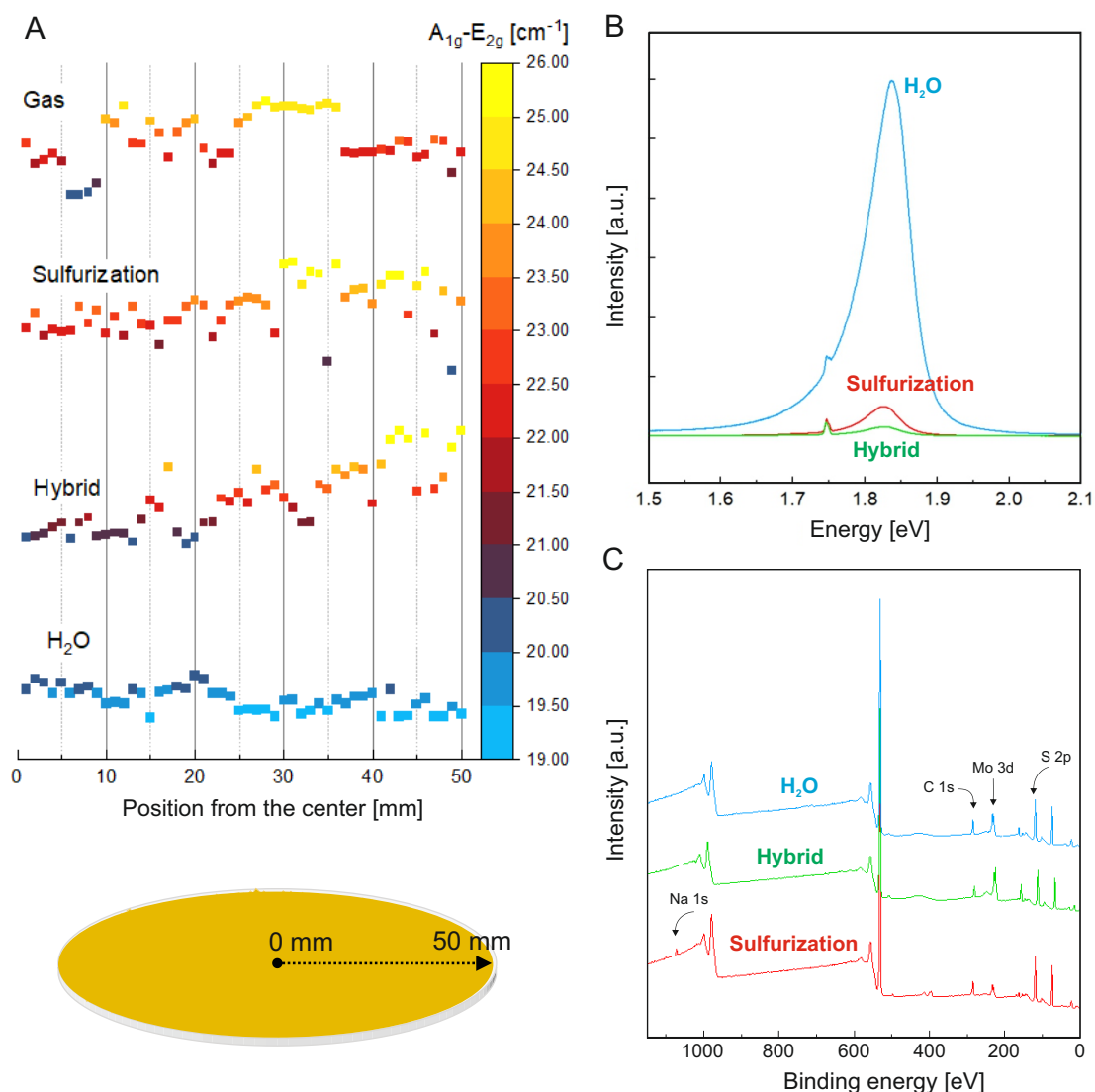


Figure 2.29: An average separation of E₂g and A₁g Raman peaks taken from 50 measurements with a 1mm interval performed across the radial direction of the wafer (A). Measurements were performed in a line-scan fashion, from the center to the edge of the 4-inch substrate. Comparison of characteristic Raman peak separation shows the radial uniformity of MoS₂ synthesised with water-vapor assisted growth method. A representative PL spectra (B) showing significantly higher PL emission from water assisted growth. A comparison of wide XPS spectra (C) shows no residual Na present with H₂O assisted growth. Detailed analysis of Mo 3d and S 2p XPS peaks are shown in Supplementary Figure S2.34.

ligand-reduction. Raman and PL spectra show an evidence of high quality monolayer MoS₂ obtained with water-assisted process.

XPS analysis. An XPS measurement was performed to investigate the chemical states and stoichiometric ratio of the grown MoS₂. Trace sodium was only detected on liquid-phase sulfurized MoS₂ substrates (Fig. 2.29C and table S2.2) as this process relies on coating substrate with relatively concentrated Na₂MoO₄/NaCl solution compared to hybrid approach

(0.03/0.1M as compared to 0.005/0.1M). Comparing the growth methods, water-vapor assisted approach produces the least oxide states (Fig. S2.34A-C), attributed to the Mo⁶⁺ ratio. It is explained by water-assisted enhanced reduction of metal precursor which results in higher crystallinity. Detailed atomic ratios, molybdenum oxides and sodium contents of each method are shown in Supplementary Information, table S2.2.

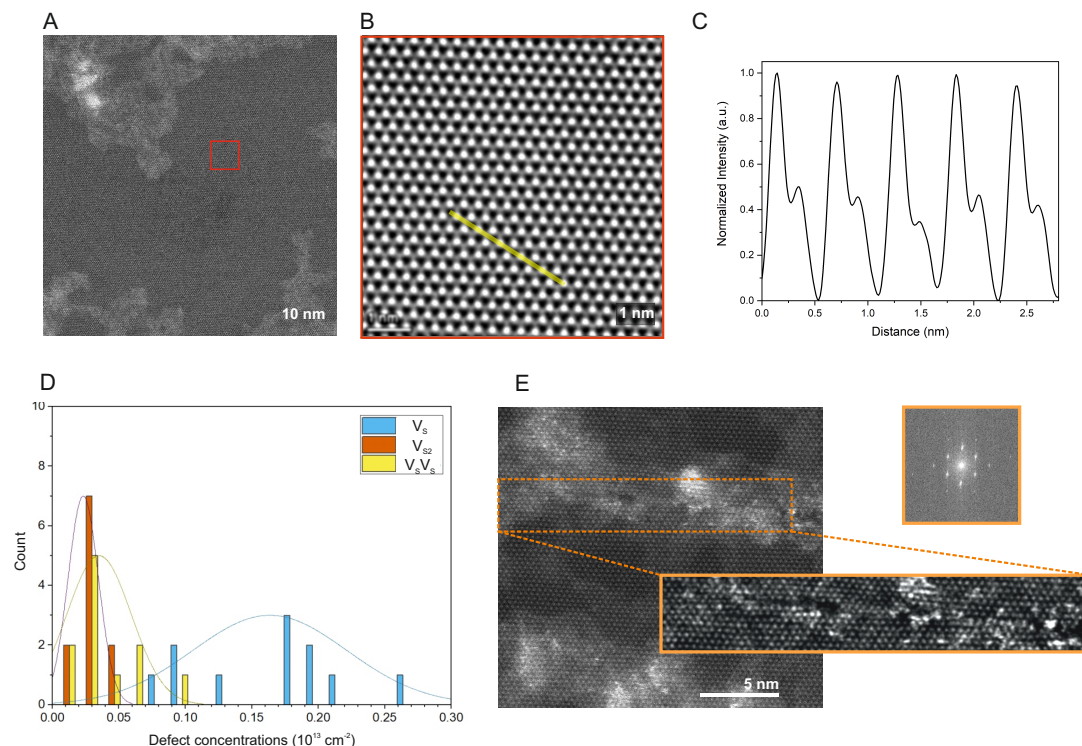


Figure 2.30: A small magnification STEM image (A) of MoS₂ synthesized with water-assisted method with a large magnification zoom at typical MoS₂ area (B) (marked with red) with an intensity line-section (C) showing high crystal quality. Typical defect concentration is presented in the bar plot (D) and its calculated separately for single sulfur V_S, double sulfur V_{2S} and sulfur-next-to-sulfur V_SV_S defect types. Concentrations are calculated from the 16 images taken from different regions. A grain boundary image (D) and its closer inspection shows seamless grains stitching (FFT), a sign of epitaxial growth mode.

STEM imaging. Aberration-corrected STEM imaging was used to image and characterize structural properties of the MoS₂ at atomic resolution. Small and large magnified high angle annular dark field (HAADF) images (Fig. 2.30A and B) shows clean and perfect hexagonal crystal lattice of monolayer MoS₂ film in 2H phase. Due to the Z-contrast dependency of HAADF, atomic intensities of Mo and 2S can be distinguished directly from the atomically resolved images. In case of earlier reported exfoliated and MOCVD grown monolayer MoS₂, different types of defects have been reported. However, here only sulfur mono- and divacancies can be observed which are very common due to their lower formation energies. Moreover, the electron beam can also induce sulfur defects even at lower acceleration voltages. Thus to extract the intrinsic S defects concentrations, number of mono- and divacancies can be calculated with respect to the accumulated electron beam dose in an image series³⁷³.

Further defect concentration analysis shows pristine defect concentration at 1.4×10^{13} per cm² for single sulfur vacancies (V_S) and 0.3×10^{13} per cm² for double sulfur vacancies (V_{S2}) as extrapolated from E-beam dose rate test (Fig. S2.35). A distribution of V_S , V_{S2} and sulfur-next-to-sulfur ($V_S V_S$) defects taken from 11 STEM images (measured area of $\approx 925 \text{ nm}^2$) are presented on fig. 2.30C. MoS₂ synthesized in the water-assisted process does not show any signs of unwanted etching nor oxidative damage. Interestingly, the grain boundaries found during imaging are stitched seamlessly (Fig. 2.30D), proving epitaxial growth mode. Due to the reactive nature of grain boundaries, it attracts contamination along it. However, filtered STEM image (highlighted in orange color) shows no misorientation angle between it. The fast Fourier transform (FFT) of the corresponding image shows only one set of hexagonal pattern, further confirming the high-quality growth of MoS₂.

2.6 Conclusion

All experimental evidence point at a strong advantage of combining the hybrid gas/liquid phase growth approach in the coldwall showerhead system. We have successfully achieved an uniform and continuous MoS₂ film over a large-scale 4-inch substrate with spincoated Na₂MoO₄/NaCl solution and gas-phase Mo(CO)₆ and H₂S by limiting growth reaction imbalances with water-vapor introduced during the growth phase. We found the water to regulate growth reaction by removing carbonaceous products and reduce excess molybdenum oxides. Material characterization confirms good material quality and no negative impact of using moderate and carefully controlled amounts of H₂O. Synthesized MoS₂ maintained epitaxial connection with sapphire substrate. Our findings provide a direct step forward towards developing scalable, reproducible and large-scale MoS₂ synthesis with showerhead reactors and demonstrate the potential of combining key advancements in the field of 2D material growth to overcome the process limitations.

2.7 Authors contribution

A.R, A.K. and M.M. conceived and designed the experiments; M.M. synthesized samples and optimized the process, M.M., H.G.J., Y.Z. and J.Z. developed the process parameters, M.M. performed optical, SEM, HRTEM, Raman and PL measurements, H.G.J. and M.M. analyzed the data, M.Thakur transferred the substrates on TEM grids, M.Tripathi performed and analyzed STEM images. M.M. wrote the paper, with inputs from all authors; A.K. and A.R. supervised the project; All authors discussed the results and commented on the manuscript.

2.8 Methods

MOCVD growth All MoS₂ synthesis experiments were performed at Aixtron BM Novo MOCVD system with coldwall, showerhead, horizontal growth chamber. Prior to growth, 4-inch c-plane sapphire wafers (MTI) were cleaned in IPA, acetone and DI and annealed in 1000°C for 6h to

obtain atomically smooth surface. For sulfurization, hybrid and H₂O assisted growth methods sapphire wafer was additionally treated in 50W O₂ plasma for 5min to ensure hydrophilic surface needed for efficient spincoating of a growth promoter (a solution of Na₂MoO₄ (Sigma Aldrich, 98.0%) and NaCl (Sigma Aldrich, 99.5%) in DI with concentrations of 0.03M/0.1M for sulfurization and 0.005M/0.1M for hybrid and H₂O). All growth processes started with heating the reactor with a sapphire wafer to 950°C under constant flow of 300sccm of high purity argon (Carbagas 99.999%). After reaching set temperature, substrates were exposed to 20 sccm of hydrogen gas (Vici DBS NM Plus 100 Hydrogen Generator, purity 99.999%) and 60sccm of H₂S (Carbagas, 99.9%). For gas-phase, hybrid and H₂O assisted approaches a Mo(CO)₆ (Sigma Aldrich 99.9%) was supplied by 150sccm of Ar gas flowing through bubbler kept at 10°C. In H₂O assisted variant, an additional 10sccm of Ar flowing through DI-filled bubbler at room temperature was introduced. All MoS₂ growths were done at 830mbar with growth steps set to 150min (albeit sulfurization method underwent the complete reaction in only 30min). After that, reactor was cooled under ambient H₂S and Ar flow. After a growth run the reactor chamber was thoroughly cleaned and annealed and all the ceramic elements were additionally air-baked to prevent unwanted carbon contamination.

Raman spectroscopy and PL Raman and PL spectroscopy were done with a Renishaw inVia Confocal Raman Microscope with a 532nm laser beam at a low power (<0.3mW) to avoid defect nucleation and substrate damage. A diffraction grating of 3000mm⁻¹ was used for good spatial resolution.

SEM imaging Scanning electron microscopy was done at Zeiss Merlin SEM with GEMINI II column. All imaging was done at 1kV acceleration voltage to minimize substrate charging. STEM imaging As-grown MoS₂ was transferred from growth substrate using wet-transfer method²⁷³ on 5x5 mm Si/SiN TEM grids (norcada). Scanning transmission electron microscopy imaging was conducted using an aberration-corrected (with double spherical corrector) FEI Titan Themis TEM 60 - 300 kV, equipped with Schottky X-FEG electron source and a monochromator to reduce the effect of chromatic aberrations. To avoid the electron-beam induced knock-on damage, a low acceleration voltage (80 kV) was used for the imaging³⁷⁴. The electron probe current, C₂ aperture size, and a beam convergence angle was 25pA, 50μm, and 21.2 mrad, respectively. Images were acquired with a Velox software (ThermoFisher Scientific) using 185 mm camera length which corresponds to an angular range (49.5 - 198 mrad) in a HAADF detector. To avoid the sample drift, a serial imaging was performed using 512 × 512 pixels with 8 s dwell time. Images were aligned and were processed using “double-Gaussian filtering” method in ImageJ.

2.8.1 Supplementary Information

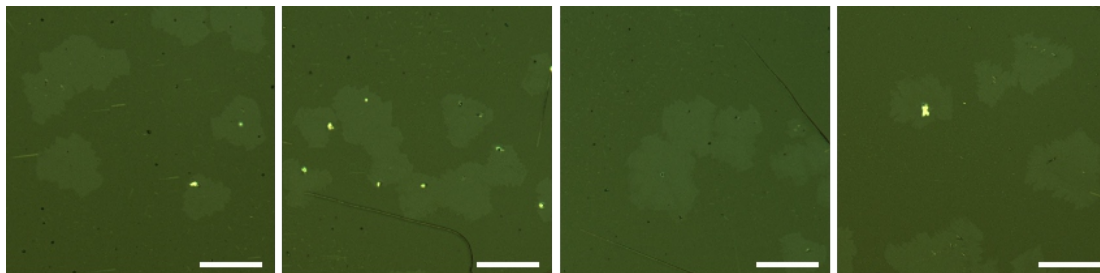


Figure 2.31: Optical images of single crystals spotted during growth recipe optimization. Ranging from mono- to double-layer MoS₂. Scale bar is 100 μm .

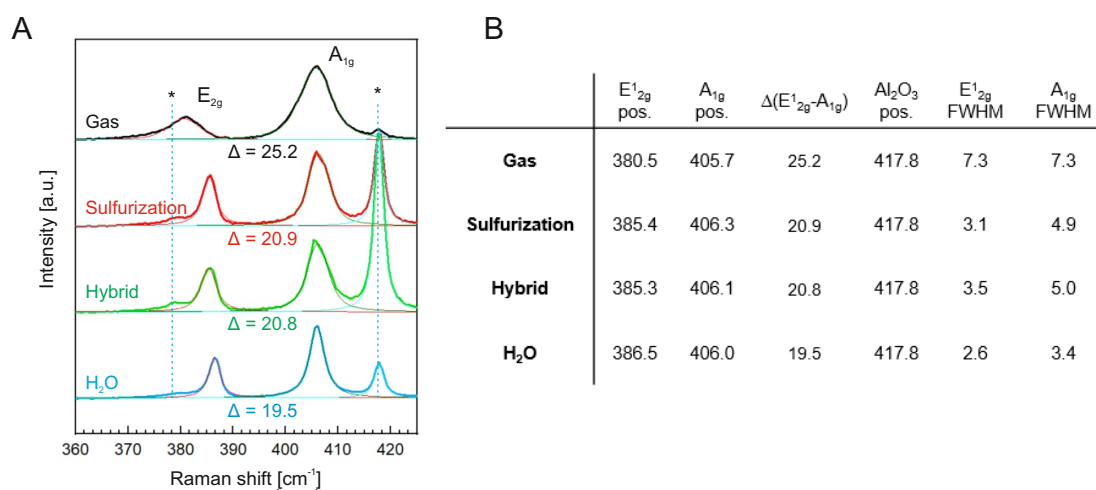


Figure 2.32: A detailed look at typical MoS₂ Raman peaks taken at monolayer locations of MoS₂ synthesized with gas-phase (black), sulfurization (red), hybrid (green) and H₂O assisted (blue) method (A) with detailed peak positions. Positions marked with * represent sapphire substrate Raman peaks. (B) Comparison of MoS₂ properties and their significant improvement for water-assisted growth method.

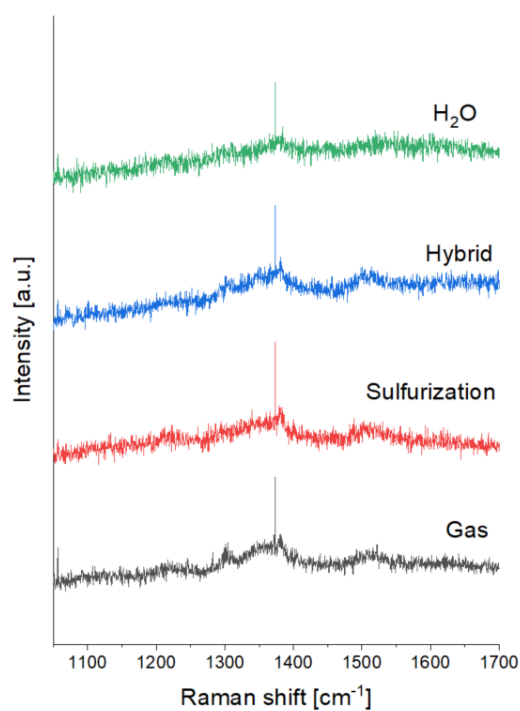


Figure 2.33: Raman spectra of all growth methods show no or trace presence of carbon peaks occurring at 1340 cm⁻¹ and 1580 cm⁻¹. This measurement indicates no detectable carbon deposition on MoS₂.

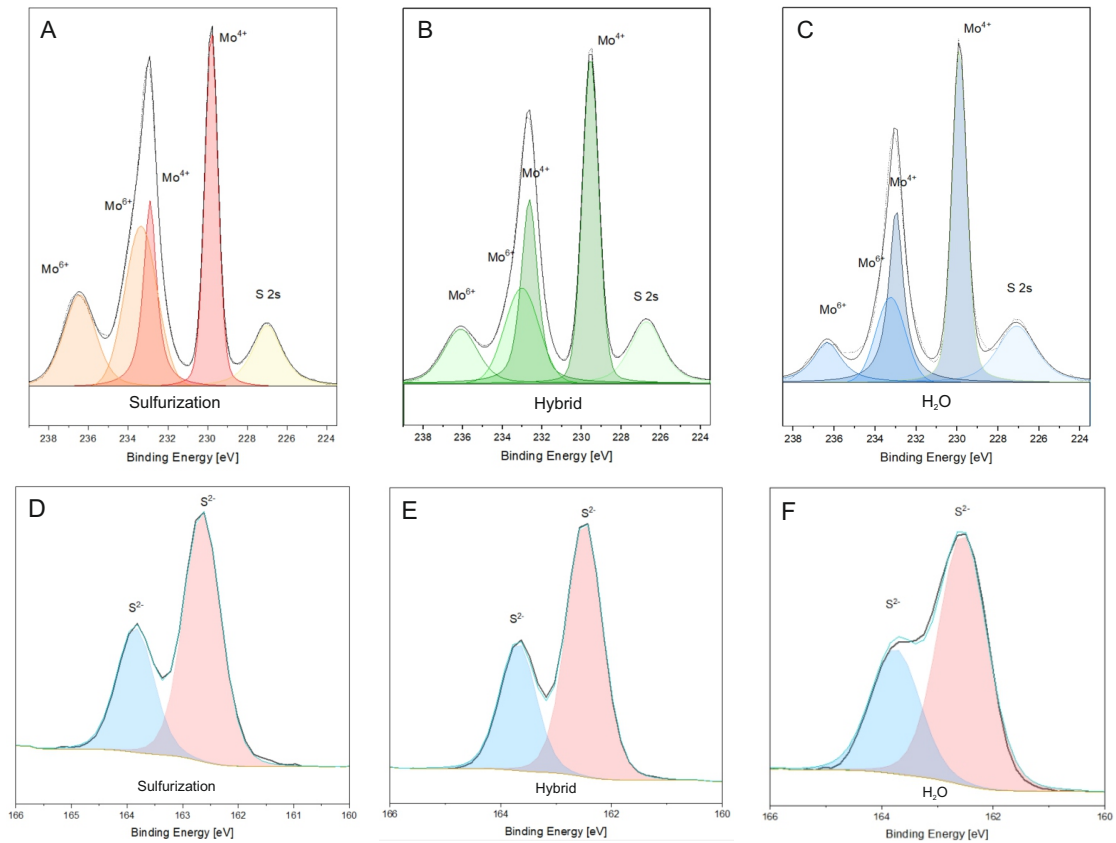


Figure 2.34: Analysis of Mo 3d XPS peaks and its intensities for sulfurization (A), hybrid (B) and H₂O (C) growth methods corroborates a decrease in residual molybdenum oxides. S 2p peaks of monolayer MoS₂ synthesized with sulfurization (D), hybrid (E) and H₂O assisted (F) growth methods.

Sample	MoOx %	MoS ₂ %	Mo : S	Na %
Sulfurization	54.99 ±2.42	45.00 ±2.41	2.22 ±0.17	11.58 ±0.78
Hybrid	31.325 ±7.42	68.675 ±7.42	6.175 ±1.14	0.435 ±0.43
H₂O	37.58 ±0.95	62.41 ±0.95	3.38 ±0.57	0.425 ±0.42

Table 2.2: Average atomic ratios taken from 3 substrates synthesized with each, consecutive growth method along with oxide and sodium content.

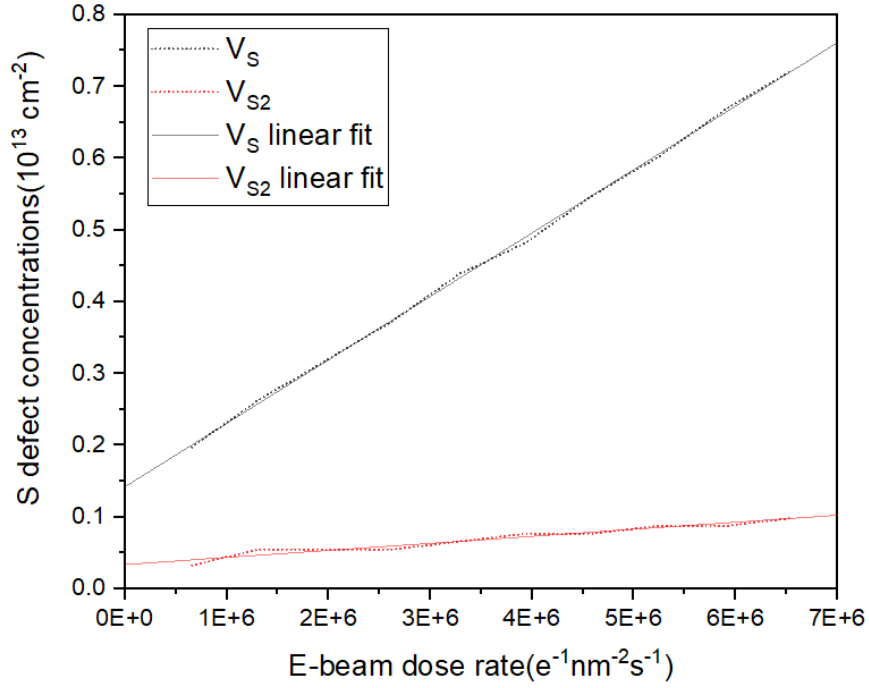


Figure 2.35: The general defect density was calculated using a E-beam dose rate test and remains at 1.4×10^{13} single sulfur (V_S) vacancies per cm^2 and 0.3×10^{13} double sulfur defects (V_{S2}) per cm^2 .

2.9 Conclusions

Throughout years of work on MoS₂ synthesis a clear, large-area methodology was developed. The use of powder-based CVD approach turned out to be unreliable for the goal of uniform and large-scale process and major efforts were quickly put into developing and optimizing the MOCVD recipe. 2-inch, and later 3-inch grown MoS₂ substrates quickly became the basis for FIB-irradiation and nanofluidics experiments not only for me but also for other collaborators and members of the laboratory. The biggest difficulty and challenge however was to establish the synthesis on the commercial Aixtron BM Novo setup - a showerhead system differing significantly from tube-furnace design. Allowing order of magnitude more detailed process control with precise gas control, temperature, pressure and plasma ignition capabilities it also brought a plethora of time-consuming technical and engineering difficulties (which were eventually overcome). The largest problem in this particular case was the maintenance and constant need for system upgrades and fixes. As this machine is one of its kind, the problems encountered during first years of use were unique and had to be carefully investigated. Some required a thorough recipe rework, some major system re-engineering. Due to that, the work was progressing slowly and was consisting of constant process troubleshooting, supplier communication and reiterating recipes, each time with new, incremental knowledge on the growth conditions. Eventually, a deep knowledge of the system gained through years of detailed troubleshooting and process analysis led to developing a working 4-inch scale MoS₂ synthesis recipe presented in previous section.

During the time of writing this thesis the Aixtron system, more than anything, still requires a significant technical attention and engineering efforts to yield a reliable and reproducible results. The proof of concept of 4-inch synthesis was accomplished, however the promise of an uniform, high-quality and high-mobility MoS₂ as well as other TMD materials and in-situ heterostructures growth is absolutely within the reach and still yet to be realized.

3 Pore and defect engineering with Focused Ion Beam

In this chapter we discuss the viability of Focused Ion Beam (FIB) techniques to engineer defects, including controlled formation of nanopores on suspended films. As discussed in the Introduction Chapter, FIB systems, especially double-column ones, equipped with both SEM and FIB columns allow to pinpoint target area and irradiate or mill substrate accordingly to ones desire. Typical FIB software also consist of a semi-lithographic capabilities of drawing basic shapes - feature used in lamella milling or MEMS manufacturing. In here, it is used to study finely spaced defect patterns. Finally, the choice of using the FIB system as a designated pore-fabrication tool was a compromise between scalability and parameter precision necessary for obtaining specific defect patterns and nanopore geometries (i.e. to obtain desired ion transport properties).

3.1 Introduction to Focused Ion Beam nanofabrication

Focused ion beam technique shares many similarities with SEM imaging. In both cases a focused beam is being raster scanned over the substrate area and in both cases secondary electrons can be used to create an image. FIB however typically uses the liquid metal ion source (e.g. gallium, gold or iridium) and tungsten tip to cause ionization and field emission of source atoms. Typical beam can be accelerated from 1 to 50 keV and beam current, through apertures and electrostatic lenses, can be adjusted from 1 pA up to several μA of probe current³⁷⁵. Due to its microscopic precision, FIB is commonly used to fabricate TEM lamellas and semiconductor devices but also to perform FIB tomography and image substrate slice by slice³⁷⁶. When hitting the substrate surface, accelerated ions create a set of events: incident ions penetrate the surface (depth depends on the molecular weight of the ion and accelerated voltage) and cause cascade collisions leading to displaced substrate atoms, ion implantation within the bulk, local amorphization and recrystallization, ejecting atoms out of the bulk or inelastically scatter out of the substrate, effectively exciting secondary electrons from area wider than the beam spot size (Fig. 3.1A). This means, that the incident beam not only sputters

the substrate material around the spot size but also influences wide area around it (through emission of secondary electrons and backscattered ions) and also the volume deep underneath it (interaction volume). This effect is often used to deposit material through ion beam induced deposition (IBID) or selectively etch the substrate with ion beam induced etching (IBIE)³⁷⁵.

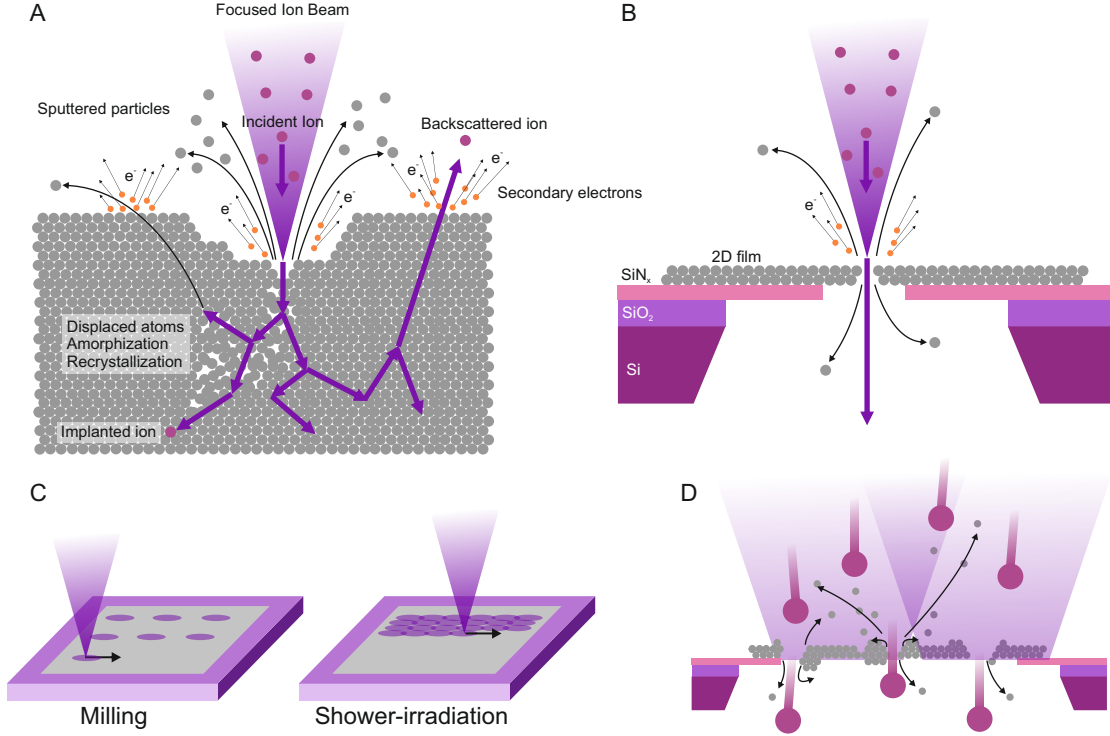


Figure 3.1: FIB principle and schematic. A schematic of FIB interactions with the bulk substrate (A) where collision cascades dominate the interaction volume underneath the incident beam spot, and the schematic of this process on thin, suspended film (B), where higher precision can be achieved. A diagram (C) representing two distinct FIB use cases: a location-specific milling and shower irradiation, where uniform dose is evenly affecting substrate area. The latter is considered to create atomic defects on suspended 2D materials through direct ion bombardment (D).

On thin, suspended film however, the effective interaction volume is few atoms thick and does not significantly impact the milled material. Ion beam energy is being transferred directly into the irradiated spot through ions kinetic energy. Outcome is direct substrate atom sputtering without causing major effects on the bulk of the irradiated area (Fig. 3.1B). Thus, it is highly feasible to use this technique as an atomically precise nanopore fabrication and defect patterning tool^{272,312}. Careful tuning of the ion beam exposure parameters can significantly impact defect/pore size, porosity and spatial distribution through pattern design and beam spot overlap (Fig. 3.1C). Ion beam exposure can be quantified by calculating the irradiation dose:

$$D_I = \frac{t_d I}{A} \quad (3.1)$$

where t_d is the exposure time, I is beam current and A is exposed area. Output dose is represented in coulombs per surface area. Another way, more commonly used in the field, is to use ions per area as an irradiation unit to represent the fluence through formula³¹²:

$$D_f = \frac{t_d I N_s}{q A_{beam}} \quad (3.2)$$

where N_s represents total amounts of repeated scans, q is the ion charge and A_{beam} this the beam spot size. Formula 3.2 allows to accurately measure amount of ions hitting the surface.

In essence, FIB can be used both as a nanofabrication tool but also as a precise "scalpel" to create spot defects and "shower" the surface with ions to create arrays of nanopores or atomic vacancies in suspended films (Fig. 3.1D). Following sections show the use of Xe-ion Plasma FIB (PFIB) double column system to pattern large-areas of nanopores on thin but also optically active defects on thick (10-100nm) van der Waals materials. Primary reason of using Xe-ion system instead of commonly used Ga+ was inert character of ion source (xenon) as well as faster milling rates³⁷⁶ allowing for rapid irradiation on large-area substrates.

3.2 Ion-beam nanopore fabrication and pore-edge classification

The following section is based verbatim on the manuscript in preparation:

Michal Macha^I, Sanjin Marion^I, Mukesh Tripathi^{II}, Mukeshchand Thakur^I, Martina Lihter^I, Andras Kis^{III}, Alexander Smolyanitsky^{III}, and Aleksandra Radenovic^I

High-throughput nanopore fabrication and classification using FIB irradiation and automatic pore edge analysis, In Preparation.

M.M and S.M contributed to this work equally. M.M. designed and performed ion-irradiation experiments. S.M. created and optimized image analysis script. A.S. performed the molecular dynamics modelling. M.M performed TEM imaging, M.M and M.Tripathi performed STEM imaging. M.Thakur and M.L. transferred the MoS₂. M.M., A.S. and S.M. wrote the manuscript. A.K., S.M. and A.R. supervised the project; All authors discussed the results and commented on the manuscript.

3.2.1 Introduction

Defect engineering is an important tool for enabling and exploring various physical phenomena at the nanoscale. From electronics³⁷⁷ and spintronics³⁷⁸ to optical^{379–381} applications, the control over the material's crystal lattice structure is paramount to pushing the boundaries of modern technology^{382–384}. Atomically thin materials are especially interesting, as they also promise to become the next-generation porous membranes for desalination^{3,385}, gas filtration²⁷², energy generation⁹, optoelectronics³⁸⁶, biosensing^{4–6,387}, and mechanosensing^{12,265,388,389} applications. In these areas, defect engineering is used to fabricate nanometer-scale defects or pores. With atomically thin and van der Waals materials such as graphene or molybdenum disulphide (MoS₂) as host membranes, the membrane thickness can also be controlled during fabrication. By tuning the size, pore-edge termination, and pore density, one possesses sensitive control over the membrane properties such as ion selectivity⁹⁹ and water permeability¹⁶¹, making the level of precision in controlling the geometry and composition of the fabricated defects (nanopores) a crucial fabrication component⁹.

Among the numerous available nanopore fabrication methods^{9,390,391}, the electron beam⁹⁰ and ion irradiation¹⁸⁸ techniques offer a desirable compromise between the precision of fabricated pore geometries and scalability of the irradiated area¹⁸⁸. However, even upon achieving the finest parameter control, one has to employ a thorough pore characterization and statistical analysis to begin obtaining the full picture in terms of the nanopore properties and the resulting membrane-wide behaviour. Multidisciplinary efforts in combining nanopore fabrication protocols with computer vision image analysis³⁹² are showing a great promise for

^ILaboratory of Nanoscale Biology, Institute of Bioengineering, , EPFL ,Lausanne, Switzerland

^{II}Laboratory of Nanoscale Electronics and Structures, Electrical Engineering Institute and Institute of Materials Science, EPFL ,Lausanne, Switzerland

^{III}Applied Chemicals and Materials Division, National Institute of Standards and Technology, Boulder, Colorado 80305, USA

future development of membrane technologies and study of nanoscale physics.

In this work, we investigate Xe-ion FIB as a tool for scalable, large-area nanopore fabrication on atomically thin, freestanding MoS₂. We analyze the irradiation parameters and their effect on the obtained nanopore sizes and porosity based on transmission electron microscope (TEM) and aberration-corrected scanning transmission microscope (AC-STEM) imaging. We present an image analysis script that enables automatic nanopore edge identification and classification as well as statistical and geometrical pore analysis based on AC-STEM nanopore images. For the first time, we demonstrate an experimental method to study the membrane-wide pore edge analysis. Finally, we connect this data to atomistic molecular dynamics simulations to gain a detailed insight into the water- and ion-permeation properties of the resulting porous membranes. Our findings provide a new methodology to precisely control and analyze nanoporous membrane properties through a deeper understanding of transport phenomena occurring at the nanoscale.

3.2.2 Experimental Section

3.2.3 Focused Ion Beam Irradiation

In our study, we used a Xe-ion PFIB system (see Methods section) as a nanopore fabrication platform. An MOCVD grown monolayer MoS₂ (see Methods section) was transferred over a Si/SiN aperture and irradiated with Xe ions (Fig. 3.14A) under varied ion beam parameters to investigate the nanopore fabrication performance, *i.e.* porosity and effective nanopore diameters (Fig. 3.14B,C). In all irradiation experiments, ion beam was kept at constant 30kV accelerating voltage with varying beam current of 10, 30, and 100pA, beam dwell time per pixel of 30, 60 and 90 μ s and x/y distances between pixels (pitch distance) of 100, 350 and 600nm. Ion fluence was kept relatively low between 4.9×10^{11} and 1.7×10^{14} ion/cm² to minimize beam damage and promote shower-like single ion collisions rather than wide-area milling. Resulting membrane porosity was prescreened and quantified with Ilastik software package³⁹³ (see Methods section) to obtain general insights into porosity and average pore size (Fig. S3.7A). Within the investigated FIB parameters, the nanopore-yielding parametric window is relatively narrow. Large pitch distances tend to yield no nanopores at lower beam currents, while membrane breakage was observed at 100pA, 90 μ s, and 100nm pitch (Fig. S3.7B), corresponding to 1.7×10^{14} ion/cm². The parameters and the effective diameters of the obtained nanopores are mapped in Fig. S3.7C. A more detailed parameter description of the used beam current, dwell time, and pitch distance is accessible in the supplementary information (Fig. S3.8-3.10). After investigating a range of nanopore-yielding parameters through HRTEM imaging, a second, in-depth nanopore analysis was performed on a membrane irradiated with 30kV, 30pA ion beam, 350nm in x/y pixel pitch distance and 60 μ s dwell time per pixel (fluence of 6.77×10^{12} ion/cm²). The porous membrane obtained with such a set of irradiation parameters yields pores of dimensions most relevant for applications such as desalination or biosensing (average of 1nm in Fig. S3.9).

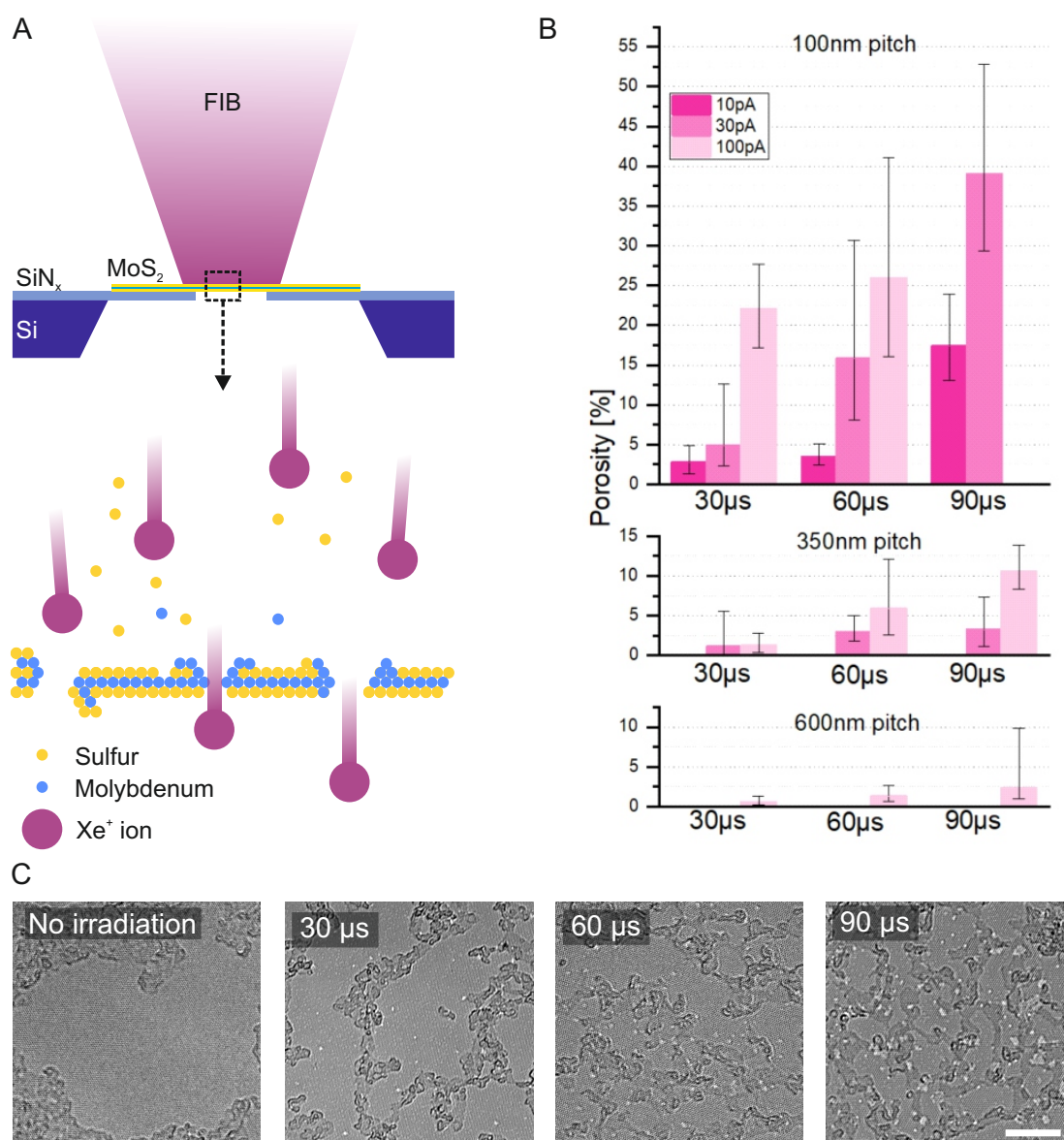


Figure 3.2: **Focused ion beam irradiation.** A schematic representation of FIB irradiation principle (A) with Xe ions bombarding the freestanding MoS_2 to create nanopores. (B) Depending on process parameters such as beam current, pitch distance and dwell time formed nanopores vary in density and sizes. Dependence on the beam dwell time on porosity and pore size is shown on panel C).

3.2.4 Pore-edge detection

AC-STEM image analysis After prescreening the pore fabrication parameters with HRTEM imaging, MoS_2 irradiated at the fluence of 6.77×10^{12} ion/ cm^2 was selected for further, in-depth analysis with an expected average pore size of $\approx 1\text{nm}$. Aberration-corrected scanning transmission microscope (AC-STEM) was used to take detailed images of the irradiated film (see Methods for details). The resulting images were then used for further analysis and automated pore edge detection (Fig. 3.3). This task was divided into two parts: first, determining

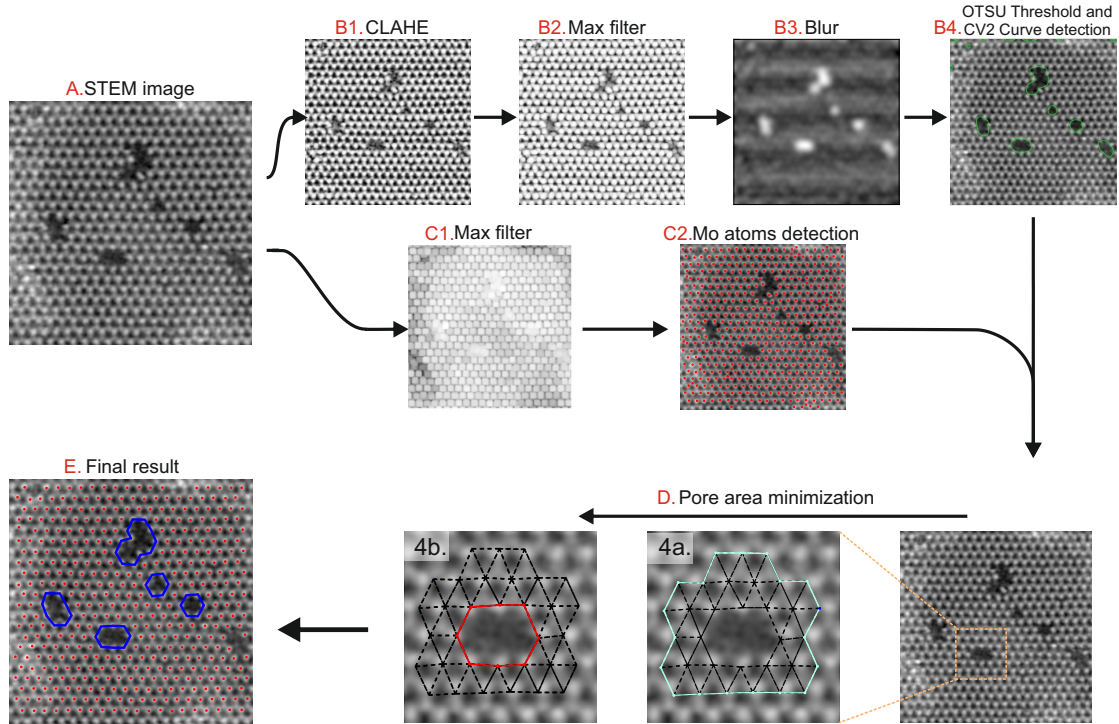


Figure 3.3: Pore edge detection algorithm outline. A) The detection workflow starts with a STEM image, which is then processed in two parallel pathways. B) To obtain the locations of the nanopores first a CLAHE³⁹⁴ is performed (B1), followed by a maximum filter (B2) and blur of the inverse (B3). The resulting images are then Otsu thresholded, followed by the application of the OpenCV curve find routine³⁹⁴, which provides the contours of the detected nanopores (B4). C) in the second pathway, a maximum filter (C1) is applied to the STEM image followed by a peak-finding routine (C2), which produces the location of the Mo atoms. D) Starting with each individual nanopore location from (B4), we take the Mo atoms surrounding the nanopore contour up to two nearest neighbours (4a), to which a custom optimisation algorithm is applied (4b), as described in the main text. E) The result of the pore detection algorithm constitutes the locations of Mo atoms that form the edge of the nanopore (marked as a blue polygon).

the positions of each atom species in the image, and second, determining the pore locations and extracting a polygon marking the pore edge. The latter also enabled us to study the distribution of fabricated pore shapes and the corresponding pore edge terminations.

STEM image processing and obtaining atom positions. Obtaining the atomic positions in the lattice is critical to ensuring proper pore edge detection. A maximum filter with a constant fill is used with a lattice parameter roughly equal to approximately half the nearest-neighbour interatomic Mo-Mo distance a_0 . This maximum filtered image (Fig. 3.3C) is then processed to find the positions of the local maxima using the scikit-image³⁹⁵ toolkit. The resulting maxima correspond to the positions of the individual Mo atoms. The positions of S atomic sites can then be obtained by repeating this procedure with a smaller maximum filter lattice parameter, followed by removal of the already detected Mo atom peaks from the population.

This approach is robust, as it depends exclusively on the lattice unit cell distance; it could be further improved by taking into account the lattice symmetries of the given 2D material. We find that the positions of the sulphur atoms are less reliable due to a lower intensity relative to that of the molybdenum atoms, as well as the various contaminants or dirt present on the imaged surface. Consequently, the Mo atom sites are used as the reference for defining the pore locations.

Detecting the general pore locations. Detecting pore locations using their general shape is a complex computer vision problem, which require the use of machine learning algorithms. In our case, due to the limited number of imaged pores and the complexity of the task, we opt for a classical image vision approach instead. We start with an approach similar to that described in Ref.³⁹². We implement a contrast-limited adaptive histogram equalization (CLAHE) of the images to remove any variations in intensity due to variable illumination or dirt/contamination (Fig. 3.3B1). Unlike in the previous studies³⁹², our aim is not to obtain the exact pore edge at this stage, but to identify prospective pore locations for further analysis. We first use a maximum filter and then blur the resulting images in order to remove any smaller areas of a different contrast, which enables us to emphasize the nanopore locations (Fig. 3.3B2,B3). We use a maximum filter size, which is comparable to the Mo-Mo lattice distance a_0 in MoS₂. We then combine thresholding using the Otsu method³⁹⁶ with OpenCV contour find³⁹⁴ to locate different pore contours (Fig. 3.3B4). The Otsu threshold algorithm does not involve any user defined parameters, leaving the expected lattice parameter a_0 used for the atom detection and maximum filtering as the only user defined parameter in the analysis. The end result is an approximation of the nanopore edge shape, which is then used with the Mo atom positions to detect the exact pore edge.

Pore edge optimisation. By using the obtained nanopore contours (Fig. 3.3B4) and the positions of the Mo atoms (Fig. 3.3C2), we are able to identify nanopore edges with reasonably high precision without freely adjustable parameters. For each detected nanopore contour curve, we consider a group of Mo atoms consisting of the first two to three rows of atoms closest to it (Fig. 3.3D). First, a convex hull is constructed from this group of atom positions, and then from it a polygon with edges between the sites corresponding to the distance between the nearest Mo-Mo neighbours ($\approx a_0$) is composed. This polygon (blue in Fig. 3.34A) is then optimized using a custom algorithm (Supplemental Sec. 3.2.8) so that its surface area is minimized, while maintaining nearest-neighbour distances on the triangular Mo sub-lattice. The algorithm seeks out any local changes in the polygon edges that reduce the total polygon surface area by removing or adding Mo sites. In case the algorithm is unable to converge to a valid pore shape, the group of atoms used for the original convex hull is expanded toward any nearby neighbouring groups of atoms, which did not yield a valid pore shape either. If no such group of atoms is found, the pore is then rejected from the statistic. This procedure automatically rejects all pores located close to the STEM image edge, such that parts of the missing edges are not visible.

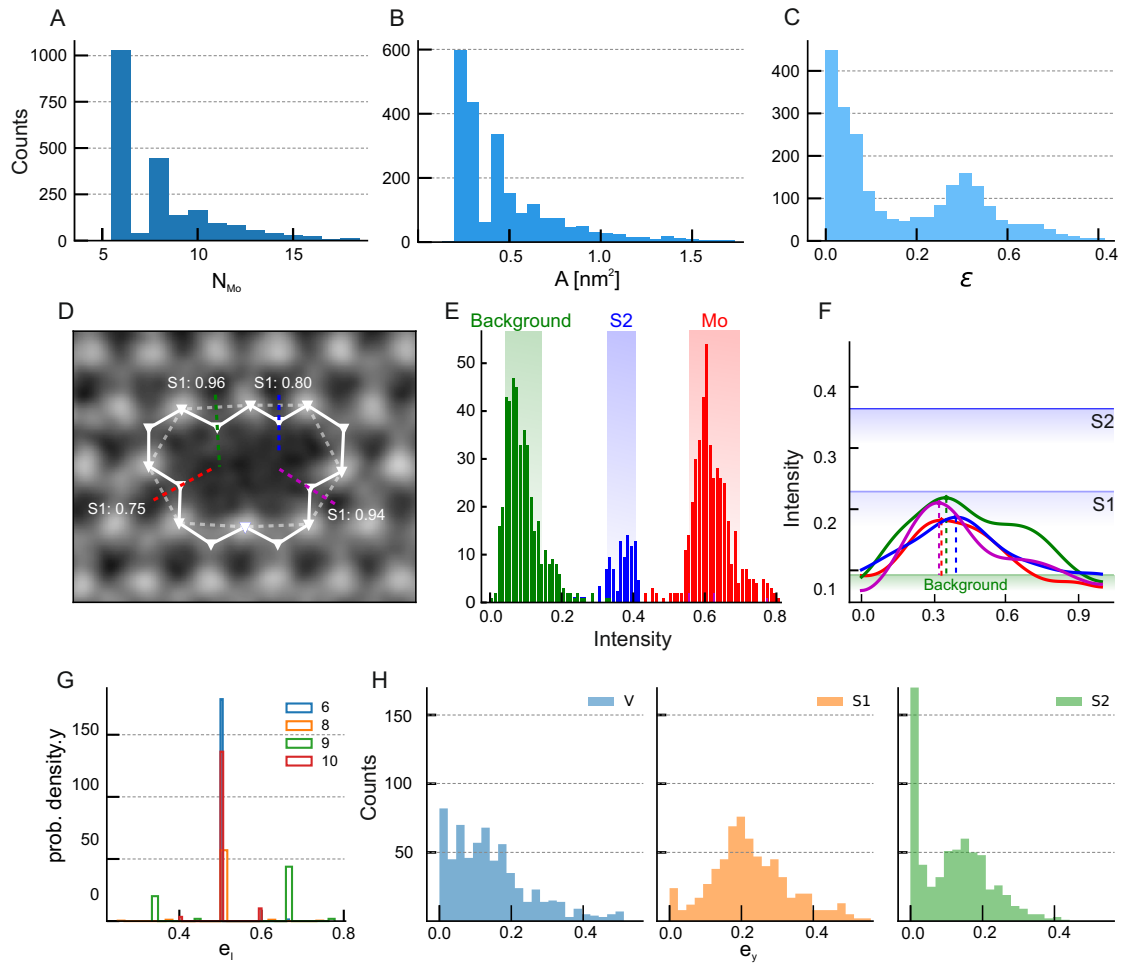


Figure 3.4: Pore edge analysis and statistical indicators obtained from pore edge detection. a) A histogram of the number of Mo atoms detected in the population of nanopore edges detected using the custom-made edge detection software. b) Histogram of the area of detected nanopores. The reported area is that of the polygon marking the edge of the nanopore (crossing Mo and S atoms), c) A histogram of the elongation (eccentricity) parameter of the studied nanopore edge population. d) Magnification of a single nanopore with the detected nanopore edge (in blue). Dashed lines of different colours indicate the location of intensity slices as shown in panel f. Letters indicate the detected pore edge atom type. e) Intensity histogram obtained from Mo and S_2 atom positions from one image. f) Intensity slices along the dashed lines of panel d. Horizontal lines mark the mean intensity level corresponding to various pore edge sites as determined from panel e. g) Normalized density of probability of finding a pore with a fraction e_I of S_2 sites internal to the lattice (not exposed to the edge) for different numbers of Mo atoms present in the edge (6,8,9,10). h) Density of probability of finding a pore with a fraction e_y sites populated by two sulphur atoms (S_2), one sulphur atom (S_1) or vacant (V) at the pore edge.

Identifying pore edges Having obtained the coordinates of the Mo atoms forming a polygon outlining each nanopore, we can identify the composition of the pore interior edge and thus attempt to estimate its permeation properties on theoretical grounds. Depending on whether the edge composition is dominated by Mo and S atoms (carrying positive and negative partial atomic charges, respectively), a rich variety of tunable permeation properties is

expected^{167,168}, as also discussed in greater detail later in the text. In this sense, nanopores in single-layer MoS₂ are in fundamental contrast from those graphene-based, where pore edge termination appears to be close to neutral⁹⁶ without functionalization. In addition, unbiased graphene membranes carry no overall surface charge density that could electrostatically boost osmotic currents through small pores. Within the scope of this work, we assume that the in-solvent MoS₂ pore structures are close to those imaged post-fabrication. Of course, further in-solvent functionalization (*e.g.*, with hydroxyl groups) is possible to for example control hydrophilicity of the pore interior. More generally, the character of pore edge chemistry directly influences the electrostatic interactions inside the pore and thus further modifies the permeation properties^{92,119,167–169}. The first step in predicting the properties of porous 2D membranes is thus to identify the pore edge composition of the manufactured pores.

Starting with a polygon marking the Mo sites at the nanopore edge, we determine the positions of the sulphur sites in the lattice (Fig. 3.4). This subsequently enables us to identify the complete atomic pattern marking the edge of the nanopore. Such a pattern will have the form of Mo- y_1 -Mo- y_2 -Mo- y_3 -... with y_k either a Sulphur site that is not directly exposed to the nanopore (it is interior to the lattice, marked as I) or an edge-exposed site. Exposed sites can be a double sulphur (marked as S₂), single sulphur (S₁) or empty (V). Intensities of atoms are known to scale with the atomic number³³⁰ so we proceed by comparing the intensities at the edge atomic sites with reference values. As shown in Fig. 3.4, reference atom intensities are obtained from full STEM images, which usually feature multiple nanopores. The same peak identification algorithm as described in Fig. 3.3C is used to detect S₂ and the background levels, except the lattice parameter is appropriately reduced and an inverse of the image used, respectively. The population of each sites is then obtained by removing each sub-population from the full statistic. The statistics for S₂ sites is of lower quality, as it is harder to identify positions of S₂ in the lattice compared to the more intense Mo positions or similar S₁. The S₁ intensity value is determined as the average of the background intensity (V) and S₂ intensity values. Based on the obtained distributions of intensity values for different atoms, we proceed to identify each S site at the pore edge. For each sulphur site at the pore edge we perform slicing of the intensity perpendicular to the sites corresponding to the Mo-Mo polygon edge (Fig. 3.4b), starting from the position of the dark spot and towards the nanopore interior. We calculate the mean intensity values and the corresponding standard deviations for each intensity group corresponding to four possible atom types (V, S₁, S₂, Mo). If a site does not have a prominent well-defined peak or is buried under the noise level defined by the background intensity distribution (V in Fig. 3.4a), it is identified as invalid (marked X). We find that invalid sites occur when either the pore edge was improperly recognized, or when the pore is contaminated. Full details of the algorithm are provided in the supplement. Assuming that the site intensity is obtained from the four independent normal probability distributions, we can extract the probability p_k^y that a site y_k on the edge corresponds to any of the three possible site types (V, S₁, S₂).

We are now able to compare the different parameters obtained with analysis software from STEM images of irradiated samples. Fig. 3.4a,b,c shows histograms on the full statistic of

nanopores identified using our algorithm. The distribution of the number of molybdenum atoms N_{Mo} in the nanopore edge indicates that there are preferential shapes for the pores involving $N_{Mo} = 6, 8, 9, \dots$ Mo atoms, along with the corresponding nanopore areas as seen for the histogram of pore area values A . The elongation of different pores is represented by the eccentricity $\epsilon = 1 - m/M$ with m and M being the minor and major axis of the nanopore, respectively, as estimated from the dimensions of the corresponding minimum and maximum bounding rectangles. This approach yields a value of $\epsilon = 0$ for perfectly circular nanopores, and $\epsilon \rightarrow 1$ for a pore of infinite length in one dimension. In our case, there is a population of nanopores of circular shapes ($\epsilon \approx 0$), and those with a defined elongation of about $\epsilon \approx 0.3$ and $\epsilon \approx 0.5$, matching the most populous elongated pore shapes (marked as 8 in Supplemental Fig. S3.11).

Our analysis also allows investigating the sulphur content of the nanopore edge. We define e_y as the fraction of y -sites for each pore edge, such that the fraction of interior (non-edge-exposed) sites is $e_I = N_I/N_{Mo}$ and the fraction of $y = V, S_1, S_2$ sites, as $e_y = \sum_k p_k^y/N_{Mo}$. Here N_I is the number of interior sites for a given pore. For arbitrary pore shapes, as shown in Fig. 3.4g, half of the sulphur sites are on average interior to the lattice, with another half exposed at the pore edge. A small sub-population of nanopores (linked to the shapes associated with $N_{Mo} = 9$, for instance) has longer zig-zag edge segments. Depending on the orientation of the lattice, this group produces two types of pores with different fractions of edge-exposed S-sites, as shown in Fig. 3.4h. We note that there appears to be a slightly higher probability of finding S_1 sites at these edge-exposed sites, compared to S_2 or V sites. Overall, the dominance of Mo-terminated edges is due to the relatively high knock-on energy threshold needed for the incident beam to displace the Mo atom²²⁸ compared to that required for S atoms. Additionally, this threshold is further lowered for the edge atoms due to reduced coordination, thus making edge sulphurs (especially the single-sulphur sites) fundamentally less stable during irradiation²²⁸ as compared to molybdenum.

Edge shape detection at the atomic resolution Once the polygon shapes marking the Mo and S atoms at the nanopore edge are known, we can identify the likely nanopore shapes in the analysed images. Combinatorially, with $N_{Mo} > 12$, a near-exponential increase in the number of the pore structure possibilities is expected³⁹⁷. Taking into account that our analysis indicates a small probability of generating pores past that size, we limit our analysis of shapes up to $N = 12$. This constitutes a maximum number of 3 (7) removed Mo (S) atoms. We also limit ourselves to not considering the removal of pore edge exposed S atoms, including them in our analysis of the site occupancy n_y in Fig. 3.4h. To classify our pores (See Supplemental Fig. S3.11 for a complete list of pores included in our classification), we first match the unique pattern of interior and exterior edge S atom sites between an unknown pore and the database of known nanopore shapes. Any shapes that are not recognized are removed as invalid. If there are multiple shapes with the same pattern (in our case, for $N_{Mo} = 12$ there are only two such shapes), we use the hu-moment based image recognition to determine the most probable match. Fig. 3.5 show the histogram of identified pore shapes up to $N=12$. Herein, all pores with

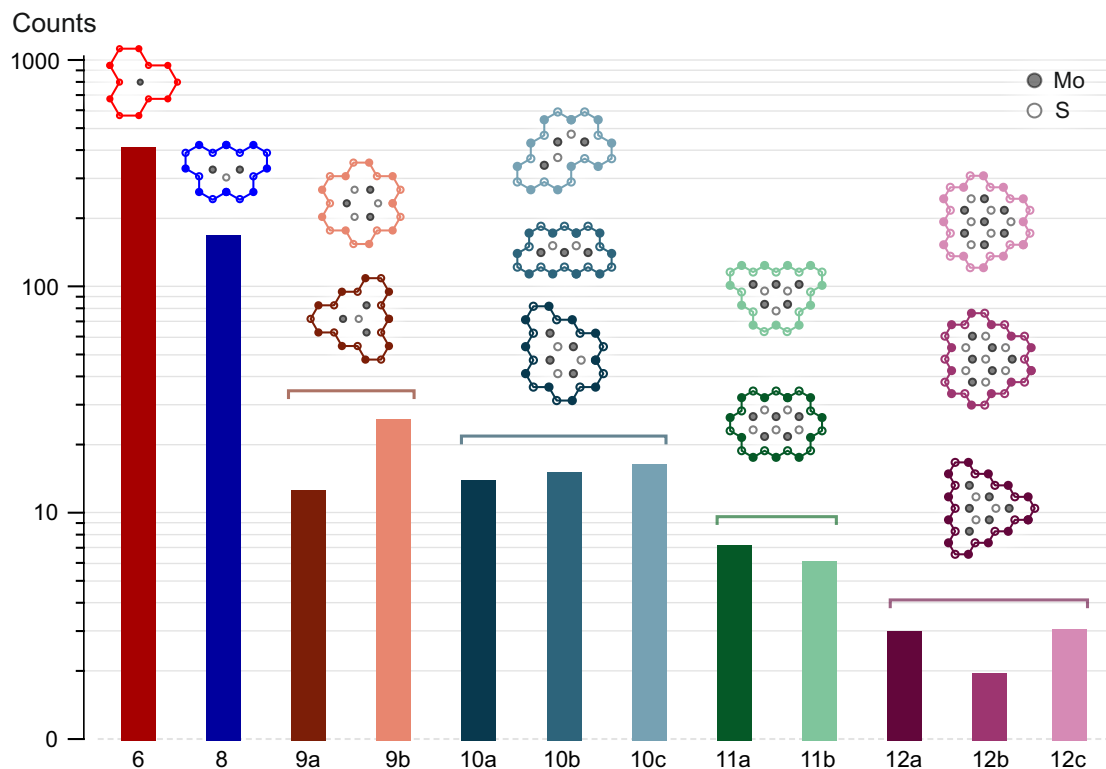


Figure 3.5: **Pore edge shape distribution in Xe irradiated nanopores.** Histogram of identified pore shapes from STEM images of Xe irradiated MoS_2 , here grouped in the clusters of pores containing 6, 8, 9, 10, 11 and 12 Mo atoms.

invalid geometries, or with unidentifiable (classified as X) edge sites, have been removed from the presented statistic. We see that certain pore types are considerably more probable, *e.g.*, the shape identified as 9b with more Mo atoms exposed to the pore interior is more probable than 9a, which has more sulphur sites exposed to the pore edge. Larger pores, with $N_{\text{Mo}} > 10$, appear to be overall improbable in the Xe irradiated samples presented here. We find that the major source of error for the algorithm stems from the uncertainty in identifying what is an actual Mo atom in the lattice, and differentiating the atom from adatoms and contaminants. Most cases of irregular shapes identified with the algorithm, which are rejected from the analysis in Fig. 3.5 as they do not match a known shape, come from anomalous lattice atom positions. Such cases result from STEM imaging artifacts or unexpected adatoms or pore contamination. This can be improved upon in the future by using a better algorithm to detect atoms which takes into account the symmetry of the atomic lattice.

Permeation property prediction Once the individual pore structures have been obtained, their properties can be estimated. Here we consider ion and water permeation through the pores comprising the statistics in Fig. 3.5 and shown in Fig. 3.6A, as obtained from all-atom molecular dynamics (MD) simulations described in detail in Section 3.2.5. To investigate ion flow driven by a constant electric field, MD simulations were set up similarly to our previous

work on the transport mechanisms in subnanoporous 2D materials^{388,389}. For pressure-driven water flow, external hydraulic pressure was induced in the form of a constant force acting upon a solid piston. Sketches of systems driven by electric field and hydraulic pressure are shown in Fig. 3.6B.

As summarized in Fig. 3.6B, most pores in Fig. 3.5 are ion-impermeable under a realistic electrostatic bias. The obvious factors here are the pore size (the number of removed atomic sites) and the pore eccentricity, *i.e.*, sufficiently elongated pores preclude ionic permeability through high steric repulsion regardless of the pore length along the larger dimension. Other mechanisms consistent with earlier observations³⁸⁹ are more subtle and arise from the fact that Mo and S₂ carry partial positive and negative charges, respectively. Consider the fact that all ionic currents reported in Fig. 3.6B were contributed by anions (Cl⁻). This observation likely owes to the electric field distribution near bulk MoS₂ monolayer surface, which is a finitely-spaced S⁻-Mo⁺⁺-S⁻ sandwich from the electrostatic standpoint. This electrostatic configuration appears to be overall repulsive to cations, also partly responsible for interlayer adhesion in multilayer MoS₂. Given this broad selectivity, anion transport is further boosted in pores featuring Mo⁺-lined edges, despite the net zero charge of both the pore and the host membrane. Consider for example the 9b' and 12a pores, which are structural conjugates (geometrically identical, except the S₂ and Mo atomic sites are swapped): while 9b' lined with Mo atoms features sizeable ionic conductance, 12a is impermeable to anions. For the same reason, 12b, which is primarily lined with Mo atoms, has a significantly larger conductance than its structural conjugate 12c, except that now both 12b and 12c are ion-permeable due to their considerably larger size. Simulated pressure-induced water transport is shown to be rather low, being of order $\frac{aL}{\text{min} \times \text{bar}}$, as shown in the table in Fig. 3.6B. Although such a low permeability renders the pore sizes considered here likely unfeasible for broad nanofluidic applications⁹, given the overall high levels of ion rejection, they remain promising for desalination^{3,385} and possibly gas filtration systems²⁷².

The simulated properties of the individual pores identified here enable us to make several observations regarding mechanosensing^{12,388,389}, which is another emerging area of application for solid 2D nanopores. Some of the structures identified here have ion transport properties, which can be modulated by the application of mechanical strain to the membrane hosting the pore. Fig. 3.6C shows ionic currents under an electrical bias as a function of isotropic membrane strain. Observing this effect in experiments introduces a potential challenge. Currently, applying hydrostatic pressure in the direction perpendicular to the membrane appears to be the only realistic way to induce dilation of 2D nanopores³⁹⁸. Consequently, the resulting streaming flow may in principle compete with the effect of pore dilation on the ionic transport. Furthermore, depending on the relative directions of pressure and the external electrostatic bias, the two effects could in fact oppose each other. Although the data in Fig. 3.6B suggests overall low streaming couplings that at the most contribute currents of order 0.8 pA for pressures of order 20 bar, the coexistence of these effects must be taken into account when probing mechanosensitivity with the use of hydrostatically pressurized nanofluidic cells.

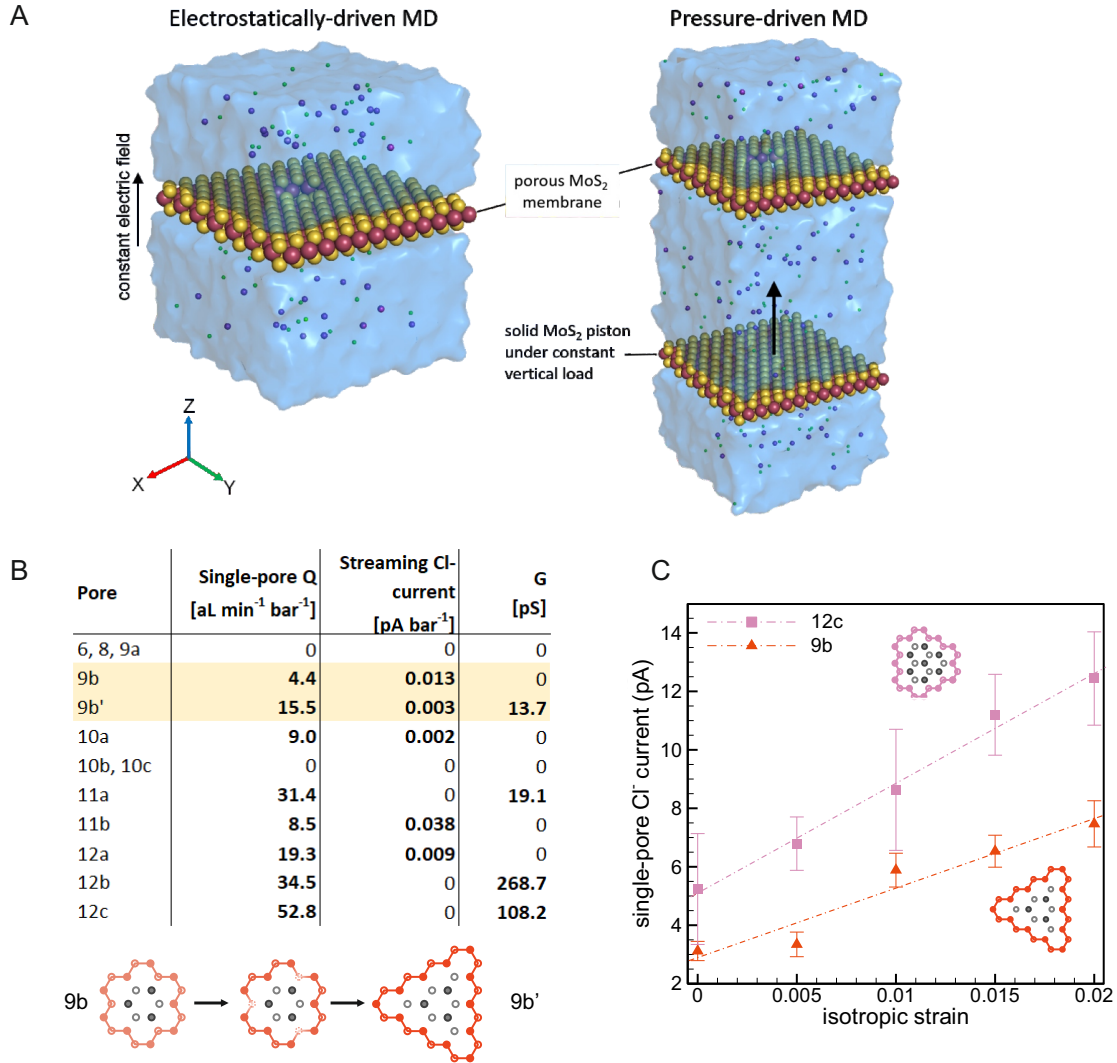


Figure 3.6: Simulated pore properties A) Sketches of MD simulation setups for electrostatically- and pressure-driven systems. B) Ionic and water permeability properties for the identified pore shapes labeled as shown in Fig. 3.5. Note that we classify pores 9b and 9b' as a specific cases with and without interior sulphur sites at the edge. C) Ionic current as a function of isotropic strain applied to membranes featuring select S₂- and Mo-lined pores. The bars in C are estimates of the average irregularities in the cumulative ionic fluxes used to calculate the ionic currents (e.g., see Ref.³⁸⁹).

Once the individual pores have been quantified, for a given membrane hosting a large population of pores described in Fig. 3.5, a predictive estimate of the membrane-wide permeation properties becomes possible. In the simplest case, assuming that the pores are spaced sufficiently sparsely so as not to affect each other's properties, these estimates are straightforward. For example, for a total of N pores possessing a set of ionic conductance values G_i and corresponding selectivity values S_i , the membrane-wide conductance and selectivity are $G_m = \sum G_i$ and $S_m = \frac{\sum G_i S_i}{\sum G_i}$, respectively. Similarly, the mechanosensitivity (as defined earlier³⁸⁸) for the entire membrane is $\mu_m = \frac{\sum G_i \mu_i}{\sum G_i}$, where μ_i are the individual mechanosensitivity values of the

constituent pores. These estimates underscore the importance of obtaining accurate statistics of both the pore structures and the corresponding structure histograms. It is important to keep in mind that large numbers of impermeable pores in a given population have virtually no effect on permeability, while a relatively small number of highly permeable non-selective pores can readily "smear" the desirable membrane-wide properties. Overall, judicious use of the estimates discussed above may result in a promising fabrication parameter tuning tool that enables achieving desirable membrane-wide permeation properties and reduces the number of trial-and-error permeation measurements.

3.2.5 Conclusion

We have demonstrated the viability of Xe-ion irradiation as a large-scale nanopore fabrication tool. The presented irradiation protocol enables designing membranes with tunable porosity and pore dimension tuning, along with spatial uniformity across large-area substrates. Fabricated nanoporous membranes were characterized using STEM imaging and observed nanopore geometries were analyzed through a pore-edge detection script which depends only on one user defined parameter, the lattice constant of the 2D material in question. Our pore detection algorithm allows resolving individual pore structures and combining it into a membrane-wide statistical analysis of the entire pore population. We then demonstrated that the obtained structural and statistical data can be readily passed on to computational and analytical tools to predict the permeation properties at both individual pore and membrane-wide scales. As an example, membranes featuring angstrom-scale pores were investigated in terms of their emerging fluid and ion flow properties through extensive all-atom MD simulations.

High-quality structural and statistical descriptions of as-fabricated porous membranes are key to predicting the corresponding membrane-wide permeation properties. It is worth noting that as presented here and as would be the case with any image-based analysis, there fundamentally exists a degree of uncertainty in the resulting data. This arises from both uncertainty of the pore edge Sulphur sites being vacant, but also in the specifics of identifying the exact pore shapes. Therefore, the subsequent use of highly accurate (assuming proper parameterization), but computationally intensive methods (*e.g.*, MD) to convert the structural and statistical data into permeation property predictions may be excessive. Instead, semi-analytical estimates of the permeation properties of individual nanopores and entire membranes could prove both reasonably accurate and highly computationally efficient. Although such estimation methods are challenging to implement, individual steps are already being taken towards for example rapid screening of nanopores or a detailed analytical formulation of how water molecules behave near nanopores. We believe that further improvements in the on-the-fly conversion of the structural and statistical data into accurate physics-based property estimates should yield software tools that enable a true function-by-design approach to fabrication for applications such as mechanosensing, osmotic power generation, desalination, and filtration.

3.2.6 Acknowledgements

I want to thank and acknowledge and thank Alex Smolyanitsky for an enormous help, passion and support with the MD simulations, discussions and preparation of the manuscript.

3.2.7 Methods

Substrate fabrication MoS₂ was synthesised on c-cut sapphire wafer in MOCVD tube-furnace using large-scale growth methodology^{273,316}. As-grown material was transferred onto TEM SiN holey grids (Norcada) via polymer-assisted transfer method²⁷³. Before and after FIB processing suspended MoS₂ membranes were washed in acetone and soft-baked at 150°C for 2h to minimize airborne hydrocarbon contamination and beam-induced deposition.

Focused Ion Beam Irradiation Ion irradiation was performed at ThermoFischer Helios G4 PFIB DualBeam with Xenon Plasma FIB column. All FIB irradiation experiments were performed at constant 30kV with varying beam current, dwell time and pitch distance. Irradiated area was 200x200/*μm*, centered at the substrate grid/membrane location.

HRTEM image analysis and machine learning Transmission Electron Microscopy imaging was done on the ThermoFischer Talos F200S at 80kV accelerating voltage. Obtained high resolution images of nanoporous films were then cropped and bandpass-filtered. Subsequent machine-learning pore segmentation was performed in Ilastik and further processed and analyzed with Fiji ImageJ2. Due to the complexity of pore-detection and insufficient resolution, the more detailed analysis was performed with AC-STEM micrographs and custom-made analysis script described in the main text.

STEM imaging Scanning transmission electron microscopy imaging was conducted using an aberration-corrected (with double spherical corrector) FEI Titan Themis TEM 60 - 300 kV, equipped with Schottky X-FEG electron source and a monochromator to reduce the effect of chromatic aberrations. To avoid the electron-beam induced knock-on damage, a low acceleration voltage (80 kV) was used for the imaging³⁷⁴. The electron probe current, C₂ aperture size, and a beam convergence angle was 25pA, 50 μ m, and 21.2 mrad, respectively. Images were acquired with a Velox software (ThermoFisher Scientific) using 185 mm camera length which corresponds to an angular range (49.5 - 198 mrad) in a HAADF detector. To avoid the sample drift, a serial imaging was performed using 512 × 512 pixels with 8 s dwell time. Images were aligned and processed using the *double-Gaussian filtering* method in ImageJ.

MD simulations The all-atom MoS₂ model was set up according to recently published work, implemented within the OPLS-AA framework. The atomic charges of Mo and S sites at the zigzag edges of the pores were set to 2/3 of their bulk counterparts, corresponding to +0.3333 and -0.1667, respectively. Such an assignment guarantees overall electrostatic neutrality of the zigzag edge and thus all pore structures considered in this work regardless of their geometry. Explicitly simulated water molecules were described according to the TIP4P model while ions were described according to default.

The simulations were performed using the GPU-accelerated Gromacs package (version 2021.4). Ion and water transport through the pores was simulated in the presence of water-dissociated 1M KCl. The simulation cell sizes were approximately $3.82 \times 3.86 \times 5.0 \text{ nm}^3$ and $3.82 \times 3.86 \times 10.0 \text{ nm}^3$ for the ion and water flow simulations, respectively. In all simulations, the atoms at the perimeter of the porous membrane were harmonically restrained against displacement along X, Y, and Z ($k_X = k_Y = k_Z = 34 \text{ N/m}$), while the piston membrane in the pressure-driven simulations was free to move. The constant vertical force acting upon the piston was $F = pA$, where p (in the range 10-50 bar) is the desired pressure, $A = 3.82 \times 3.86 = 14.75 \text{ nm}^2$ is the in-plane cross-sectional area of the simulation cell. In the ion flow simulations, the external electric field (of order 0.02 V/nm) was $E = \Delta V / h$, where $\Delta V \approx 0.1 \text{ V}$ is the potential difference consistent with voltages typically applied in experiments and $h = 5 \text{ nm}$ is the height of the simulation cell, respectively. Periodic boundary conditions were applied in the XYZ -directions. After initial equilibration at constant $p = 1 \text{ atm}$ and $T = 300 \text{ K}$, constant-volume production simulations were performed at $T = 300 \text{ K}$ for at least $0.5 \mu\text{s}$ to ensure reasonable permeation statistics.

3.2.8 Supplementary information

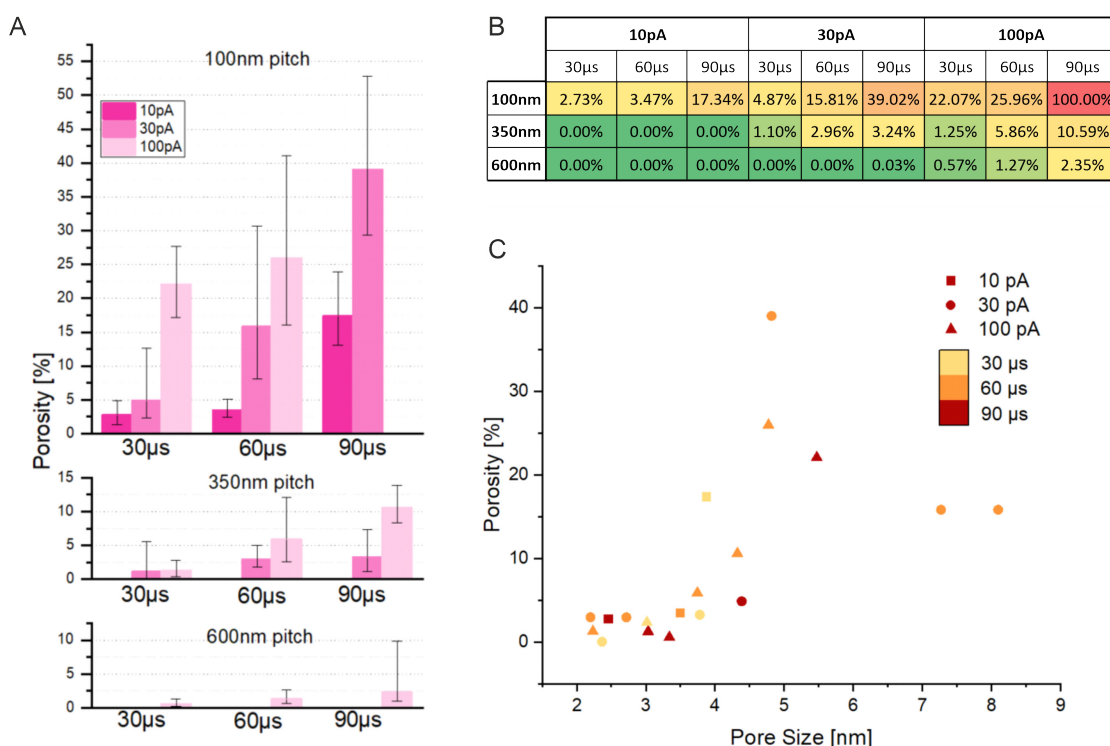


Figure 3.7: Porosity and pore-size distribution. A dependence of membrane porosity versus used FIB parameters of dwell time, pitch-distance and beam current (A and B) for a constant 30kV Xe FIB. A chart of achieved pore size (in the longest direction) and porosity is shown on panel C. These data were used to find and optimize nanofabrication protocols.

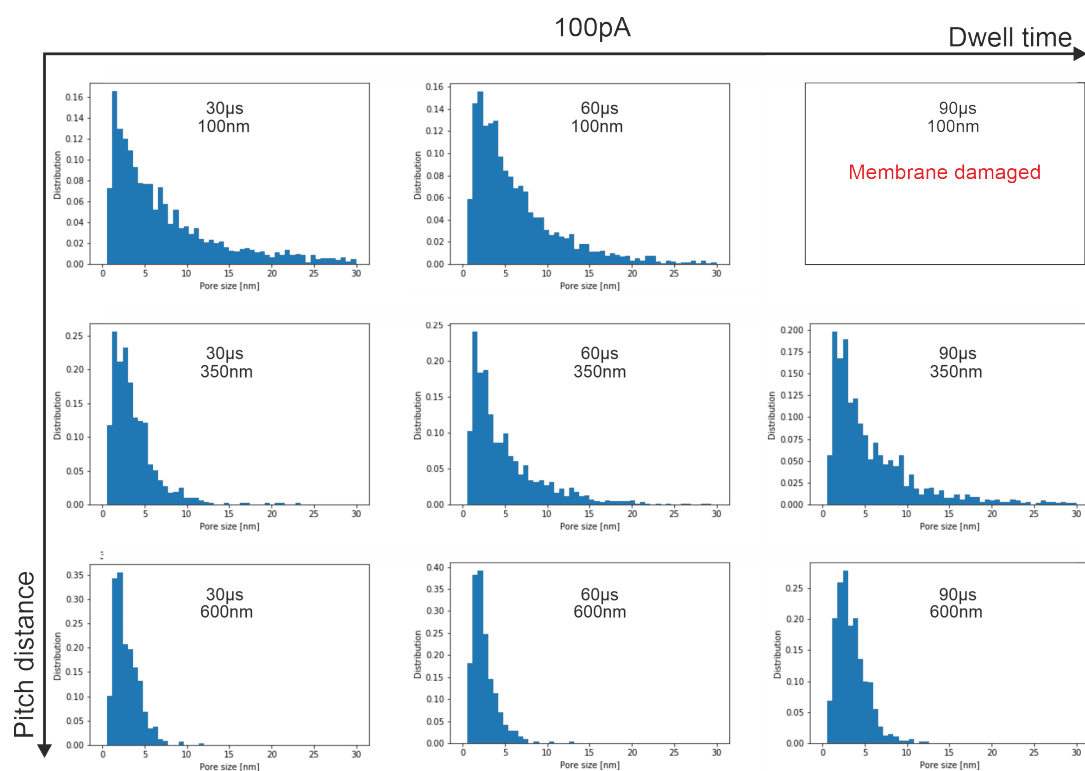


Figure 3.8: **Pore size histograms for 100pA FIB.** Histograms of pore sizes obtained at set irradiation parameters. Data obtained from the average of 10 HRTEM images taken from 10 substrates.

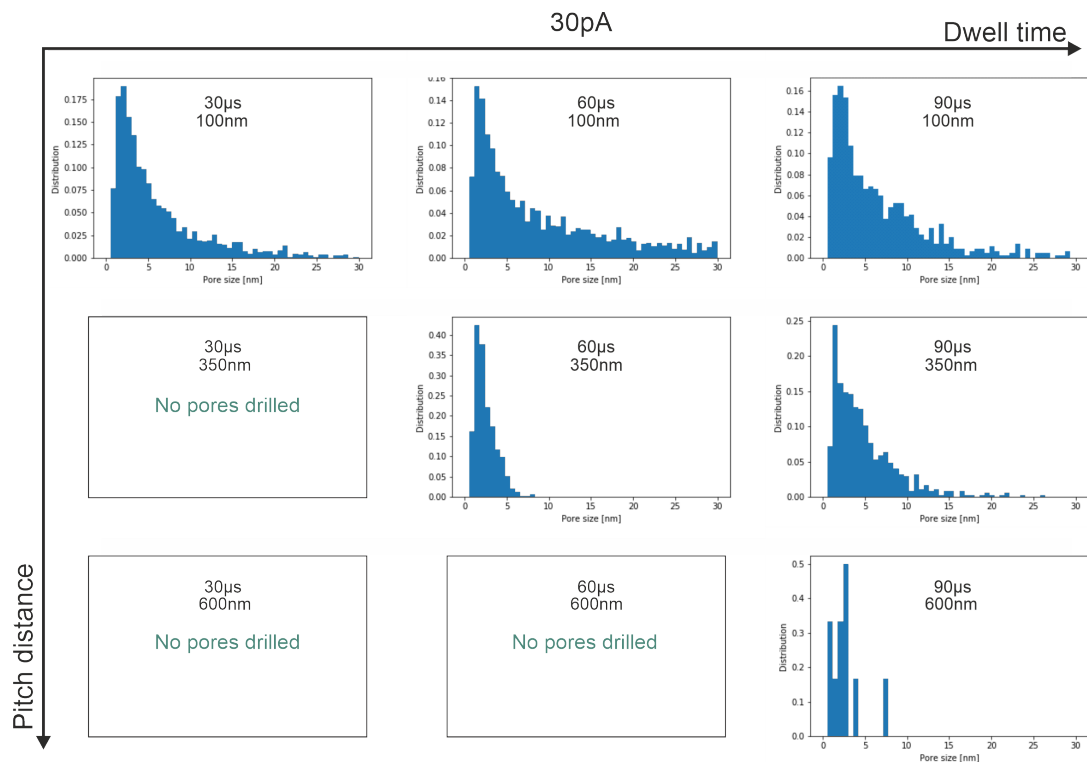


Figure 3.9: **Pore size histograms for 30pA FIB.** Histograms of pore sizes obtained at set irradiation parameters. Data obtained from the average of 10 HRTEM images taken from 10 substrates.

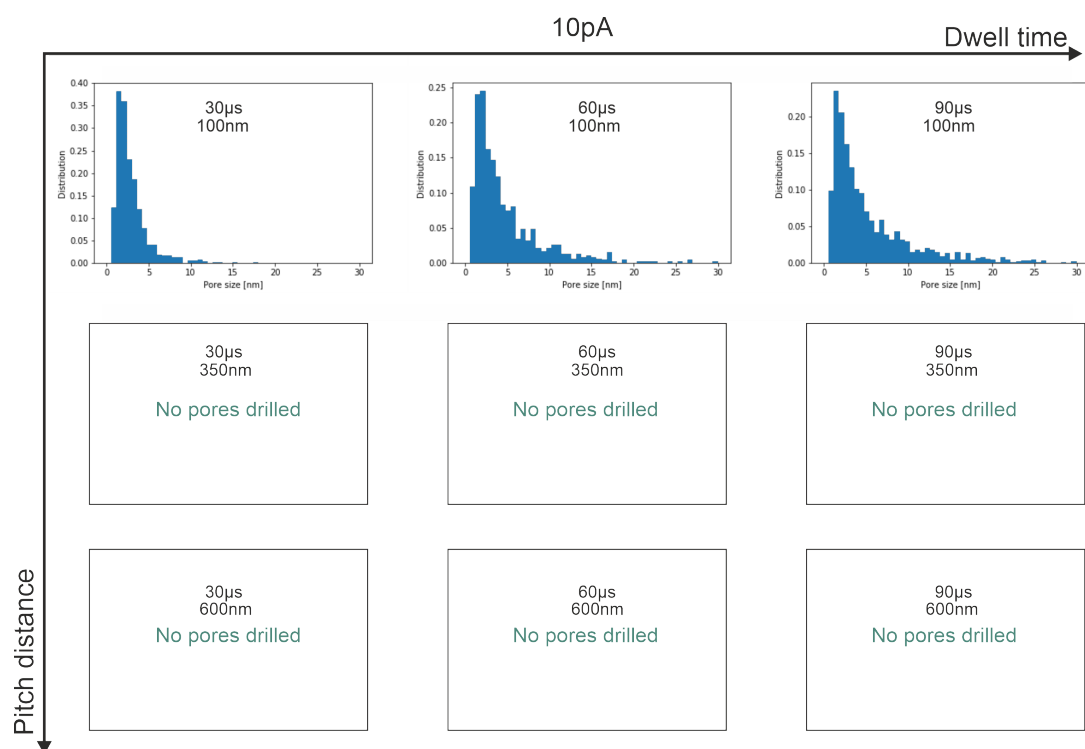


Figure 3.10: **Pore size histograms for 10pA FIB.** Histograms of pore sizes obtained at set irradiation parameters. Data obtained from the average of 10 HRTEM images taken from 10 substrates.

Pore shape optimisation

To obtain the exact edge of a nanopore we start with a group of atoms $\{a_i\}$ each with coordinates $\{x, y_i\}$ centered around a suspected nanopore location. For each pore we proceed as follows.

First, a convex hull polygon is generated which by its definition envelops all the points in the group. For each edge pair of atoms in this polygon, we find the shortest path between them on a matrix of nearest neighbour atoms $(\delta_{i,j})$. A new polygon with N points $P = \{p_k\}$ is then generated as a union of all shortest paths between the original convex hull polygon edge points. The resulting polygon approximates the original convex hull but with edge/side lengths corresponding to the individual Mo-Mo atom distances.

Secondly, we repeat the following procedure over the polygon, generating a new polygon P' which then replaces the original polygon P until the algorithm converges to the new polygon matching the old one ($\{p_k\} = \{p'_k\}$).

For each atom p_i in the polygon P , taking into account that the polymer is cyclic ($p_{N+1} = p_1$), test for one of the following cases:

1. **Remove dangling atom:** If $p_i - p_{i+1} - p_{i+2}$ form a dangling bond ($p_i = p_{i+2}$), then remove p_i from the polygon P to form P' if the resulting polygon P' would have a smaller area than P .
2. **Remove extra atom:** If p_i and p_{i+2} are nearest neighbours ($\delta_{i,i+2} = 1$), then remove p_{i+1} from the polygon P to form P' if the resulting polygon P' would have a smaller area than P .
3. **Exchange atom:** If there is an a_k such that it is a nearest neighbour of both p_i and p_{i+2} ($\delta_{i,k} = \delta_{i+2,k} = 1$), then replace p_{i+1} with a_k to form a new P' if the resulting polygon P' would have a smaller area than P .
4. **Add new atom:** If there is an a_k such that it is a nearest neighbour of both p_i and p_{i+1} ($\delta_{i,k} = \delta_{i+1,k} = 1$), then add a_k between p_i and p_{i+1} to form a new P' if the resulting polygon P' would have a smaller area than P .

If $P = P'$ the optimized pore edge has been found and the algorithm is stopped, if not make P' the new P and repeat the previous procedure.

Pore edge atom detection

For each possible Sulphur site exposed at the nanopore edge, a slice is made by using a spline interpolation of the STEM image between two points perpendicular to the line connecting the two closest nanopore edge Molybdenum atoms (gray dashed lines in Fig. 3.4D). The starting point for the slice is located at a distance of two Mo-S-Mo triangle heights $2h$ on the opposite side of the expected Sulphur atom position in respect to the Mo-Mo line. The end point of the slice is located at $2h$ away from the expected triangle site. Note that the intensity values plotted are normalized to 1 for the highest intensity pixel in the whole image, and 0 for the lowest intensity pixel.

The intensity along the slice (colored dashed lines in Fig. 3.4D) is then evaluated to determine the probability of finding a certain "atom type" at that side: a vacancy (V), double sulphurs (2S), single sulphur (S), or an invalid site (X).

A site is declared invalid (X) if the last or first point in the slice curve is also the maximum of the curve, unless the curve is constantly below the mid value between the expected sulphur and vacancy intensity level. In addition, if the values at the beginning or end of the slice are at the level expected for S1 or higher, they are rejected. These tests ensure that an invalid pore polygon shape is not used for further recognition. Also, each Mo polygon obtained from the pore shape optimisation algorithm can yield two possible Mo-S-Mo-... polygons. In order to detect the correct of the two possible polygons which match the proper crystal lattice arrangement, we perform two edge detection runs for each of the two possible polygons and reject the one with more invalid sites in the nanopore edge.

The final criteria for a valid pore edge detection is the value of the most prominent peak found in the contour as obtained using the find peaks function of the Scipy signal processing library. The parameters used are minimal peak height of 0.05 and prominence of 0.01. If there is no peak found or if the most prominent peak doesn't have at least twice the prominence of all the detected peaks combined, then this site is declared as a vacancy (V).

If a site has not been identified as a vacancy or as invalid, then the most prominent peak value is compared to the average values of the Mo and 2S intensity levels obtained from the histograms of the atom sites in the whole STEM image studied (Fig. 3.4E). From this we obtain the probability that the site corresponds to a certain atom type, as described in the main text.

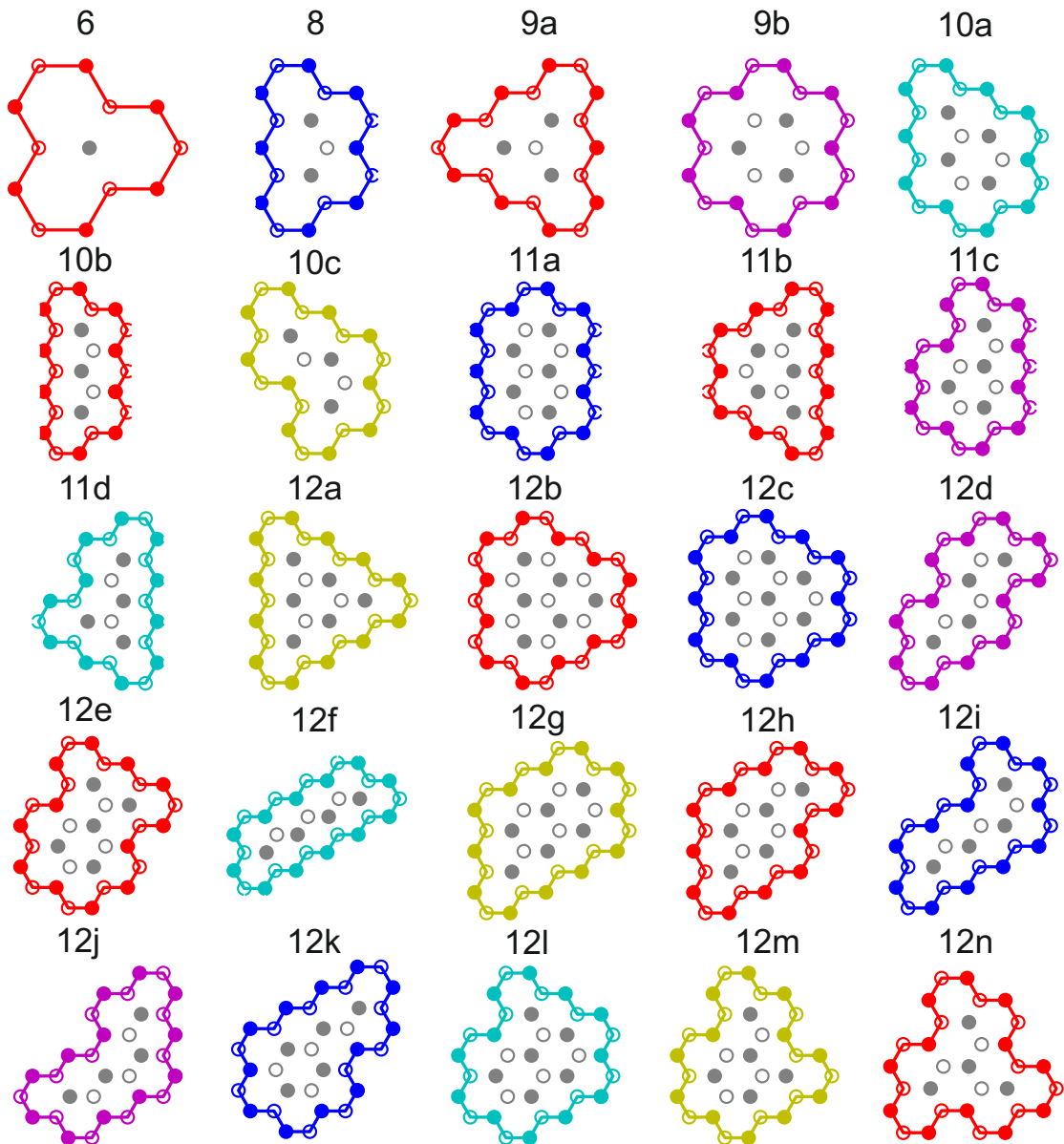


Figure 3.11: **Pore shape library.** The compilation of most frequently occurring pore shapes considered in the classification.

Pore shape optimisation

To obtain the exact edge of a nanopore we start with a group of atoms $\{a_i\}$ each with coordinates $\{x, y_i\}$ centered around a suspected nanopore location. For each pore we proceed as follows.

First, a convex hull polygon is generated which by its definition envelops all the points in the group. For each edge pair of atoms in this polygon, we find the shortest path between them on a matrix of nearest neighbour atoms ($\delta_{i,j}$). A new polygon with N points $P = \{p_k\}$ is then generated as a union of all shortest paths between the original convex hull polygon edge points. The resulting polygon approximates the original convex hull but with edge/side lengths corresponding to the individual Mo-Mo atom distances.

Secondly, we repeat the following procedure over the polygon, generating a new polygon P' which then replaces the original polygon P until the algorithm converges to the new polygon matching the old one ($\{p_k\} = \{p'_k\}$).

For each atom p_i in the polygon P , taking into account that the polymer is cyclic ($p_{N+1} = p_1$), test for one of the following cases:

1. **Remove dangling atom:** If $p_i - p_{i+1} - p_{i+2}$ form a dangling bond ($p_i = p_{i+2}$), then remove p_i from the polygon P to form P' if the resulting polygon P' would have a smaller area than P .
2. **Remove extra atom:** If p_i and p_{i+2} are nearest neighbours ($\delta_{i,i+2} = 1$), then remove p_{i+1} from the polygon P to form P' if the resulting polygon P' would have a smaller area than P .
3. **Exchange atom:** If there is an a_k such that it is a nearest neighbour of both p_i and p_{i+2} ($\delta_{i,k} = \delta_{i+2,k} = 1$), then replace p_{i+1} with a_k to form a new P' if the resulting polygon P' would have a smaller area than P .
4. **Add new atom:** If there is an a_k such that it is a nearest neighbour of both p_i and p_{i+1} ($\delta_{i,k} = \delta_{i+1,k} = 1$), then add a_k between p_i and p_{i+1} to form a new P' if the resulting polygon P' would have a smaller area than P .

If $P = P'$ the optimized pore edge has been found and the algorithm is stopped, if not make P' the new P and repeat the previous procedure.

3.3 Patterning vdW materials

Besides nanopore drilling in suspended films, PFIB irradiation was also performed on non-suspended VdW materials: MoS₂ and hBN. In both cases the goal was to study defect engineering and defect mapping via super resolution microscopy. Atomic vacancies in these materials can detrimentally impact the electronic performance by lower carrier mobility and PL quenching^{399,400}. At the same time, defects can be purposefully introduced to the material to induce single-photon emitters^{401,402}, introduce memristive^{403,404}, magnetic effects⁴⁰⁵ or catalytic effects^{406,407}. Following sections focus on precisely that: defect engineering. The goal of these studies was to irradiate monolayer MoS₂ and exfoliated hBN at deterministic locations to induce defects and study the material through single emitters imaging.

3.4 PFIB irradiation of MoS₂

The following section is adapted verbatim from the following publication:

Miao Zhang^{IV}, Martina Lihter^{IV}, Tzu-Heng Chen^{IV}, **Michal Macha**^{IV}, Archith Rayabharam^V, Karla Banjac^{VI}, Yanfei Zhao^{VII}, Zhenyu Wang^{VII}, Jing Zhang^{VII}, Jean Comtet^I, Narayana R. Aluru^{II}, Magali Lingenfelder^{III}, Andras Kis^{IV}, and Aleksandra Radenovic^I **Super-resolved Optical Mapping of Reactive Sulfur-Vacancies in Two-Dimensional Transition Metal Dichalcogenides**, ACS Nano, 2021.

A.R. conceived, supervised and coordinated all aspects of the projects. M.Z. and A.R. designed the experiments. M.Z. performed the 2D-PAINT measurements and data analysis. M.Lihter designed the chemical agent. M.M. performed FIB patterning. K.B. performed AFM measurements. K.B. and M. Lingenfelder analyzed the AFM data. Y.Z. and J. Z did the growth of MoS₂ and WS₂ under the supervision of A.K. Z.W. performed Raman spectroscopy measurements. M.Z. and J.C. wrote the manuscript with input from A.R., K.B., M.Lihter and M. Lingenfelder.

Detailed discussion on thiol-functionalized fluorescent emitters and physics is not included here and is available in the full manuscript online.

3.4.1 Motivation

Sets of experiments were conducted on studying point defects on MoS₂ using single molecule localization microscopy (SMLM). Large-area visualization was possible by using thiol-functionalized fluorescent probes which react specifically with sulfur vacancies in MoS₂ lattice. The fluo-

^{IV}Laboratory of Nanoscale Biology, Institute of Bioengineering, , EPFL ,Lausanne, Switzerland

^VDepartment of Mechanical Science and Engineering, University of Illinois at UrbanaChampaign, Urbana, 61801 Illinois United States

^{VI}Max Planck-EPFL Laboratory for Molecular Nanoscience and Institut de Physique, , EPFL ,Lausanne, Switzerland

^{VII}Electrical Engineering Institute, EPFL ,Lausanne, Switzerland; Institute of Materials Science and Engineering, EPFL ,Lausanne, Switzerland

rescent probe anchors to the S defect^{408–412} and can be observed with SMLM technique as blinking. Method developed in this study - point accumulation for imaging in nanoscale topography (2D-PAINT) demonstrates a general method for mapping of a broad range of nonradiative defects in 2D materials in liquid and can be used for in situ and spatially resolved monitoring of the interaction between chemical agents and defects in 2D materials that can potentially lead to defect healing, 2D material modification, as well as biosensing applications. This work demonstrated an important step towards defect characterization tool that can facilitate defect engineering in 2D materials.

3.4.2 Results

FIB irradiation and patterning were performed at Helios G4 PFIB UXe microscope using a focused xenon plasma beam. All investigated patterned samples were irradiated at a constant 90 μ s dwell time, 2 μ m pixel distance, and 30 kV beam with varying beam currents (10–100 pA) for different irradiation doses. The irradiation dose was calculated with the ion beam exposure formula for 2D materials. From defect engineering point of view an interesting result was, after

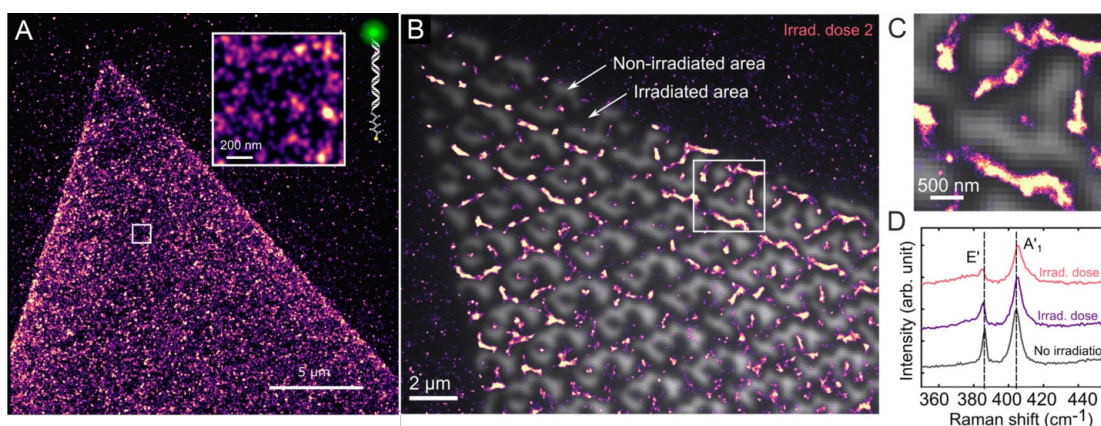


Figure 3.12: The affinity of thiol binding on MoS₂ surface: 2D-PAINT reconstructed images of a MoS₂ flake with fluorescent probes of different compositions. (a) The 2D-PAINT image acquired using fluorescent probes consisting of a fluorophore head, dsDNA of 70bp as linker molecule, and a thiol tail (FAM-dsDNA70bp-SH). The zoomed-in image reveals a high density of binding on MoS₂. Specific binding of thiol probe on sulfur vacancy defects: 2D-PAINT imaging on FIB patterned MoS₂. (b) Overlay of a PL image (gray scale) and a 2D-PAINT reconstructed image (color-coded) taken on a prepatterned MoS₂ flake by the focused-ion beam at dose of 1.1×10^{14} ions/cm₂. The 2D-PAINT image is reconstructed from 5×10^3 frames with averaged shifted histogram rendering. Imaging was performed with ATTO-dsDNA70bp-SH probes with a concentration of 10 nM under excitation power of ≈ 19 W/cm₂. (c) Zoomed-in image of the highlighted area in (a). (d) Raman scattering spectra of MoS₂ flakes with no irradiation, irradiation dose 1 of 3.4×10^{13} ions/cm₂, and dose 2 of 1.1×10^{14} ions/cm₂.

establishing thiol binding affinity on pristine MoS₂ (Figure 3.12a), validating the 2D-PAINT imaging principle by applying PFIB patterning. A high density of defects was deliberately introduced in MoS₂ flakes by xenon focused-ion beam (FIB) irradiation⁴¹³. Periodical patterns

with a pitch distance of 2 μm are irradiated on MoS_2 with carefully tuned ion dose and dwell time to avoid complete removal of the material, which is confirmed by the Raman scattering spectra, as shown in Figure 3.12d and AFM (Figure 3.13). On irradiated samples, we observe a downshift of E mode and an upshift of A_1 mode with a clearly decreasing amplitude ratio of E/ A_1 and broadening of both peaks. In addition, disorder-induced modes emerge as the dose of irradiation increases, one of which is at the low-frequency shoulder of E ($\approx 377\text{ cm}^{-1}$) and the other LA(M) mode at $\approx 227\text{ cm}^{-1}$ ⁴¹⁴ (Figure S3).

These transitions in Raman scattering spectra strongly indicate an increasing concentration of sulfur vacancies, which has been reported previously upon ion and electron beam irradiation^{414–416}. The highly defective crystal structures induced by the ion bombardment lead to a diminished PL emission of MoS_2 , as shown in Figure 3.12b (gray scale). Similar PL quenching has been reported on MoS_2 with distorted lattice after oxygen plasma exposure⁴¹⁵. Performing 2D-PAINT imaging on the flake using ATTO-dsDNA70bp-SH probes, we observe a highly selective binding on the irradiated area. Overlaying the reconstructed localization density map (color-coded) with the PL image of the same area demonstrates a strong correlation between the area of diminished PL and the area of high-localization density. Details of the overlay can be seen in the zoomed-in image in Figure 3b. The absence of binding in the non-irradiated area is most likely due to re-deposition of the knocked-off materials that block the binding sites. These results clearly demonstrate favorable binding between the thiol probes and the sulfur vacancies.

3.4.3 Conclusions

FIB defect patterning was found to reliably create defect areas on deterministic areas.. AFM measurements confirmed MoS_2 remained on the surface and was not etched away during the irradiation. This finding enabled to study thiol-bindings to S-vacancies and opened a path towards studying fluorescent defects, their spatial distribution and ion-parameter dependance. Xe-ion microscope was especially useful in this case. Opposite to Ga-ion systems, xenon ions are inert and do not change the material's chemistry. The location-specific patterning enabled to manipulate the defect density and study the effects of defects (and emitters) proximity further.

Monolayer MoS_2 presented here was merely one example of the vdW material that was studied during the FIB project. Another interesting case is the use of multilayer systems with different chemistry and physics - such as insulating hexagonal boron nitride (hBN), to study single photon emitters, ion irradiation-based defect engineering and single molecule localization microscopy techniques. In the next section, exfoliated, multilayer hBN is used to peer into the defect formation and their optical properties.

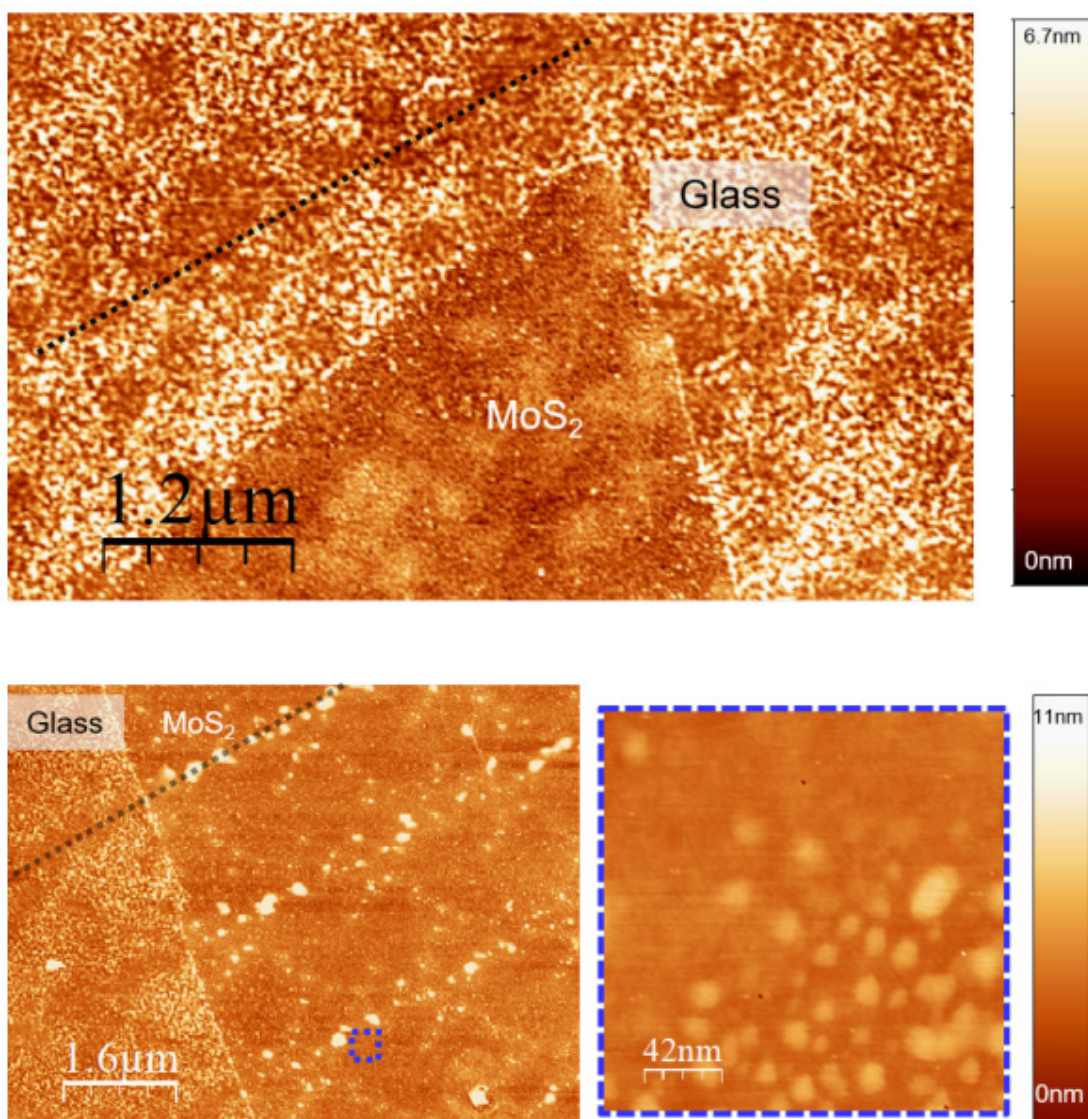


Figure 3.13: **AFM height images of two FIB patterned MoS₂ flakes** with irradiation dose of 3.4×10^{13} ions/cm². The dashed lines indicate one of the approximate irradiation areas on each flake. The images show that the MoS₂ monolayer in the irradiated areas is not etched away. Raman scattering spectra of MoS₂ monolayers under different irradiation ion dose with irradiation dose-1 of 3.4×10^{13} ions/cm² and dose-2 of 1.1×10^{14} ions/cm². It shows a downshift of E' peak and upshift of A' peak due to defect-induced phonon confinement as well as the presence of defect-activated peaks at ≈ 377 cm⁻¹ at the shoulder of E' peak and LA(M) peak at ≈ 227 cm⁻¹.

3.5 PFIB irradiation of hBN

The following section is based verbatim on the following publication:

*Evgenii Glushkov^{VIII}, **Michal Macha^{VIII}**, Esther Rath^{IX}, Vytautas Navikas^V, Nathan Ronceray^V, Cheol Yeon Cheon^X, Ahmed Aqeel^{XI}, Ahmet Avsar^{VII XII}, Kenji Watanabe^{XIII}, Takashi Taniguchi^{XIII}, Ivan Shorubalko^{XIV}, Andras Kis^{VII}, Georg Fantner^{VI}, and Aleksandra Radenovic^V*

Engineering Optically Active Defects in Hexagonal Boron Nitride Using Focused Ion Beam and Water, ACS Nano, 2022.

E.G. and M.M. contributed equally to this work. A.R., E.G. and M.M. conceived and designed the experiments; E.G., A.A. and C.Y.C. prepared the samples and M.M. performed the FIB irradiation; E.R. did the AFM measurements, helped by N.R. and C.Y.C. E.G. performed the optical measurements with help from V.N., A.A. and N.R.; M.M. did the TEM measurements; E.G, V.N. and N.R. analyzed the data; K.W. and T.T. contributed materials; I.S. helped with interpretation of results; E.G. wrote the paper, with inputs from all authors; A.K., G.F. and A.R. supervised the project; All authors discussed the results and commented on the manuscript.

Parts of the SI related to single molecule localization microscopy, in-depth analysis of absorption and fluorescence as well as measurements details were not included here and are accessible in the main text online.

3.5.1 Introduction

Optically-active defects in van-der-Waals (vdW) materials have attracted a lot of attention recently, finding applications in the fields of nanophotonics and nanofluidics^{102,417–420}. In particular, hexagonal boron nitride (hBN) has emerged as a promising material platform, hosting a plethora of optically-addressable defects within its large bandgap (≈ 6 eV)³⁸⁰. Initially established as bright and stable single-photon sources⁴⁰², defects in hBN have since been proven to be useful for the integration into hybrid photonic devices⁴²¹, super-resolution imaging^{422–427} and studying complex charge dynamics in aqueous environments^{428,429}. Moreover, several recent works have demonstrated spin-dependent emission from defects in hBN⁴³⁰ at room temperature^{431–433}, opening numerous applications for this material platform⁴³⁴.

Defects in hBN are either randomly formed during growth^{423,435}, post-growth doping⁴³⁶ or exfoliation from bulk crystals^{437,438}, or can be intentionally induced in the pristine/unirra-

^{VIII}Laboratory of Nanoscale Biology, Institute of Bioengineering, , EPFL ,Lausanne, Switzerland

^{IX}Laboratory of Nano-Bio Instrumentation, Institute of Bioengineering, EPFL ,Lausanne, Switzerland

^XLaboratory of Nanoscale Electronics and Structures, Electrical Engineering Institute and Institute of Materials Science, EPFL ,Lausanne, Switzerland

^{XI}Laboratory of Quantum Nano-Optics, Institute of Physics, EPFL ,Lausanne, Switzerland

^{XII}School of Mathematics, Statistics and Physics, Newcastle University, Newcastle upon Tyne, NE1 7RU, United Kingdom

^{XIII}National Institute for Materials Science, Tsukuba, Japan

^{XIV}Laboratory for Transport at Nanoscale Interfaces, Empa – Swiss Federal Laboratories for Materials Science and Technology, Dübendorf, Switzerland

diated material using large-area irradiation with ions^{424,439,440}, neutrons⁴⁴¹, or using high-temperature annealing⁴⁰². While these approaches reliably produce quantum emitters in hBN, they result in randomly spatially distributed defects, thus complicating their proper and reliable characterization using correlated microscopy⁴⁴², and hindering their applications in integrated devices for nanophotonics⁴²¹ and nanofluidics (*e.g.* to systematically study the dynamics of charge transfer at liquid-solid interfaces^{428,429}). Recent attempts to generate defects in hBN at precise spatial locations included strain engineering through either transfer/exfoliation⁴⁴³ of hBN flakes or growth of hBN films on patterned substrates⁴⁴⁴, offering scalability, but limited subsequent integration. Other patterning approaches included the use of pulsed lasers^{445,446}, focused electron⁴⁴⁷ and ion beams^{432,448} to locally damage the hBN lattice and generate emitters with desired properties.

Focused ion beam (FIB) seems an especially appealing technique for the generation of optically-active defects in vdW materials due to its versatility, high resolution, ease-of-use and scalability. Notably, FIB has found widespread use for patterning of 2D materials as a resist-free method^{449,450}, mitigating omnipresent polymer contamination of the patterned material. And emergence of commercially-available plasma FIB (PFIB) machines, employing ions of inert gases, such as argon and xenon, instead of liquid metals, has solved the long-standing problem of sample contamination by gallium ions in the traditional FIB systems^{451,452}. Nevertheless, while deterministic defect generation in hBN using FIB has been recently demonstrated^{432,448}, achieving sub-micron spatial accuracy, a clear understanding of the FIB irradiation effects and the formation of defect sites in hBN is lacking.

In this work, we present a systematic study of these effects, arising from the beam interacting not only with the thin layer of hBN itself, but also with the underlying substrate, performing transmission electron microscopy (TEM) analysis of cross-sections of irradiated hBN flakes. We further show that the FIB-induced defects are strongly influenced by the environment in which the irradiated samples are placed. In particular, we uncover a mechanism of water-assisted etching of FIB-irradiated hBN defects, leading to drastic structural and optical transitions in irradiated sites. Moreover, by utilizing a state-of-the-art super-resolution microscopy technique correlated with atomic force microscopy (AFM) imaging, we explicitly show the localization of emitters in hBN at the rim of FIB-induced defect sites, in good agreement with a hypothesis that exists in literature⁴⁴⁸.

3.5.2 Results and discussion

We employed the Helios G4 Xe PFIB system to investigate the influence of Xe ion irradiation on pristine hBN flakes, containing very few intrinsic defects⁴⁵³. The flakes were prepared on cleaned SiO₂ substrates with gold markers and grounding electrodes by mechanical exfoliation from high-quality hBN crystals⁴⁵⁴, resulting in a typical thickness of hBN flakes of 10-100 nm. Directly after exfoliation, the samples were loaded into the Xe FIB and irradiated with a pre-defined pattern (Fig. 1a). The irradiated flakes were briefly checked in the built-in SEM, clearly demonstrating the FIB-induced changes in the morphology of the sample (Fig.

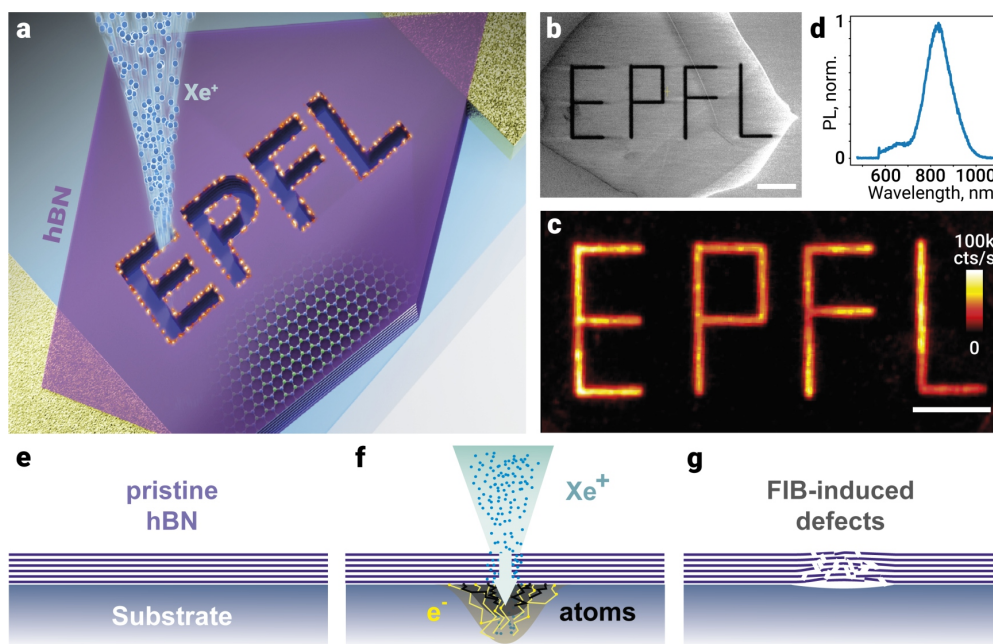


Figure 3.14: **Generation of FIB-induced optically active defects in exfoliated hBN flakes.** a) Schematic representation of the defect writing process on a pristine/unirradiated hBN flake using Xe FIB. Gold electrodes on the sides reduce charging effects during irradiation. b) A scanning electron microscope (SEM) image of a patterned flake inside the FIB chamber. c) Fluorescence image of the generated pattern of optically-active defects from a confocal microscope. Imaging was done in water. d) Characteristic spectrum of FIB-induced defects, taken from a dried sample in air. The sharp little peak, seen on the short-wave side, is the Raman peak of the hBN material. e-g) Simplified schematic of the FIB-induced defect generation process: being a result of Xe ions interacting with the substrate, which is partially milled (f), creating a defected region and a void beneath the hBN flake (g). Scale bars: 10 μm (a, inset), 5 μm (e)

3.14b). After unloading from the FIB chamber, the samples were inspected on a home-built fluorescence microscope, confirming the creation of optically-active defects at the irradiated sites on hBN flakes (Fig. 3.14c). The spectral characteristics of FIB-patterned defects qualitatively matched the previously reported ones for Xe FIB⁴³², with the broad emission peak centered around 830 nm, shown in Fig. 3.14d (see Materials and methods for the details). The simplified mechanistic understanding of these changes is shown in Fig. 3.14e-g, where defects are generated as a result of Xe ions interacting with the substrate, creating showers of backscattered electrons and sputtered ions that locally damage the crystalline structure of hBN layers.

To verify the structural changes induced on hBN flakes by the ion beam a detailed high-resolution transmission electron microscopy (TEM) study of the milled area cross-section was performed (Fig. 3.15). An hBN flake irradiated with typical experimental parameters (see Methods) was cut along the irradiated spots (Fig. 3.15a) with a Ga FIB system to create a thin lamella (Fig. 3.15b) suitable for TEM imaging. A high resolution TEM image of the hBN/glass area on the irradiated spot (Fig. 3.15c) shows visible signs of mechanical damage

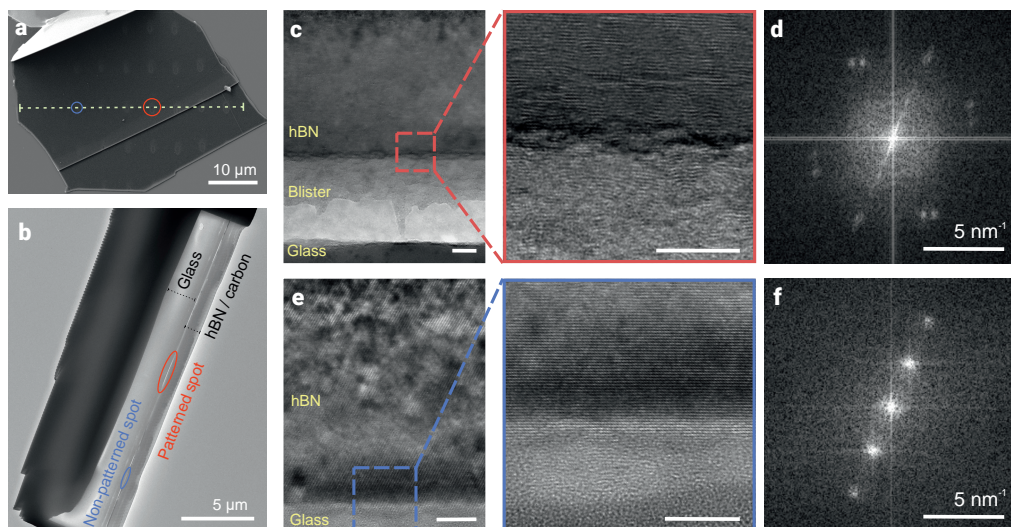


Figure 3.15: Exploring mechanical effects of FIB irradiation using TEM. a) Irradiated hBN flake on a glass substrate, with $3\mu\text{m}$ -spaced defect sites (seen as brighter spots on top of a dark hBN surface, marked with the dotted line). b) a lamella of the hBN flake cross-section cut along the dashed line marked in a). A thin layer of carbon was sputtered on top of the flake to prevent charge accumulation. c) A cross-sectional image of the irradiated hBN area and d) corresponding fast Fourier Transform (FFT) compared to e) the pristine/unirradiated area image of the hBN/glass interface and its FFT f) shows an evident mechanical deterioration of hBN layers and the local amorphization of the material. Scale bars: 10 nm

and perforation caused by the PFIB on the hBN flake layers. Most of the damage is seen at the hBN/glass boundary due to the ion collision cascades, secondary electron emission and substrate particle sputtering occurring in the interaction volume area underneath the patterned spot (schematically marked in Fig. 3.14c). These effects lead to the hBN milling selectively occurring from beneath the flake, at the hBN/glass interface. Consecutively, this leads to the creation of the blister in between the hBN and glass substrate filled with the milled debris comprising of amorphized and recrystallized hBN as well as particles sputtered from within the substrate. The FFT of the irradiated flake area (Fig. 3.15d) shows signs of substantial amorphization and mechanical damage (smearing of the FFT pattern) of the hBN crystal lattice which can be associated with hBN blistering. The PFIB milling damage is especially visible when compared to unirradiated, pristine hBN/glass interface area (Fig. 3.15e) and its corresponding, clear FFT (Fig. 3.15f) image. Further details of the TEM-based study of irradiated sites are given in Fig. S3.19.

To explore the optical properties of FIB-induced defects, we have used both a home-built confocal setup and a widefield super-resolution microscope, optimized for single-molecule localization microscopy (SMLM)⁴²⁴. We started with an hBN flake irradiated with line patterns of varied irradiation dose ($1 - 8 \times 10^{14}$ ions/ cm^2 , Table 3.1 in SI) to see how it affects fluorescent emission from defects. From the averaged image stack, shown in Fig. 3.16a, one can see four horizontal lines of varying intensity corresponding to the irradiated pattern of a gradually

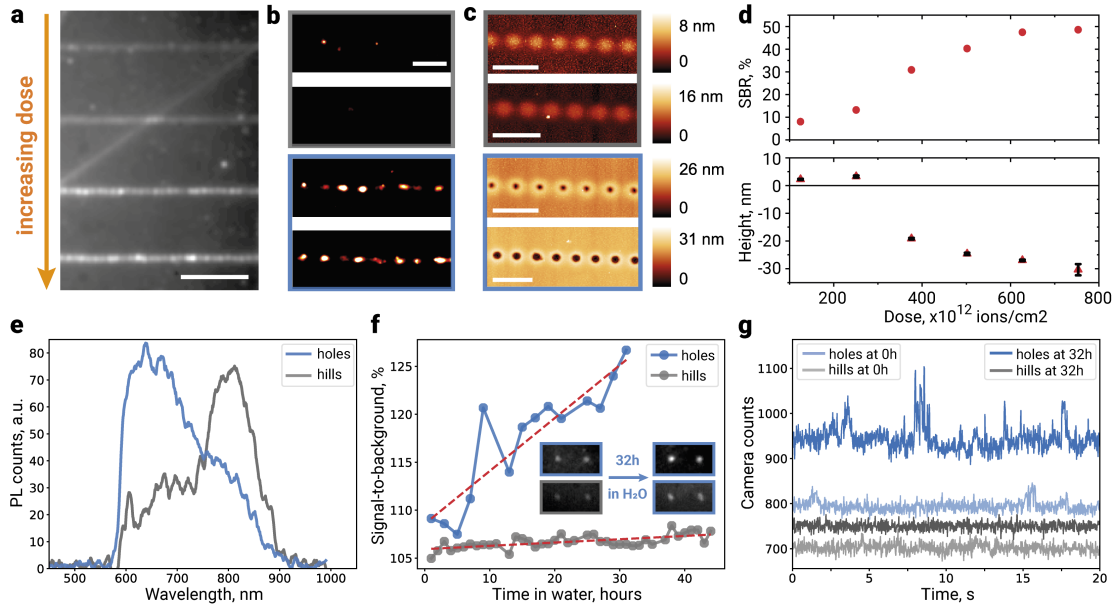


Figure 3.16: Optical and morphological characterization of irradiated defect sites. a) Widefield fluorescence image of an hBN flake with FIB-irradiated horizontal line patterns of a gradually increasing dose, which results in the creation of optically-active defects of increasing intensity. For all measurements in this figure 561 nm laser excitation is used. Imaging is performed in DI water, pH 5.8. b) Zoom-ins from (a), processed using localization microscopy algorithm⁴⁵⁵, reveal two different types of emission: dim diffused emitters (type I) which are not localized by the algorithm due to low signal-to-noise (SNR), and bright localized ones (type II) which are clearly visible. c) AFM scans of respective areas. Two types of emitters from optical images can be easily correlated with the difference in morphology, depending on the irradiation dose: hills are formed for lower doses and holes for higher ones. Imaging was done in air, after thoroughly drying the immersed sample with a nitrogen gun. d) Extracted signal intensities (signal-to-background ratio, SBR) and height/depth of the FIB induced defects *vs* irradiation dose, showing the dose-dependent hill-to-hole transition. e) Spectra of two defect types, acquired in water. When measuring in air, only the peak around 800 nm is distinguishable (Fig. 3.14d). f) Change in the brightness of two types of emitters after a long immersion in water. g) Comparison of the temporal dynamics of hill *vs* hole emitters before and after the long immersion. Scale bars: 5 μm (a), 1 μm (b,c)

increasing dose. The zoom-ins into each of these lines in Fig. 3.16b are processed using an SMLM algorithm⁴⁵⁵ to precisely localize the isolated emission spots. However, one can see that in the top two, the localization algorithm fails to localize the emitters as their emission intensity is rather dim and diffused resulting in a low signal-to-noise (SNR) and low signal-to-background (SBR) values of $\sim 5 - 10\%$. In contrast to that, the emitters in the bottom two lines are easily localized and are seen as regular bright spots with SBR of $\approx 30 - 50\%$ and ≈ 500 nm pitch distance (Fig. S3.20).

To understand the origin of this emission difference we performed AFM measurements on the same lines (Fig. 3.16c). One can immediately see that two types of emitters correspond to either hill-type or hole-type structures created by the FIB depending on the irradiation dose. This dose-dependent transition of irradiated hBN areas is shown in Fig. 3.16d. Focusing on

the optical properties of the optically-active defects hosted within created hills and holes, we show that their differences go much beyond just emission intensity. In Fig. 3.16e one can see an appearance of another spectral emission peak around 650 nm, measured from hole defects in water, while hill defects still show predominant emission around 800 nm. While the microscopic origin of this spectral transition is not clear, one can attribute it to the dangling bonds⁴⁵⁶ appearing at the edge of the created holes in hBN. The 800 nm emission is also present in the spectrum of holes and is attributed to the remaining damaged material and/or strain around the hole.

Another difference concerns the long-term evolution of the measured emission from holes *vs* hills when the sample is immersed in an aqueous solution for a long time (tens of hours). In Fig. 3.16f one can see the steady increase in the signal intensity for holes and an absence of such increase for hills. This graph was obtained by analysing the timelapse images of the irradiated area, fitting the maximal intensity values at each defect site and normalizing it to its local background. Finally, the temporal traces from both types of defects in the steady-state, shown in Fig. 3.16g, demonstrate sharp transitions between different intensity levels (blinking) for the emission originating from holes, but not from hills. This blinking behaviour is further intensified after an extended stay in water which we link to the accumulation of dangling bonds and functional groups in the circumference of hole structures and enhanced interaction with diffusing charges⁴²⁸. The exact chemical composition of the defect sites is not yet known and remains the topic of future studies.

Separate attention deserves the observed optically-detected magnetic resonance (ODMR) at 3.4 GHz, closely matching the previously reported one⁴³² and verifying the creation of spin defects in the hBN lattice using FIB. Based on our observations and results from literature^{431,432,434}, one can conclude that the spin-dependent emission comes primarily from the 830 nm peak, for both hole and hill defects. However further studies are needed to clarify this question and to uncover the reason why the ODMR at sub-GHz frequencies, reported for the 600 nm emission line^{430,433}, could not be observed for the created hole-type defects.

Following the structural-optical transitions between two types of FIB-induced defects, immersed in the imaging medium (DI water), we explored in more detail its influence on the formation of defects. Having obtained an AFM scan of a marked area of an hBN flake just after FIB irradiation, we observed the creation of only hill-type structures, even though the irradiation doses were high enough to create holes (in comparison to Fig. 3.16). However, after immersing the sample in water and imaging the same area with AFM again we have noticed the immediate creation of holes in the irradiated regions (Fig. 3.17a). The observed hill-to-hole transition happened at a timescale of 2 consecutive AFM scans of the same area (20 minutes long), suggesting a fast dissolution process (Fig. S3.24) in comparison to the slow SBR increase of the fluorescent signal in Fig. 3.16f. The 3D zoom-ins of the selected defect before and after immersion in water are shown in Fig. 3.17b and perfectly illustrate the water-mediated hill-to-hole transition. Fig. 3.17c shows a simplified schematic of the etching process, where the damaged hBN material at the irradiated sites (seen in Fig. 3.15) is quickly

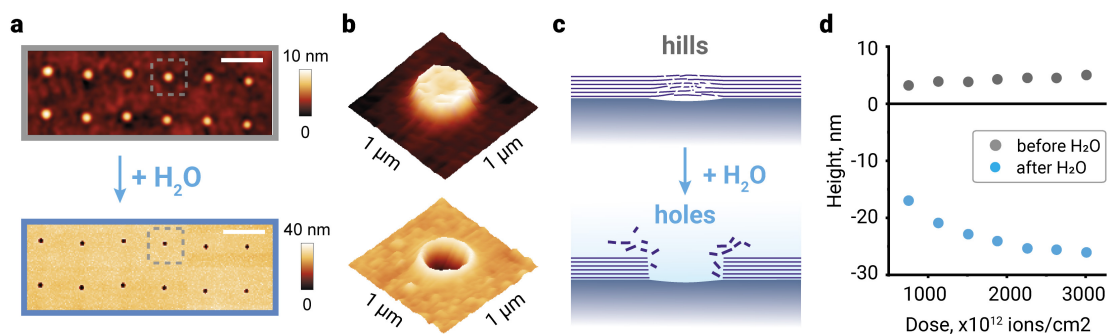


Figure 3.17: **Water-assisted etching of irradiated defect sites.** a) AFM images of the same area on the irradiated hBN flake before and after immersion in water. Scale bar: $3\ \mu\text{m}$ b) Pseudo-3D reconstruction of a single defect site before (top) and after water (bottom). c) Schematic representation of the water-assisted hill-to-hole transition. d) Dependence of the average peak height/depth of irradiated sites on irradiation dose (before and after water).

removed by water. However, once the holes are created their lateral size and depth do not noticeably change both in air and in water over the course of days (Fig. S3.25). This indicates that only damaged hBN material is removed by water⁴⁵⁷.

The dependence of the created height/depth of the hills/holes, respectively, on the irradiation dose is shown in Fig. 3.17d, suggesting a continuous hill-to-hole transition at a lower dose ($\sim 3 \times 10^{14}$ ions/cm² on Fig. 3.16d). The slight linear increase in the height of the hills at longer irradiation times probably comes from either more sputtering or a continuous cavity growth underneath hBN, which makes the thin flake bulk up. The saturation behaviour for the depth of the created hills can be explained by water fully etching through the hBN flake and reaching the substrate material. Combining these findings with data from Fig. 3.16, we conclude that the observed hill-to-hole transition is caused by water and is dose-dependent, *i.e.* starting from a certain FIB irradiation dose, which mechanically damages the hBN material enough for the water to dissolve it. This claim is supported by the TEM inspection of the irradiated areas in Fig. 3.15 and literature studying the reactivity of mechanically damaged bulk hBN in water⁴⁵⁷. This defect formation process specific of hBN flakes deposited on substrates with thicknesses much larger than the typical beam penetration depth ($< 100\ \text{nm}$)⁴³², due to the FIB-substrate interaction effects, illustrated in Fig. 3.14e-g and confirmed using TEM in Fig. 3.15. No hole formation or subsequent structural or optical changes in water were observed for FIB-irradiated hBN flakes which were suspended over holes or supported on thin membranes. An example of such sample and its AFM analysis directly after irradiation is shown in Fig. S3.27, demonstrating the creation of hole defects created by the ion beam in the suspended hBN without any influence of water.

Finally, to better understand the origins of the emission, we performed correlative SMLM and AFM imaging of the hole defects. Briefly, we first acquired stacks of thousands of widefield images of irradiated hBN flakes with isolated defect sites immersed in DI water. The averaged image from one of these stacks is shown in the top-left part of Fig. 3.18a, while in the bottom-

right part we show a reconstructed super-resolved image, processed by a state-of-the-art localization algorithm⁴⁵⁸. In some of the bright defect sites in the averaged widefield image one can notice the presence of a darker central region, hinting on the probable emission from the edges of the formed hole as was suggested in literature⁴⁴⁸. Super-resolved images of FIB-induced defects provide the direct evidence of such edge-related emission, which is shown in detail in the zoom-in in Fig. 3.18b. The acquired AFM image of the same area matches well the SMLM data (Fig. 3.18c). To further verify and visualize the spatial distribution of emitters, we show the overlaid image in Fig. 3.18d, where one can clearly see the emergence of fluorescent emission from the edge of the hole defects.

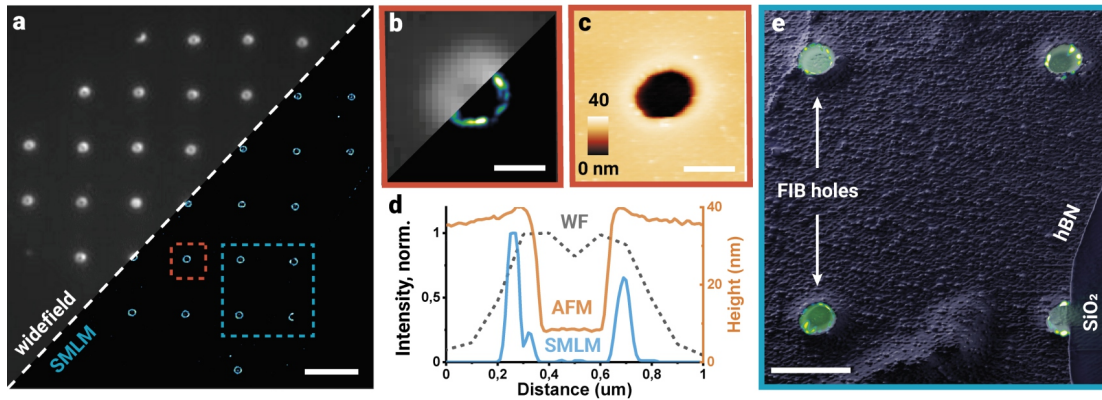


Figure 3.18: Correlated super-resolution and atomic force microscopy of FIB-induced defects in hBN. a) Averaged fluorescence image of an irradiated hBN flake (2D array of isolated defects, $3\ \mu\text{m}$ apart), overlaid by the super-resolved image of the same flake. b) Zoom-in into the dashed red area around the isolated defect site (overlaid widefield/SMLM) c) AFM scan of the same area, perfectly matching fluorescence data. d) Line profiles from zoom-ins in (b) and (c), showing cross-sections of the same defect site in widefield, SMLM and AFM images e) Correlated AFM-SMLM image of four defect sites from a dashed blue area in (a), clearly showing precise spatial localization of optically-active emitters at the rim of the holes, formed by FIB irradiation and activated by water. Scale bars: $3\ \mu\text{m}$ (a), $400\ \text{nm}$ (b,c), $1\ \mu\text{m}$ (e)

While the hole defects, demonstrated in Fig. 3.18, are relatively large, smaller sub-100 nm defects were successfully created using the current technique and measured with AFM (see Fig. 3.17a and Fig. S3.26). However, having dense emitters on the rim of the defect sites hinders their analysis with SMLM-based super-resolution optical microscopy. Further optimization of irradiation parameters and imaging conditions will enable the use of the FIB-created emitters for multiple super-resolution microscopy modalities. Moreover, better spatial resolution and smaller waist of the ion beam, such as in the Helium Ion Microscopes (HIMs), can further decrease the affected defect sites by 1-2 orders of magnitude^{459–461}, enabling deterministic creation of atomically-small isolated defects with nanometer precision emitting single photons. Further miniaturization of optically-active defects to below 100 nm scale should also facilitate in-depth studies of nanofluidic phenomena at the liquid-solid interfaces^{428,429} with precise spatial control over the nanoscale charge dynamics.

3.5.3 Conclusion

We presented a systematic study of the focused ion beam interactions with supported thin exfoliated hexagonal boron nitride flakes, leading to the creation of optically-active spin defects. We showed that the defect creation is the result of the ion beam interacting not only with the thin hBN flakes, but also with the substrate, on which it is supported. Moreover, both the structural and optical properties of the induced defects are dose-dependent and undergo irreversible transitions in aqueous solutions, representing a particular mechanism of water-assisted formation of FIB-irradiated hBN defects. By utilizing super-resolution microscopy correlated with AFM imaging, we were able to explicitly show the localization of emitters at the rim of the created defect site. Our findings lay the foundation for FIB-assisted engineering of optically-active defects in hBN with high spatial control for nanophotonics, nanoscale sensing and nanofluidics.

3.5.4 Methods

Sample preparation

hBN flakes from high quality crystals⁴⁵⁴ were exfoliated onto glass coverslips (no. 1.5 Micro Coverglass, Electron Microscopy Sciences, 25 mm in diameter), pre-patterned with gold markers for easier navigation and electrode mesh to prevent accumulation of charges. Exfoliation was done either using tape or gel-pack stamps. The flakes for TEM grids (Norcada, NT025C) were polymer-transferred. Si/SiO₂ substrates have also been used, with similar patterning results.

FIB irradiation

Irradiation and hBN patterning was done on Helios G4 PFIB UXe system with Xenon Plasma FIB column. All experiments were done at 30kV and 100pA Xe beam with varying parameters of

dwell time and pitch distance between irradiated spots. By varying the dwell time from $100\mu\text{s}$ to up to 2ms we effectively increase the irradiation dose and pattern outcome in the form of irradiated spot size. Pitch distance is typically set to $3\mu\text{m}$ for studying isolated defects and between 300 and 500 nm in case of tighter arrays and line patterns. Typical ion fluence/dose ranges from 1.2×10^{14} to 2.5×10^{15} ions/ cm^2 for dwell time range of $100\mu\text{s}$ to 2 ms. Several tens of samples have been routinely created using this technique.

Optical inspection

Widefield imaging has been done on a custom widefield fluorescence microscope, described elsewhere^{423,424}. Briefly, the emitters are excited using either 488 or 561 nm laser (Monolithic Laser Combiner 400B, Agilent Technologies), which is collimated and focused on the back focal plane of a high-numerical aperture oil-immersion microscope objective (Olympus TIRFM 100X, NA: 1.45). This creates a wide-field illumination of the sample in an area of $\approx 25\mu\text{m}^2$. Fluorescence emission from the sample is collected by the same objective and spectrally separated from the excitation light using dichroic and emission filters (ZT488/561rpc-UF1 and ZET488/561m, Chroma) before being projected on an EMCCD camera (Andor iXon Life 897) with EM gain of 150. An additional spectral path, mounted in parallel to the localization path allows for simultaneous measurements of the emission spectra from individual emitters⁴²⁴. The sample itself is mounted in a sealed fluidic chamber, which is placed on a piezoelectric scanner (Nano-Drive, MadCityLabs) for fine focus and drift compensation using an IR-based feedback loop which is especially important for long-term measurements. Typical exposure time is 20-50 ms and typical laser power 50-100 mW for the widefield excitation area of $2\times 10^3\mu\text{m}^2$, resulting in a power density of $2.5 - 5\text{ kW}/\text{cm}^2$. A typical acquired image stack contained 2-10 thousand frames.

Confocal imaging was done on two different setups, utilizing either 532 nm or 561 nm excitation lasers and APDs as well as spectrometers to detect the emitted light. The first setup was used to obtain both emission and absorption spectra of defects to make their 2D spectral maps. However, due to the limitations in construction this setup could only be used to image samples in air. In order to perform emission measurements, a diode pumped solid state (DPSS) laser (DJ532-40, ThorLabs) at 532 nm was used. The laser beam was passed through a single mode fiber (P3-460B-FC-1, ThorLabs) to obtain a gaussian beam profile. Afterwards, a narrow bandpass filter (FL05532-1, ThorLabs) was placed in the beam path to remove any unwanted features from the laser spectrum. A 100X, 0.9 NA objective (MPLFLN, Olympus) focused the beam on the sample and collected the emission. The sample was mounted vertically on a piezoelectric stage (Nano-Drive, MadCityLabs) and a raster scan was performed to obtain the spectral maps. The laser line was removed from the emission spectra by a longpass filter (FELH0550, ThorLabs) and the signal was recorded using a spectrograph (Kymera 193i, Andor) with a CCD (iDus, Andor). For absorption measurement, the sample was illuminated from the back by a calibrated halogen lamp (SLS201L, ThorLabs). The transmitted light was collected, on the opposite side of the sample, by 100X, 0.9 NA objective (MPLFLN, Olympus) and the

spectrum was recorded with the CCD. In order to extract the absorption, a measurement was first made on the substrate and used a background signal.

To compensate for this we utilized a second confocal setup in an inverted microscope configuration allowing us to image samples in liquid. Here the emission was split between two fiber-coupled APDs (SPCM-AQRH, Excelitas) in an HBT configuration. One of the APDs could be switched with a fiber-coupled spectrometer (QE Pro, Ocean Optics) to measure the emission spectra in liquid. The setup could also perform lifetime and photon correlation measurements using the PicoHarp TCSPC module (PicoQuant).

TEM Imaging

The lamella for cross-section imaging was cut using the Zeiss NVision 40 CrossBeam system. Irradiated flake chosen for cross-section imaging was patterned using default array parameters i.e. 30kV, 100pA Xe FIB. High resolution TEM imaging was performed at Talos L120C G2 using 80kV electron beam.

AFM imaging and image processing

For the AFM imaging a customized AFM, consisting of a Dimension Icon AFM head (Bruker) mounted above an optical microscope (Olympus IX83), was used⁴⁶². The position of the hBN flakes with respect to the cantilever was detected with the optical microscope. AFM images in air were recorded at a line rate of 0.5Hz with RTESPA-150 cantilevers (Bruker) with a nominal spring constant of 6Nm^{-1} in tapping mode. The cantilever drive frequency and amplitude were determined by automated cantilever tuning. AFM images in fluid were acquired at 0.5Hz line rate using ScanAsyst Fluid cantilevers (Bruker) with a nominal spring constant of 0.7Nm^{-1} in PeakForce quantitative nanomechanical mode (QNM) at an oscillation rate of 1kHz and a force setpoint of 3nN . The images were processed with a standard scanning probe software (Gwyddion).

Supplementary Information

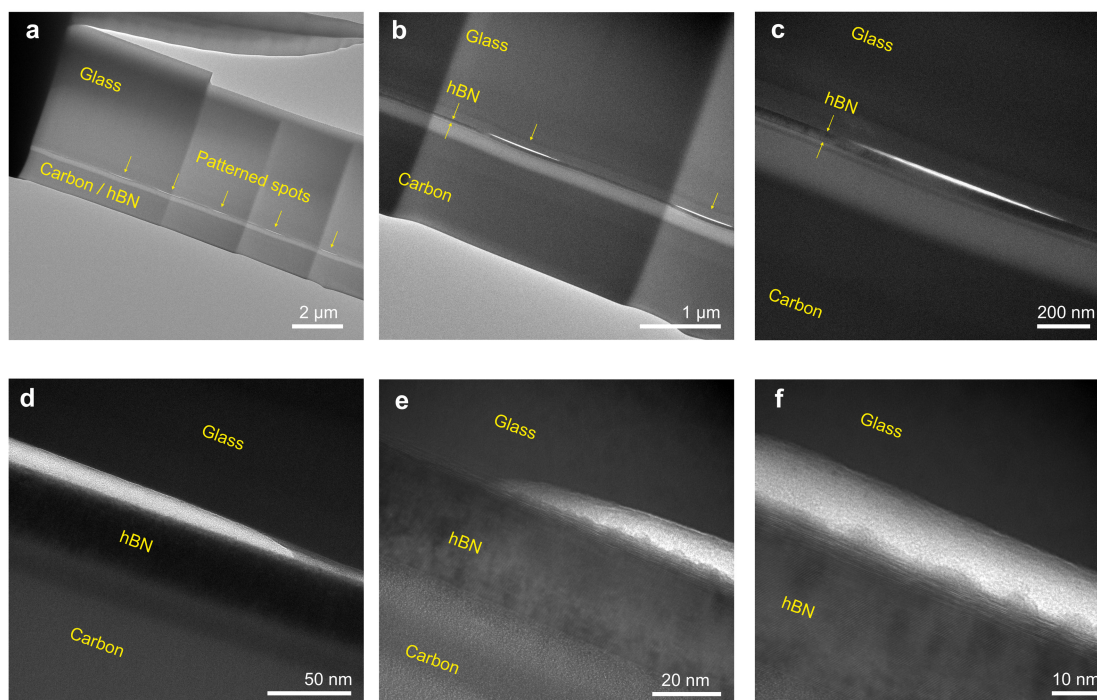


Figure 3.19: **TEM micrographs of FIB-cut hBN lamella.** Each subsequent image a-f) shows a detailed structure of the irradiated cross-section with increasing magnification and focus on the interior of the patterned spots.

Dwell time	100	200	300	400	500	2000	[μ s]
Fluence	1.3E+14	2.5E+14	3.8E+14	5.0E+14	6.3E+14	2.5E+15	[ions/cm ²]
Dose	3.2E-05	6.4E-05	9.5E-05	1.3E-04	1.6E-04	6.4E-04	[C/cm ²]

Table 3.1: Xe ion fluence and dose calculated for various dwell times used in experiments. Calculations were done using the following, widely used in the field^{Huey_2003, Hopman_2007, Thiru2019}, formula:

$$D = \frac{It}{qA}$$

where I is the beam current (constant 100 pA for all experiments), t is the total exposure time, q is the ion charge (for Xe FIB assuming $2.538\text{E-}19$ C which is $1.5\times$ of elementary charge) and A is the exposed area (beam diameter, in our case ≈ 100 nm)

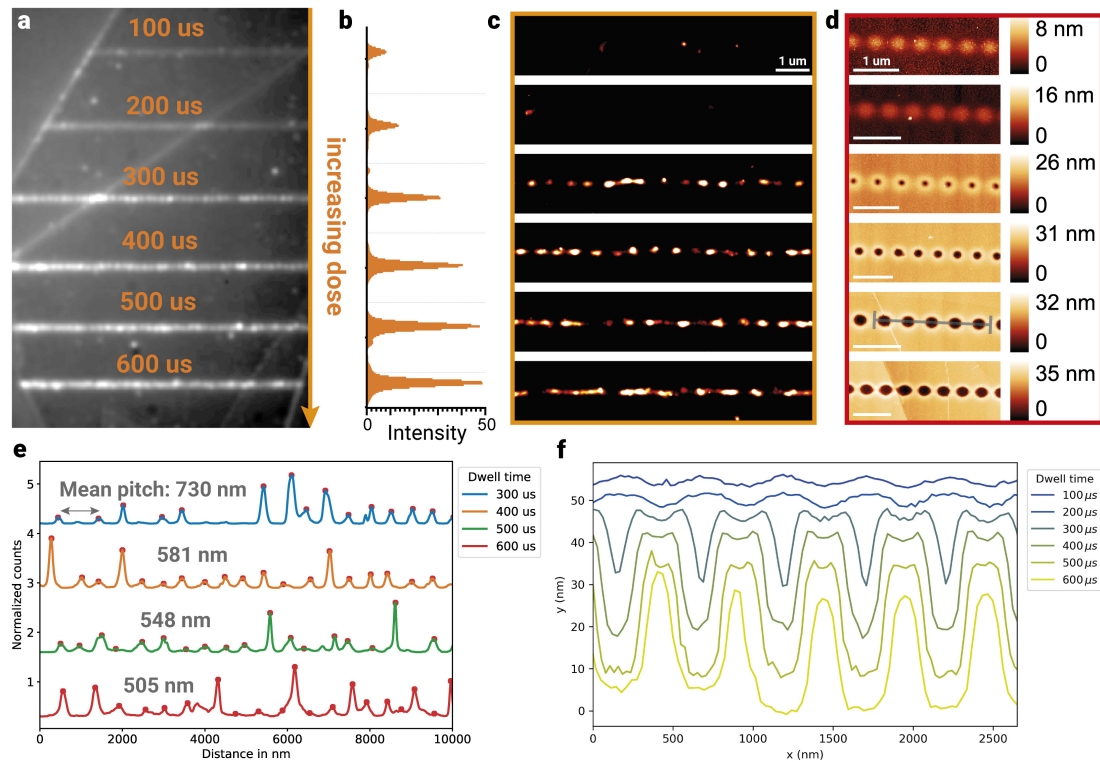


Figure 3.20: Analysis of FIB-induced line patterns of structural and optically active defects.

a) Fluorescence image of an exfoliated hBN flake, with lines of defect sites, induced by the FIB. Irradiation dose increases from the top to the bottom line. In-line pitch: 500 nm. b) Average intensity of each line of defects. c) SMLM images of the defect lines. d) AFM images of the defect lines. Two distinct groups of defects are produced, depending on the irradiation dose: hills for lower doses and holes for higher ones. e) Line profiles of the emitters in (c) with calculated average pitch distance. f) Line profiles of the AFM images in (d). Scale bars: 5mm (a), 1mm (c,d)

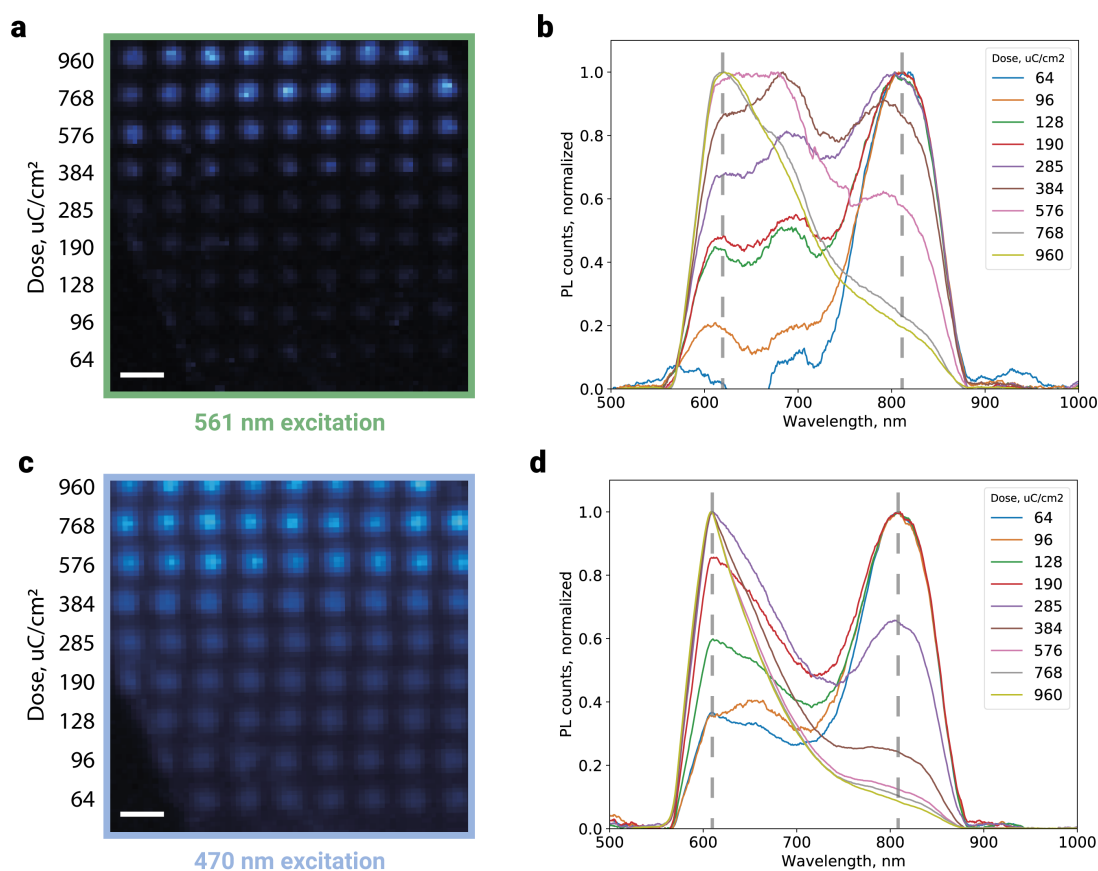


Figure 3.21: **Spectral dependence of fluorescence from induced defects on irradiation dose.** (a) Intensity map of the irradiated hBN flake with irradiation doses varying along the vertical lines (from 64 to $960 \mu\text{C}/\text{cm}^2$), under 561 nm illumination. (b) Corresponding spectra of representative defect sites: the 830 nm emission dominates for low-dose irradiation, while the 610 nm one appears primarily at higher doses. (c-d) Same measurements, performed with 470 nm excitation. Interestingly, here the 610 nm emission peak, seems to be blue-shifted relative to its position at 561 nm excitation. Scale bars: $2 \mu\text{m}$ (a,d)

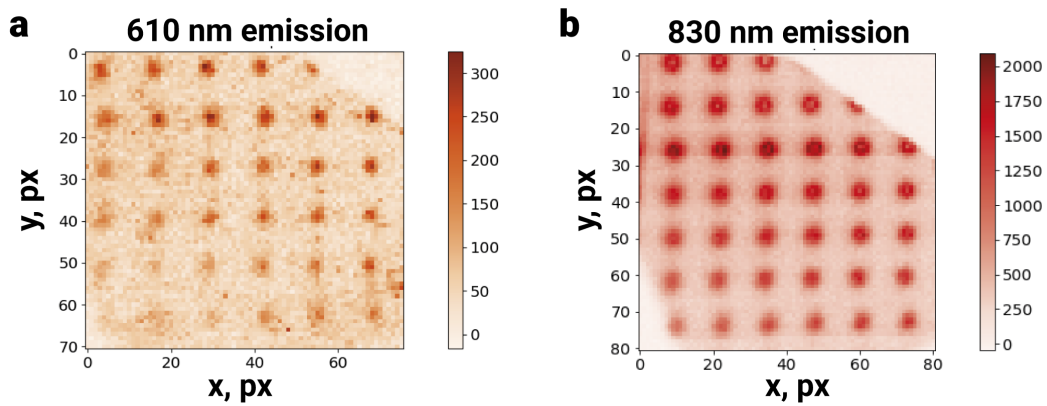


Figure 3.22: **Confocal spectral mapping of produced defects with varying irradiation dose.** Emission pattern at a) 610 nm and b) 830 nm, corresponding to two spectral peaks observed in Fig. 3 in the main text. The emission at 830 nm seems to come from a larger ring around the defect site, while the 610 emission is more localized towards the center. Pixel size: 250 nm

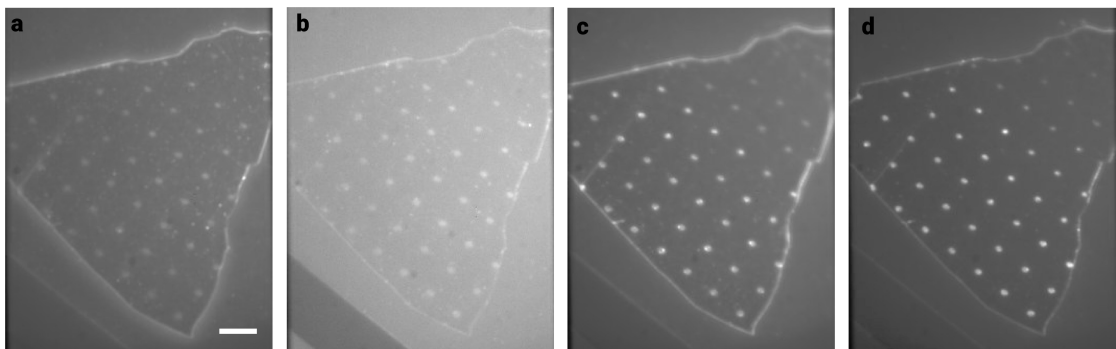


Figure 3.23: **Widefield image of the irradiated hBN flake in air and in liquid.** a) sample directly after irradiation, imaged in air b) sample imaged just after immersion in liquid c) after 10 hours in solution d) after 20 hours in solution. Scale bar: 3 μm

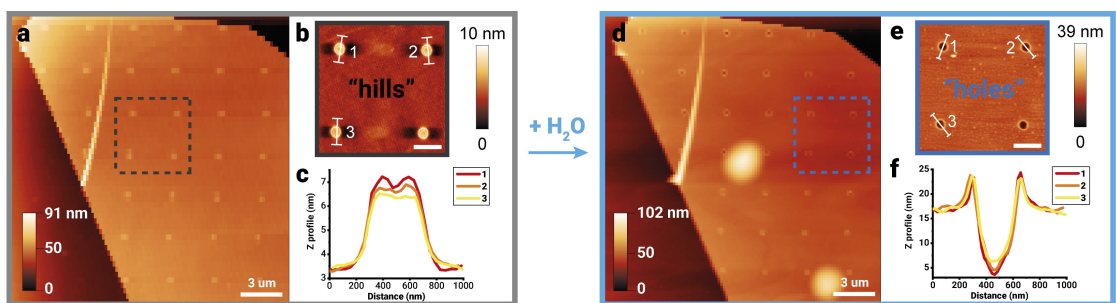


Figure 3.24: **AFM analysis of FIB-irradiated hBN flakes** before (a-c) and directly after (d-f) immersing the sample in water. The hole formation therefore happens on a timescale faster than a single high-resolution AFM scan (≈ 20 minutes). Scale bars: 1 μm (a,d), 500 nm (b,e)

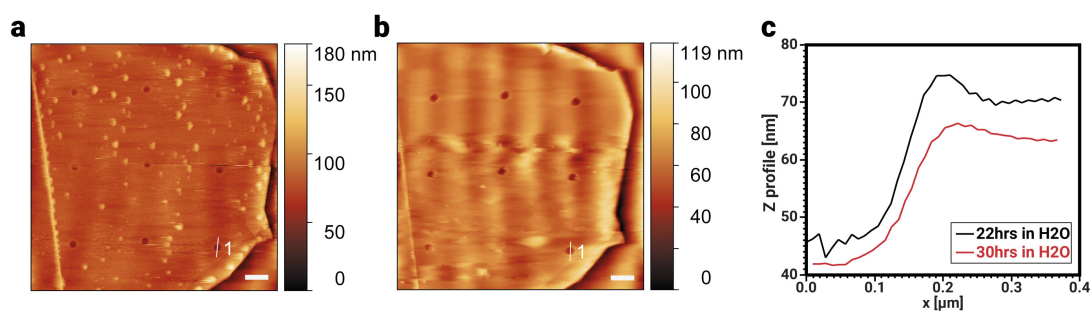


Figure 3.25: **AFM timelapse of the same irradiated hBN flake immersed in water.** a) After 22 hours. b) After 30 hours. c) Height profiles along respective lines in (a, b), showing that the holes are not changing their diameter (≈ 400 nm) much over time. Scale bars: $1\ \mu\text{m}$ (a,d), 500 nm (b,e)

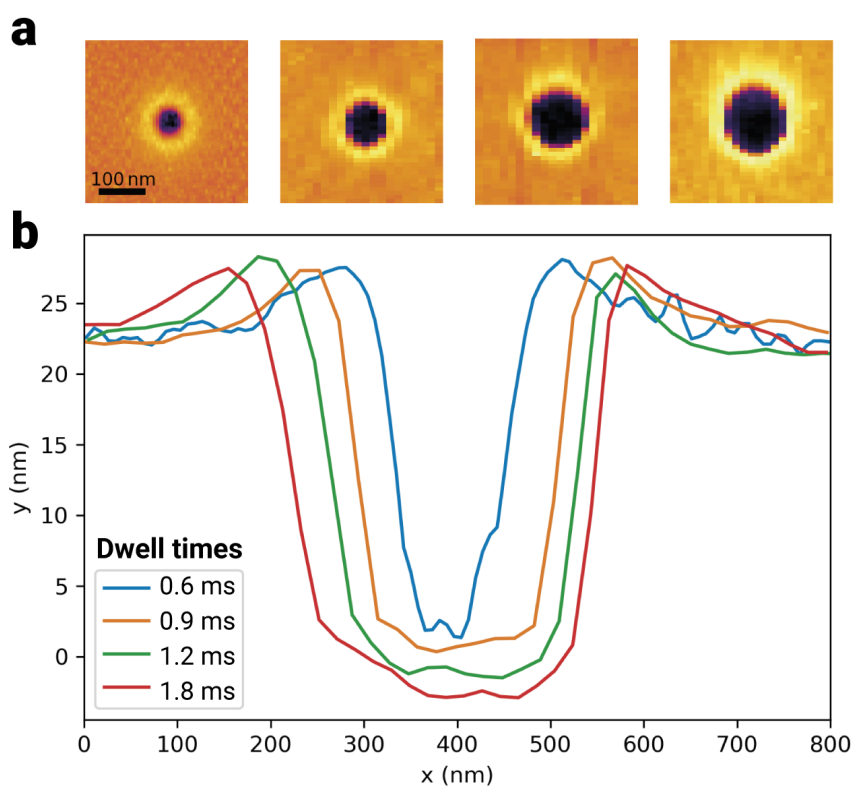


Figure 3.26: **Dependence of hole size on irradiation dose (dwell time).** a) AFM images of isolated holes after water. b) Height profiles of their cross-sections. Scale bar: 100 nm

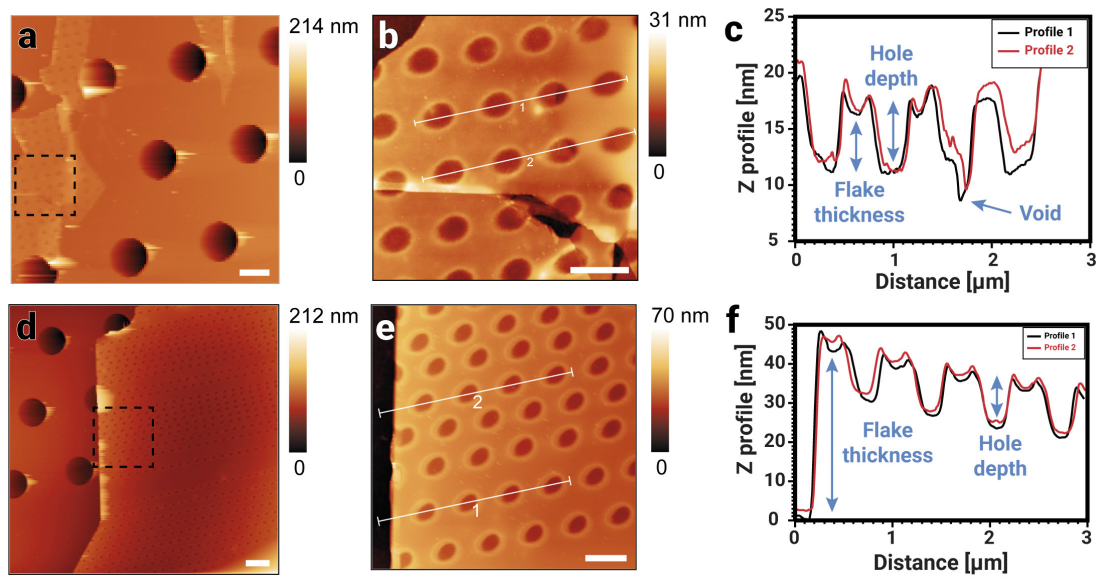


Figure 3.27: **AFM analysis of suspended FIB-irradiated hBN flakes.** a) Silicon nitride TEM grid with a thin hBN flake, irradiated with a 2D array of defects (pitch distance 600 nm, beam current 100 pA, dwell time 1.4 ms). b) Zoom-in into highlighted region in (a). c) Height profiles along respective lines in (b), showing that the flake is fully pierced by the ion beam. d) A thicker hBN flake on the same TEM grid, patterned with the same FIB parameters. e) Zoom-in into highlighted region in (d). f) Height profiles along respective lines in (e), showing that the flake is only partially milled by the ion beam. Scale bars: 1 μm (a,d), 500 nm (b,e)

3.6 Conclusion

This summarizes the deep investigation of applying Xe-ion PFIB system as a defect engineering tool. The ion irradiation was used to explore the nanopore drilling of suspended, monolayer MoS₂ and its application in nanofluidics. Albeit still work in progress, the fine control over the irradiation yield demonstrated in this chapter enabled to map the PFIB parameters and paved the way to more detailed study of tailoring the fabrication to specific pore geometries.

The PFIB nanofabrication capacity was discussed further in the photonics research and enabled to study the defect binding sites in MoS₂ via fluorescent thiol probes as well as photon emitters on hexagonal boron lattice. The patterning of vdW materials demonstrated an interesting and rich application of ion beam as a platform of 2D materials defect engineering and defect characterization tools coupled with super-resolution microscopy.

The next, final chapter is strictly correlated with the ion irradiation methodology discussed here. Nanoporous MoS₂ membranes are irradiated with the discussed here PFIB system and used to study the nanoscale physics of nanopores and atomically thin materials in aqueous solutions.

4 Study of fundamental ionic transport properties of nanoporous membranes

Nanofluidics experiments using nanoporous membranes were mostly done with devices consisting of suspended MoS₂ monolayer films irradiated with Xe ions. All experiments were performed on homemade setup with the flowcell specifically designed to allow applying AC/DC signals as well as hydrostatic pressure pulses through the membrane to ensure proper wetting (through pressure-induced wetting described in details in the next section) and directly measure properties such as membrane capacitance or ionic current rectification. The pressure setup enabled study of artificial mechanosensitivity induced by small nanopores as well as peek into physics of osmotic power generation with highly porous membranes. These studies however uncovered unexpected issues such as pore-obstructing nanobubbles, MoS₂ adhesion problems such as delamination and wrinkling and consequent nanopore clogging. Work presented here is of high relevance to the nanopore research field. Most of these events cannot be identified without using additional pressure probe and can be misinterpreted as an actual, expected signal instead of an artifact or a device failure.

4.1 Experimental setup

The following section is based verbatim on the following publication:

Sanjin Marion^I, **Michal Macha**^I, Sebastian J. Davis^I, Andrey Chernev^I and Aleksandra Radenovic^I

Wetting of nanopores probed with pressure, *Phys. Chem. Chem. Phys.* 2021.

*S. M. designed and built the experimental set-up and designed the study. **M. M. designed the microfluidic chamber.** S. M. and **M. M. performed the experiments.** A. C. fabricated the devices, transferred and prepared MoS₂ devices. **M. M. grew the MoS₂.** A. R. initiated and supervised the research. S. M. analyzed the data, made the FEM model and wrote the manuscript. All authors provided important suggestions for the experiments, discussed the results, and contributed to the manuscript.*

Technical details available in the full manuscript, available online.

All experiments discussed here were performed using homemade flowcell setup designed to apply high hydrostatic pressure (up to 8 bar) on nanopore membranes. A closed microfluidic chamber was made of PEEK and PTFE components to sustain pressure in excess of 10 bar and minimize water evaporation and gas permeation (Fig. 4.1a).

The sample is placed between the two halves of the chamber and sealed using two nitrile O-rings. On each side of the chip there are three fluid pathways: one for an electrode, one for a fluid inlet, and one for a fluid outlet. On both outlets exchange reservoirs are placed onto which compressed gas with pressures up to 7 bar is applied using a microfluidics pressure controller which is also used to measure the applied pressure P . The design has minimal crevices and corners to minimize bubble formation during filling of the chambers⁴⁶³. Filling of the chamber is done with solutions which have been degassed from dissolved ambient air in the connecting fluid pathway using a degassing tube so they are undersaturated with gas. We find that any mixing of the solution or contact with ambient air results in significant gas absorption, regassing the liquids.

Keeping the solutions degassed during experiment is indeed crucial in order to obtain repeatable and reliable results. With pressure setup we have proved, that wetting issues caused by improper pore wetting (e.g. due to nanobubble residing around or directly over the nanopore opening) can manifest as ionic conductance artifacts. Pressure, applied on frontside, backside or from both directions simultaneously (compression) can identify and remove nanobubbles or other wetting artifacts thus allow a reliable tool for probing the state of nanopores.

By applying a voltage bias between the two Ag/AgCl electrodes on different sides of the membrane we are able to measure current passing through the nanopore (Fig. 4.1b). In addition, we apply a sinusoidal set voltage (AC) and measure the corresponding current

^ILaboratory of Nanoscale Biology, Institute of Bioengineering, School of Engineering, EPFL, 1015 Lausanne, Switzerland

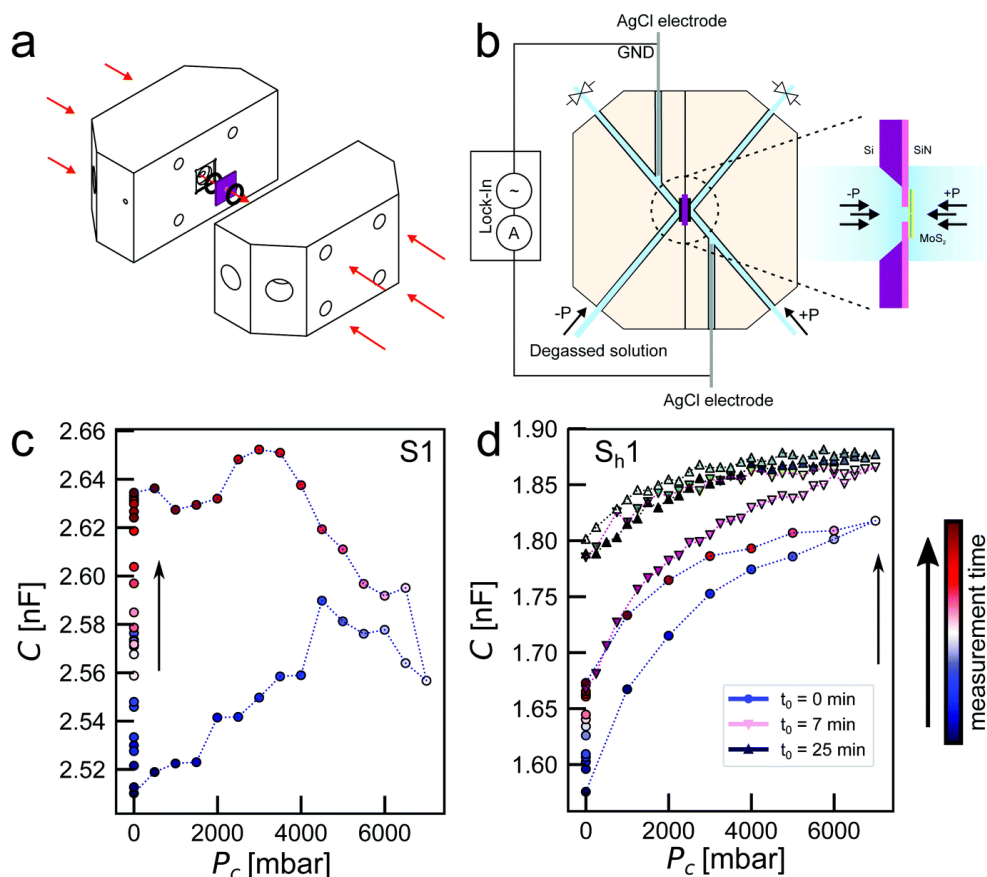


Figure 4.1: **Applying pressure to solid-state nanopores.** (a) Diagram of the sample chamber. (b) Simplified diagram of the fluidic and electrical connections. (c) Capacitance of a partially wetted supported membrane of $\approx 20 \times 20 \mu\text{m}^2$ and 20 nm thickness as a function of applied compression pressure during the wetting process (sample S1). The pressure P is swept from 0 to 7 bar, with intermediate steps at $P = 0$ to check for changes in the baseline value of the pressure. The solution was 1 M KCl Tris buffered to pH 8. Colours of the points go from blue (first measurement) to red (last measurement) in a continuous fashion, as marked by the arrow. The measurement took about 5 minutes. (d) The same as in panel (c) except the chip has a smaller supported membrane size of $\approx 12 \times 12 \mu\text{m}^2$ and the chip was coated with a hexamethyldisilazane (HMDS) before use to make the surface more hydrophobic and was not cleaned in any way afterwards. A series of three consecutive measurements are provided with start times at t_0 . The first measurement took about 5 min, the last two lasted for about 10 min.

using a phase sensitive amplifier (lock-in). This allows the use of the delay in the AC signal to calculate the capacitance of the membrane. We assume the simplest case of a parallel connection of a capacitance C and resistor R_{ac} , where the resistance R_{ac} corresponds to the resistance of the pore R as obtained at DC values when the frequency of the AC signal is kept at around 1 Hz. In reality the frequency response of a membrane has other contributions but they are only relevant at higher frequencies^{179,464} with a flat plateau at sufficiently low frequencies where measurements are conducted. For 20 nm thick suspended silicon nitride membranes in the size ranges of 10×10 to $50 \times 50 \mu\text{m}^2$ which we use here we obtain the

expected values for the capacitance on the order of ≈ 1 nF (in 1 M KCl Tris buffered to pH 8)⁴⁶⁴ and proportional to the supported membrane area.

The microfluidics chamber allows the application of hydrostatic pressure in a gradient condition ΔP , with a positive pressure gradient defined as pressure applied from the front side of the membrane, and negative from the back side (Fig. 4.1b). It also allows applying compression pressure P_c on both sides of the membrane simultaneously. Applying pressure on one or both sides of the chip is used as an additional probe of the system. We alternate between no applied pressure $P = 0$ and a cycle of pressures P_i going from $P_0 = 0$ to $P_i = P_{max}$, and back down to $P_i = 0$. In the case that a gradient of pressure is applied, negative (backside) pressures are also applied following the same procedure. This allows the detection of any hysteresis in a measured response to the pressure and if the base value at $P = 0$ is changing during the measurement. During the pressure cycle either the current response to a bias voltage or the resistance and capacitance using an AC response are measured. The representative value is measured after a sufficient settling time.

Compression of solutions, especially ones under-saturated with gas, has been shown to be comparable in effectiveness to alcohol wetting⁴⁶³. To demonstrate this and to prove proper wetting of membranes, the amount of surface area of the membrane in contact with the liquid is monitored via the membrane capacitance C . An example measurement of capacitance for several sweeps of compression pressure is shown on Fig. 4.1c and d for a hydrophilic and a hydrophobic surface. As pressure is applied to a under-saturated solution the baseline value of C , at intermediary $P = 0$ steps in the sweep protocol, increases throughout the protocol. In the case of solid state nanopores the largest contribution to the capacitance at low frequencies is known to come from the suspended membrane itself⁴⁶⁴. If part of the suspended membrane with a surface area ΔA is not wetted, i.e. there are bubbles or air patches present, then the total capacitance of the membrane will be reduced by an amount $\Delta C \approx \Delta A$. In that sense, the increase of capacitance as pressure is applied is interpreted as the membrane being wetted and gas from the bubbles being absorbed into the liquid which was under-saturated with gas. Hydrophilic membranes fill fast, within tens of seconds of applied compression pressure with a degassed solution which is undersaturated with dissolved gas, while hydrophobic pores sometimes seem to have remnants of bubbles left on the surface (Fig. 4.1d). In contrast if a non-degassed solution is used, we report that the capacitance often returns close to its original value, implying that if the solution is saturated excess dissolved gas can return to the membrane in the form of gas bubbles, or that the bubbles are impervious to absorption. In all the following measurements the membranes were flushed with degassed solutions and compression pressures of up to 7 bar were applied for ≈ 5 minutes to ensure proper wetting.

4.2 Wetting artifacts

We interpret the wetting issues as a nanobubble pinned on the membrane, obstructing the pore entrance which, depending on the membrane surface conditions, can be reabsorbed

by compression pressure and/or high voltage electrowetting (not applicable to 2D materials, detailed wetting mechanism is shown in Appendix Fig. A.4) or moved by front- or backside pressure induced flow (Fig. 4.2a and b). If the nanobubble is present in our system, typically after positive-negative pressure sweep we see a characteristic, non-linear IV shapes and dynamic changes in membrane resistance which we attribute to obstruction being moved out of the pore vicinity. The permanence of this bubble state depends on the gas remnants in the solution and possible bubble nucleation sites on the membrane surface.

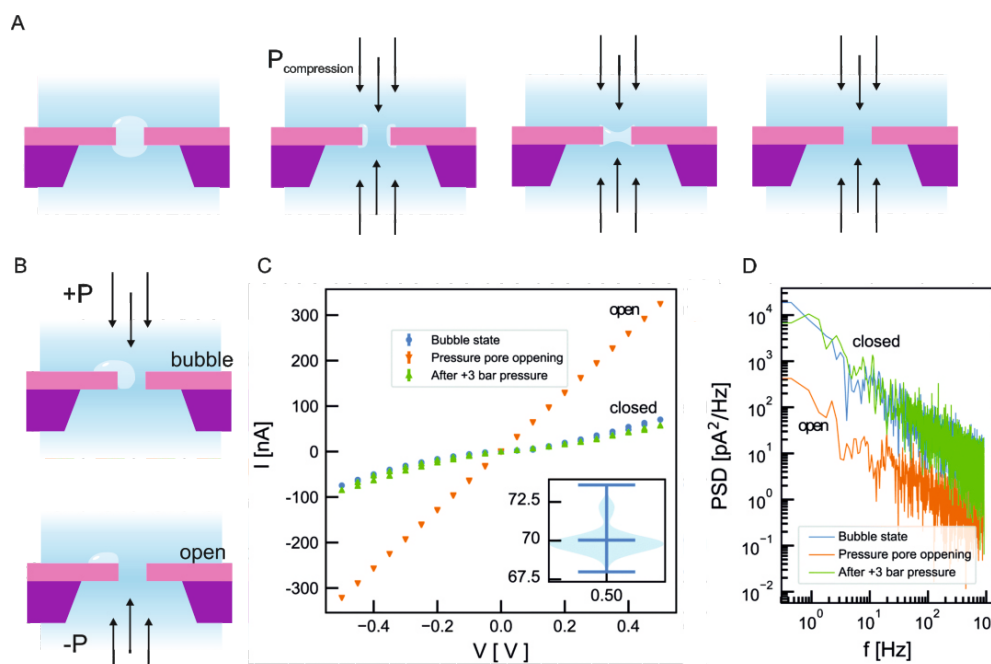


Figure 4.2: Pressure and voltage wetting of a nanopore. (a) Schematic diagram of an unwetted pore based on the electrowetting model, same can be accomplished by applying compression pressure. (b) Model of the hypothesized nanobubble wetting behavior with different applied pressure gradients. An example of wetting a hydrophobic pore obstructed by a bubble: (c) IV curve of a bubble inside a $d \approx 75$ nm diameter nanopore before applying pressure (blue), after opening with pressure (orange), and after closing with pressure using +3 bar (green). The resistance of the open pore is found to be $R = 1.61 \text{ M}\Omega$ which is within 10% of the expected resistance of the nanopore in 1 M KCl Tris buffered to pH 8. Inset shows the extrema and probability density for current fluctuations at $V = +0.5 \text{ V}$ for the bubble state. (d) Power spectral densities of the current traces at +0.2 V from panel (c).

To differentiate between wetting-dewetting transition and nanobubble obstruction we study the noise level, the dependence of the resistance on pressure, and the presence of ionic current rectification. The current power spectral density (Fig. 4.2b) is consistent with previous works predicting that nanobubbles in solid state pores increase the noise level¹¹³. The noise power spectral density (PSD) at frequencies below several kHz is dominated by flicker noise, which is known to scale with frequency as $S \approx Af$ with ≈ 0.5 – 1.5 and A the flicker noise amplitude^{465–467}. We find the flicker noise level in all the samples presenting bubble issues to be slightly higher than ideal for such samples^{113,465,466}. As the flicker noise amplitude is

expected to scale according to the empirical Hooge relation⁴⁶⁸ such that $A \approx I^2$, care needs to be taken when comparing power spectral densities. The flicker noise amplitude has also been predicted to increase in the case of wetting issues⁴⁶⁹. We notice several pressure induced behaviors in our measurements. First, the noise would sometimes increase or decrease after applying a pressure gradient, probably depending on if the pore was wetted or dewetted with the pressure. Secondly, we note that in some cases a decrease of resistance after applying pressure was followed with an increase in flicker noise amplitude. We speculate that the nature of the flicker noise will most likely depend on the surface charge of the air bubble, its shape, and position within the pore. For example if the bubble is changing the resistance dominantly from obstructing the pore channel or the access area to the pore, the contributions to the flicker noise will be different⁴⁶⁸, with predictions that the surface contribution is more pronounced than the bulk contribution in nanopores smaller than 20 nm. We conclude that the noise level can strongly vary based on the position and shape of the obstructing bubble, with the lowest possible noise level only achieved once the whole pore region is completely wetted^{466,469}. Based on the available literature on surface nanobubbles⁴⁷⁰, and the AFM study on nanobubbles pinned next to pores in 2D materials⁴⁷¹, we would expect the surface nanobubbles to be below $\approx 1 \mu\text{m}$ in size and no smaller than $\approx 50 \text{ nm}$.

4.2.1 Wetting of MoS₂

To demonstrate nanobubble-related artifacts on 2D materials, a single layer MoS₂ supported on the $\approx 75 \text{ nm}$ diameter pores in 20 nm thick silicon nitride is used. An example of measurements obtained on a TEM drilled MoS₂ nanopore with several $\approx 2 \text{ nm}$ pores are shown on Fig. 4.3. Only degassed solutions of 1 M KCl Tris buffered to pH 8 were used and compression pressures of up to 7 bar were applied while filling the nanopore until the measured capacitance of the membrane C stabilized. The IV response of the nanopore is shown on Fig. 4a. This IV curve shape was persistent for one day of measurements, with fluctuations in the IV curves initially reducing after several hours and the flicker noise increasing. The shape of the IV curve indicates a pinned bubble at the pore entrance and wetting/de-wetting, non-linear behaviour (more details in Appendix Fig. A.4).

As the TEM-imaged size of the pore is above the size where any hydration layer or single ion effects could take place, we attribute this state to a wetting issue. After flushing with degassed solution the pore exhibited a linear IV curve corresponding to a resistance of $R = 4.6 \text{ M}\Omega$, or a pore in MoS₂ of diameter $d \approx 20 \text{ nm}$ (Fig. 4.3b). Details about MoS₂ pore size calculations are provided in the Supplementary Figure 4.4. The pore was then probed with a pressure sweep of $\pm 4 \text{ bar}$ to test the stability of the pore resistance. The pore resistance was consistent. At this point the influence of using an alcohol wetting technique was investigated. To do so a solvent exchange procedure²⁷ was performed in which a liquid of higher gas capacity (i.e. alcohol) is exchanged for one of lower gas capacity (i.e. water). A simplified explanation is that in this case the first solvent due to its higher affinity for the hydrophobic surface and higher gas capacity acts as a catalyst for nucleation of gas bubbles. The solution in the chamber was exchanged to

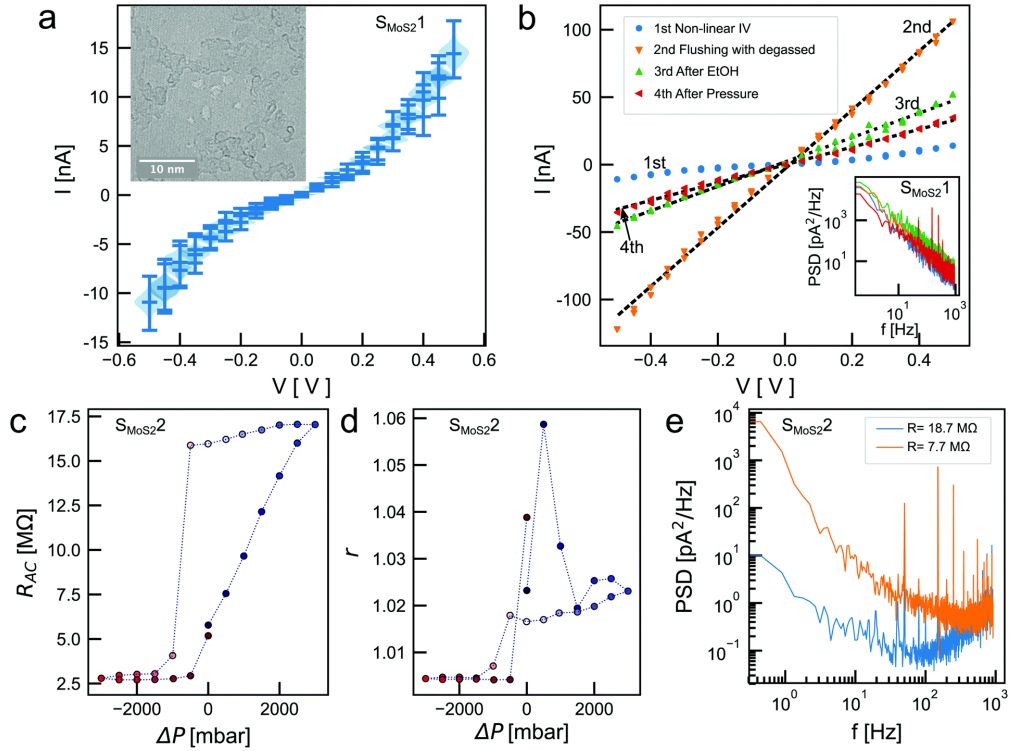


Figure 4.3: Wetting of nanopores in single layer MoS₂ membranes. (a) Stabilized IV curve of an MoS₂ sample (S_{MoS₂ 1) after 1 day of measurements. The plot bars show the extrema of the current distributions, while the width of the plots represent the probability density for the measured current level at that voltage. Inset is an TEM micrograph of the drilled pores located above the supporting ≈ 75 nm diameter nanopore in silicon nitride. (b) Change of IV curve after wetting with freshly degassed solution from the value shown in panel b (blue circles) to a linearized IV curve (orange, flushing with degassed). The dashed line represents a linear fit giving a resistance of $R = 4.8$ MΩ. After a solvent exchange (from 1 M KCl Tris buffered to pH 8 to 50% ethanol 50% water and back to degassed 1 M KCl Tris buffered to pH 8) is performed the resistance of the nanopore increases (dashed line through green points is a linear fit giving a resistance $R = 11$ MΩ). After further pressure and voltage is applied the resistance further increases to $R = 15.2$ MΩ (“After pressure”, red points). Inset shows the current noise power spectral density for the IV curves in panel (b) at a +0.2 V bias. (c) AC measured resistance R_{AC} versus pressure gradient ΔP for MoS₂ sample S_{MoS₂ 2. (d) AC measured ionic current rectification r versus pressure obtained simultaneously as the measurement in panel (c). (e) Ionic current power spectral density before and after pressure sweeps for S_{MoS₂ 2. The noise spectrum is given for a state of resistance $R = 18.7$ MΩ, measured at a state before a pressure gradient was used to switch it to the stable ($\Delta P = 0$) state in panel (c), and $R = 7.7$ MΩ after the pressure sweeps. The noise spectra were obtained under a DC voltage bias of +0.2 V.}}}

50% ethanol/water mixture, twenty minutes of equilibration time was allowed followed by an exchange back to degassed 1 M KCl Tris buffered to pH 8. The solvent exchange procedure increased the resistance of the nanopore to $R = 11$ MΩ (calculated pore diameter $d \approx 9$ nm) while retaining a linear IV curve. The flicker noise amplitude A remained the same during all these procedures (Fig. 4.3b inset), but taking into account the empirical von Hooge relation⁴⁶⁸

$A \approx 12$ implies that the 2nd curve has the lowest noise as it supports the largest current at a fixed potential V (lowest resistance), and thus the best wetting. The linearity of the curve is in contrast with previous observations where bubbles were shown to produce rectification of the ionic current⁴⁷². A further application of compression pressure of 7 bar did not change the resistance, but a pressure gradient sweep in the range $P = \pm 3$ bar changed the resistance to $R = 15.2 \text{ M}\Omega$ or a calculated pore of diameter $d \approx 7 \text{ nm}$. In this case the rectification did not change, as seen in the linearity of the IV curves. Further flushing with degassed solution reduced the resistance to $\approx 2 \text{ M}\Omega$ (close to the value of $1.5 \text{ M}\Omega$ for the supporting nanopore of 75 nm) and was accompanied by a large reduction in the noise level at low frequencies. The potential differences applied on the sample never exceeded $\pm 0.5 \text{ V}$ as higher voltages can cause an electrochemical induced opening of MoS_2 pores⁶. We hypothesize that the MoS_2 was punctured from the start or damaged during one of the flushing procedures and that all measurements except the 2nd (after flushing with degassed solution) were of improper wetting of the pore. Notably, the resistance of this pore was changed, with degassed solutions decreasing it and alcohol wetting increasing it, all at a constant level of flicker noise.

Fig. 4.3c shows another MoS_2 sample ($S_{\text{MoS}_2 2}$) which was switched between a high ($R_{ac} \approx 16 \text{ M}\Omega$, $d \approx 7 \text{ nm}$) and low ($R_{ac} \approx 3 \text{ M}\Omega$, $d \approx 30 \text{ nm}$) resistance state but with a stable state at no applied pressure ($R_{ac} \approx 6 \text{ M}\Omega$ at $\Delta P = 0$). Raw timetrace of applied pressure steps and measured R , C and r is shown on Figure 4.10. In the high resistance and intermediate state the ionic current rectification was increased (Fig. 4.3d), indicating as previously the presence of a bubble. A comparison of the noise before any pressure was applied and after pressure sweeps (Fig. 4.3e), indicates that the noise level in the system was increased in the low resistance state. A plot of the scaling of the flicker noise amplitude versus current supporting this is provided in Supp. Fig. 4.6c. In addition, we performed a streaming potential measurement showing stable fluid flow between two sides of the membrane through the pore before and after this pressure dependent switching (see Supp. Fig. 4.6d). We interpret this as the bubble changing in size or position, and influencing the noise level at low frequencies. This is consistent with the theory of charge binding/debinding at the bubbles surface being responsible for the low frequency flicker noise⁴⁶⁸, where changing the amount of surface area exposed to the solution and its properties, e.g. liquid–gas or liquid–solid interface, would change the noise spectrum. Additional data on three more samples is provided in the Supplementary Information, out of which two have been imaged prior to measurements. Fluctuations between linear and nonlinear IV curves are found to be common, and a lower level of the noise power spectral density is not a good measure of bubbles being absent. As with the results from the previous section, the flicker noise can be larger in smaller pores. The gradient pressure clearly shows the ability to change the state of the pore, while compression pressure only changes the state of the pore when a freshly degassed solution is used. One could argue that pressure gradients are damaging the MoS_2 and opening up pores. The total force applied on the 75 nm diameter exposed MoS_2 is $\approx 1.5 \text{ nN}$ at 3 bar which is orders of magnitude smaller both than typical forces applied in atomic force microscopy indentation experiments⁶⁶ and forces required to delaminate MoS_2 ⁴⁷³. We also note that the 20 nm thick supporting silicon nitride membrane

can break due to applied pressure gradients at $\approx 5\text{--}7$ bar only if the membrane area is larger than $\approx 30 \times 30 \mu\text{m}^2$. That being said even if the MoS_2 is being enlarged, it does not modify the observations that bubbles are present and can produce both linear and nonlinear IV curves of varying noise levels. The resistance of the pore comes from two series connected terms¹¹⁵, one being the resistance of the pore interior and the other from the access area. This access area contribution to the resistance and noise is larger for smaller pores^{115,468}, and we speculate that a bubble obstructing the access area could have a lesser contribution to the noise level than one which has entered the pore interior.

We note that all measured MoS_2 samples show similar pattern. All samples show apparent resistances at low voltages (± 0.25 V) indicating either smaller pores than imaged (samples $S_{\text{MoS}_2}1$, $S_{\text{MoS}_2}4$) or pores in materials which were known to have no pores ($S_{\text{MoS}_2}3$). One could naively use this resistance value to infer nanopores in the ≈ 1 nm range if only ionic current measurements were used. At higher voltages they present nonlinear conductivity with the same pattern as seen in the wetting of hydrophobic pores (Fig. 4.2c). This nonlinear conductivity disappears after flushing with degassed solution and compressing with pressure. The resistance of the pores can be reduced by applying negative pressure inducing fluid flow from the back side to the front side of the membrane, and increased by applying positive pressure. This is consistent with the bubble being present on the side of the membrane onto which MoS_2 was transferred, as negative pressure (from the back side) would then move the bubble away from the pore opening. A recent study on nanopores in supported graphene using atomic force microscopy demonstrated that bubbles in the ≈ 100 nm size range are common and can increase the resistance of the pore and provide a nonlinear signal⁴⁷¹, which we interpret as wetting issues similar to the non linear curves obtained in Fig. 4.2c, and 4.3b. The explanation given for this process is that it stems from the use of solvent exchanges from alcohol to aqueous salt solutions, identical to the procedures performed in this study to increase the resistance of the MoS_2 pore (Fig. 4.3b). We conclude by induction that the most probable explanation of such effects is the presence of a bubble in the nm-size range at the nanopore entrance with the supported MoS_2 being damaged either before or during wetting.

The possible causes for nanobubbles being stable on the 2D material surface remain to be explained. It is clear that a basic requirement is that the surface of the material be at least mildly hydrophobic⁴⁷⁰. 2D materials like graphene, MoS_2 , hBN have contact angles which can be larger than the minimum reported for generation of stable nanobubbles on surfaces. This will highly vary on the sample quality and type of supporting surface^{470,474–476}. Nanobubbles have been directly visualized so far only on graphene⁴⁷¹. Another possibility is contact line pinning of the nanobubble to the surface via any surface defects or contaminants which have been shown to stabilize the bubbles and aid growth^{470,477}. Contaminants on 2D material surfaces are a common occurrence in typical methods of transfer from growth to supporting surfaces which involve the use of some form of polymer based stamp^{90,177,314,478}. The degree of contaminants has been reported to be significantly reduced if a polymer-free transfer method is used.⁷³ Usually polymers used for transfer involve PMMA or hydrophobic PDMS. In the case of PMMA, while a homogeneously smooth coating is not expected to support nanobubble

pinning, patches are expected to⁴⁷⁹. The MoS₂ samples in this study used a PMMA stamp based transfer method which is known to leave hydrocarbon residues. This is also confirmed by electron micrographs of the samples (TEM images of three MoS₂ samples provided in the Supplementary Information). Nanobubble nucleation at surfaces has been shown to be possible even at low levels of overgassing (100–120%) with a temperature change of a few degrees around room temperature inhibiting or promoting nanobubble formation⁴⁸⁰. The presence of nano-pits or crevices has been found to increase nanobubble stability^{481,482}, large holes in supported 2D membranes would play this role in the nanopore system. The mechanism of nanobubble nucleation and stability on 2D materials is something which would require further study.

4.2.2 Microfluidics chamber

The microfluidic flow-cell was designed to accommodate 5 × 5 mm Si/SiN_x membrane devices under high working pressure and closed salt solution circulation providing precise pressure control, electrical and thermal insulation. All flow-cell components in contact with the fluid are made from polyether ether ketone (PEEK). Fluid connections to the flow-cell are made with PTFE tubing and connections made with HPLC grade ferrules and fittings. The fluidic pathways are sealed with mechanical shut-off valves. All liquid exchanges are done by flushing liquid through these fluidic connections using Luer-lock syringes. Liquids are degassed by pushing the fluid first through a 4 ml internal volume degassing hose (Biotech Fluidics BT-9000-1549) connected to a vacuum pump at 10 mbar absolute vacuum. Nitrile O-rings were used to ensure sealing of the chip between the two halves of the chamber. The internal volume of each side of the chamber is 0.125 ml so we always performed exchanges of solutions by flushing at least 2–3 mL of liquid through each side of the chamber, with added pauses to ensure proper mixing even in dead areas without flow. The flow-cell was cleaned by 20 min sonication in 70 °C MiliQ water (18.2 MΩ cm¹, 200 nm filtered) to dissolve any remnant salt crystals, then for 20 minutes by sonicating in isopropanol to remove any greasy residues, then for at least two 20 min sonications in MiliQ water before drying overnight at 70 °C. The chamber and the O-rings were treated with oxygen plasma for 30 s to make the surface hydrophilic prior to use. Chlorinated Ag/Cl electrodes were sealed using the same fittings and ferrules as the connecting tubing. To ensure there are no air pockets near the electrodes they were partially unscrewed and liquid in the chamber was used to push any air out.

4.2.3 Measurements

All electrical measurements were done using a Zurich Instruments MFLI lock-in amplifier with the MF-DIG option. Both DC and AC bias was applied using the signal output of the instrument, while the current through the sample was measured using the built in current to voltage converter. All DC (AC demodulator) signals were sampled at 1.83 kHz (1.6 kHz) and acquired using the MFLI lock-in amplifier. The input noise used by the amplifier depended on the current input range used and was generally below $200 \frac{fA}{\sqrt{Hz}}$. All measurements were

done inside a Faraday cage. Note that the presence of mains line noise in some of the current spectral power densities was because a short coaxial cable was used between the Faraday cage and MFLI instrument, which coupled with the connection for signal output from the lock-in produced a ground loop. All DC IV curves were recorded in a sweep from 0 to +V, down to V and back to 0 to ensure any hysteresis is visible. Thus, for all set voltage values, except the highest and lowest, two points are shown on all figures. Pressure was applied and controlled with 99.99% nitrogen using a 7 bar FlowEZ microfluidics pressure controller (Flugient). All interfacing with the measurement instruments was done using a custom made program in LabVIEW. All measurement data was analysed using a custom made script in Python using SciPy signal analysis tools⁴⁸³.

All electrical measurements performed while sweeping the pressure were done after the pressure level has stabilized to at least 5% of the target value. In the case of DC current measurements an additional wait time of 1 s was performed after the pressure settling. In the case of lock-in measurements the wait time was 15 times the lock-in base time plus 2.5 s. The base time constant used was usually 300 ms to 1 s for an AC signal at 1 Hz, which was a compromise between the speed of measurements and measurement precision. Pressure measurements and electrical measurements were synchronized only within ≈ 0.25 s which was taken into account during the analysis.

We used 1 M KCl with 10 mM Tris buffered to pH 8 for all conductance measurements. All buffers were prepared using MiliQ grade water ($18.2 \text{ M}\Omega \text{ cm}^1$). The conductivity of all solutions was checked before use with a Mettler-Toledo FiveEasy Plus. For solvent exchange we used a 50%/50% mixture of Ethanol and MiliQ water with a measured conductivity of $\approx 10 \mu\text{S cm}^1$. All solutions were filtered through a 20 nm filter before use (Whatman Anotop 25 plus).

4.2.4 Supplementary information

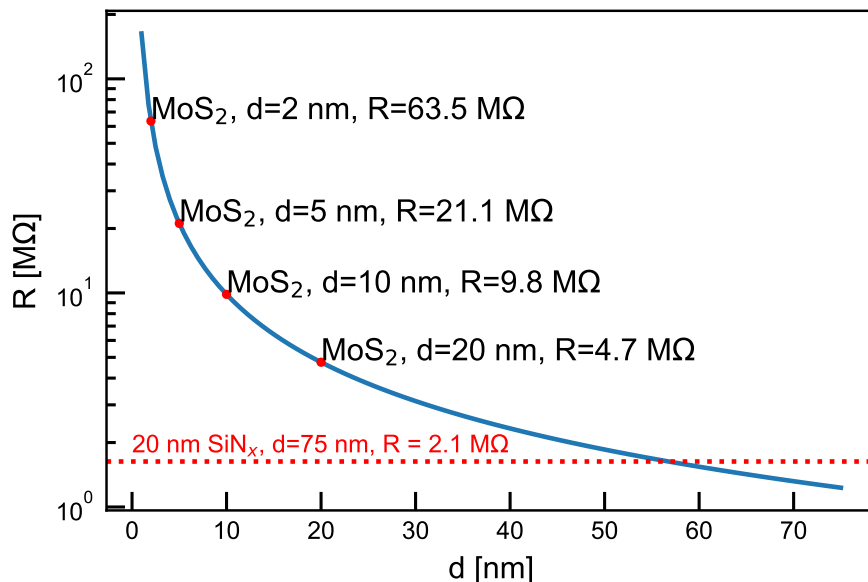


Figure 4.4: **Dependence of a MoS₂ nanopore resistance R versus diameter d .** Dependence of a MoS₂ nanopore resistance R versus diameter d . MoS₂ is taken to have a thickness $L = 0.615$ nm. The solution conductivity is taken to be 110 mS/cm.

Sample S_{MoS₂} 1: The sample was imaged in TEM and drilled to have several pores of several nanometers in diameter (Fig. 4.5). The pore was filled with degassed 1M KCl buffered at pH8 as described in the main text. After the application of 7 bar compression pressure for several minutes it demonstrated a fluctuating nonlinear IV curve (Fig. 4.5b) which relaxed in time to a higher resistance and noise level matching the trends shown in the first IV curve (Fig. 4.5c). After about 12h of wait, the system exhibited a stable and more conductive nonlinear IV curve (Fig. 4.3a in the main text), which was then linearized with compression pressure and flushing with fresh degassed solutions (Fig. 4.3b). After that a solvent exchange with ethanol was performed which increased the resistance. Application of a pressure gradient in this state indicated that there were further wetting issues.

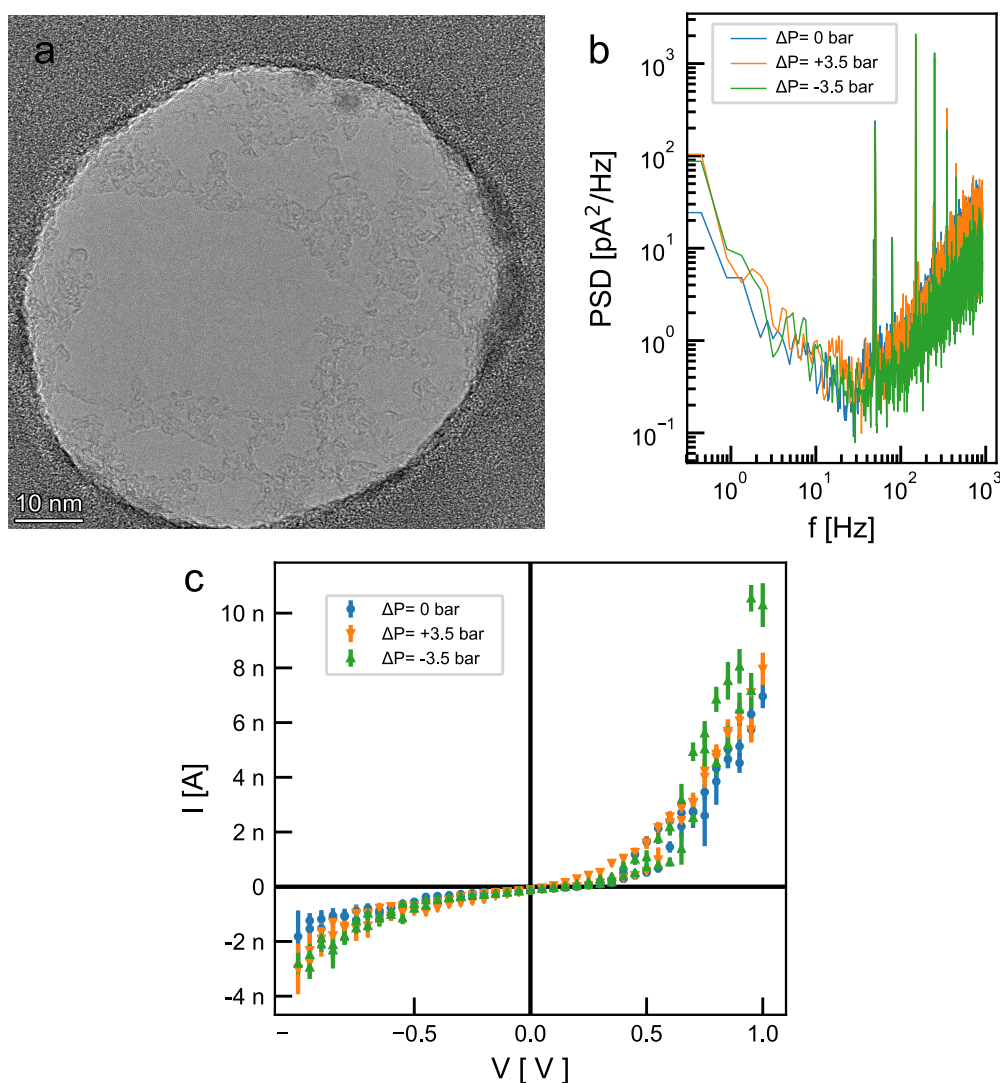


Figure 4.5: **Sample S_{MoS₂} 1 1**: a) Transmission electron microscope images of MoS₂ sample before measurements. Imaged with FEI TEM Talos at 80 kV in HRTEM mode. Visible nanopores were drilled by beam condensation with in-situ control of the pore formation. b) Immediately after filling and a day before the measurements in Fig. 4.3a,b of the main text. The bars denote extrema of the current probability density distributions, while the shapes denote the probability density for finding the current at that value (violin plot). The amplifier range was limited to measuring ± 10 nA. c) Time evolution of the IV curve from panel b. During this time the IV curve was let to settle with no disturbances. Further applications of pressure in the range of ± 3 bar did not change the IV curve shape. If one were to extrapolate the resistance of these pores in the ± 0.2 V range one would obtain resistances (and effective MoS₂ diameters) of 140 M Ω (1.1 nm) and for the last two curves 500 M Ω (0.5 nm). Yet, from TEM images we expect a nanopore in the several nm size range. d) The noise power spectral density for the data presented on panel c (at 0.2 V) increased considerably during the time that the apparent resistance also increased and fluctuations of the current reduced. Note that the amplifier noise in this current range is about 20 fA/ $\sqrt{\text{Hz}}$. e) Supporting figure for main text figures 4a,b inset showing the scaling of the flicker noise amplitude A versus the magnitude of the current I obtained from a fit to an equation of the form A/f for the noise PSD for different driving voltages. Triangles denote I values at negative currents, crosses at positive currents.

Sample S_{MoS₂} 2: The sample was put in a 1:1 ethanol and de-ionized water for 20 minutes, before being placed into the chamber and filled with 1M KCl solution buffered at pH 8 (as described in the Methods section of the main text). After filling, the system was found to be switchable between two states (Fig. 4.3c,d,e and Fig. 4.6a as described in the main text. A measurement of the DC under applied voltage during a pressure sweep is provided (Fig. 4.6b matching the AC measurements. Two two streaming curves (streaming potential Vs versus pressure P) obtained with the sample before and after the data shown on Fig. 4.3c in the main text are also shown on Fig. S9c. We used streaming potential as it does not have a specific dependence on the resistance of the sample, as in the case of streaming current which is more commonly used. The streaming potential is related to the zeta potential ζ of the surface and the applied pressure gradient ΔP as $V_s = r_0 \zeta \Delta P / \eta \sigma$ in the regime of high salt concentrations when surface conduction effects can be neglected, with η the dynamic viscosity of the fluid and σ the bulk conductivity of the sample. Measurements were obtained with a home-made electrometer buffer amplifier with a $> 1 \text{ T}\Omega$ input impedance. Here, the zeta potentials obtained before and after. We find that stable streaming potential is an indicator of an open fluidic pathway between two sides of the membrane. But, a thus obtained zeta potential value will highly depend on the pore size and the geometry⁴⁸⁴, so we can not infer the correct value of the zeta potential and correlate it with different states of the sample.

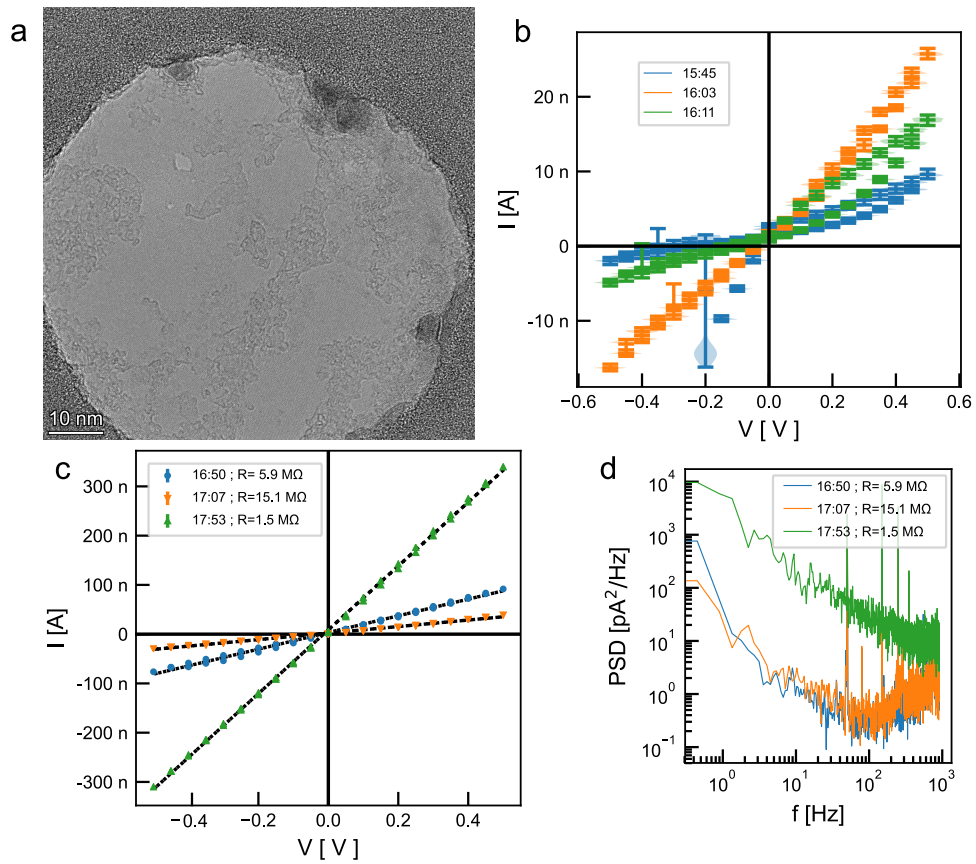


Figure 4.6: **Sample S_{MoS_2} 2:** . a) IV curves from which the current power spectral density in Fig. 4.3e of the main text was obtained. b) DC pressure sweep done after the Fig. 4.3c,d in the main text. This curve confirms that the switching behavior seen in the AC measurement is not an artifact of using AC current for the measurement. The curve is obtained at a 0.1 V DC bias. c) A plot of the flicker noise amplitude A scaling versus current amplitude I obtained from a fit of $A/f + B + Cf$ to the noise PSD shown in Fig. 4.3e in the main text for different driving voltages (panel a). Here due to low noise in the high resistive state a model including both the shot and dielectric noise was used. Triangles denote I values at negative currents, crosses at positive currents. d) Streaming potential Vs curves performed before and after Fig. 4.3c in the main text.

Sample S_{MoS₂} 3: The sample was TEM imaged and no pores were found (Fig. 4.7a). After that the sample was put in a 1:1 ethanol and de-ionized water for 20 minutes, before being placed into the chamber and filled with 1M KCl solution buffered at pH 8 (as described in the Methods section of the main text). We found that the system filled under compression pressure, indicating an nonlinear IV curve which was consistent with the application of gradient pressures (Fig. 4.7b,c) with a high level of noise present and instabilities in the current levels. Even though we applied voltages larger than the limit for electrochemical enlargement of the pores (> 0.75 V)¹⁶, there was no change in the behavior in time suggesting that the exposed pore area is not due to MoS₂. The nonlinearity of the curve matches the models for gas bubble temporary electrowetting by Smirnov et al⁴⁸⁵. We interpret this as a wetting issue (air bubble) over the membrane due to the use of alcohol prewetting, which the original MoS₂ membrane possibly damaged.

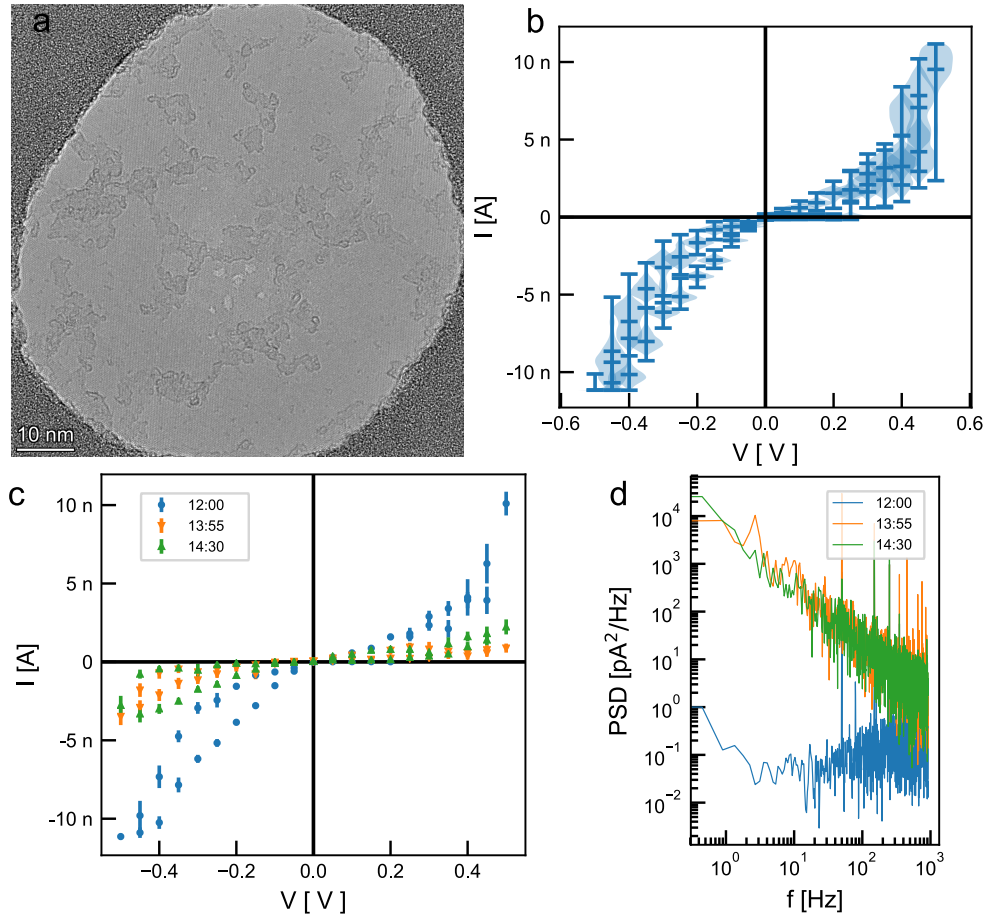


Figure 4.7: Sample S_{MoS₂} 3: a) Transmission electron microscope images of MoS₂ sample before measurements. Imaged with FEI TEM Talos at 80 kV in HRTEM mode. b) IV curve of the sample IV curves after alcohol prewetting and then flushed with degassed solution. c) Noise power spectral densities (at +0.2 V). Both panel b and c are given under three different pressure gradients $\Delta P = 0, 3.5, -3.5$ bar showing no significant pressure dependence. Further application of compression pressure and flushing degassed solution did not change the state of the system until the membrane broke. The IV curve in the range of ± 0.5 V would indicate a nanopore in the ≈ 1 nm range. We interpret this as being a wetting issue due to the alcohol prewetting.

Sample S_{MoS_2} 4: The membrane was filled with degassed 1M KCl buffered at pH8 as described in the main text. After the application of 7 bar compression pressure for several minutes. First measurements indicated a high resistive IV curve (Fig. 4.8a) which was fluctuating between levels indicating current levels comparable to just the supporting membrane with no MoS_2 present (Fig. 4.8b). We conclude there are wetting issues due to the presence of gas bubbles and possible other contaminants. Application of pressure gradients and compression pressure (Fig. 4.8c) indicate that under compression the resistance of the pore is stable and high, but that gradient pressure moves the pore between low and high resistances, with the low resistance state indicating a low level of ionic current rectification indicating better wetting.

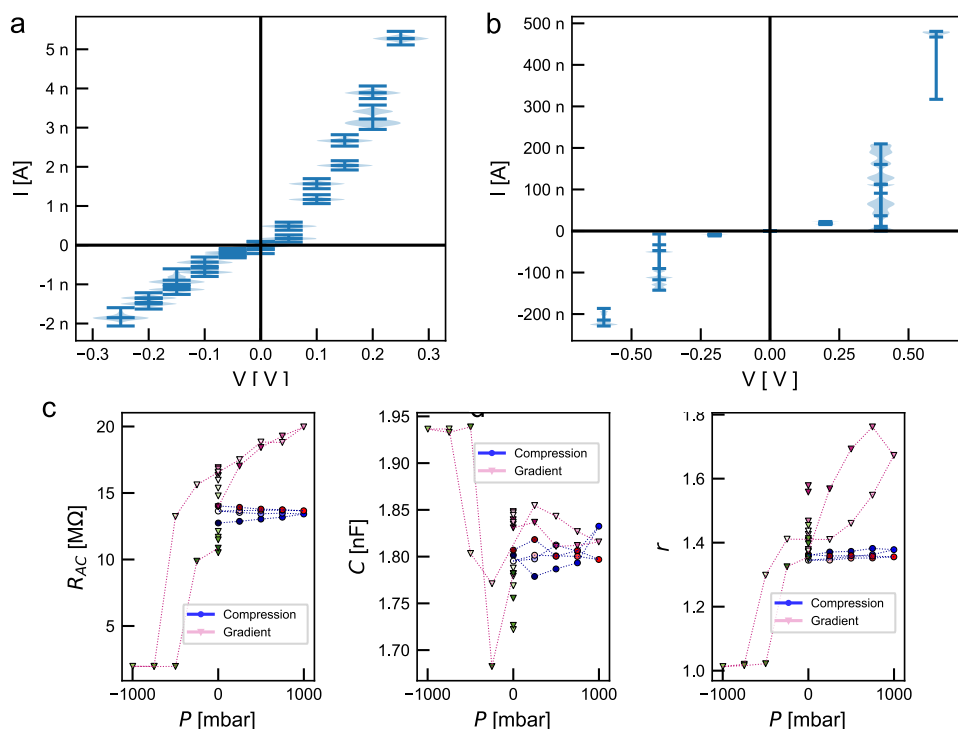


Figure 4.8: **Sample S_{MoS_2} 4:** a) Immediately after filling of the chamber. The bars indicate extrema and the mean value while the shape of the curve represents the current probability density (violin plot). The system stayed in this state for an hour or more without any noticeable change in the noise spectrum. b) Testing the sample with voltages up to 0.7 V a day after panel a. The bars indicate extrema and the mean value while the shape of the curve represents the current probability density (violin plot). The voltage was not varied in a regular way as in all other IV curves. Note that the applied voltages in this stage were below the reported voltages expected to cause an electrochemical reaction (0.75 V)⁶. Note the high level of current fluctuations especially above 0.3 V. We attribute this to bubble or wetting/dewetting fluctuations. c) AC Pressure sweeps done after panel b. The first measurement is done using compression pressure and shows no change of the IV curves between two states, while in the gradient pressure the resistance changes between two states with a different state stable under no applied pressure. The lowest resistance state at $P < 0$ has no ionic current rectification.

Sample S_{MoS_2} 5: The sample was imaged in TEM and drilled to have a pore of about $d \approx 3-4$ nm with at least one smaller satellite pore (Fig. 4.9a). The pore was filled with degassed 1M KCl buffered at pH8 as described in the main text. After the application of 7 bar compression pressure, its current versus voltage characteristic was measured with the voltage always lower than the voltages known to cause electrochemical enlarging of the pores (< 0.75 V)¹⁶. Time evolution of the IV curves in the system indicated that the current levels were fluctuating between several states in time (Fig. 4.9b) with the most conductive state corresponding to roughly the expected pore resistance based on the TEM imaging. All these curves had the same level of Flicker noise. The sample was then flushed with freshly degassed solution and compression pressure was applied for several minutes. All the IV curves linearized and each further application of compression pressure was changing the pore resistance (Fig. 4.9c), with the high resistance state having the largest Flicker noise level (Fig. 4.9d). We believe this was a nanobubble pinned near the pore entrance (wetting issue) which was being slowly dissolved by applying compression pressure and a degassed solution. The original pore in MoS_2 possibly enlarged during handling (as it had at least one smaller satellite pore) or the membrane broke.

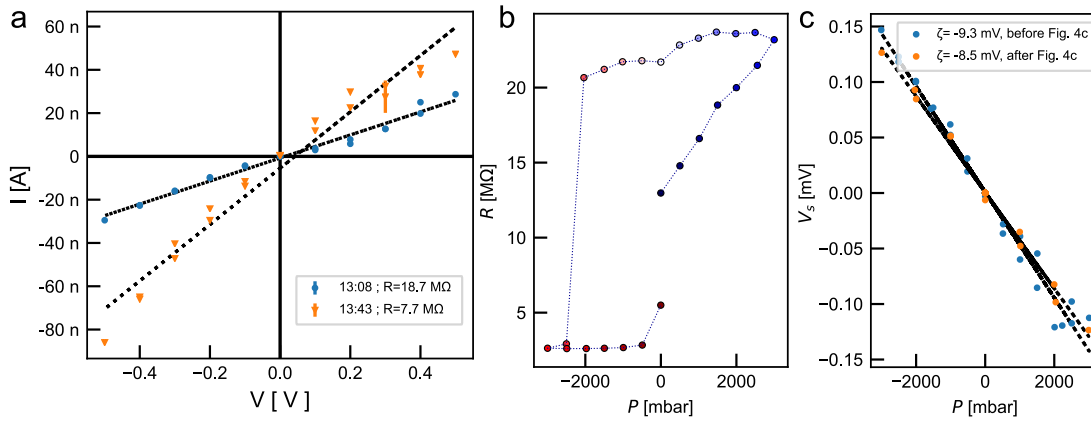


Figure 4.9: Sample S_{MoS_2} 5: a) Transmission electron microscope images of MoS_2 sample before measurements. Imaged with FEI TEM Talos at 80 kV in HRTEM mode. Visible nanopores were drilled by beam condensation with in-situ control of the pore formation. b) Three IV curves recorded about 10 minutes apart show fluctuations between a highly rectifying and almost linear IV curve. Power spectral densities of the ionic currents showed no significant difference in the flicker noise of the sample during this evolution. The most linear curve would correspond to a resistance of $R \approx 25$ M Ω , or to a MoS_2 pore of size $d \approx 4$ nm. Based on the drilled TEM image we would expect the pore to have a size of $d \approx 3-4$ nm.

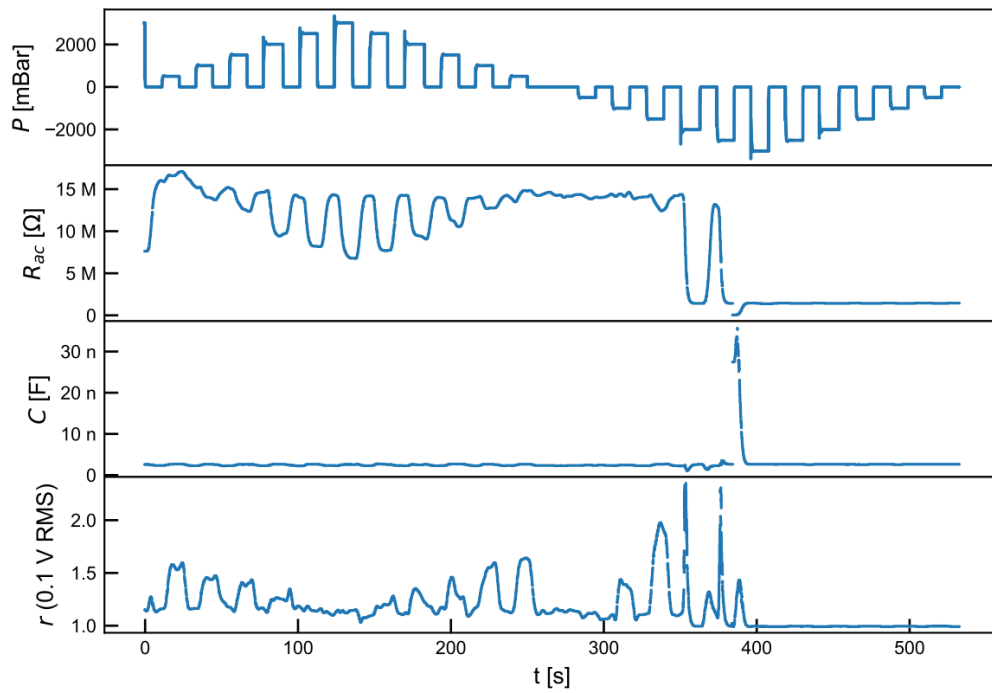


Figure 4.10: **Pressure measurement time trace.** Time trace for Fig. 4.3 . Raw time trace of the applied pressure and the measured R_{ac} , C and r . Between each pressure step increase, system is measured at 0 bar for baseline drift correction.

4.3 Artificial mechanosensing with MoS₂ nanoporous membranes

At nanoscale, mimicking biological systems is often a primary driver in experimental and theoretical research. 2D nanopores, such as our MoS₂ membranes, are a great platform to study and understand sensory, ion-transport functionalities existing in organic cells - including mechanosensing¹². Mechanosensitive, piezo ion channels are commonly present in living organisms and are essential in many physiological processes such as erythrocytes volume regulation, hearing or touch sensing⁴⁸⁶.

4.3.1 Mechanosensing mechanism

Biological, mechanosensitive ion channels, formed of piezo proteins such as TREK1 and TRAAK⁴⁸⁷ respond to mechanical stimuli. Mechanism of this process stems from 'force-from-lipid' principle⁴⁸⁷: a lipid bilayer with ion channels can be deformed or stretched directly or indirectly by applied pressure. This force-induced bilayer change is transferred to the ion channel and can change its conformation - allowing charged ions to pass through into the cell (Fig. 4.11a).

With 2D nanopores however the mechanism is slightly different. Applied pressure can lead to mechanically induced structural lattice change²⁶⁵ which can enhance ion transport through direct change in pore size (allowing mechanically activated ion transport through otherwise impermeable pore) and change of interactions between ion hydration shell and pore edges leading to lower energy barrier for ion to translocate through the pore. With sufficiently small subnanometer pores, applied strain will therefore gate the pore ionic current. As it was shown in 1-dimensional carbon nanotubes, under external membrane potential the current response has a nonlinear (quadratic) dependence on applied strain (or pressure)⁴⁸⁸. Thus by observing ion transport through the membrane via ionic current passing between the membrane sides we can measure the applied pressure difference¹².

MoS₂ is composed of two atoms with varying electrostatic charge : molybdenum and sulfur. It is assumed⁴⁸⁹, that by fine-tuning the nanopore fabrication method one can have control over the pore geometry i.e. create predominantly Mo- or S- terminated pores. Depending on the pore size, a tensile strain (via pressure) applied to a non-ion conductive MoS₂ pore (or channel) can be used to not only boost water permeation already at the 6% strain⁴⁸⁹ but can also induce ion permeation in the case of Mo- or S- only terminated subnanometer pores⁴⁸⁹. The high degree of mechanosensitivity comes from strain induced reduction of ion-repulsive interactions at the pore entrance. Depending on the edge termination, consecutive pore charge and applied strain MoS₂ nanopores can become conductive to cations, anions or both simultaneously⁴⁸⁹ (Fig. 4.11b) with ionic current increasing with applied strain (Fig. 4.11c). One would think, that such a precise pore-tuning (engineering pores with only one type of atom on the edge - Mo or S) seems to be possible only in theoretical models. Interestingly, the Xe- irradiation method described in previous chapter opens an opportunity to fabricate small enough nanopores that match the predicted mechanosensing properties^{388,489} of 2D materials.

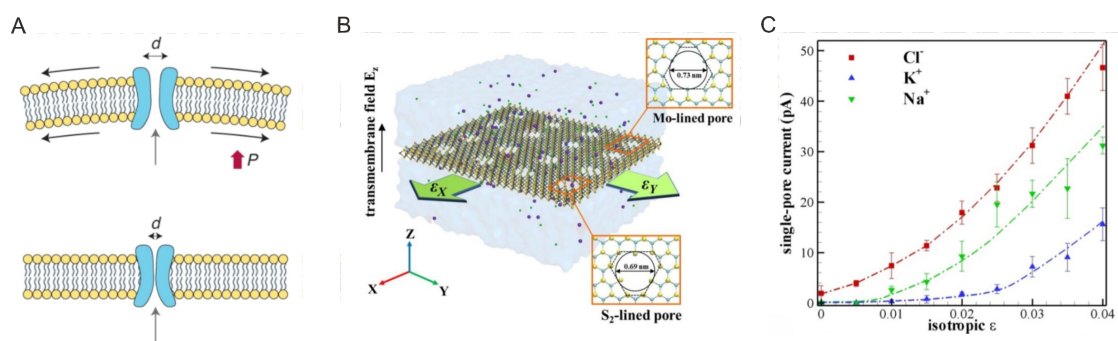


Figure 4.11: **Mechanosensitivity principle.** In biological pores, lipid bilayer is deformed by applying mechanical force (a). Elastic deformation is then transferred to the ion channel increasing its diameter¹². With 2D materials such as MoS₂, ideal mechanosensing pores are within subnanometer diameter range (b) and depending on the edge termination (S- or Mo-) can exhibit anion- or cation-selectivity⁴⁸⁹. Molecular dynamics models predict increase in ionic current with increasing strain σ for KCl and NaCl salt solutions (c)⁴⁸⁹.

Given the theoretical predictions^{388,489}, high mechanical strength of MoS₂ monolayer (sustaining up to 11% strain before breaking⁴⁹⁰) and established large-area fabrication protocols it was a great opportunity to experimentally study this phenomenon and work towards establishing first, nature-mimicking, mechanosensing ion-channels in 2D materials.

4.3.2 Results

All measurements were performed at the setup described in the previous section. Solid state chips (Si/SiN_x and Si/SiO₂/SiN_x) used as a MoS₂ support were supplied either by external manufacturer (Norcada) or in-house fabrication and all were within the dimensions range of 5x5 mm with a 20-30 μ m SiN_x membrane window a single aperture opening of 60 nm. All batches of devices were first investigated in the flowcell without the MoS₂ to obtain a baseline reference parameters for following experiments and compensate for substrate variance. MoS₂ monolayers were transferred by Mukeshchand Thakur using wet-, dry- or hybrid transfer methodologies described in section 2.3. All substrates were inspected in HRTEM to confirm successful transfer and clean MoS₂ surface at this stage. The next processing step involved PFIB irradiation with 30 kV, 30 pA beam at 30 μ s dwell time and 350 nm pitch distance. Result was a "gentle" irradiation yielding a range of subnanometer pores which would show an expected mechanosensing behaviour²⁶⁵. PFIB irradiation methodology was described in previous chapter, section 3.2. After irradiation most substrates were used directly in the nanofluidic measurements without a TEM inspection. At this stage, e-beam imaging often lead to substrate contamination due to beam induced hydrocarbon deposition (matter discussed in details in the next section).

Chips were mounted in the flowcell chamber and flushed with degassed 1M KCl salt solution on both positive and negative side. Typical measurement consisted of several sets of

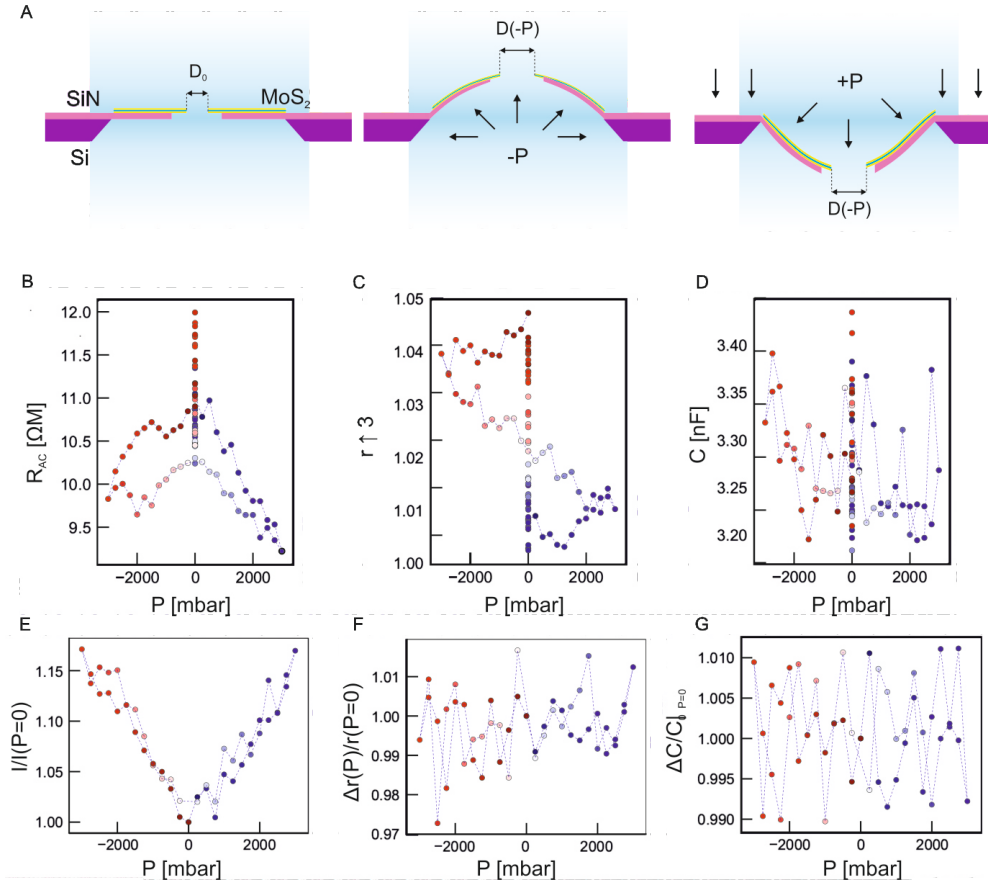


Figure 4.12: **Mechanosensing measurements.** A schematic representation of Si/SiN_x membrane chip with a freestanding MoS₂ under applied pressure from the positive side (frontside) and negative side (backside) of the membrane aperture (A). Panels B, C and D shows a direct measured values of AC resistance R_{AC} , rectification r and capacitance C respectively under varying pressure. Dashed lines and color gradient represent the direction of pressure steps: blue for positive pressure and red for negative one. First measurements start at pale blue, transition to negative pressure at dark blue/dark red and finish at pale red, forming a hysteresis of applied pressure. After each measured pressure step systems performs a control measurement at 0 bars to compensate for baseline shifts. Panels E, F and G are normalized plots of R_{AC} , r and C after baseline compensation. Measured ionic current increase in this case is significantly higher than expected strain enlargement of MoS₂ nanopores and represent mechanosensitive response (E) while maintaining stable rectification (E) values indicating no presence of nanobubbles or particle obstruction which may affect ionic flow through the nanopore.

V_{AC} pressure sweeps (applying pressure on both sides under constant 100 mV AC bias) and compression measurements with cyclic voltammetry (measured at -0.5 to +0.5 V to avoid electrochemical MoS₂ damage) to ensure nanopores wetting and stable conductance, capacitance and rectification ($\Delta C < 1\%$ and $\Delta r < 1\%$, indicating no bubbles nor contaminants residing on the membrane). In the case of porous MoS₂ the wetting is concluded after membrane resistance measured from IV sweep remains stable (does not change) after applying symmetric, compression pressure on both membrane sides. Expected membrane resistance

is measured based on the Figure 4.4 R /diameter plot. In addition to stable membrane resistance, properly wet pore does show a \approx constant capacitance (of 1-4 nF) as well as rectification under applied positive and negative pressure. Changes under asymmetric pressure probe indicate an obstruction on the membrane surface (a bubble or particle) which is moved by fluid flow. As we observe membrane resistance, capacitance and rectification directly from measurement we can have a direct information on the nanopore wet state. Pressure-induced wetting procedure was preferred as irradiated MoS₂ membranes tend to be more prone to contamination (discussed in details in the next section) however in some cases manual flushing of the frontside and backside flowcell chamber was performed to eradicate nanobubbles and/or other wetting issues. A schematic representation of pressure sweep is presented on Fig. 4.12A. After establishing proper wetting, membranes were swept with a gradient ± 3.5 bar of pressure on front- and backside in 250-500 mbar steps with a 0 bar pause in between each to compensate for the baseline drift (as described in previous section and depicted on Figure 4.10). Sweeps were performed at constant 100 mV AC (Fig. 4.12B). As described in the section 4.1, in a single measurement values of R_{AC} , rectification r (Fig. 4.12C) and capacitance C (Fig. 4.12D) were obtained simultaneously (note constant, stable parameters of R_{AC} and rectification shown on panel C and D). Obtained data was normalized (all data points were divided by the corresponding values measured at 0 bar pressure) to show the increase in strain-induced ionic transport (Fig. 4.12E) and ideally constant or stable rectification and capacitance (Fig. 4.12F and G).

The example shown in Fig. 4.12 shows a symmetric 15% of current increase at ± 3.5 bar pressure and represent the mechanosensing behaviour. Substrate R_{AC} cyclically dropped to $\approx 9 \text{ M}\Omega$ under applied pressure and relaxed to 10-11 $\text{M}\Omega$ at no pressure. Resistance values here directly correspond to a pore of 10 nm in diameter (Fig. 4.4) however one has to expect a range of pore diameters obtained with ion irradiation where large ones dominate the ionic transport while small ones still manifest mechanosensitive response, influencing ionic current²⁶⁵. A clear example of a proof of a concept of mechanosensitive ion channels in 2D MoS₂ is shown on Fig. 4.13A and B. Ion transport through porous membrane (Fig. 4.13C) increase with applied pressure with a dependence order of magnitude higher than what is expected just with strain enlargement of a "large" MoS₂ nanopore. This indicates a restructurizing of the solvation and ion-pore interactions at a molecular level. After obtaining the mechanosensing state, membrane was measured several times over period of up to few days. Its symmetric and stable character was indicating no pressure induced delamination nor MoS₂ layer liftoff. Moreover, no dependence on salt concentration was found (Fig. 4.12B, Mechano 2 substrate) indicating a regime where ion transport is dominated by the ion dwell time at the pore interior which was in agreement with proposed models^{491,492}.

However, this behaviour was observed on only few MoS₂ membranes out of over 60 measured ones. The most common problems were persistent wetting issues, processing-induced contamination, varying surface properties from one substrate batch to another and non-linear mechanosensing (i.e. seen only on one side of applied pressure, shown in Appendix, Fig. A.6). The latter have started to indicate possible problems related to adhesion of monolayer

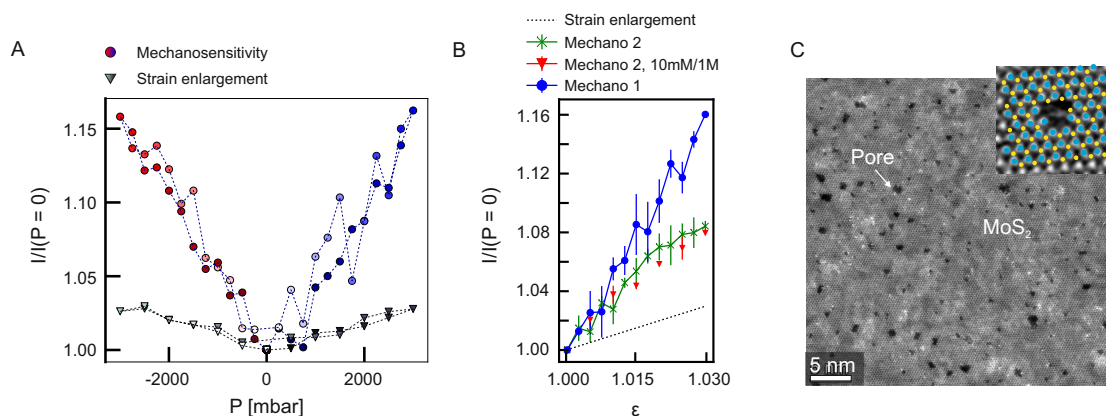


Figure 4.13: Mechanosensing obtained with MoS_2 nanopores. An experimental demonstration of mechanosensitive increase in ionic transport through pores (A). Bottom line corresponding to a reference strain enlargement result was obtained with large MoS_2 pore, without mechanosensitivity. A relation between strain ϵ and increase in ionic current for the same substrate (Mechano 1) as well for additional data set (Mechano 2) with no change after switching to gradient conditions of 1M/1mM KCL solution (B). Current data is divided by the current at no applied pressure to normalize the curves. A AC-STEM image of the porous MoS_2 membrane used to obtain mechanosensitive ionic response (C) for Mechano 1 substrate. The inset shows a high-magnification close-up on the pore area with MoS_2 lattice atoms marked.

MoS_2 , particle contamination or hydrocarbon patches pinning nanobubbles around the pore area. Cumulative experimental issues made further proving and testing mechanosensing (e.g. dependence on salt solution pH, ion types, voltage/current probes etc.) highly problematic.

Finally, a routine, control measurement of new solid state chip batch obtained from an external manufacturer (considered as proven and reliable) has shown an anomalous, unseen before wetting behaviour. All measured devices from the new batch (with 90 nm SiN_x aperture, without MoS_2 on it) has shown a change (as compared to all other substrates) in their surface hydrophobicity manifesting in persistent wetting issues and inability to fully wet the aperture. Even after most rigorous substrate cleaning prior to experiments (plasma cleaning, piranha solution immersion, EtOH/IPA/DI wash) and most "aggressive" electrowetting protocol (voltammetry at ± 10 V at 7 bar compression pressure from both chip front- and backside) did not result in permanent wetting with R_{AC} values unable to settle at expected resistance value for a 90 nm pore size ($\approx 0.9 \text{ M}\Omega$). All substrate inspections using SEM and TEM did not found any oddities in the membrane thickness, composition, aperture shape nor structure. The high pressure wetting cycle measurements performed at high pressure values ± 7 bar on positive/negative side have revealed an increase in ionic current indicating strain-induced mechanosensitivity on control substrates - not only without any MoS_2 but also on a pore that should not exhibit such an effect due to its size, reaching values significantly higher than anticipated. Anomalous results are presented on a Fig. 4.14 A and B during initial wetting protocol showing evolution of AC resistance, capacitance and rectification. An anomaly is the unexpected increase in the ionic current at applied pressure and return to the base value at 0 bar. An

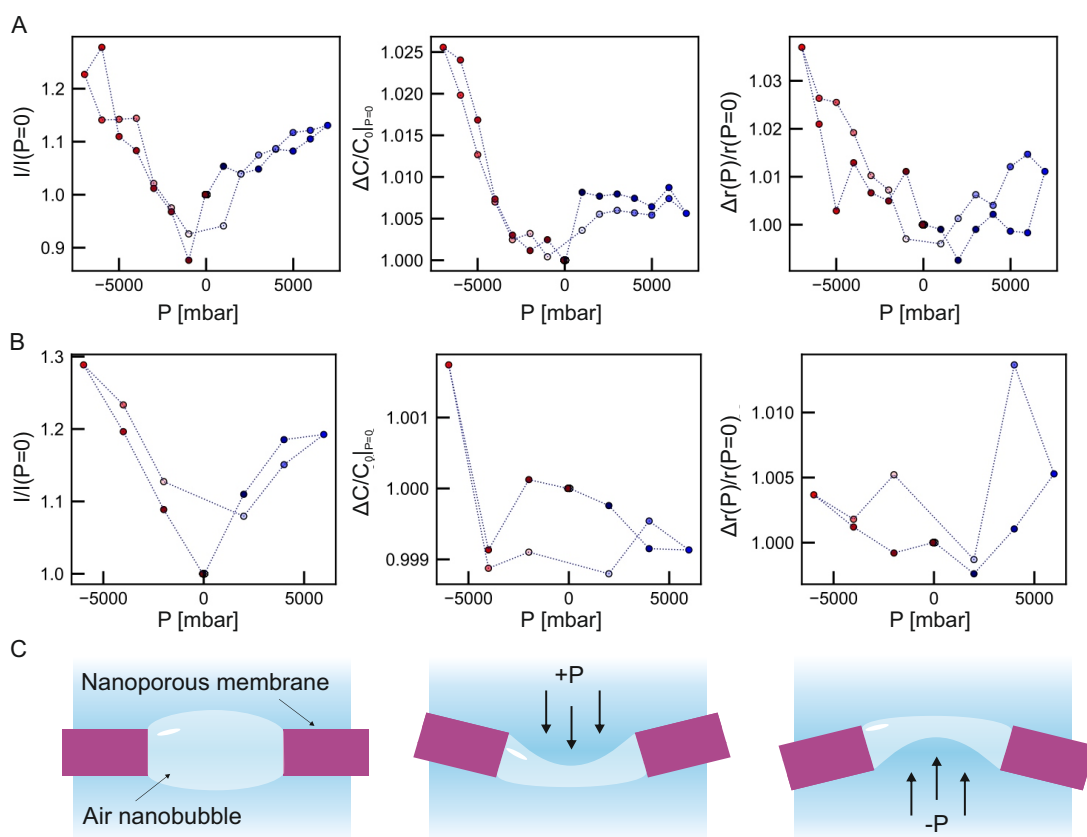


Figure 4.14: Anomalous pressure-induced ionic transport on solid state chips. Control measurements performed on 90 nm aperture on Si/SiN_x membrane. Pressure gradient sweeps at 100 mV AC at +/- 7 bar (A,B), and their measured and normalized capacitance and rectification values show a potential mechanosensitivity artifact. We hypothesize that this behaviour is related to the air nanobubble pinned inside the ionic channel which is symmetrically squeezed by applied pressure (C), and in contrast to pressure-induced wetting of hydrophobic pores presented on Fig. 4.2 is not being reabsorbed back into the solution.

additional current sweep of Test substrate 1 (Fig. 4.15) shows anomalous "mechanosensing" also at pressure probes applied 0.1 mV DC bias. This state have remained after prolonged measurement time (Fig. 4.16) and multiple attempts of electrowetting, flowcell salt solution flushing, setup subcomponents (e.g. electrodes, tubing, o-rings) check and exchange. Results obtained from this unseen before anomaly were similar to previously investigated MoS₂ mechanosensitive membranes and proved impossible to distinguish mechanosensing from the wetting problem. The only logical hypothesis was a persistent nanobubble stuck in the middle of ionic channel (Fig. 4.14H) symmetrically deformed by our applied pressure from each membrane side. In contrast to our prior wetting experiments using pressure these particular gas/air bubble have been impervious to our wetting procedure, was not moved by pressure driven flow nor was it affected by high-voltage applied bias. All other troubleshooting efforts: setup, salt solutions and substrate/material investigation and characterization did not found anything out of ordinary. Thus the "bubble" hypothesis remained only possible

explanation, especially given the odd wetting behaviour of this particular chip batch, giving hints on hydrophobic character of the pore interior. This wetting artifact was a surprising result and definitely needs further investigation, however due to time constraints related to the end of PhD it was not pursued further and all mechanosensing experiments were halted. It is impossible to make a distinction between the symmetrically "squeezed" nanobubble confined in hydrophobic channel and an actual mechanosensing nanopores on 2D membrane.

4.3.3 Conclusion

Initially promising mechanosensitivity obtained with 2D-MoS₂ pores was eventually put on hold by a routine control tests of large, 90 nm SiN_x pores. Very low general yield of successful experiments and end-of-thesis deadlines did not allow to investigate and pursue this project further. To ensure repeatable measurements we have employed rigorous protocol of chip cleaning (piranha solution immersion, plasma cleaning, DI/EtOH wash with purest, chromatography-grade solutions) and normalized all experimental conditions but not even that ensured repeatable experiments. From our observations it is evident that majority of wetting issues and substrate problems had came from prior fabrication steps. A manufacturing process consisting of photolithography, 2D material growth and transfer, TEM imaging and FIB irradiation lead to the complex, manual-labor heavy fabrication protocol which can be potentially prone to human errors. The last batch of false-positive, "mechanosensing" test substrates was a great example. Even with proven, outsourced manufacturer, some minor, unknown differences in the lithographic processes of Si/SiN_x chips fabrication can lead to varying surface properties (i.e. unexpected hydrophobicity inside the pore) which in turn can lead to observed behaviour of bubbles pinning, wetting problems and also pressure-induced MoS₂ wrinkling and delamination (discussed in details in the next sections).

Nonetheless, the main conclusion is even though we have discovered a potential nanopore wetting anomaly that can mimic strain-induced effects, the MoS₂ results shown on figures 4.12 and 4.13 can still be indicative of the mechanosensitive ion channels present in this system, especially since they are in accordance with theoretical predictions^{265,388}. However, more efforts have to be put on understanding wetting problems and nanobubbles in the nanoporous membranes. A thorough analysis and step-by-step investigation of fabrication protocols and their impact on substrate surface properties would have to be employed to ensure absolute control over the end product - suspended, nanoporous MoS₂ membrane. All, even most minor imperfections of nanoporous membranes (e.g. nanobubble-pinning areas, not properly degassed salt solutions, unfiltered particles in the solution causing pore clogging, 2D film delamination) are additionally amplified by using high pressure probes with applied driving potential and have to be minimized. This work is highly relevant to the nanofluidic field, as it uncovers potentially unseen world of improper wetting - something one can only identify and distinguish from artifacts by applying precise hydrostatic pressure to the membrane.

4.3.4 Supplementary information

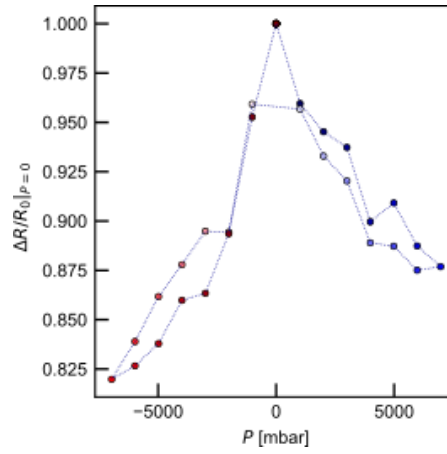


Figure 4.15: **Anomalous pressure-induced ionic transport on solid state chips - current sweep measurement.** Pressure cycle measurement performed at constant 100mV DC, showing a change in DC resistance and anomalous current modulation.

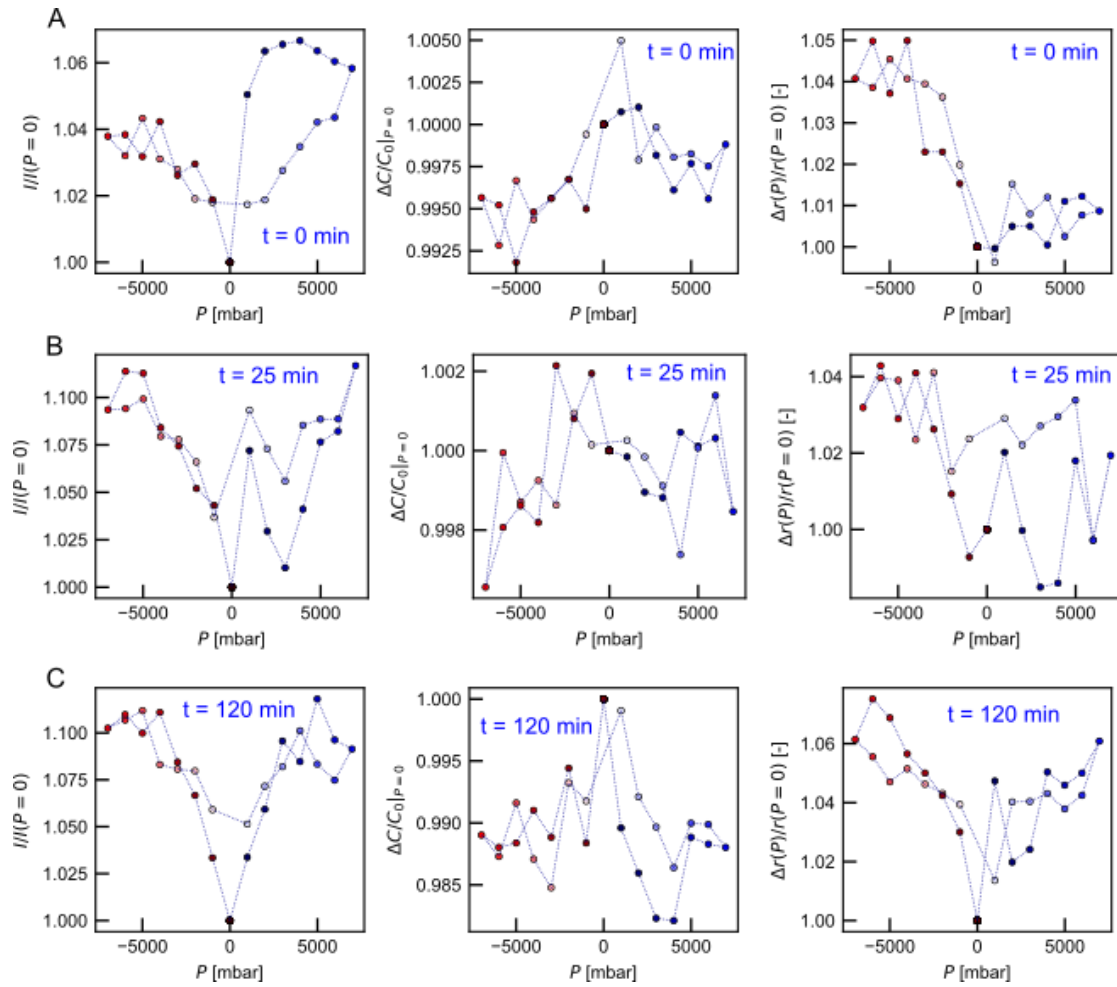


Figure 4.16: **Anomalous pressure-induced ionic transport on solid state chips - dependence over time.** Pressure cycle at 100mV AC, measuring membrane R_{AC} , capacitance and rectification (A) and repeated measurement after 25min (B) and 120min (C).

4.4 Osmotic Power Generation with FIB-irradiated MoS₂

One of the main motivation behind developing and optimizing large-scale fabrication and synthesis processes discussed in previous chapters was contributing towards 2D-nanopore osmotic power generation technology. As discussed in Chapter 1, the reported small-scale results from salinity gradient harvesting experiments^{8,164} with MoS₂ nanopores show a promising avenue leading towards developing efficient and potentially commercially viable devices⁹. Some of the most crucial technological challenges were identified as large-area 2D film synthesis, nanopore fabrication and multi-pore system power generation scaling. To address these bottlenecks the large-scale 2D material synthesis and transfer protocol discussed in Chapter 2 were used for batch device fabrication. Nanopores were created through Xe⁺ PFIB irradiation discussed in Chapter 3. Finally, the nanofluidic experiments in salinity gradient conditions were performed in the homemade flowcell with hydrostatic pressure application to ensure good wetting conditions. This section summarizes and concludes the salinity gradient experiments with PFIB irradiated MoS₂ membranes.

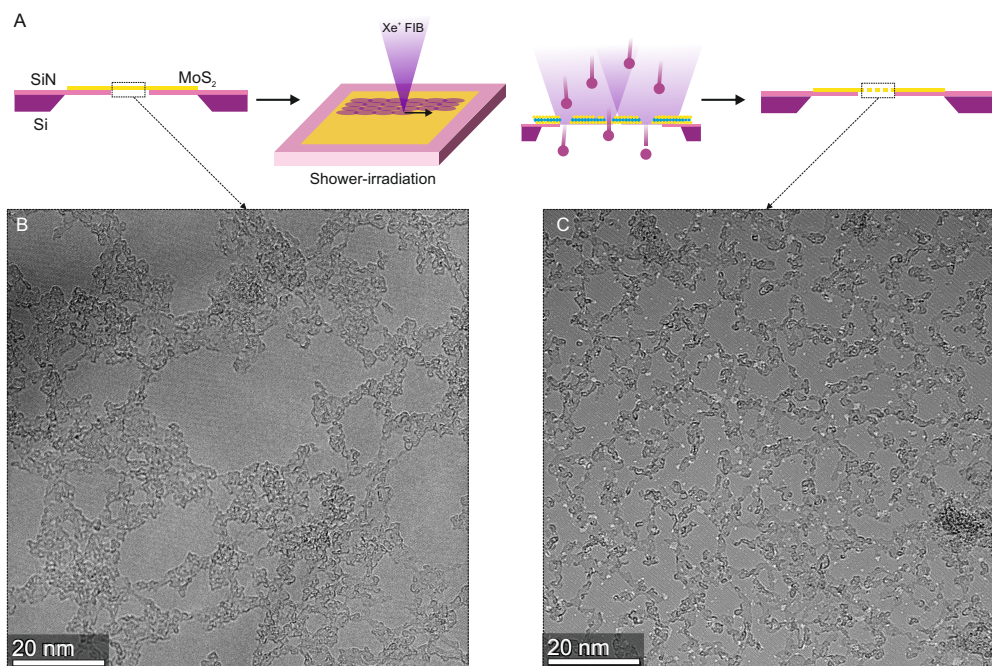


Figure 4.17: **Osmotic power generation with PFIB-irradiated MoS₂**. The schematic representation of PFIB irradiation (ion shower) regime yielding a porous membranes (A). Suspended MoS₂ membranes were imaged in HRTEM prior to (B) and post (C) irradiation to investigate the porosity and obtained pore dimensions. The PFIB nanopore fabrication methodology is discussed in details in section 3.2.

4.4.1 Experiment and measurements protocol

Similarly to mechanosensing, the osmotic power generation experiments were performed with a wide variety of Si/SiN_x substrates as a suspending membrane for MoS₂. Initially house-

made, Si/SiN_x chips fabrication was soon outsourced to an external company (Norcada) for repeatability reasons. The substrates were within the parameters range of 5x5 mm in dimensions, with a 20-30 μm SiN_x membrane window and a single aperture opening of 60 nm with suspended MoS₂. The as-transferred MoS₂ was irradiated with Xe ions (as shown in the Fig. 4.17A). The irradiation parameters were chosen to be in the range of 3.4×10^{12} to 9.0×10^{13} ions/cm² to ensure the balance of nanopore dimensions (expected size of 5 nm) supporting ion-selectivity and average porosity ($\leq 10\%$) to not risk compromising the mechanical stability of the membrane. Membranes were initially imaged in HRTEM before (Fig. 4.17B) and after (Fig. 4.17C) the irradiation to confirm pore fabrication. However, for most experiments the suspended film was not imaged after the nanopore-drilling FIB irradiation due to large risk of electron-beam induced deposition (EBID) contaminating the film. The issue of EBID is discussed further in the following section.

All measurements were performed on the setup described in Fig. 4.1. The salinity gradient conditions were realized with buffered salt solutions (1M/100mM and 10mM/1mM KCl/Tris) at pH 8. All the experiments started first with 1M KCl solutions on both sides of the membrane to establish the baseline parameters of membrane resistance ($R \approx 10 - 100\text{M}$), ensure good nanopore wetting (no rectification and stable capacitance under applied pressure) and investigate the potential mechanosensing response. Following that, the backside chamber of the flowcell (negative pressure side) was flushed with DI, EtOH+DI, DI again and finally with low salinity solution (Fig. 4.18A). Such a flushing protocol was established to minimize the risk of nanobubble nucleation from the exchange of solutions with different gas solubility (specifically water to ethanol)⁴⁹³. The compression pressure (i.e. pressure applied on both positive and negative membrane side simultaneously) was applied after each solute exchange to ensure membrane stability.

4.4.2 Results

The salinity gradient measurements and resulting values of voltage and current are summarized in the table 4.1. After compensating for electrode redox potential using Nernst equation^{7,8} the obtained power from 5 successfully measured devices was ranging from 2 to 500 pW in 1M/10mM salt gradient at pH 8. Analysis of obtained values of osmotic current I_{OS} (0.1 - 3.9 nA) and osmotic potential V_{OS} (20 - 210 mV) suggests the dominating presence of smaller than 8-10 nm size range estimated to be optimal for energy harvesting⁸. Detailed STEM image analysis confirms this hypothesis with the observation of predominantly sub 1-2 nm pores (Fig. 3.4 in the section 3.2). The highest generated power from measured device was reaching ≈ 500 pW with $I_{OS} = 3.9$ nA and $V_{OS} = 130\text{mV}$. This results however was not reproduced. The wide ranges of I_{OS} and V_{OS} suggest variable porosity, although anomalously high V_{OS} can be indicative of artifacts and hence uncontrollable experimental conditions.

We have observed, that due to the nature of experimental protocols (including pressure application and multiple electrolyte exchange), the membrane pores often have been compromised or partially clogged. Porous 2D membranes are volatile in nature and we hypothesize that

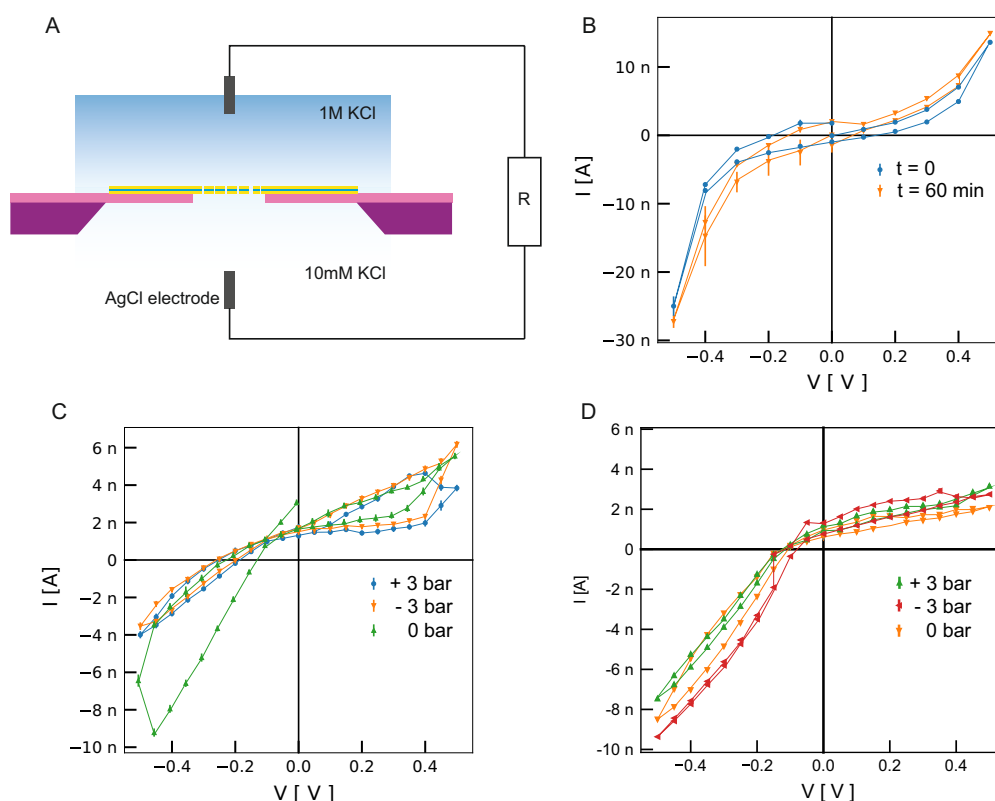


Figure 4.18: **Non-linear ionic currents in gradient conditions.** The experimental setup is shown on panel A. Examples of non-linear current response measured in gradient conditions which are stable over 60 minutes of measurement (B) and under applied positive and negative pressure to the membrane (C and D). Panel D shows a highly rectifying IV characteristic indicating highly selective nanopores in the system.

pores and structure observed in HRTEM prior to experiment will not remain the same in the aqueous solution. Measured membranes on average are exhibiting relatively low open circuit current of ≈ 1 nA. The highest obtained values most likely originate from pores being expanded due to pressure or electric fields. From cyclic voltammetry, we have frequently observed a non-linear IV pattern (Fig. 4.18B) which may indicate underlying nanobubbles or pore-obstructing issues (e.g. due to MoS_2 delamination) which become more conductive with higher applied potential. Interestingly, the I_{OS} and V_{OS} seemed to be stable and impervious to applied hydrostatic pressure, which is shown on the Fig. 4.18C and D. Some measured devices (eg. Fig. 4.18C and D) show the presence of hysteresis in measured I_{OS} and strong rectifying, non-linear character. This is the evidence of highly ion selective nature of small nanopores, leading to lower ionic flux under positive bias due to asymmetric electrical double layer structure⁴⁹⁴.

Table 4.1: Measured osmotic power. Compilation of measurements in 1 M : 10 mM KCl, at pH 8 from 5 consecutive substrates with brief history of measurements in Comment column. All substrates showed in the table were measured in 1M/1M solution prior to switching to the gradient conditions, and were exhibiting a membrane resistance within a stable membrane range of 50 - 100 M Ω . After switching to gradient conditions, substrate no. 1 exhibited a high increase in P_{os} after electrolyte exchange and pressure sweeps measurements which may suggest pore expansion or more contribution from wetted nanopores. Following decrease and fluctuation in P_{os} points toward particle contamination. Substrate no. 2 showed a strong increase in generated P_{os} achieved only after wetting protocol and electrolyte exchange. Substrate no. 3 has shown stability under long measurement time, substrates 4 and 5 were probed with measuring I_{os} and V_{os} under positive and negative pressure and showed minor fluctuations. Substrate no. 5 shows a clear behaviour of clogged or nanobubble-obstructed membrane.

Sample no.	V_{os} [V]	I_{os} [nA]	P_{os} [pW]	Comment
1	0.11	0.32	35.2	before wetting protocol
1	0.11	1.8	198	after flushing procedure
1	0.11	1.1	121	
1	0.13	3.9	507	Peak measured P_{OS} after pressure gradient sweep, +/-3.5 bar
1	0.12	0.8	96	
1	0.11	0.35	38.5	
1	0.06	0.9	54	
1	0.21	0.7	147	
2	0.11	0.9	99	
2	0.19	2.5	475	after flushing and wetting protocol
3	0.09	1.8	162	t = 0 min
3	0.11	1.6	176	t = 60 min
4	0.15	0.96	144	measured at P = +3 bar
4	0.15	1.1	165	measured at P = -3 bar
4	0.12	1.1	132	measured at P = 0 bar
4	0.11	0.96	105.6	measured at P = +3 barr
4	0.11	1.1	121	measured at P = -3 bar
4	0.03	1.2	36	measured at P = 0 bar (broken)
5	0.01	0.2	2	measured at P = 0 bar
5	0.02	0.12	2.4	measured at P = +3 bar
5	0.02	0.23	4.6	measured at P = -3 bar
5	0.03	0.2	6	measured at P = 0 bar
5	0.03	0.11	3.3	measured at P = +3 bar
5	0.02	0.18	3.6	measured at P = -3 bar

4.4.3 Conclusions

Relatively low yield of successful gradient experiments (due to wetting problems, damaged membranes, fabrication issues or rapid nanopore clogging) and wide range of obtained I_{os} , V_{os} and P_{os} were a significant obstacle in drawing valid conclusions. A hypothetical explanation for the non-linear events observed in IV characteristics Fig. 4.18 might be related to in-situ pores expansion due to electrolyte exchange and/or simultaneous application of pressure and electrical fields. Relatively frequent events of membrane clogging (observed through rapid increase in membrane resistance, e.g. from 1-50 M Ω up to several G Ω) can originate from the delaminated MoS₂ floating in the solution. Substrates were fabricated with large-area, continuous monolayer but also multicrystalline MoS₂ which edges can potentially be prone to delamination through supporting membrane expansion or solute intercalation and lift-off. Nonetheless, scarce results show a promising application of PFIB as a pore fabrication tool, albeit irradiation parameters have to be revised and tailored to energy harvesting applications.

4.5 Challenges of using FIB-irradiated thin films

Ion beam irradiation was widely used across multiple projects in this thesis to create defects and fabricate nanopores. However, in the latter application some limitations of this method became apparent. We have investigated the suspended, irradiated MoS₂ in TEM and STEM (Fig. 4.19A and B) to assess the beam parameters influence on the average pore size. Hydrocarbon patches, intrinsic and always present on the surface of 2D materials due to airborne contamination and all prior processing, seem to be significantly affected by the FIB. We have observed a significant spread of these with increasing ion beam parameters (e.g. of dwell time influence is shown on Fig. 4.19C).

This effect has a direct impact on nanofluidic membrane performance. Firstly, such a spread increases the difficulty of TEM imaging. We have noted that even though the material suspended over large-area TEM-dedicated imaging grids was unaffected, the single aperture devices (i.e. ones used in experiments) became heavily prone to e-beam induced contamination (EBID) after irradiation. This has limited the capacity of imaging MoS₂ before and after irradiation on each substrate. Instead porosity and PFIB parameters were analyzed based on film suspended over TEM grids. Secondly, hydrocarbon surface patches are expected to be hydrophobic⁴⁹³ thus their spread over the surface might lead to wetting problems and nanobubble pinning. Few devices that were successfully imaged after PFIB irradiation show a significant decrease in MoS₂ surface cleanliness (Fig. 4.19A-C). A low yield of successful nanofluidic experiments due to large number of these events seem to confirm that hypothesis. Out of 80 measured devices, only few has shown mechanosensing (3) or osmotic energy harvesting capacity (5) and the rest had to be discarded due to wetting issues, clogs, delamination etc. Lastly, the spread of hydrocarbon patches inevitably is related with decreasing clean MoS₂ areas. This may in general impact MoS₂ conductance but in the case of nanopore fabrication (or defect creation) such a matrix of hydrocarbons also can act as an additional mechanical

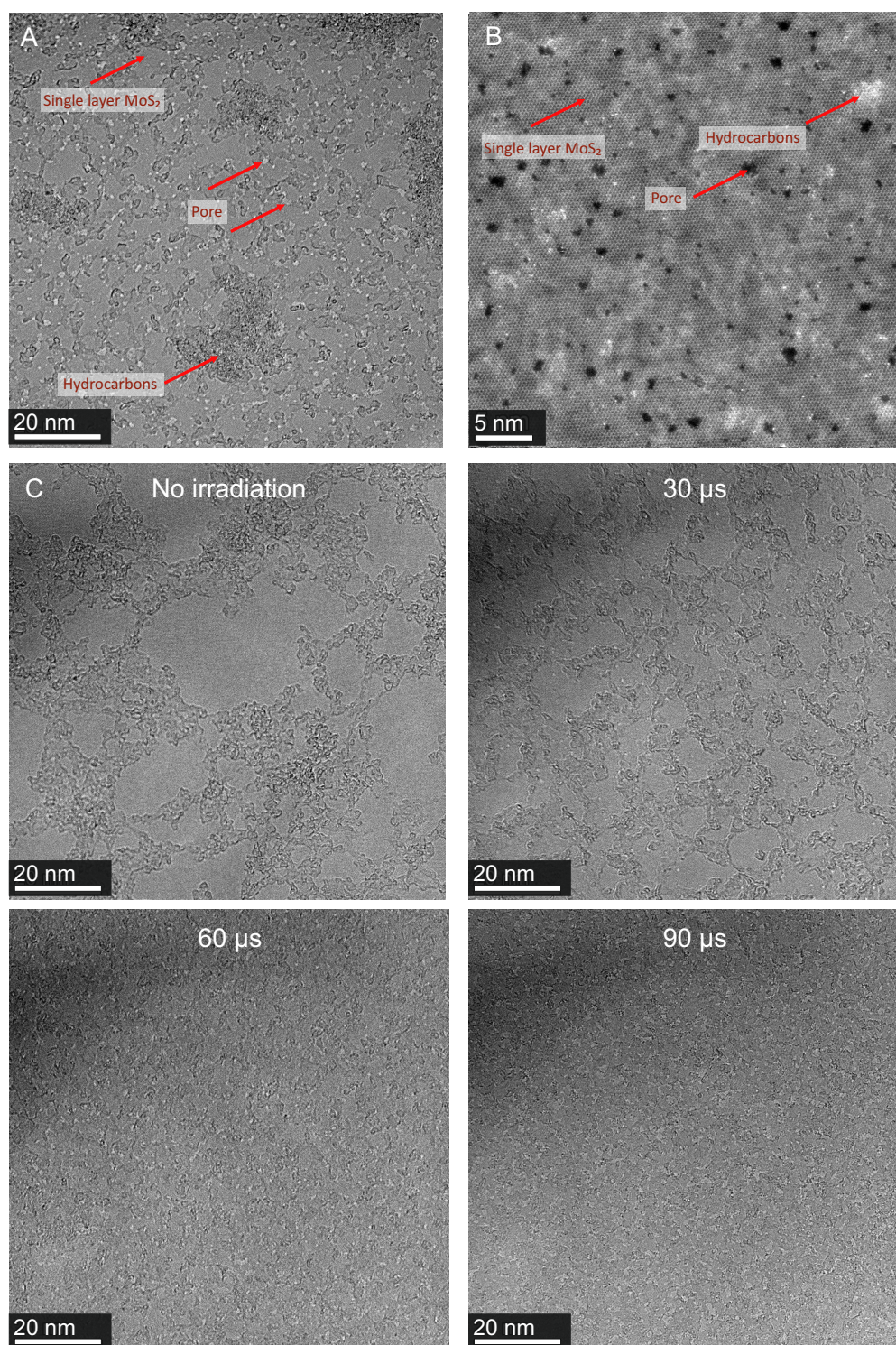


Figure 4.19: **PFIB-created nanopores and MoS₂ structure.** The structure analysis of TEM (A) and STEM (B) imaged MoS₂ membrane shows a presence of nanopores but also hydrocarbon patches. The latter tend to expand with increasing PFIB parameters such as beam dwell time shown on panel C.

support to porous membrane.

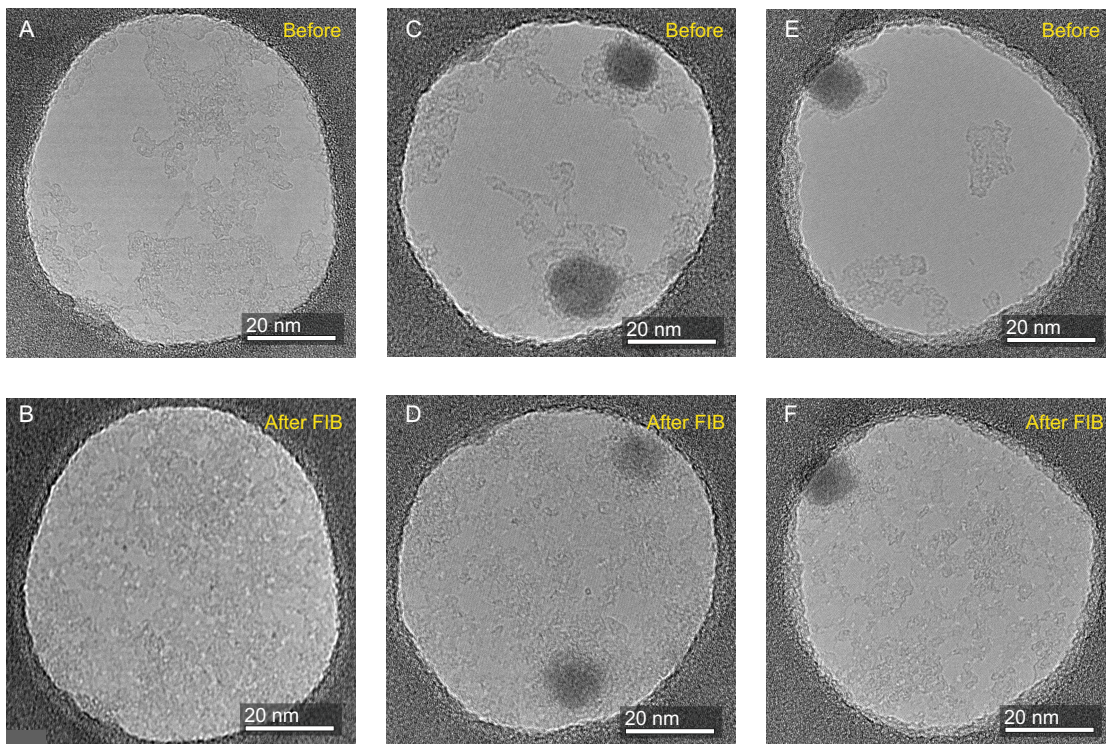


Figure 4.20: **HRTEM images of MoS₂ device prior and post irradiation.** Panels A, C, E represent devices imaged after transfer and the state of the MoS₂ surface. After FIB, the surface becomes significantly more contaminated with hydrocarbons (B,D,E).

4.5.1 Outline

PFIB irradiation can be used for nanopore creation with a significant degree of control. However, the beam induced deposition caused by the FIB is a limiting factor one has to take into consideration. The work presented so far is merely a fraction of efforts needed to develop this approach and fully realize its potential for this application. Irradiation parameters have to be further optimized and explored to find most efficient pathway to create uniform nanopores of size ranges relevant for osmotic power generation purposes and with minimal surface contamination. FIB irradiation method presented here might also be re-engineered and explored as a part of two-step process where it will be used for seeding defects, further expanded by chemical, electrochemical or plasma processing⁹. With potential commercialization in mind, it is important to consider the principal, technological aspects of the device fabrication such as batch processing and scalability on the early design and research phase. Hence, developing the FIB irradiation further remains still highly promising.

However, before tackling the scalability or investigating further the nanofluidics in large-area confined channels one has to address the problem with repeatability and device stability. In previous section we have addressed the wetting and nanobubbles pinning as well as how to

spot them. In the following section we are continuing this topic by discussing MoS₂-adhesion related artifacts (e.g. delamination and wrinkling) which can significantly influence ionic transport and induce non-linear transport phenomena.

4.6 Delamination and wrinkling phenomena of suspended MoS₂ under applied pressure

The following section is based verbatim on the manuscript in preparation:

Michal Macha^{II}, Sanjin Marion^{II}, Mukeshchand Thakur^{II}, and Aleksandra Radenovic^{II}

Delamination and wrinkling phenomena of single layer, suspended MoS₂ under applied pressure in aqueous environment, In preparation.

M.M., S.M. and A.R. designed the experiment. M.M. performed the measurements, S.M and M.M. analyzed the data and wrote the manuscript. M.M. performed material characterization and MoS₂ synthesis. M.T. transferred the material on the supporting membrane devices. A. R. and S.M. supervised the research. All authors provided important suggestions for the experiments, discussed the results, and contributed to the manuscript.

4.6.1 Introduction

The unique properties of atomic thickness, mechanical and electric properties^{250,277,317,337,495,496} as well as rapid advancements in 2D materials synthesis methods^{497,498} have made 2D-material-based devices a platform of choice to study nanoscale physics in aqueous environments⁴⁹⁹. Suspended, nanoporous 2D-membranes are used in applications such as biosensing¹⁶⁷, DNA translocation⁶, osmotic energy harvesting^{8,9,164}, water desalination¹⁶¹ and gas filtration²⁷². In most nanofluidic experiments, the application of electrical fields is used as a basic tool to probe the ion transport properties of the system^{90,500}. Lately however, the use of hydrostatic pressure as an additional probe has been found to be critically important to study the nonlinear coupling of ion transport with fluid flow^{398,488} as well as a tool to probe proper wetting behaviour⁴⁹³.

It has been established, that applying high voltage can be potentially damaging to the 2D material as it can cause the breakdown of a membrane^{6,198} and membrane delamination through electrolyte intercalation^{501,502}. It is not fully explored however, how applying hydrostatic pressure can influence the membrane performance and 2D film adhesion to the substrate. It was shown, that surface-related phenomena such as material damage, delamination or nanobubbles can exhibit nonlinear current signals^{398,493,501}, analogous to those reported as coulomb blockade⁵⁰³. Thus, even though MoS₂ was proven stable at working pressure of up to 3.5 bar^{12,398}, further investigation of the application of both electrical fields and pressure is crucial to uncover adhesion-related artifacts, help understand the 2D-nanofluidic system and bring insights into designing an artifact-free 2D-material platforms.

In this work we are using a symmetrical hydraulic pressure based setup to investigate the MoS₂/membrane adhesion behaviour during nanofluidic operations^{398,493}. We investigate

^{II}Laboratory of Nanoscale Biology, Institute of Bioengineering, School of Engineering, EPFL, 1015 Lausanne, Switzerland

the influence of applying high voltages (including voltage-mediated pore-drilling protocols) on the reversible 2D film delamination. We demonstrate how the membrane deformation through applied hydrostatic pressure can lead to adhesion defects such as MoS₂ wrinkling and flapping manifested through extremely non-linear current signals and unstable streaming currents. With transmission electron microscopy (TEM) images taken before and after the measurements we showcase the reversibility of the delamination processes. Finally, by analyzing the asymmetric and unstable system behaviour under pressure we show how to properly identify and study membrane properties. The experimental methodology presented here enables to uncover the adhesion issues and brings a deeper understanding of nanoscale physics of suspended atomically thin films in aqueous solutions and their ion transport behavior under experimental stimuli.

4.6.2 Results and Discussion

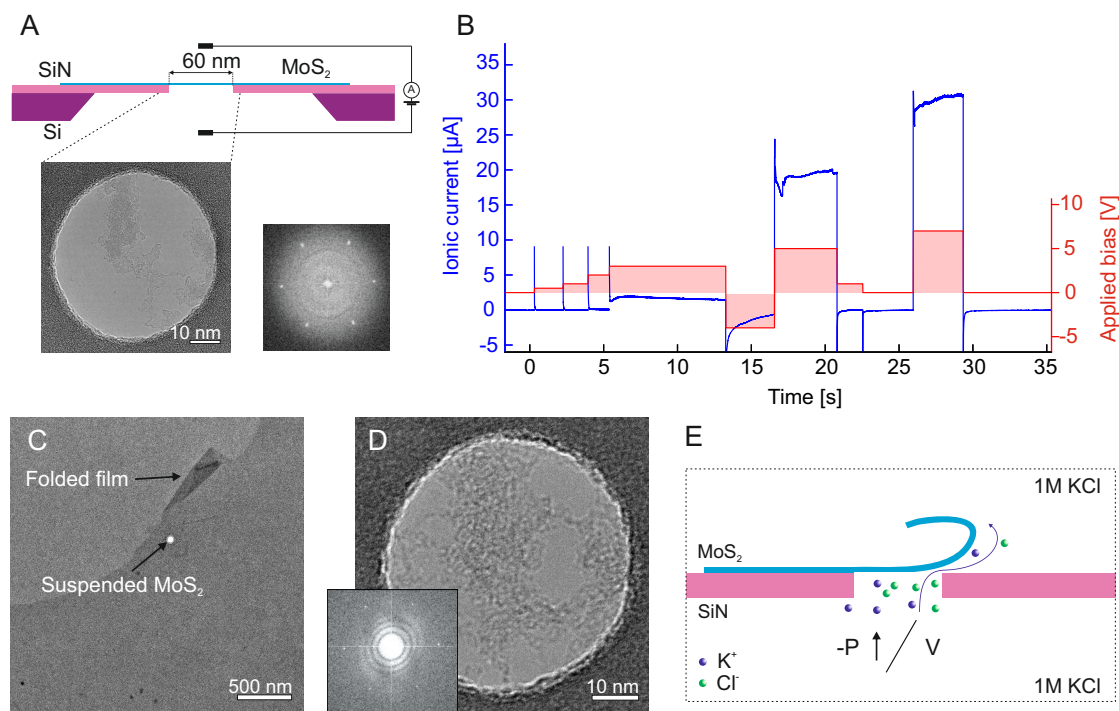


Figure 4.21: Temporary delamination of MoS₂ during nanofluidic measurements. A) Schematic description of the measurement geometry with a TEM image of suspended MoS₂ and the corresponding FFT. The experimental setup and details match those described in^{398,493}, including the transfer method for MoS₂ and pressure setup schematics. B) Measured values of the ionic current (blue, left axis) and applied potential difference (red, right axis) on a MoS₂ sample versus time. Panels C and D show the same substrate as in panel A imaged after the ionic measurement in liquid, indicating that the MoS₂ has survived the liquid immersion and measurement, and the presence of a "flap" near the aperture (panel C). In the proposed model, applied high voltage (or pressure) can cause intermittent delamination of MoS₂ leading to ionic conduction through a created fluidic pathway (E).

Voltage-driven delamination of MoS₂ We have used an atomically thin MoS₂ membrane, irradiated with Xe ions and suspended over the Si/SiN aperture (see Methods section) to probe the adhesion properties in an electrolyte solution. The MoS₂ membrane was placed in the flowcell adapted to apply pressure gradients and test wetting of nanopores^{398,493} (Fig. 4.21A). Degassed 1M potassium chloride (KCl) solution was used as an electrolyte on both cis- and trans- sides of the MoS₂. A typical experiment with freestanding MoS₂ membranes starts with probing the membrane conductance with voltage sweeps and ensuring proper wetting of the system through the application of hydrostatic pressure (i.e. achieving stable values of membrane resistance and capacitance expected of monolayer MoS₂ suspended over the Si/SiN aperture⁴⁹³). Our wetting protocol involves flushing with a degassed electrolyte solution and applying hydrostatic pressure to both sides of the membrane (i.e. compression pressure) to reabsorb any potential, obstinate vapor bubbles back into the solution as reported previously⁴⁹³.

In-situ nanopore creation is the crucial step of substrate preparation which can compromise the sample membrane. We have observed that this step, often regarded as robust and facile, can introduce crucial MoS₂ delamination issues. Most commonly used method is the electrochemical reaction (ECR) drilling protocol^{6,198,504}. A methodology widely used in nanopore research field to create pores in-situ⁹⁰ based on applying gradually increasing high electric fields. These short, periodic voltage spikes are expected to cause defect expansion through an electrochemical reaction and eventually form a nanopore of controlled dimensions^{6,198}. In such attempts to use high voltages to produce nanopores from pristine membranes, we have applied voltages up to several volts. In some cases we noted that after such applications, the resistance of the sample would afterwards return to its original value. An example of such a measurement with a pristine MoS₂ membrane is shown on Fig. 4.21B. Typically, the ECR and subsequent MoS₂ pore formation is expected to occur at applied voltages as low as 0.75 V in MoS₂⁶ with up to 7 V reported for graphene¹⁹⁸. In the case of our experiment, we went as high as 7 V and after comparing the substrate before and after experiments in TEM (Fig. 4.21C and D) we have noted not only that the intact MoS₂ surface has survived the ECR protocol, but also a presence of a folded layer in close vicinity to the suspended area (Fig. 4.21C) indicating that the MoS₂ has shifted in its placement on the substrate.

As observed previously in graphene, applying a high electric field can cause direct membrane delamination from the substrate⁵⁰¹ which can impact membrane conductance (Fig. 4.21E). Such a loss in adhesion was found to occur after exceeding a threshold transmembrane voltage of 0.25 - 0.5V depending on factors such as 2D film surface roughness, existing defects or surface folds⁵⁰¹. The process was found to be reversible i.e. delaminated 2D material relaminates after the transmembrane potential difference is removed and the electrolyte intercalation between 2D film and substrate is no longer energetically favorable⁵⁰¹. A possible mechanism used in the literature for similar effects would involve local Joule heating at the pore causing liquid superheating producing explosive nucleation of a vapor bubble^{505,506}. In our case MoS₂ delamination via local bubbling on the MoS₂/SiN interface is unlikely as we use an electrolyte solution which is undersaturated with gas and the starting ionic current

through the pore is too small to induce significant Joule heating. On the other side, ionic-current induced pore enlargement is also not anticipated as it is reported to occur at low- and moderate applied electric fields and would cause permanent pore etching⁵⁰⁷. We do confirm the delamination hypothesis by observing the reversible increase in ionic conductance while applying high voltage and measuring a nonlinear IV curve shape (Fig. S4.25). This is in accordance to reported studies of voltage-driven graphene delamination⁵⁰¹. We provide additional proof with TEM images showcasing the survival of intact suspended MoS₂ after the experiment (Fig. 4.21E). We hypothesize a forming of a reversible conductive pathway through locally delaminated MoS₂ (Fig. 4.21E) which then collapses back when there is no external stimuli.

Pressure driven delamination of MoS₂ We have observed that reversible delamination may in some cases occur without high voltages but with applying pressure from the backside of the membrane (causing membrane bulging). We see the opening of a conductive channel in the membrane manifested through rapid increase in conductance as the pressure crosses a critical value due to the membrane being bulged. This is seen with multiple samples imaged post-experiment (See supplemental Fig. S4.26), with the exact pressure value at which it happens varying from sample to sample (ranging from approx. 2 to 3 bar). The possible cause may be the difference between the MoS₂ film area transferred over the SiN aperture, varying between substrates, and batch-to-batch differences in the roughness of SiN surface⁵⁰⁸. The normal force on the suspended MoS₂ can be estimated from the diameter of the pore of $d = 60$ nm to be about 1.5 nN at 3 bar of pressure, which is order of magnitude smaller than typical forces applied in mechanical indentation experiments with AFM^{12,490} should not compromise the mechanical stability of the suspended film. This leads to the conclusion that hydrostatic pressure applied from the backside can temporarily delaminate the MoS₂.

MoS₂/SiN delamination events are also present while applying pressure from the frontside of the membrane (i.e. causing membrane indentation), albeit different in character. In comparison to MoS₂ indentation experiments⁵⁰⁹ and bulging/indentation experiments with graphene^{510–512} this is not expected to cause delamination. In our case, we believe that the possible cause could be linked to substrate induced wrinkling. This effect has been seen in materials where the underlying substrate was compressed^{513–515}, where the 2D material detaches as it is energetically more favorable to loose adhesion than to conform to the deforming substrate topography⁵⁰⁸.

In addition to ion transport measurements shown previously, we can characterize the behaviour seen in Fig. 4.22 by doing streaming current and voltage measurements (Fig. 4.23 and 4.24). Streaming current measurements indicate the presence of liquid flow between the two sides of the membrane when the membrane is in a bulged state (Fig. 4.23a most likely due to water permeating between the 2D material and the substrate, but in the indented state the streaming current is recovered only after a certain critical pressure is applied (\approx 2-3 bar, Fig. 4.23b). This critical pressure matches qualitatively the pressure values seen in

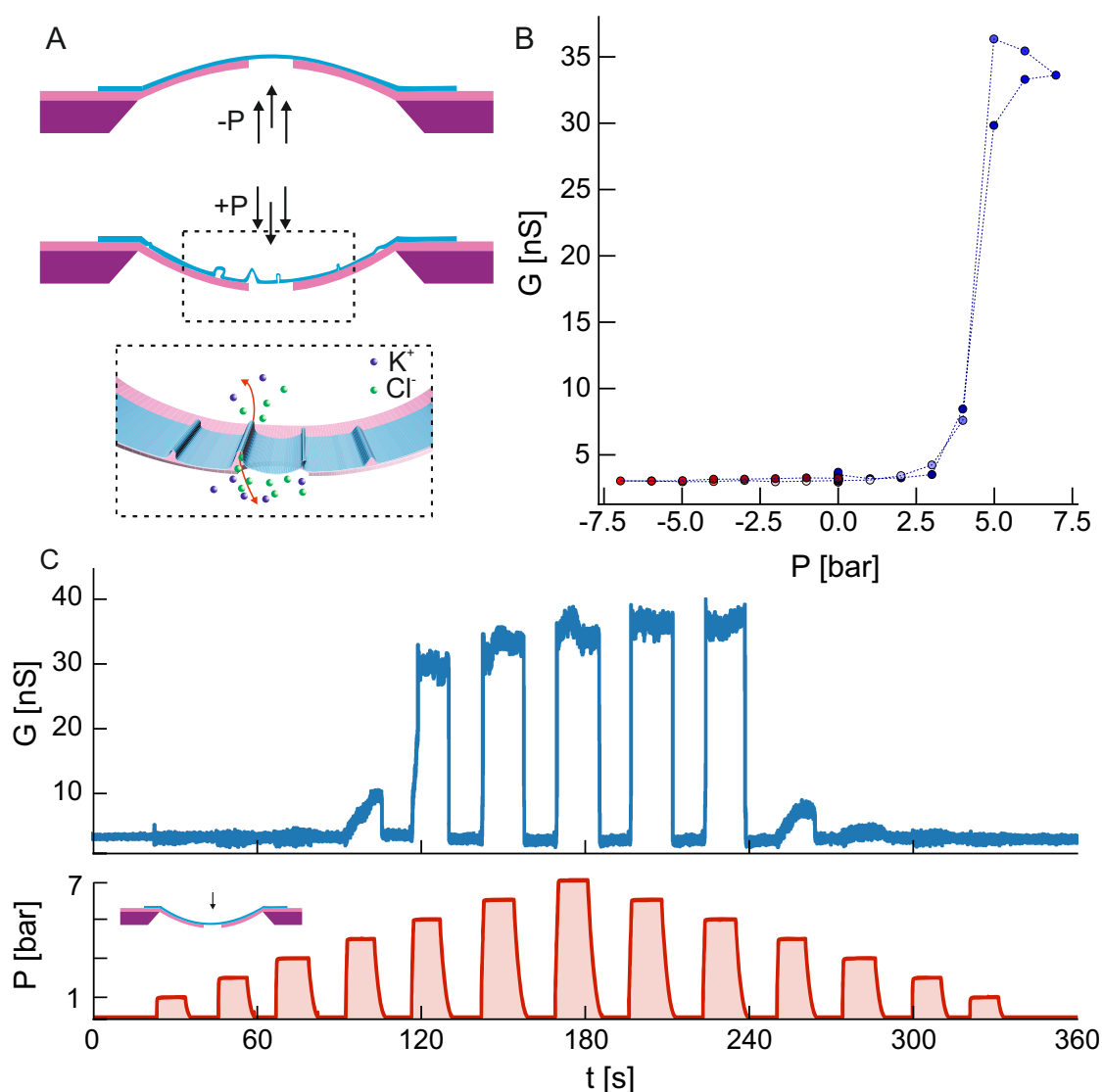


Figure 4.22: **Delamination of suspended MoS₂ due to surface indentation.** A) Toy model demonstrating bulging (top) and indentation (bottom) of the membrane under positive and negative pressure gradients. The bottom inset shows the proposed mechanism for the formation of conductive channels between two sides of the membrane due to local compression and detachment of the MoS₂. B) Conductance G of the sample obtained through ionic current measurements at 100 mV at different values of the pressure gradient P applied to the membrane. The measurement protocol involved subsequent measurements at different pressure values followed by a measurement at $P = 0$ bar to confirm that the baseline value has not changed. Panel C) shows the time traces of the pressure P and conductance G as shown in panel b. Note that only positive pressure gradient values are shown to emphasize the abrupt increase in conductance seen in panel B.

ionic current measurements (Fig. 4.22b,c). In order to clarify the nature of the ion transport, we opted to perform streaming potential measurements (Fig. 4.24c) using an electrometer grade buffer preamplifier. Streaming potential, unlike streaming current, does not in the first approximation depends on the effective size of the ionic channel (i.e. the geometry), and can

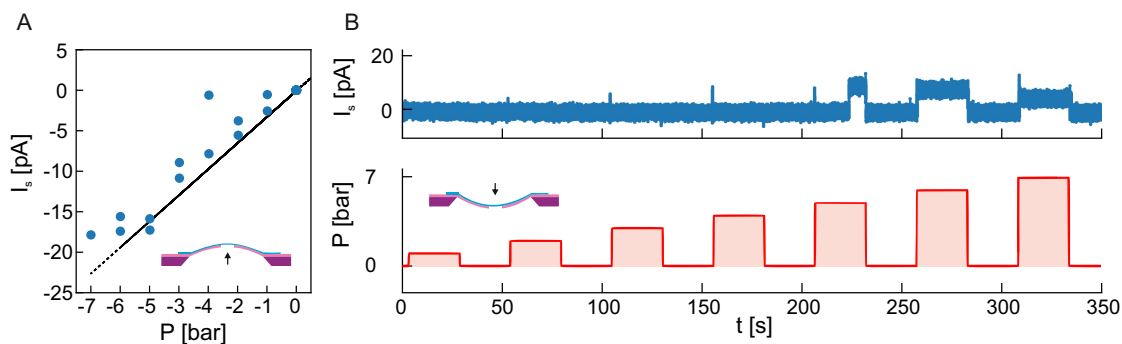


Figure 4.23: Streaming measurements on suspended MoS₂ during delamination. A) Streaming current I_s as measured on the sample shown in Fig. 4.22b,c during the membrane bulging state. No external potential was applied to the sample (closed circuit measurement). B) Anomalous increase of streaming current I_s for positive pressures matching the delaminating state in Fig. 4.22b,c. The top panel shows the time trace of the measured streaming current I_s , while the bottom panel shows the applied pressure gradient P .

be written as $V_S = \epsilon_r \epsilon_0 \zeta P / (\sigma \eta)$ with ϵ_r the relative permittivity of water, ϵ_0 the permittivity of vacuum, ζ the surface zeta potential, P the pressure gradient, σ the electrolyte solution conductivity and η the viscosity of the solution.^{484,493,516} In four samples showing the same qualitative behaviour as presented here we obtain comparable results i.e. reversible, local delamination or loss in adhesion that is caused directly by measurement conditions (high voltage or applied pressure). The reversible, impermanent character of this state is confirmed by comparing TEM images before and after measurements (See supplemental Fig. 4.26). In the bulging case we note the presence of a streaming potential with zeta potential values ranging from 11 to 17 mV, typical for MoS₂ pores and higher than the usual value of 8-9 mV we see in these conditions without any MoS₂ present (pristine SiN_x). This would indicate an occurrence of a water flowing through the MoS₂ membrane and dragging solute ions in the surface double layer while in an indented/wrinkled state, possibly either through defects in the MoS₂ or through a channel formed due to the normal force of the pressure lifting the MoS₂ away from the aperture. The streaming potential in the indented case shows unstable and almost an order of magnitude larger values as pressure is applied. The pressure sweep protocol used in this work assumes the application of gradually increasing hydrostatic pressure with a pause at 0 bar in between the pressure steps (Fig. S4.24B and C). The observed, unstable variations in measured streaming potential do occur at each application of the pressure. This suggests pressure-induced changes to MoS₂ surface charges. We propose, that this phenomenon is directly related to the ion-conducting-wrinkle pathways changing and reshaping under each application of a hydrostatic pressure step.

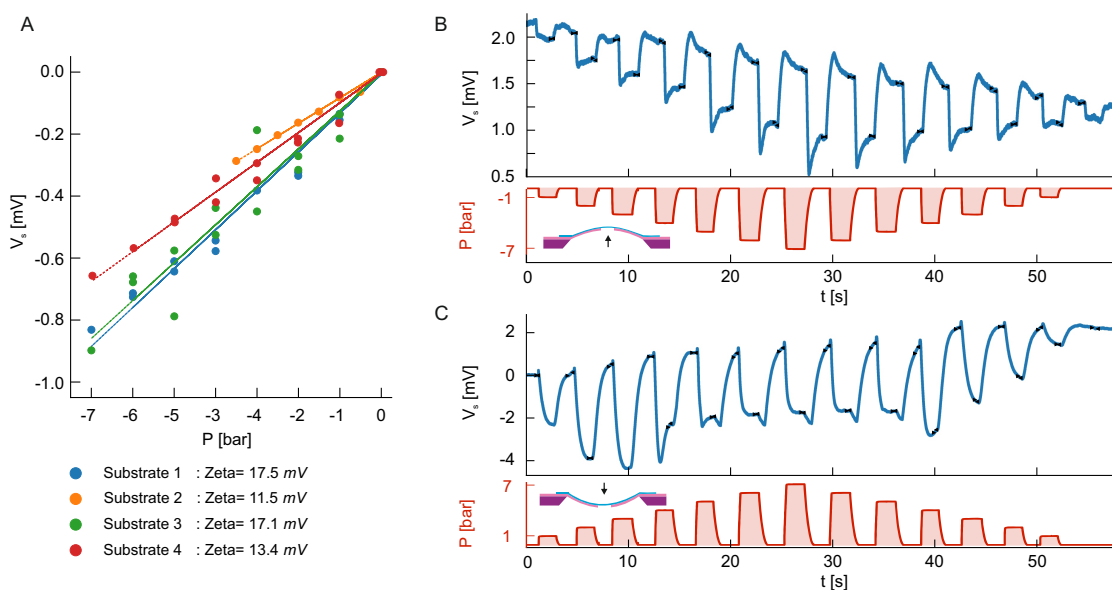


Figure 4.24: **Streaming measurements on suspended MoS₂ during delamination.** A) Streaming potential V_s measurements obtained for four different samples showing analogous behaviour as in Fig. 4.22b,c. Measurements were done in the open circuit configuration. A linear fit gives the values of the apparent *zeta* potential for the membrane. (Note that the measurement protocol follows the same approach as before with intermediary measurements at $P = 0$ to check for baseline drift, and two measurements at each intermediary pressure value to check for hysteresis after the maximal pressure value was applied) Time traces of the streaming potential V_s and applied pressure gradient for Sample 1 are shown in panels B and C. Panel B) shows measurements of the streaming potential during the bulging case, while panel C during the delaminating case.

4.6.3 Conclusion

The use of pressure with suspended 2D materials on a thin membrane substrate is of interest as it allows probing the effects of lateral strain on the ion transport of nanopores in 2D materials^{388,398} as well as coupling of ion transport with fluid flow^{398,488}. Both these effects require a good understanding of the behaviour of such systems under mechanical and electrical strain. This work demonstrates how both permanent and temporary delamination of 2D materials can be induced by pressure and potential differences between the membrane. We demonstrate that the application of pressure pulses can change the adhesion and shape of delaminated 2D film wrinkles leading to unstable and chaotic surface charges resulting in unexpected transmembrane streaming currents. We show a measurement methodology that allows to detect these adhesion issues and accurately identify them. The suspended 2D film wrinkling phenomenon needs to be taken into consideration while using pressure probes for wetting, bubble gating through applied hydrostatic pressure⁴⁹³ and probing ionic properties using pressurized setups^{12,398,517}. Although the large modulation of ionic transport due under partial delamination is similar to the case of pressure induced nanoparticle blockages⁵¹⁷ and could be used to produce more robust mechanical pressure sensors, it is still far away from true mechanosensitivity where ion transport is modulated by mechanical stress directly modulating the energy barriers for single ion translocations^{388,518}. Our approach allows better

understanding of measurements with supported 2D materials, i.e. avoiding misinterpreting the measured data and could be used to probe how the electrical field and fluid flow at the nanoscale could influence membrane adhesion for future applications. Given the dynamic and volatile nature of the delamination events, the design and fabrication of nanofluidic devices with 2D films has to be revised to ensure stable and reliable device performance.

4.6.4 Methods

Substrate preparation MoS₂ was synthesized on 3-inch sapphire substrate with tube-furnace MOCVD setup using the liquid-promoter approach^{273,316}. Cleaned and annealed in air sapphire wafers were coated with sodium molybdate mixture and heated to 870 °C under ambient argon flow. After reaching the designated temperature the substrate was subjected to the flow of 12 sccm of molybdenum hexacarbonyl (MoCO₆), 4 sccm of diethyl sulfide (DES), 4 sccm of hydrogen and 1 sccm of oxygen for 30 min. Synthesized MoS₂ on sapphire was then cooled naturally under argon atmosphere. As-grown monolayer MoS₂ was transferred onto holey Si/SiN membrane chips (Norcada) using wet transfer method^{90,273} and imaged in transmission electron microscope (TEM) to confirm the successful fabrication of a suspended MoS₂ membrane.

TEM imaging Before and after nanofluidic experiments suspended MoS₂ membranes were imaged at ThermoFischer Talos F200S at 80 kV accelerating voltage. After the nanofluidic measurement, substrates were taken out of the flowcell and bathed several times in hot DI water to dissolve remaining salts and minimize subsequent device contamination and salt crystallization. Substrates were then gently dried and imaged. All salt-cleaning steps were performed with caution to minimize the fluid flow and potential MoS₂ delamination caused by that.

Nanofluidic measurements Samples used were in the form of 5x5mm Si/SiN membrane devices mounted into a fluidic chamber as described previously and using the same measurement protocols^{398,493}. All liquids in touch with the sample were in situ degassed using a 925 l Systec AF degassing chamber. Electrical measurements were done using a Zurich Instruments MFLI lock-in amplifier with the MF-DIG option using chlorinated Ag/Cl electrodes. Both DC and AC bias was applied using the signal output of the instrument, while the current through the sample was measured using the built in current to voltage converter. Streaming potential measurements were performed using a ultra-low input bias current (femtoampere level) electrometer grade buffer using the ADA4530 opamp. All electrical measurements done while sweeping the pressure were done after the pressure level has stabilized to at least 5% of the target value. In the case of DC current measurements an additional wait time of 1 s was performed after the pressure settling.

We used 1M KCl with 10 mM Tris buffered to pH 8 for all conductance measurements. All buffers were prepared using MiliQ grade water(18.2 M Ω /cm). The conductivity of all solutions was checked before use with a Mettler-Toledo FiveEasy Plus. All solutions were filtered through

a 20 nm filter before use (Whatman Anotop 25 plus).

4.6.5 Supplementary Information

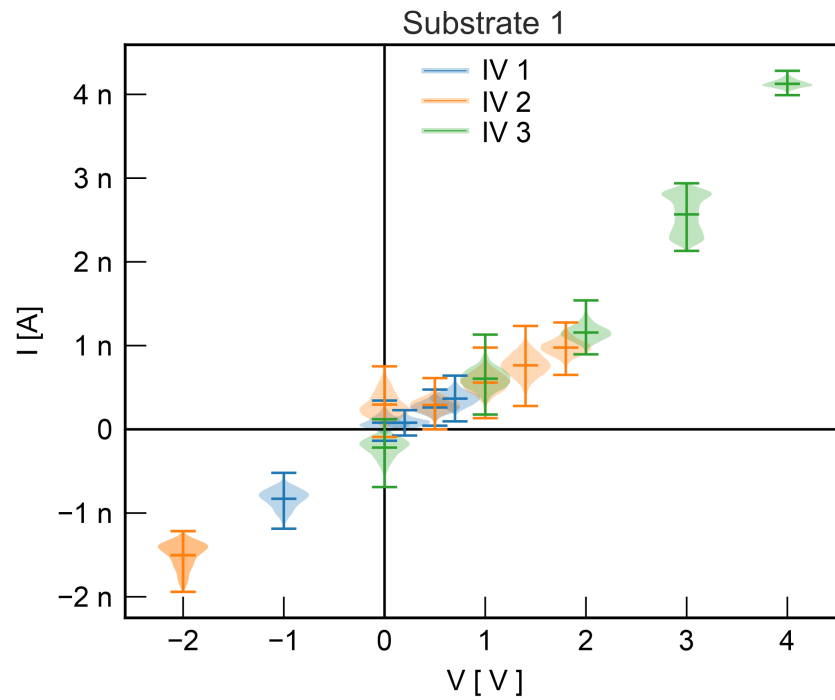


Figure 4.25: **Non-linear IV of delaminated MoS₂**. The IV characteristic was compiled from three separately performed ECR drilling experiments, showing high membrane conductance and a non-linear character of the ionic current at higher applied bias.

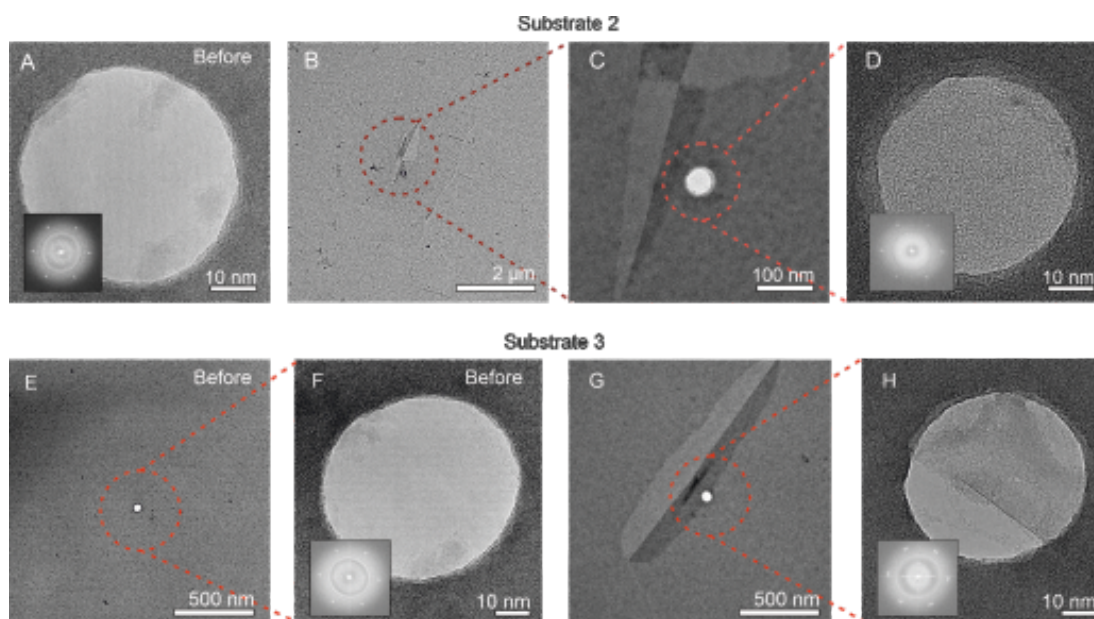


Figure 4.26: **TEM images of pressure-induced delaminated MoS₂**. Compilation of images prior to nanofluidic measurement (A) and after (B,C,D) showing a delaminated MoS₂ in the close vicinity of the nanopore, with the suspended MoS₂ still present over the aperture. Similarly, MoS₂ on the substrate 3 shown on panel E and F, does delaminate after the pressure sweeps and lead to the 2D film delamination event (G and H).

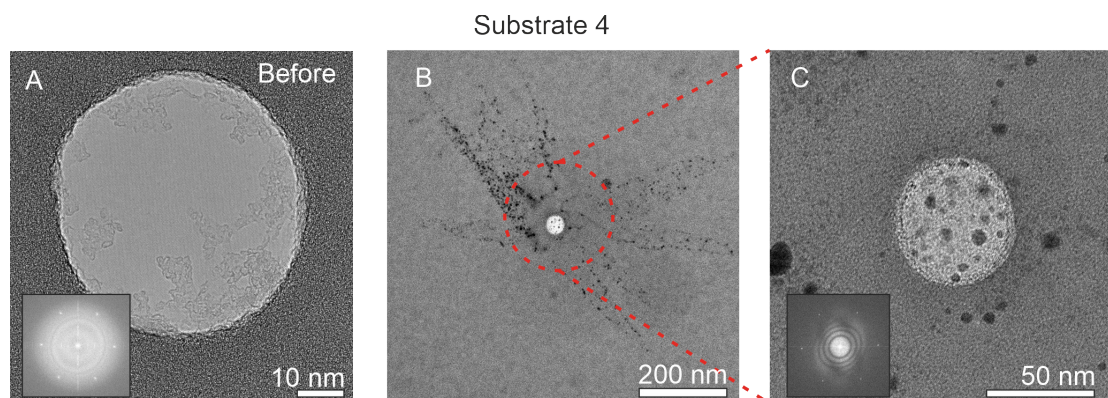


Figure 4.27: **TEM images of pressure-induced wrinkled MoS₂**. Images of Substrate 4 before (A) and after the experiment (B and C) show a proof of intact MoS₂ film suspended over the aperture, even after applying registering high ionic currents and conductance indicating punctured or lifted off MoS₂ under applied pressure. Due to significant substrate contamination related to post-experiment cleaning and drying, insets are presenting the FFT images proving the existence of MoS₂ over the aperture area.

4.7 Conclusion

Nanofluidics experiments discussed in this section are focused around the application of MoS₂ membranes irradiated with Xe-ion PFIB system described in Chapter 3. The centerpiece of the experiments is the homemade measurement setup which allows to apply hydrostatic pressure as an additional probe of the membrane device. Substantial efforts were put into setup design and pressure experiment interpretation. Gained results enabled to investigate frequently omitted in the nanofluidic research events of wetting artifacts and nanobubble-pore obstructions manifesting in asymmetric IV curves and increased flicker noise. The wetting was studied on hydrophobic and hydrophilic solid state pores as well as on suspended, porous MoS₂ monolayer and showed a pressure-induced switching behaviour.

Insights gained on how to identify and consequently avoid wetting artifacts were used to further study Xe-irradiated MoS₂ membranes and their mechanosensitivity under applied pressure. Initial results were indicative of the mechanosensitive ion transport through the membranes, however underlying substrate wetting anomalies halted further development of this project. The osmotic power generation with Xe-irradiated MoS₂ was similarly limited by the device instabilities. Frequent events of wetting artifacts, MoS₂ delamination and pore clogging lead to low yield of measured devices as well as wide range of acquired data. This marks the Xe-irradiated membranes as a promising work-in-progress in need of further study and focus on fine-tuning and optimizing fabrication steps to avoid potential contaminants, delamination events and hydrophobic, bubble-pinning surfaces.

Finally, the data acquired through numerous nanofluidic experiments with applied pressure gradients on MoS₂ membranes was used to identify and discuss the pressure-induced delamination and wrinkling of 2D materials. We have demonstrated how the permanent and intermittent loss in adhesion can lead to the formation of channels allowing ion transport coupled with fluid flow and lead to unstable surface charges and transmembrane streaming currents. The use of pressure pulses in the nanofluidic applications with suspended 2D materials allow to better understand how the electrical fields and fluid flow influence the membrane adhesion at the nanoscale.

In general, studies presented in this chapter are highly relevant to the development and study of suspended, nanoporous 2D membranes. The experimental methodology allows to revise non-linear and asymmetric events and identify wetting and adhesion artifacts.

5 Conclusion and Outlook

This chapter summarizes the broad, multidisciplinary efforts discussed in this thesis in engineering and studying large-area nanoporous MoS₂ membranes. Insights acquired during the study are used to advance the state-of-art knowledge in field as well as provide a general outlook and a personal perspective on the synthesis and application of 2D membranes in osmotic power generation and mechanosensing.

A significant portion of the thesis was dedicated to developing the CVD and MOCVD MoS₂ synthesis methods. Starting with the location-specific growth and later focusing on large-area substrates, the general application of chemical vapor deposition systems was proved versatile and tunable. Following the goal of synthesizing monolayer material on a wafer scale, the use of metallorganic, gaseous precursors quickly became a dedicated approach allowing most uniform and reproducible results. The utilization of spin-coated precursor/seeding mixtures combined with adding O₂ during the growth step enabled to establish a facile, self-regulating monolayer synthesis recipes, scalable to 2- and 3-inch substrates. After extensive experiments, the recipe was adapted to a commercial showerhead system thus paving a way towards establishing an industrial, 4-inch scale process. In all cases, the yielded material was characterized and analyzed to assess the quality, uniformity and crystallinity in the context of an application in nanofluidics membranes. In general, discussed in this thesis synthesis protocol was a backbone of the laboratory work, used to supply my colleagues and collaborators with the material to study applications in biomolecule sensing, photonics, energy harvesting, ion transport, nanoelectronics and defect engineering. Providing a continuous, reliable supply of the MoS₂ was a difficult task, requiring a significant engineering and maintenance efforts as well as attention towards process safety, proactive and reactive troubleshooting and deep understanding of MOCVD physics. Developing, optimizing and improving the MOCVD was done during the entire period of the thesis, and yet the nature of the 2D materials growth leave a lot of room for further academic work and development (e.g. to establish recipes for other materials from the TMD family such as WS₂, MoSe₂, Nb₂ etc. and their heterostructures).

Ion irradiation was used as a large-area nanopore fabrication tool. The Xe-ion PFIB system was employed to investigate the nanopore drilling parameters of a suspended, monolayer

MoS₂ and its application in nanofluidics. Explored irradiation settings allowed to map the beam parameters and output nanopore densities and geometry. Combined with pore-edge analysis, the irradiation was used to evaluate the statistics of nanopore edge atomic sites and their potential influence on ion and water permeation. In parallel to the nanopore-focused irradiation of suspended films, the PFIB system proved to be useful in the defect engineering and study of multilayer MoS₂ and hBN. Ability to fine control the milling depth with high spacial precision created an excited opportunity to study structural and optical transitions in irradiated hBN as well as create defect maps in MoS₂ through thiol-functionalized fluorescent probes attached to sulfur vacancies. The Xe-ion irradiation is a versatile nanofabrication tool enabling to design and create a wide variety of surface modifications crucial in materials science and photonics research. For nanofluidics application however, PFIB irradiation should be carefully redesigned in order to minimize beam-induced deposition and surface contamination.

The atomically thin MoS₂ naturally synergizes with nanofluidics research. Suspended, 2D films are a rich platform to study ion transport and fluid flow through nanopores. Combining the large-area synthesis and precise Xe-ion irradiation-drilling technique was one of the main goals of this thesis. To expand the research area we have designed a unique setup allowing for application of hydrostatic pressure. We have established an experimental baseline allowing to identify and investigate the gas nanobubbles obscuring the ionic channels. The hydrostatic pressure applied on front- and backside of the membrane was used for studying the mechanosensing behaviour of nanoporous MoS₂ membranes. Ion irradiated films were also used in salinity gradient conditions and studied in the context of osmotic energy harvesting. Even though we were not able to reliably measure and prove neither mechanosensing nor osmotic power generation with Xe⁺ irradiated membranes, the experiments were fruitful in information related to fluid flow, non-linear ion transport, adhesion and wetting artifacts. Discussed here incremental steps in understanding multipore systems under pressure are of high importance in nanofluidic field and should be further investigated. Atomically thin films, such as studied here MoS₂, are fundamentally prone to contamination and, as discussed in the Introduction chapter, do require a particular cleanliness regime in order to reach their full, estimated potential.

To achieve the goal of upscaling the 2D-nanopore membranes, one has to be aware of their intrinsic limitations. Long and complex device fabrication protocols are a significant bottleneck and leave a wide room for improvement. To ensure a high fabrication yield and reproducible device parameters, the steps such as thin film transfer and supporting substrate surface treatment have to be revised. Among many nanopore drilling methods, the PFIB ion irradiation has proved to be a powerful tool for creating large-area pore arrays, however it does require further development. The substrate surface contamination has to be minimized to limit the ion-beam induced contamination occurring during irradiation and subsequent TEM imaging. Maintaining the precise control over the 2D membrane porosity with a minimal divergences from the desired nanopore diameter is the most desired feature of a nanopore drilling process. With that in mind, the ion beam irradiation might be attractive if combined with other processes

such as plasma treatment or etching in aqueous solutions (e.g. in-situ, in the experimental, fluidic setup) to establish a two-step drilling methodology. Finally, there is a plenty of the room to use the pressure-nanofluidic setups to study the nanoscale physics of confined ion channels and nanopores. The application of MoS₂ in artificial mechanosensing requires a systematic approach combining the nanopore fabrication, high-resolution imaging and ion- and fluid flow modelling in order to understand this phenomenon and demonstrate the working, mechanosensitive, synthetic 2D membranes. Similarly, the study of 2D nanopores in osmotic energy harvesting is a highly promising avenue. In my opinion, the nanopore fabrication upscaling efforts should continue in order to tackle the nanotechnological challenges and keep using atomically thin films viable for this application.

This summarizes the final conclusions and motivation behind tackled research challenges. The highly interdisciplinary nature of the thesis enabled me to specialize in multiple, nanotechnology-oriented research fields and gain invaluable research experience. My studies made me believe that the ion irradiated, atomically thin films are highly attractive membrane materials. They show a great promise in broad nanofluidic applications and if given sufficient academic and engineering attention will contribute to solving grand, global problems in the field of renewable energy, water filtration and desalination.

A An appendix

Material	Pore diameter	Pore Length	porosity	pH	Type of experiment	Power density	Power per pore	Osmotic conductivity per pore	Electrokinetic energy conversion efficiency	Ref.
Commercial appli-										
cations										
Statkraft PRO power plant	/	/	/	/	/	1 W/m ²	/	/	/	21
Mega Ton PRO power plant	/	/	/	/	/	13 W/m ²	/	/	/	22
Global MVP Project	/	/	/	/	/	5 W/m ²	/	/	/	23
REAPower RED power plant	/	/	/	/	/	0.83 W/m ²	/	/	/	24,25
Solid state pores										
Silica	4nm x 25um	140um (channels)	nanochannels	5.6	Experimental studies	7.7 W/m ² in 0.001/1M	0.16pW in 0.1/1nmM	73.4 pS	31 %	52
Porous alumina	2-3nm	90nm	4 * 1012 pores/cm2 (16.7% porosity)	~7	Experimental studies	0.024 W/m ²	6 * 10 ⁻⁷ pW	1.53 fS	/	145
	10 – 100nm	4um	108 – 109 pores/cm2	5.4	Numerical studies	0.01/0.5M	0.14pW	256.8 pS	/	54
	10 nm	60um	1.18 * 1011 pores/cm2	5.4	Experimental studies	0.001/0.1M	0.1/1nmM	/	/	53
	100nm	60um	1.2 * 109 pores/cm2	5.4	Experimental studies	542nW per cell?? 10/100nmM 0.98nW/m ² 0.1/10nmM	4.9 - 8.2 * 10 ⁻⁵ pW	150 - 360 fS	16%	51
Alumina with porous carbon (Janus membrane)	200nm	60um	1.2 * 109 pores/cm2	/	Experimental studies	0.59mW/m ² 0.1/1mM	1.5 * 10 ⁻³ pW	4.9 pS	/	252
	7/80nm	4.2um	109 – 1010 pores/cm2	~7	Experimental studies	17.3mW/m ² 0.017/0.51M	3.5 * 10 ⁻² pW	87.9 pS	37.30%	142
	60nm	85um	10 12 pores/cm2	11	Experimental studies	0.01/0.5M	5.8 * 10 ⁻⁴ pW	472.9 fS	~30%	135
	15nm	20um	/	5.6	Experimental studies	2.87 Wm2 0.01/0.5	2.9 * 10 ⁻⁴ pW	729.7 fS	/	250
Conical Polymer pores	10-50nm (tip)	12um	108 – 109 pores/cm2	5.6	Experimental studies	0.001/1M	26pW	21.2 nS	4%	58
	2um (base)	12um	1 pore	5.6	Experimental studies	0.001/1M	45pW	36.7 nS	/	93
	10-40nm (tip)	6um	2 106 pores/cm2	7.6	Experimental studies	0.078 W/m ² 0.01/0.5M	25pW	20.4 nS	/	180
	1.5um (base)	11um	10*6	6	Experimental studies	945 W/m ² 1/300mM	120pW	120.1 nS	/	137
Polymer Janus membrane	30-300nm (tip)	500nm	/	4.3	Experimental studies	0.7 W/m ²	7.0 * 10 ⁻³ pW	17.8 pS	17.50%	60
	>1um (base)	11um	14-22%	~8	Experimental studies	0.01/0.5M	2.7 * 10 ⁻² pW	67.6 pS	35.70%	61
	2um (base)	12um	1011 pores/cm2	~8	Experimental studies	2.66 W/m ² 0.01/0.5M	3.5 * 10 ⁻⁴ pW	889.9 fS	/	181
	10/50nm	24x500um	microchannels	5.6	Experimental studies	0.01/0.5M	7.0 * 10 ⁻⁴ pW	471.4 fS	36%	251
Nafion® perfluorinated membrane	>10nm	1 um	1 pore	11	Experimental studies	0.001/2M	20pW	16.3 nS	/	85
hBN Nanotube	15 – 40nm					4 * 104 (est) W/m2 0.001/1M				
2Dnanopores										
GO flake RED cells	0.9nm	0.5 – 100 um (stacks)	/	5.6	Experimental studies	0.77 W/m ²	/	/	36.60%	249
Graphene	0.4 – 10.0nm	0.34nm	Intrinsic defects	7	Experimental studies	700(est) W/m ² 0.001/1M	10pW	18.4 nS	/	91,124
MoS2	2-20nm	0.65nm	1 pore (30% estimation = 3*1012)?	11	Experimental studies	3*106 (est) W/m2 0.001/1M	0.01/1M 1nW	815.4 nS	20%	80
	3nm	0.65nm	1 pore	7.4	Experimental studies	/	1.2 - 2.8 pW	22.5 - 51.4 nS	8 - 44%	156
	10nm					7.1 * 105 W/m2	130 - 160pW	238.5 - 293.6 nS	40-45%	253
	1nm	0.65nm	1 pore	5	Numerical studies	0.001/1M	/	/	/	

Table A.1

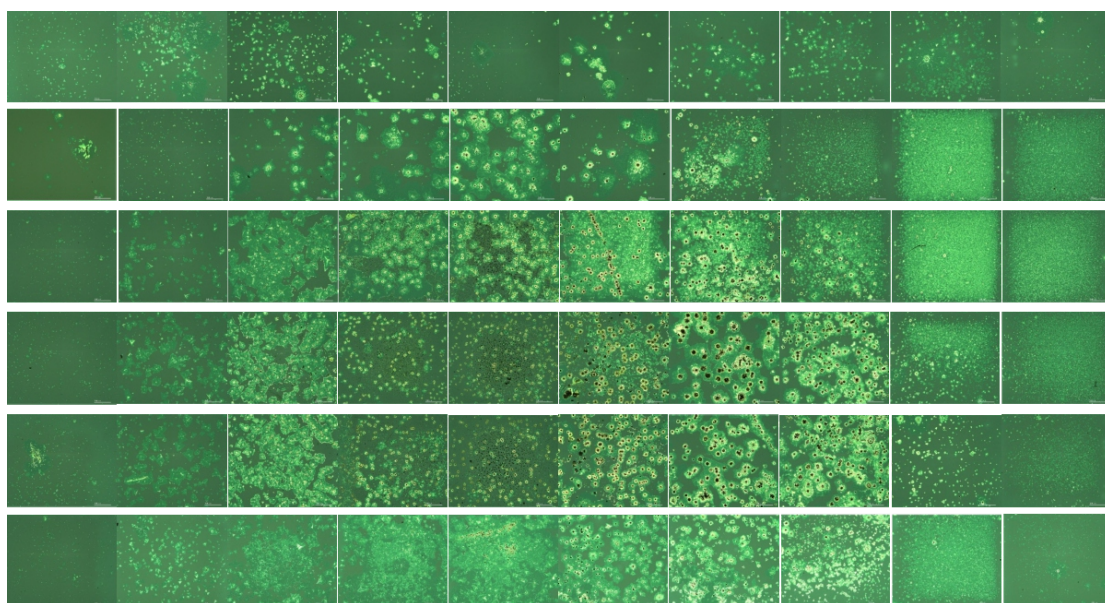


Figure A.1: **Location-specific synthesis - coverage map.** A map of MoS₂ coverage done on chip deposited in location-specific experiments using large-scale chip holder. Middle part was found unusable due to the direct exposure of MoO₃ vapor.

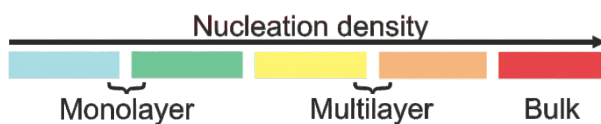
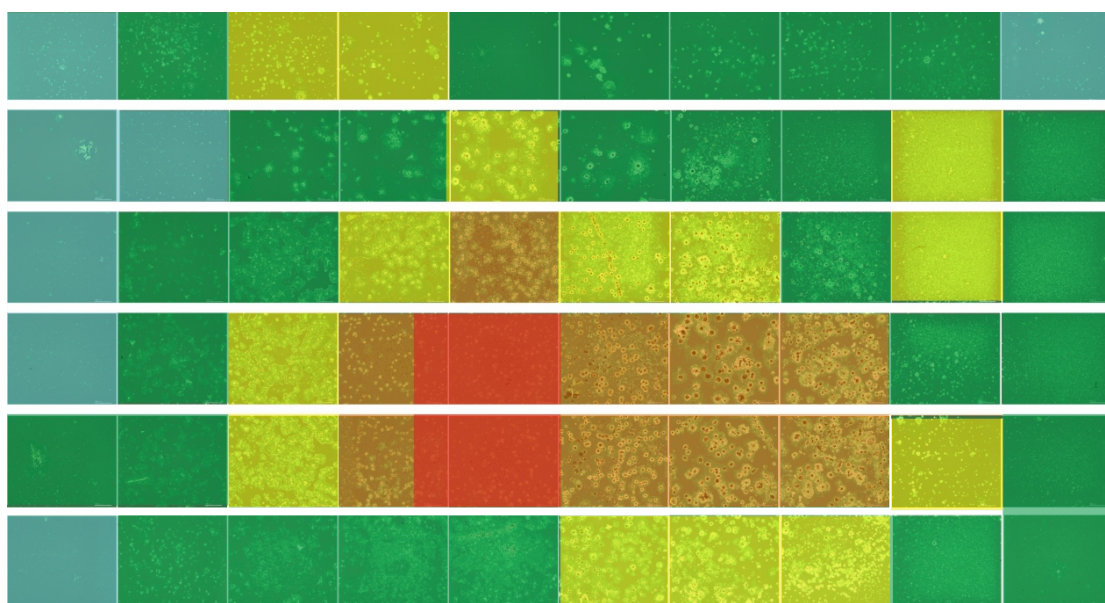


Figure A.2: **Location-specific synthesis - coverage map, unmarked.** A map of MoS₂ coverage done on chip deposited in location-specific experiments using large-scale chip holder. without color coding.

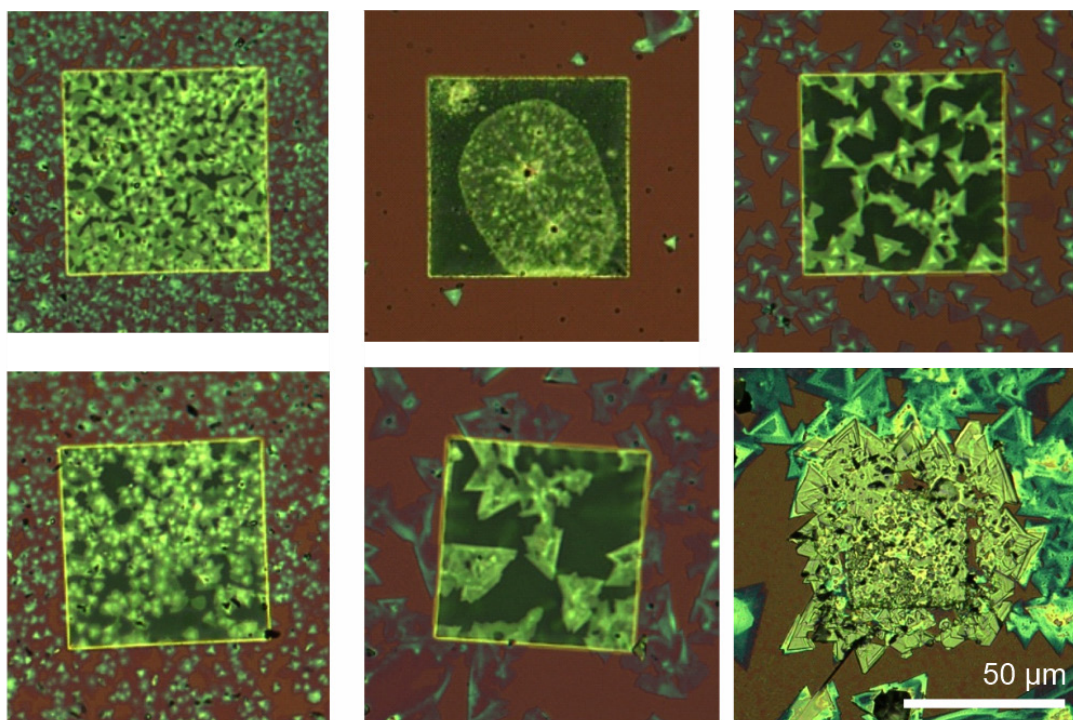


Figure A.3: **Overgrowth of MoS₂ on apertures.** Examples of SiN_x apertures with MoS₂ nucleated at the opening site thus inevitably clogging the membrane.

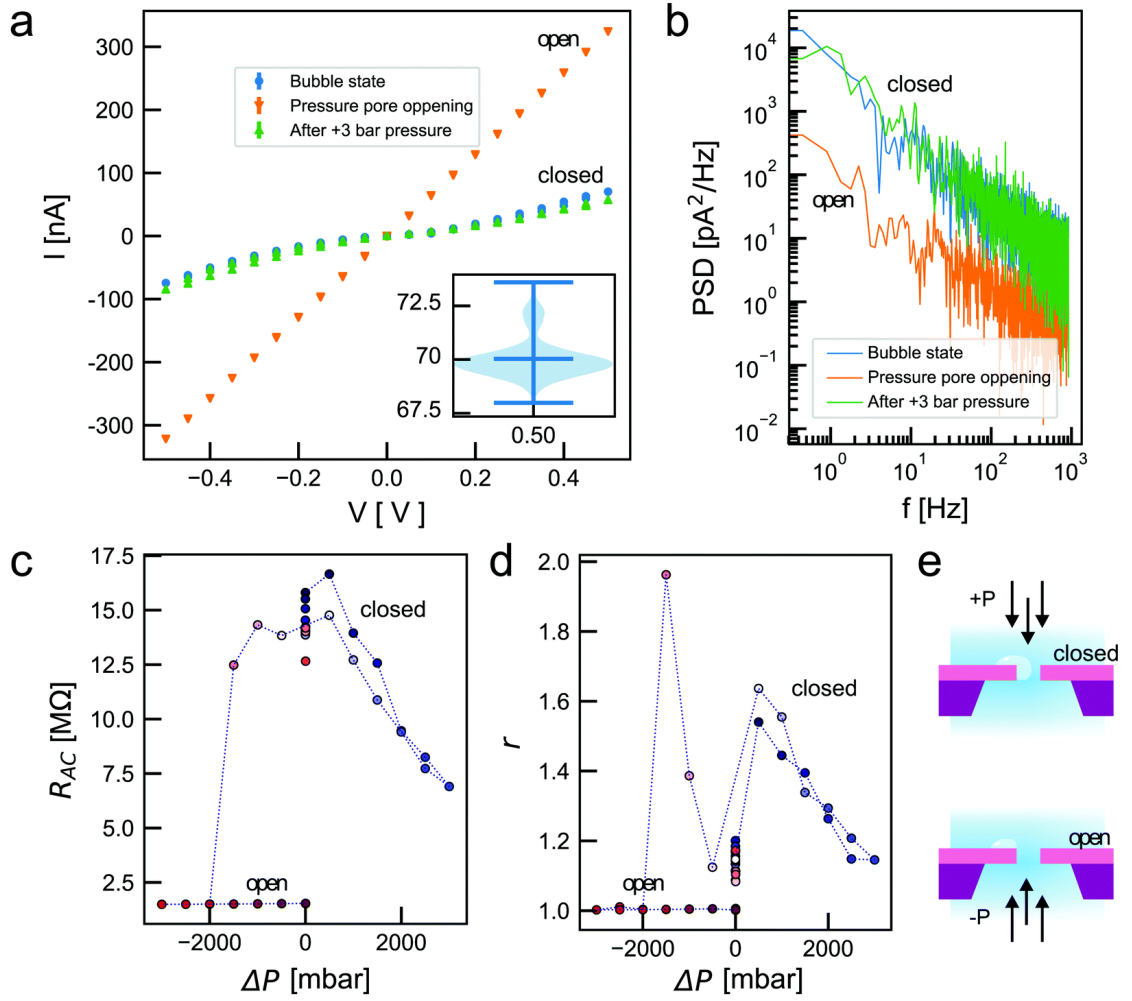


Figure A.4: **Pressure gating of nanobubbles in hydrophilic nanopores.** (a) IV curve of a bubble inside a $d \approx 75$ nm diameter nanopore before applying pressure (blue), after opening with pressure (orange), and after closing with pressure using +3 bar (green). The resistance of the open pore is found to be $R = 1.61 \text{ M}\Omega$ which is within 10% of the expected resistance of the nanopore in 1 M KCl Tris buffered to pH 8. Inset shows the extrema and probability density for current fluctuations at $V = +0.5$ V for the bubble state. (b) Power spectral densities of the current traces at +0.2 V from panel (a). (c) Resistance obtained during a pressure sweep performed on the pore from panel (a) which switched the pore from an obstructed to a open state. (d) Rectification $r(V) = |I(+0.1V)|/|I(-0.1V)|$ as measured during the pressure sweep in panel (c). (e) Proposed toy model of the hypothesized nanobubble wetting behavior with different applied pressure gradients. Adapted from⁴⁹³.

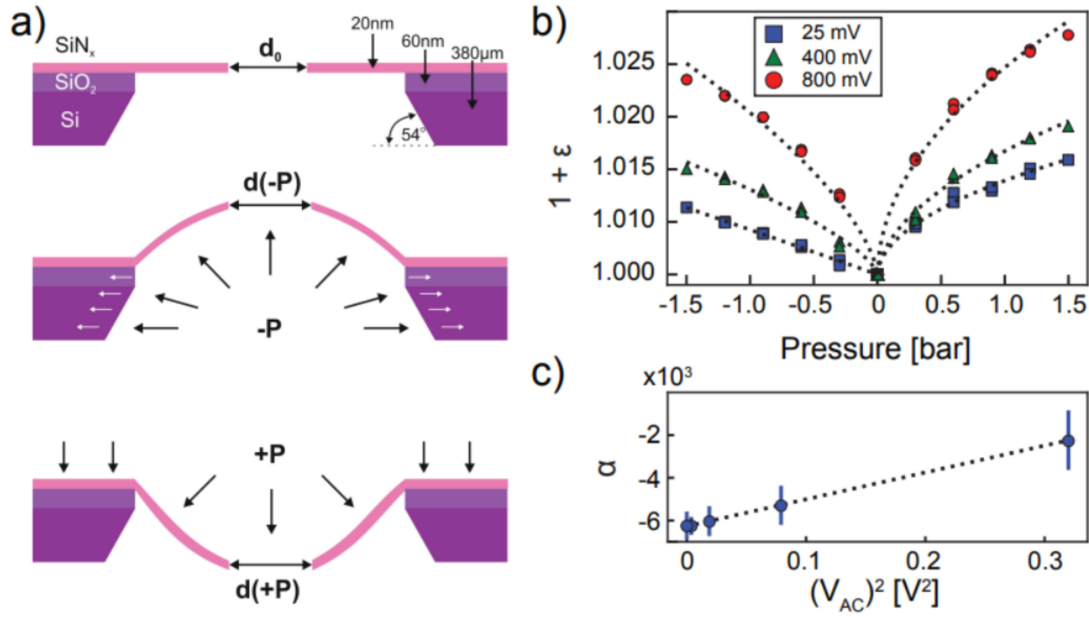


Figure A.5: **Elastic response and strain enlargement of Si/SiN_x membranes.** A schematic representation of the solid state porous membrane and the pressure-induced deformation with pore enlargement (a). Normalised strain versus the applied pressure under varying bias voltages V_{AC} (b). The dependance of residual stress factor α follows a quadratic relation with applied V_{AC}. Adapted from³⁹⁸.

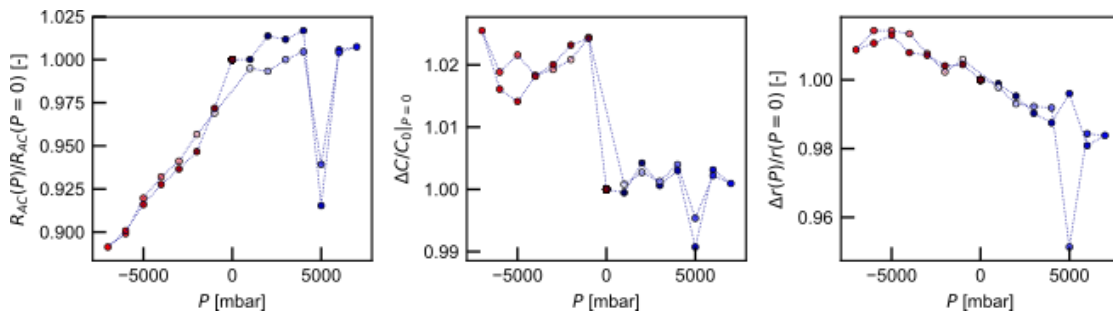


Figure A.6: **Asymmetric mechanosensitivity with MoS₂.** An example of porous MoS₂ membrane showing a asymmetric mechanosensitivity (A). Corresponding, normalized capacitance and rectification is shown on panel B and C respectively. The return to the 0-bar stable parameter values after each pressure sweep may be indicative of pressure-induced delamination of MoS₂.

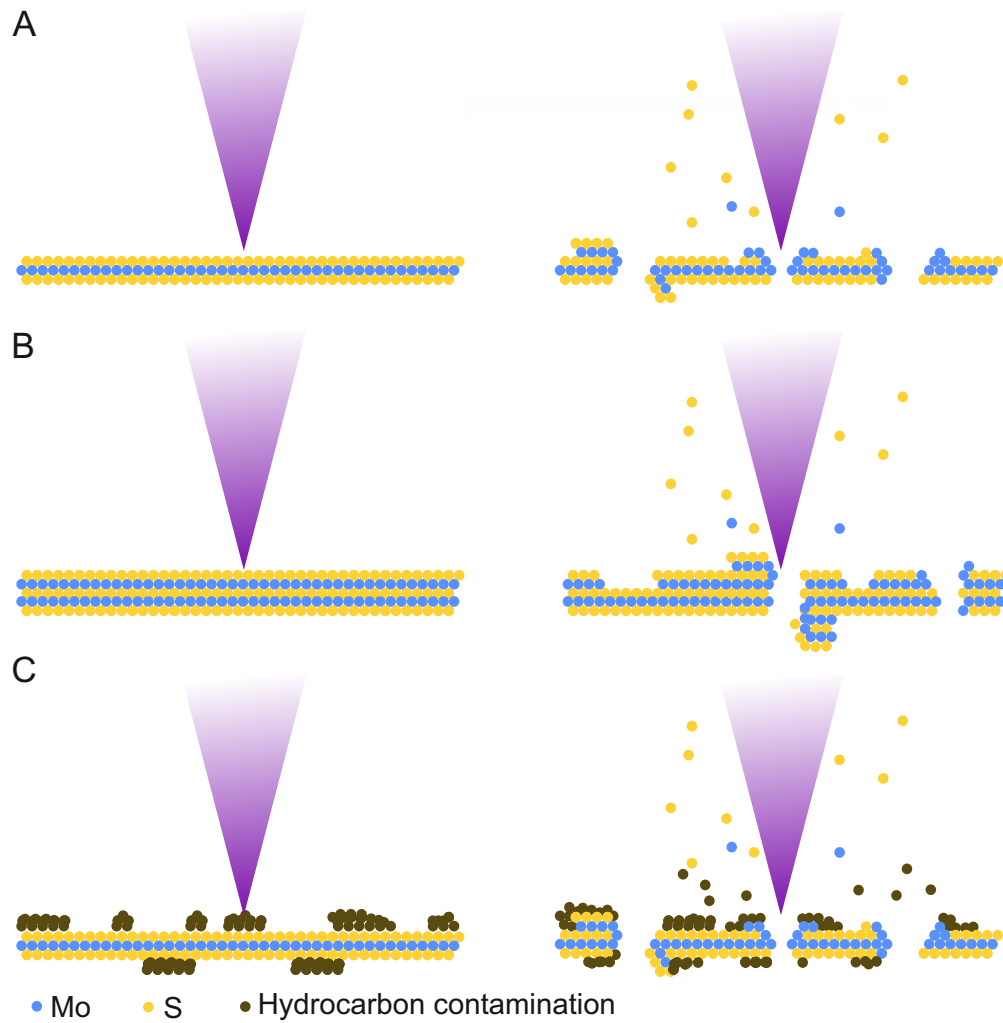


Figure A.7: **FIB-induced surface contamination.** In ideal case the FIB should directly pierce the suspended film, sputtering substrate atoms as shown on panel A. With multilayer cases, we have observed a distribution in creating pores and stripping the top layer of the thin film (B). However, due to highly charged character of incident ions, the surface contamination (hydrocarbon patches) are not sputtered but dragged all across the surface.

Bibliography

1. Bocquet, L. & Charlaix, E. Nanofluidics, from bulk to interfaces. *Chem. Soc. Rev.* **39**, 1073–1095. ISSN: 0306-0012. <http://xlink.rsc.org/?DOI=B909366B> (2010).
2. Nanofluidics is on the rise. *Nature Materials* **2020 19:3 19**, 253–253. ISSN: 1476-4660. <https://www.nature.com/articles/s41563-020-0633-8> (Feb. 2020).
3. Ali, A., Tufa, R. A., Macedonio, F., Curcio, E. & Drioli, E. Membrane technology in renewable-energy-driven desalination. *Renewable and Sustainable Energy Reviews* **81**, 1–21. ISSN: 18790690. <http://dx.doi.org/10.1016/j.rser.2017.07.047> (2018).
4. Heerema, S. J. & Dekker, C. *Graphene nanodevices for DNA sequencing* 2016.
5. Merchant, C. A. *et al.* DNA translocation through graphene nanopores. *Nano Letters*. ISSN: 15306984 (2010).
6. Feng, J. *et al.* Identification of single nucleotides in MoS₂ nanopores. *Nature Nanotechnology*. ISSN: 1748-3387 (2015).
7. Siria, A. *et al.* Giant osmotic energy conversion measured in a single transmembrane boron nitride nanotube. *Nature* **494**, 455–458. ISSN: 00280836 (2013).
8. Feng, J. *et al.* Observation of ionic Coulomb blockade in nanopores. *Nature Materials*. ISSN: 14764660 (2016).
9. Macha, M., Marion, S., Nandigana, V. V. & Radenovic, A. 2D materials as an emerging platform for nanopore-based power generation. *Nature Reviews Materials* **2019 4:9 4**, 588–605. ISSN: 2058-8437. <https://www.nature.com/articles/s41578-019-0126-z> (July 2019).
10. Akeson, M., Branton, D., Kasianowicz, J. J., Brandin, E. & Deamer, D. W. Microsecond Time-Scale Discrimination Among Polycytidylic Acid, Polyadenylic Acid, and Polyuridylic Acid as Homopolymers or as Segments Within Single RNA Molecules. *Biophysical Journal* **77**, 3227–3233. ISSN: 0006-3495 (Dec. 1999).
11. Cornell, B. A. *et al.* A biosensor that uses ion-channel switches. *Nature* **1997 387:6633 387**, 580–583. ISSN: 1476-4687. <https://www.nature.com/articles/42432> (June 1997).
12. Marion, S. & Radenovic, A. Towards artificial mechanosensing. *Nature Materials* **2020 19:10 19**, 1043–1044. ISSN: 1476-4660. <https://www.nature.com/articles/s41563-020-00811-5> (Sept. 2020).

13. Siria, A., Bocquet, M.-L. & Bocquet, L. New avenues for the large-scale harvesting of blue energy. *Nature Reviews Chemistry* **1**, 0091. ISSN: 2397-3358. <http://www.nature.com/articles/s41570-017-0091> (2017).
14. Shafiee, S. & Topal, E. When will fossil fuel reserves be diminished? *Energy Policy*. ISSN: 03014215 (2009).
15. Mohr, S. H., Wang, J., Ellem, G., Ward, J. & Giurco, D. Projection of world fossil fuels by country. *Fuel*. ISSN: 00162361 (2015).
16. Kwok, T. F., Yeung, C. H. & Xu, Y. Swaying public opinion on nuclear energy: A field experiment in Hong Kong. *Utilities Policy*. ISSN: 09571787 (2017).
17. Soni, A. Out of sight, out of mind? Investigating the longitudinal impact of the Fukushima nuclear accident on public opinion in the United States. *Energy Policy* **122**, 169–175 (2018).
18. Bisconti, A. Changing public attitudes toward nuclear energy. *Prog. Nucl. Energy* **102**, 103–113 (2018).
19. Khaligh, A. & Onar, O. *Energy harvesting : solar, wind, and ocean energy conversion systems* ISBN: 9781439815083 (2010).
20. Chou, S. *et al.* Thin-film composite hollow fiber membranes for pressure retarded osmosis (PRO) process with high power density. *Journal of Membrane Science*. ISSN: 03767388 (2012).
21. Daw, R., Finkelstein, J. & Helmer, M. *Chemistry and energy* 2012.
22. Chen, J. *et al.* Networks of triboelectric nanogenerators for harvesting water wave energy: A potential approach toward blue energy. *ACS Nano* **9**, 3324–3331. ISSN: 1936086X (2015).
23. U Khan, S. K. Triboelectric nanogenerators for blue energy harvesting. *ACS Nano* **10**, 6429–6432 (2016).
24. ZL Wang T Jiang, L. X. Toward the blue energy dream by triboelectric nanogenerator networks. *Nano Energy* **39**, 9–23 (2017).
25. Pattle, R. Production of electric power by mixing fresh and salt water in the hydroelectric pile. *Nature* **174**, 660 (1954).
26. NY Yip, M. E. Thermodynamic and energy efficiency analysis of power generation from natural salinity gradients by pressure retarded osmosis. *Environ. Sci. Technol.* **46**, 5230–5239 (2012).
27. Isaacs, J. D. & Seymour, R. J. The ocean as a power resource. *International Journal of Environmental Studies*. ISSN: 10290400 (1973).
28. O Schaetzle, C. B. Salinity gradient energy: current state and new trends. *Engineering* **1**, 164–166 (2015).
29. OA Alvarez-Silva AF Osorio, C. W. Practical global salinity gradient energy potential. *Renew. Sustain. Energy Rev.* **60**, 1387–1395 (2016).

30. Tomabechi, K. Energy resources in the future. *Energies* **3**, 686–695 (2010).
31. Klaysom, C., Cath, T. Y., Depuydt, T. & Vankelecom, I. F. J. Forward and pressure retarded osmosis: potential solutions for global challenges in energy and water supply. *Chemical Society Reviews*. ISSN: 0306-0012 (2013).
32. Kurihara, M. & Hanakawa, M. Mega-ton Water System: Japanese national research and development project on seawater desalination and wastewater reclamation. *Desalination*. ISSN: 00119164 (2013).
33. Drioli, E., Ali, A., Quist-Jensen, C. & F., M. *Water, Energy and Minerals from the Sea in Advances in Civil, Environmental, and Materials Research (ACEM16)* (2016). http://www.i-asem.org/past_conf/acem16/Keynote/k0401F.pdf.
34. Tedesco, M. Performance of the first reverse electrodialysis pilot plant for power production from saline waters and concentrated brines. *J. Membr. Sci.* **500**, 33–45 (2016).
35. Tedesco, M., Cipollina, A., Tamburini, A. & Micale, G. Towards 1 kW power production in a reverse electrodialysis pilot plant with saline waters and concentrated brines. *Journal of Membrane Science*. ISSN: 18733123 (2017).
36. Straub, A. P., Deshmukh, A. & Elimelech, M. *Pressure-retarded osmosis for power generation from salinity gradients: Is it viable?* 2016.
37. Chou, S. Thin-film composite hollow fiber membranes for pressure retarded osmosis (PRO) process with high power density. *J. Membr. Sci.* **389**, 25–33 (2012).
38. KP Lee TC Arnot, D. M. A review of reverse osmosis membrane materials for desalination—development to date and future potential. *J. Membr. Sci.* **370**, 1–22 (2011).
39. K Nijmeijer, S. M. Chapter 5 — salinity gradient energy. *Sustain. Sci. Eng.* **2**, 95–139 (2010).
40. Gerstandt, K., Peinemann, K. V., Skilhagen, S. E., Thorsen, T. & Holt, T. Membrane processes in energy supply for an osmotic power plant. *Desalination*. ISSN: 00119164 (2008).
41. Skilhagen, S. Osmotic power — a new, renewable energy source. *Desalin. Water Treat.* **15**, 271–278 (2010).
42. Hong, J. G. *et al.* *Potential ion exchange membranes and system performance in reverse electrodialysis for power generation: A review* 2015.
43. Mei, Y. & Tang, C. Y. Recent developments and future perspectives of reverse electrodialysis technology: A review. *Desalination* **425**, 156–174. ISSN: 00119164. <http://dx.doi.org/10.1016/j.desal.2017.10.021> (2017).
44. Vanoppen, M., Criel, E., Walpot, G., Vermaas, D. A. & Verliefde, A. Assisted reverse electrodialysis—principles, mechanisms, and potential. *npj Clean Water*. ISSN: 2059-7037 (2018).
45. Post, J. W. *et al.* Salinity-gradient power: Evaluation of pressure-retarded osmosis and reverse electrodialysis. *Journal of Membrane Science*. ISSN: 03767388 (2007).

46. Turek, M. & Bandura, B. Renewable energy by reverse electrodialysis. *Desalination*. ISSN: 00119164 (2007).
47. Post, J. W., Hamelers, H. V. M. & Buisman, C. J. N. Energy recovery from controlled mixing salt and fresh water with a reverse electrodialysis system. *Environmental Science and Technology*. ISSN: 0013936X (2008).
48. Veerman, J., Saakes, M., Metz, S. J. & Harmsen, G. J. Electrical power from sea and river water by reverse electrodialysis: A first step from the laboratory to a real power plant. *Environmental Science and Technology*. ISSN: 0013936X (2010).
49. Cipollina, A. & Micale, G. *Sustainable Energy from Salinity Gradients* ISBN: 9780081003237 (2016).
50. Yip, N. Y., Brogioli, D., Hamelers, H. V. & Nijmeijer, K. Salinity gradients for sustainable energy: Primer, progress, and prospects. *Environmental Science and Technology*. ISSN: 15205851 (2016).
51. Cohen-Tanugi, D. & Grossman, J. C. Nanoporous graphene as a reverse osmosis membrane: Recent insights from theory and simulation. *Desalination*. ISSN: 00119164 (2015).
52. Werber, J. R., Osuji, C. O. & Elimelech, M. *Materials for next-generation desalination and water purification membranes* 2016.
53. Liu, Y. & Chen, X. Mechanical properties of nanoporous graphene membrane. *Journal of Applied Physics*. ISSN: 00218979 (2014).
54. Logan, B. E. & Elimelech, M. *Membrane-based processes for sustainable power generation using water* 2012.
55. Ramanathan, A. A., Aqra, M. W. & Al-Rawajfeh, A. E. Recent advances in 2D nanopores for desalination. *Environmental Chemistry Letters*. ISSN: 1610-3653. <http://link.springer.com/10.1007/s10311-018-0745-4> (2018).
56. Gao, J., Feng, Y., Guo, W. & Jiang, L. Nanofluidics in two-dimensional layered materials: Inspirations from nature. *Chemical Society Reviews* **46**, 5400–5424. ISSN: 14604744. <http://dx.doi.org/10.1039/C7CS00369B> (2017).
57. Wang, Z. L., Jiang, T. & Xu, L. Toward the blue energy dream by triboelectric nanogenerator networks. *Nano Energy* **39**, 9–23. ISSN: 22112855. <http://dx.doi.org/10.1016/j.nanoen.2017.06.035> (2017).
58. De Vreede, L. J., Van Den Berg, A. & Eijkel, J. C. T. Nanopore fabrication by heating Au particles on ceramic substrates. *Nano Letters*. ISSN: 15306992 (2015).
59. Tong, H. D. *et al.* Silicon Nitride Nanosieve Membrane. *Nano Letters*. ISSN: 15306984 (2004).
60. Dai, J., Singh, J. & Yamamoto, N. Nonbrittle nanopore deformation of anodic aluminum oxide membranes. *Journal of the American Ceramic Society*. ISSN: 15512916 (2018).

61. Lee, S. W., Kim, H. J. & Kim, D. K. Power generation from concentration gradient by reverse electrodialysis in dense silica membranes for microfluidic and nanofluidic systems. *Energies* **9**. ISSN: 19961073 (2016).
62. Kim, D. K., Duan, C., Chen, Y. F. & Majumdar, A. Power generation from concentration gradient by reverse electrodialysis in ion-selective nanochannels. *Microfluidics and Nanofluidics* **9**, 1215–1224. ISSN: 16134982 (2010).
63. Kim, W. g. & Nair, S. *Membranes from nanoporous 1D and 2D materials: A review of opportunities, developments, and challenges* 2013.
64. Kang, K. *et al.* High-mobility three-atom-thick semiconducting films with wafer-scale homogeneity. *Nature*. ISSN: 14764687 (2015).
65. Kim, S. & Lee, Y. M. Rigid and microporous polymers for gas separation membranes. *Progress in Polymer Science*. ISSN: 00796700 (2015).
66. CHANG, C.-R., YEH, C.-H., YEH, H.-C. & YANG, R.-J. Energy Conversion From Salinity Gradient Using Microchip With Nafion Membrane. *International Journal of Modern Physics: Conference Series* **42**, 1660183. ISSN: 2010-1945. <http://www.worldscientific.com/doi/abs/10.1142/S2010194516601836> (2016).
67. Catalano, J. & Bentien, A. Influence of temperature on the electrokinetic properties and power generation efficiency of Nafion 117 membranes. *Journal of Power Sources*. ISSN: 03787753 (2014).
68. Guo, W. *et al.* Energy harvesting with single-ion-selective nanopores: A concentration-gradient-driven nanofluidic power source. *Advanced Functional Materials*. ISSN: 1616301X (2010).
69. Hsu, J. P., Yang, S. T., Lin, C. Y. & Tseng, S. Ionic Current Rectification in a Conical Nanopore: Influences of Electroosmotic Flow and Type of Salt. *Journal of Physical Chemistry C* **121**, 4576–4582. ISSN: 19327455 (2017).
70. Zhang, Z. *et al.* Ultrathin and Ion-Selective Janus Membranes for High-Performance Osmotic Energy Conversion. *Journal of the American Chemical Society* **139**, 8905–8914. ISSN: 15205126 (2017).
71. Zhu, Y., Zhan, K. & Hou, X. Interface Design of Nanochannels for Energy Utilization. *ACS Nano* **12**, 908–911. ISSN: 1936086X (2018).
72. Kang, D. Y. *et al.* Single-walled aluminosilicate nanotube/poly(vinyl alcohol) nanocomposite membranes. *ACS Applied Materials and Interfaces*. ISSN: 19448244 (2012).
73. Chan, W., Chen, H.-y., Surapathi, A. & Taylor, M. Zwitterion Functionalized Carbon Nanotube / Polyamide Nanocomposite Membranes for Water Desalination. *ACS Nano*. ISSN: 19360851 (2013).
74. Li, R., Jiang, J., Liu, Q., Xie, Z. & Zhai, J. Hybrid nanochannel membrane based on polymer/MOF for high-performance salinity gradient power generation. *Nano Energy*. ISSN: 22112855 (2018).

75. Dumée, L. *et al.* Carbon nanotube based composite membranes for water desalination by membrane distillation. *Desalination and Water Treatment*. ISSN: 1944-3994 (2010).
76. Dong, Y. *et al.* Stable Superhydrophobic Ceramic-based Carbon Nanotube Composite Desalination Membranes. *Nano Letters*, acs.nanolett.8b01907. ISSN: 1530-6984. <http://pubs.acs.org/doi/10.1021/acs.nanolett.8b01907> (Aug. 2018).
77. Boo, C. & Elimelech, M. *Thermal desalination membranes: Carbon nanotubes keep up the heat* 2017.
78. Vatanpour, V. *et al.* A thin film nanocomposite reverse osmosis membrane containing amine-functionalized carbon nanotubes. *Separation and Purification Technology*. ISSN: 18733794 (2017).
79. Goh, P. S., Ismail, A. F. & Ng, B. C. *Carbon nanotubes for desalination: Performance evaluation and current hurdles* 2013.
80. Zhao, S. *et al.* Ultrathin metal-organic framework nanosheets for electrocatalytic oxygen evolution. *Nature Energy*. ISSN: 20587546 (2016).
81. Ryder, M. R. & Tan, J.-C. Nanoporous metal organic framework materials for smart applications. *Materials Science and Technology* **30**, 1598–1612. ISSN: 0267-0836. <http://www.tandfonline.com/doi/full/10.1179/1743284714Y.0000000550> (2014).
82. Bunch, J. S. *et al.* Impermeable atomic membranes from graphene sheets. *Nano Letters*. ISSN: 15306984 (2008).
83. Koenig, S. P., Wang, L., Pellegrino, J. & Bunch, J. S. Selective molecular sieving through porous graphene. *Nature Nanotechnology*. ISSN: 17483395 (2012).
84. Mahmoud, K. A., Mansoor, B., Mansour, A. & Khraisheh, M. *Functional graphene nanosheets: The next generation membranes for water desalination* 2015.
85. Hegab, H. M. & Zou, L. *Graphene oxide-assisted membranes: Fabrication and potential applications in desalination and water purification* 2015.
86. Mi, B. *Graphene oxide membranes for ionic and molecular sieving* 2014.
87. Aghigh, A. *et al.* Recent advances in utilization of graphene for filtration and desalination of water: A review 2015.
88. Yoon, H. W., Cho, Y. H. & Park, H. B. *Graphene-based membranes: Status and prospects in Philosophical Transactions of the Royal Society A: Mathematical, Physical and Engineering Sciences* (2016). ISBN: 1364-503X (Print) 1364-503X (Linking).
89. Huang, L., Zhang, M., Li, C. & Shi, G. *Graphene-based membranes for molecular separation* 2015.
90. Graf, M. Fabrication and practical applications of molybdenum disulfide nanopores. *Nat. Protoc.* **14**, 1130–1168 (2019).
91. Homaeigohar, S. & Elbahri, M. Graphene membranes for water desalination. *NPG Asia Materials*. ISSN: 1884-4057 (2017).

92. Surwade, S. P. *et al.* Water desalination using nanoporous single-layer graphene. *Nature Nanotechnology* **10**, 459–464. ISSN: 17483395. <http://dx.doi.org/10.1038/nnano.2015.37> (2015).
93. Yip, N. Y., Vermaas, D. A., Nijmeijer, K. & Elimelech, M. Thermodynamic, Energy Efficiency, and Power Density Analysis of Reverse Electrodialysis Power Generation with Natural Salinity Gradients. *Environmental Science & Technology* **48**, 4925–4936. ISSN: 0013-936X (May 2014).
94. Fair, J. C. & Osterle, J. F. Reverse electrodialysis in charged capillary membranes. *The Journal of Chemical Physics* **54**, 3307–3316. ISSN: 00219606 (1971).
95. Rankin, D. J. & Huang, D. M. The Effect of Hydrodynamic Slip on Membrane-Based Salinity-Gradient-Driven Energy Harvesting. *Langmuir* **32**, 3420–3432. ISSN: 0743-7463 (Apr. 2016).
96. Rollings, R. C., Kuan, A. T. & Golovchenko, J. A. Ion selectivity of graphene nanopores. *Nature Communications* **7**, 1–7. ISSN: 20411723. <http://dx.doi.org/10.1038/ncomms11408> (2016).
97. Prieve, D. C., Ebel, J. P. & Lowell, M. E. Motion of a particle generated by chemical gradients. Part 2. Electrolytes. *Journal of Fluid Mechanics*. ISSN: 14697645 (1984).
98. Cao, L. *et al.* Towards understanding the nanofluidic reverse electrodialysis system: Well matched charge selectivity and ionic composition. *Energy and Environmental Science*. ISSN: 17545692 (2011).
99. Vlassiouk, I., Smirnov, S. & Siwy, Z. Ionic selectivity of single nanochannels. *Nano Letters*. ISSN: 15306984 (2008).
100. Muthukumar, M. *Polymer Translocation* ISBN: 978-1-4200-7516-8. <https://www.taylorfrancis.com/books/9781420075175> (CRC Press, May 2011).
101. Vermaas, D. A., Veerman, J., Saakes, M. & Nijmeijer, K. Influence of multivalent ions on renewable energy generation in reverse electrodialysis. *Energy Environ. Sci.* **7**, 1434–1445. ISSN: 1754-5692 (Jan. 2014).
102. Esfandiar, A. *et al.* Size effect in ion transport through angstrom-scale slits. *Science (New York, N.Y.)* **358**, 511–513. ISSN: 1095-9203. <https://pubmed.ncbi.nlm.nih.gov/29074772/> (Oct. 2017).
103. Suk, M. E. & Aluru, N. R. Ion transport in sub-5-nm graphene nanopores. *Journal of Chemical Physics*. ISSN: 00219606 (2014).
104. Jain, T. *et al.* Heterogeneous sub-continuum ionic transport in statistically isolated graphene nanopores. *Nature Nanotechnology*. ISSN: 17483395 (2015).
105. Feng, J. *et al.* Single-layer MoS₂ nanopores as nanopower generators. *Nature* **536**, 197–200. ISSN: 0028-0836. <http://www.nature.com/doi/10.1038/nature18593> (2016).
106. Karnik, R., Duan, C., Castelino, K., Daiguji, H. & Majumdar, A. Rectification of ionic current in a nanofluidic diode. *Nano Letters* **7**, 547–551. ISSN: 15306984. <https://pubs.acs.org/doi/full/10.1021/nl062806o> (Mar. 2007).

107. Siwy, Z., Kosińska, I. D., Fuliński, A. & Martin, C. R. Asymmetric diffusion through synthetic nanopores. *Physical Review Letters* **94**. ISSN: 00319007 (Feb. 2005).
108. Cao, L., Guo, W., Wang, Y. & Jiang, L. Concentration-Gradient-Dependent Ion Current Rectification in Charged Conical Nanopores. *Langmuir* **28**, 2194–2199. ISSN: 0743-7463 (Jan. 2012).
109. Jubin, L., Poggioli, A., Siria, A. & Bocquet, L. Dramatic pressure-sensitive ion conduction in conical nanopores. *Proceedings of the National Academy of Sciences*. ISSN: 0027-8424 (2018).
110. Lan, W. J., Holden, D. A. & White, H. S. Pressure-dependent ion current rectification in conical-shaped glass nanopores. *Journal of the American Chemical Society*. ISSN: 00027863 (2011).
111. Cervera, J., Schiedt, B., Neumann, R., Mafé, S. & Ramírez, P. Ionic conduction, rectification, and selectivity in single conical nanopores. *The Journal of Chemical Physics* **124**, 104706. ISSN: 0021-9606 (Mar. 2006).
112. Poggioli, A. R., Siria, A. & Bocquet, L. Beyond the Trade-Off: Dynamic Selectivity in Ionic Transport and Current Rectification. *The Journal of Physical Chemistry B*, acs.jp cb.8b11202. ISSN: 1520-6106. <http://pubs.acs.org/doi/10.1021/acs.jp cb.8b11202> (Jan. 2019).
113. Smeets, R. M. M. *et al.* Salt dependence of ion transport and DMA translocation through solid-state nanopores. *Nano Letters*. ISSN: 15306984 (2006).
114. Hall, J. E. Access resistance of a small circular pore. *The Journal of General Physiology*. ISSN: 0022-1295 (1975).
115. Kowalczyk, S. W., Grosberg, A. Y., Rabin, Y. & Dekker, C. Modeling the conductance and DNA blockade of solid-state nanopores. *Nanotechnology* **22**, 315101. ISSN: 0957-4484. <http://iopscience.iop.org/article/10.1088/0957-4484/22/31/315101/meta%20http://stacks.iop.org/0957-4484/22/i=31/a=315101?key=crossref.d8841d778566685e70a21fb15a961e5b> (Aug. 2011).
116. Hille, B. Charges and potentials at the nerve surface. Divalent ions and pH. *J Gen Physiol*. ISSN: 0022-1295 (1968).
117. Lee, Y. H. *et al.* Synthesis of large-area MoS₂ atomic layers with chemical vapor deposition. *Adv Mater*. ISSN: 1521-4095 (2012).
118. Pérez, M. D. B. *et al.* Improved model of ionic transport in 2-D MoS₂ membranes with sub-5 nm pores. *Applied Physics Letters* **114**, 023107. ISSN: 0003-6951. <http://aip.scitation.org/doi/10.1063/1.5061825> (Jan. 2019).
119. Walker, M. I. *et al.* Extrinsic Cation Selectivity of 2D Membranes. *ACS Nano* **11**, 1340–1346. ISSN: 1936086X (2017).
120. Ji, J. *et al.* Osmotic Power Generation with Positively and Negatively Charged 2D Nanofluidic Membrane Pairs. *Advanced Functional Materials* **27**, 1–8. ISSN: 16163028 (2017).

121. Lin, C. Y., Combs, C., Su, Y. S., Yeh, L. H. & Siwy, Z. S. Rectification of Concentration Polarization in Mesopores Leads to High Conductance Ionic Diodes and High Performance Osmotic Power. *Journal of the American Chemical Society*. ISSN: 15205126 (2019).
122. Balme, S., Ma, T., Balanzat, E. & Janot, J. M. Large osmotic energy harvesting from functionalized conical nanopore suitable for membrane applications. *Journal of Membrane Science* **544**, 18–24. ISSN: 18733123. <http://dx.doi.org/10.1016/j.memsci.2017.09.008> (2017).
123. Zhang, Z. Ultrathin and ion-selective Janus membranes for high-performance osmotic energy conversion. *J. Am. Chem. Soc.* **139**, 8905–8914 (2017).
124. Zhang, Z. *et al.* Engineered Asymmetric Heterogeneous Membrane: A Concentration-Gradient-Driven Energy Harvesting Device. *Journal of the American Chemical Society*. ISSN: 15205126 (2015).
125. Kwon, K., Lee, S. J., Li, L., Han, C. & Kim, D. Energy harvesting system using reverse electrodialysis with nanoporous polycarbonate track-etch membranes. *International Journal of Energy Research* **38**, 530–537. ISSN: 1099-114X. <https://onlinelibrary.wiley.com/doi/full/10.1002/er.3111> <https://onlinelibrary.wiley.com/doi/abs/10.1002/er.3111> <https://onlinelibrary.wiley.com/doi/10.1002/er.3111> (Mar. 2014).
126. Tsai, T. C., Liu, C. W. & Yang, R. J. Power generation by reverse electrodialysis in a microfluidic device with a Nafion ion-selective membrane. *Micromachines*. ISSN: 2072666X (2016).
127. Yan, F., Yao, L., Chen, K., Yang, Q. & Su, B. An ultrathin and highly porous silica nanochannel membrane: toward highly efficient salinity energy conversion. *Journal of Materials Chemistry A*. ISSN: 2050-7488. <http://xlink.rsc.org/?DOI=C8TA10848J> (2019).
128. Gao, J. *et al.* High-performance ionic diode membrane for salinity gradient power generation. *Journal of the American Chemical Society* **136**, 12265–12272. ISSN: 15205126 (2014).
129. Kwak, S. H. *et al.* Densely charged polyelectrolyte-stuffed nanochannel arrays for power generation from salinity gradient. *Scientific Reports*. ISSN: 20452322 (2016).
130. Tedesco, M. *et al.* Performance of the first reverse electrodialysis pilot plant for power production from saline waters and concentrated brines. *Journal of Membrane Science*. ISSN: 18733123 (2016).
131. Storm, A. J. *et al.* Fast DNA translocation through a solid-state nanopore. *Nano Letters*. ISSN: 15306984 (2005).
132. Liu, K., Feng, J., Kis, A. & Radenovic, A. Atomically thin molybdenum disulfide nanopores with high sensitivity for dna translocation. *ACS Nano*. ISSN: 1936086X (2014).
133. Fologea, D., Uplinger, J., Thomas, B., McNabb, D. S. & Li, J. Slowing DNA translocation in a solid-state nanopore. *Nano Letters*. ISSN: 15306984 (2005).
134. Fologea, D. *et al.* Detecting single stranded DNA with a solid state nanopore. *Nano Letters*. ISSN: 15306984 (2005).

135. Chen, W. *et al.* Graphene nanopores toward DNA sequencing: a review of experimental aspects. *Science China Chemistry* **60**, 721–729. ISSN: 18691870 (2017).
136. Liu, S. *et al.* Boron nitride nanopores: Highly sensitive DNA single-molecule detectors. *Advanced Materials*. ISSN: 09359648 (2013).
137. Apel, P. Y. *et al.* Fabrication of nanopores in polymer foils with surfactant-controlled longitudinal profiles. *Nanotechnology* **18**. ISSN: 09574484 (2007).
138. Cohen-Tanugi, D. & Grossman, J. C. Water desalination across nanoporous graphene. *Nano Letters* **12**, 3602–3608. ISSN: 15306984 (2012).
139. Li, L., Dong, J., Nenoff, T. M. & Lee, R. Desalination by reverse osmosis using MFI zeolite membranes. *Journal of Membrane Science*. ISSN: 03767388 (2004).
140. Cho, C. H., Oh, K. Y., Kim, S. K., Yeo, J. G. & Sharma, P. Pervaporative seawater desalination using NaA zeolite membrane: Mechanisms of high water flux and high salt rejection. *Journal of Membrane Science*. ISSN: 03767388 (2011).
141. Swenson, P., Tanchuk, B., Gupta, A., An, W. Z. & Kuznicki, S. M. Pervaporative desalination of water using natural zeolite membranes. *Desalination* (2012).
142. Gethard, K., Sae-Khow, O. & Mitra, S. Water desalination using carbon-nanotube-enhanced membrane distillation. *ACS Applied Materials and Interfaces*. ISSN: 19448244 (2011).
143. Das, R., Ali, M. E., Hamid, S. B. A., Ramakrishna, S. & Chowdhury, Z. Z. *Carbon nanotube membranes for water purification: A bright future in water desalination* 2014.
144. Corry, B. Designing carbon nanotube membranes for efficient water desalination. *Journal of Physical Chemistry B*. ISSN: 15206106 (2008).
145. Kalra, A., Garde, S. & Hummer, G. Osmotic water transport through carbon nanotube membranes. *Proceedings of the National Academy of Sciences of the United States of America*. ISSN: 0027-8424 (2003).
146. Karan, S., Jiang, Z. & Livingston, A. G. Sub-10 nm polyamide nanofilms with ultrafast solvent transport for molecular separation. *Science*. ISSN: 10959203 (2015).
147. Veerman, J., de Jong, R. M., Saakes, M., Metz, S. J. & Harmsen, G. J. Reverse electrodialysis: Comparison of six commercial membrane pairs on the thermodynamic efficiency and power density. *Journal of Membrane Science*. ISSN: 03767388 (2009).
148. Storm, A. J., Chen, J. H., Ling, X. S., Zandbergen, H. W. & Dekker, C. Fabrication of solid-state nanopores with single-nanometre precision. *Nature Materials* **2**, 537–540. ISSN: 14761122 (2003).
149. Kim, M. J., Wanunu, M., Bell, D. C. & Meller, A. Rapid fabrication of uniformly sized nanopores and nanopore arrays for parallel DNA analysis. *Advanced Materials* **18**, 3149–3153. ISSN: 09359648 (2006).
150. Deng, T., Wang, Y., Chen, Q., Chen, H. & Liu, Z. Massive fabrication of silicon nanopore arrays with tunable shapes. *Applied Surface Science* **390**, 681–688. ISSN: 01694332 (2016).

151. Verschueren, D. V., Yang, W. & Dekker, C. Lithography-based fabrication of nanopore arrays in freestanding SiN and graphene membranes. *Nanotechnology* **29**. ISSN: 13616528 (2018).
152. Hsu, J. P., Wu, H. H., Lin, C. Y. & Tseng, S. Ion Current Rectification Behavior of Bioinspired Nanopores Having a pH-Tunable Zwitterionic Surface. *Analytical Chemistry* **89**, 3952–3958. ISSN: 15206882 (2017).
153. Danda, G. & Drndić, M. Two-dimensional nanopores and nanoporous membranes for ion and molecule transport. *Current Opinion in Biotechnology* **55**, 124–133. ISSN: 09581669. <https://linkinghub.elsevier.com/retrieve/pii/S0958166918300387> (Feb. 2019).
154. Mao, M., Sherwood, J. D. & Ghosal, S. Electro-osmotic flow through a nanopore. *Journal of Fluid Mechanics* **749**, 167–183. ISSN: 14697645 (2014).
155. Fornasiero, F. *et al.* Ion exclusion by sub-2-nm carbon nanotube pores. *Proceedings of the National Academy of Sciences*. ISSN: 0027-8424 (2008).
156. Farimani, A. B., Min, K. & Aluru, N. R. DNA base detection using a single-layer MoS₂. *ACS Nano*. ISSN: 1936086X (2014).
157. Steinbock, L. J. & Radenovic, A. The emergence of nanopores in next-generation sequencing. *Nanotechnology*. ISSN: 13616528 (2015).
158. Feng, J. *et al.* Electrochemical reaction in single layer MoS₂: Nanopores opened atom by atom. *Nano Letters* **15**, 3431–3438. ISSN: 15306992 (2015).
159. Wang, Q. H., Kalantar-Zadeh, K., Kis, A., Coleman, J. N. & Strano, M. S. *Electronics and optoelectronics of two-dimensional transition metal dichalcogenides* 2012.
160. Han, Y., Xu, Z. & Gao, C. Ultrathin graphene nanofiltration membrane for water purification. *Advanced Functional Materials*. ISSN: 1616301X (2013).
161. Heiranian, M., Farimani, A. B. & Aluru, N. R. Water desalination with a single-layer MoS₂ nanopore. *Nature Communications* **6**, 1–6. ISSN: 20411723. <http://dx.doi.org/10.1038/ncomms9616> (2015).
162. Chester, R. & Jickells, T. Marine Geochemistry. *Marine Geochemistry* (Aug. 2012).
163. Shan, Y. P. *et al.* Surface modification of graphene nanopores for protein translocation. *Nanotechnology*. ISSN: 09574484 (2013).
164. Graf, M. *et al.* Light-Enhanced Blue Energy Generation Using MoS₂ Nanopores. *Joule* **3**, 1549–1564. ISSN: 25424351 (June 2019).
165. Melnikov, D. V., Hulings, Z. K. & Gracheva, M. E. Electro-osmotic flow through nanopores in thin and ultrathin membranes. *Physical Review E*. ISSN: 24700053 (2017).
166. Rankin, D. J., Bocquet, L. & Huang, D. M. Entrance effects in concentration-gradient-driven flow through an ultrathin porous membrane. *The Journal of Chemical Physics* **151**, 044705. ISSN: 0021-9606. <https://aip.scitation.org/doi/abs/10.1063/1.5108700> (July 2019).

167. Lee, J. *et al.* Stabilization of graphene nanopore. *Proceedings of the National Academy of Sciences*. ISSN: 0027-8424 (2014).
168. Yang, T., Lin, H., Zheng, X., Loh, K. P. & Jia, B. *Tailoring pores in graphene-based materials: From generation to applications* 2017.
169. Liu, Q. *et al.* Porous Hexagonal Boron Nitride Sheets: Effect of Hydroxyl and Secondary Amino Groups on Photocatalytic Hydrogen Evolution. *ACS Applied Nano Materials* **1**, 4566–4575. ISSN: 2574-0970. <http://pubs.acs.org/doi/10.1021/acsanm.8b00867> (Sept. 2018).
170. Mouterde, T. & Bocquet, L. Interfacial transport with mobile surface charges and consequences for ionic transport in carbon nanotubes. *The European Physical Journal E* 2018 **41:12** **41**, 1–10. ISSN: 1292-895X. <https://link.springer.com/article/10.1140/epje/i2018-11760-2> (Dec. 2018).
171. Grosjean, B., Bocquet, M. L. & Vuilleumier, R. Versatile electrification of two-dimensional nanomaterials in water. *Nature Communications* 2019 **10:1** **10**, 1–8. ISSN: 2041-1723. <https://www.nature.com/articles/s41467-019-09708-7> (Apr. 2019).
172. Sharma, M., Singh, A. & Singh, R. Monolayer MoS₂ Transferred on Arbitrary Substrates for Potential Use in Flexible Electronics. *ACS Applied Nano Materials* **3**, 4445–4453 (May 2020).
173. Krems, M. & Di Ventra, M. Ionic Coulomb blockade in nanopores. *Journal of Physics Condensed Matter*. ISSN: 09538984 (2013).
174. Wells, D. B., Belkin, M., Comer, J. & Aksimentiev, A. Assessing graphene nanopores for sequencing DNA. *Nano Letters*. ISSN: 15306984 (2012).
175. Venkatesan, B. M. & Bashir, R. *Nanopore sensors for nucleic acid analysis* 2011.
176. Danda, G. *et al.* Monolayer WS₂ Nanopores for DNA Translocation with Light-Adjustable Sizes. *ACS Nano*. ISSN: 1936-0851 (2017).
177. Schneider, G. F. *et al.* DNA Translocation through Grapheme Nanopores. *Nano Letters*. ISSN: 1530-6984 (2010).
178. Fanget, A. *et al.* Nanopore integrated nanogaps for DNA detection. *Nano Letters*. ISSN: 15306984 (2014).
179. Traversi, F. *et al.* Detecting the translocation of DNA through a nanopore using graphene nanoribbons. *Nature Nanotechnology*. ISSN: 17483395 (2013).
180. Siwy, Z. S. & Davenport, M. *Nanopores: Graphene opens up to DNA* 2010.
181. Schneider, G. F. & Dekker, C. *DNA sequencing with nanopores* 2012.
182. Zhang, H. *et al.* Open-Pore Two-Dimensional MFI Zeolite Nanosheets for the Fabrication of Hydrocarbon-Isomer-Selective Membranes on Porous Polymer Supports. *Angewandte Chemie - International Edition*. ISSN: 15213773 (2016).
183. Harrell, C. C. *et al.* Resistive-pulse DNA detection with a conical nanopore sensor. *Langmuir* **22**, 10837–10843. ISSN: 07437463 (2006).

184. Sonck, S., Beuls, E., Mahillon, J. & Francis, L. A. Performance of Ion Track-Etched Polyimide as Ion Exchange Membranes for Microbial Fuel Cells. *ECS Transactions* **35**, 251–256. ISSN: 1938-5862. <https://iopscience.iop.org/article/10.1149/1.3655708%20https://iopscience.iop.org/article/10.1149/1.3655708/meta> (Dec. 2019).
185. Varricchio, S. S., Piacentini, N., Bertsch, A. & Renaud, P. Multimaterial Nanoporous Membranes Shaped through High Aspect-Ratio Sacrificial Silicon Nanostructures. *ACS Omega*. ISSN: 24701343 (2017).
186. Spinney, P. S., Howitt, D. G., Smith, R. L. & Collins, S. D. Nanopore formation by low-energy focused electron beam machining. *Nanotechnology* **21**. ISSN: 09574484 (2010).
187. Li, J. *et al.* Ion-beam sculpting at nanometre length scales. *Nature* **412**, 166–169. ISSN: 00280836 (2001).
188. Thiruraman, J. P. *et al.* Angstrom-Size Defect Creation and Ionic Transport through Pores in Single-Layer MoS₂. *Nano Letters*. ISSN: 15306992 (2018).
189. O'Hern, S. C. *et al.* Selective ionic transport through tunable subnanometer pores in single-layer graphene membranes. *Nano Letters*. ISSN: 15306992 (2014).
190. Russo, C. J. & Golovchenko, J. A. Atom-by-atom nucleation and growth of graphene nanopores. *Proceedings of the National Academy of Sciences* **109**, 5953–5957. ISSN: 0027-8424. <http://www.pnas.org/cgi/doi/10.1073/pnas.1119827109> (2012).
191. O'Hern, S. C. *et al.* Nanofiltration across defect-sealed nanoporous monolayer graphene. *Nano Letters*. ISSN: 15306992 (2015).
192. Deng, Y. *et al.* Precise fabrication of a 5 nm graphene nanopore with a helium ion microscope for biomolecule detection. *Nanotechnology*. ISSN: 13616528 (2017).
193. Gierak, J. *et al.* Sub-5 nm FIB direct patterning of nanodevices. *Microelectronic Engineering*. ISSN: 01679317 (2007).
194. Latif, A. Nanofabrication using focused ion beam. <https://www.repository.cam.ac.uk/handle/1810/34605> (2000).
195. Mussi, V. *et al.* DNA-functionalized solid state nanopore for biosensing. *Nanotechnology*. ISSN: 09574484 (2010).
196. Yang, J. *et al.* Rapid and precise scanning helium ion microscope milling of solid-state nanopores for biomolecule detection. *Nanotechnology*. ISSN: 09574484 (2011).
197. Fischbein, M. & Drndic, M. Electron beam nanosculpting of suspended graphene sheets. *Applied Physics Letters* (2008).
198. Kwok, H., Briggs, K. & Tabard-Cossa, V. Nanopore fabrication by controlled dielectric breakdown. *PLoS ONE*. ISSN: 19326203 (2014).
199. Kang, K. *et al.* High-mobility three-atom-thick semiconducting films with wafer-scale homogeneity. *Nature* **520**:7549 **520**, 656–660. ISSN: 1476-4687. <https://www.nature.com/articles/nature14417> (Apr. 2015).

200. Zhou, J. *et al.* A library of atomically thin metal chalcogenides. *Nature* **556**, 355–359. ISSN: 14764687 (2018).
201. Li, X. *et al.* Large-area synthesis of high-quality and uniform graphene films on copper foils. *Science*. ISSN: 00368075 (2009).
202. Zhan, Y., Liu, Z., Najmaei, S., Ajayan, P. M. & Lou, J. Large-area vapor-phase growth and characterization of MoS₂ atomic layers on a SiO₂ substrate. *Small (Weinheim an der Bergstrasse, Germany)*. ISSN: 1613-6829 (2012).
203. Miseikis, V. *et al.* Rapid CVD growth of millimetre-sized single crystal graphene using a cold-wall reactor. *2D Materials*. ISSN: 20531583 (2015).
204. Kang, K. *et al.* Layer-by-layer assembly of two-dimensional materials into wafer-scale heterostructures. *Nature* **550**, 229–233. ISSN: 14764687. <http://dx.doi.org/10.1038/nature23905> (2017).
205. Li, X. *et al.* Large-area graphene single crystals grown by low-pressure chemical vapor deposition of methane on copper. *Journal of the American Chemical Society*. ISSN: 00027863 (2011).
206. Lee, K. H. *et al.* Large-scale synthesis of high-quality hexagonal boron nitride nanosheets for large-area graphene electronics. *Nano Letters*. ISSN: 15306984 (2012).
207. Kim, T. & Mun, J. Wafer-scale production of highly uniform two-dimensional MoS₂ by metal-organic chemical vapor deposition. *Nanotechnology* **28**. <http://iopscience.iop.org/article/10.1088/1361-6528/aa6958/meta> (2017).
208. Yang, P. *et al.* Batch production of 6-inch uniform monolayer molybdenum disulfide catalyzed by sodium in glass. *Nature Communications*. ISSN: 20411723 (2018).
209. Boandoh, S. *et al.* A Novel and Facile Route to Synthesize Atomic-Layered MoS₂ Film for Large-Area Electronics. *Small*. ISSN: 16136810 (2017).
210. Yu, H. *et al.* Wafer-Scale Growth and Transfer of Highly-Oriented Monolayer MoS₂ Continuous Films. *ACS Nano*. ISSN: 1936086X (2017).
211. Gupta, A., Sakthivel, T. & Seal, S. Recent development in 2D materials beyond graphene. *Progress in Materials Science*. ISSN: 00796425 (2015).
212. Mannix, A. J., Kiraly, B., Hersam, M. C. & Guisinger, N. P. *Synthesis and chemistry of elemental 2D materials* 2017.
213. Gurarslan, A. *et al.* Surface-energy-assisted perfect transfer of centimeter-scale monolayer and few-layer MoS₂ films onto arbitrary substrates. *ACS Nano*. ISSN: 1936086X (2014).
214. Uwanno, T., Hattori, Y., Taniguchi, T., Watanabe, K. & Nagashio, K. Fully dry PMMA transfer of graphene on h-BN using a heating/ cooling system. *2D Materials*. ISSN: 20531583 (2015).

215. Yang, R., Zheng, X., Wang, Z., Miller, C. J. & Feng, P. X.-L. Multilayer MoS₂ transistors enabled by a facile dry-transfer technique and thermal annealing. *Journal of Vacuum Science & Technology B, Nanotechnology and Microelectronics: Materials, Processing, Measurement, and Phenomena*. ISSN: 2166-2746 (2014).
216. Shinde, S. M. *et al.* Surface-Functionalization-Mediated Direct Transfer of Molybdenum Disulfide for Large-Area Flexible Devices. *Advanced Functional Materials*. ISSN: 16163028 (2018).
217. Lin, Y.-C. *et al.* Wafer-scale MoS₂ thin layers prepared by MoO₃ sulfurization. *Nanoscale*. ISSN: 2040-3364 (2012).
218. Liang, X. *et al.* Toward clean and crackless transfer of graphene. *ACS Nano*. ISSN: 19360851 (2011).
219. Waduge, P. *et al.* Direct and Scalable Deposition of Atomically Thin Low-Noise MoS₂ Membranes on Apertures Direct and Scalable Deposition of Atomically Thin Low- Noise MoS₂ Membranes on Apertures, 7352–7359 (2015).
220. Li, W. Z. *et al.* Large-scale synthesis of aligned carbon nanotubes. *Science*. ISSN: 00368075 (1996).
221. Ren, Z. F. & Huang, Z. P. Synthesis of large arrays of well-aligned carbon nanotubes on glass. *Science*. ISSN: 00368075 (1998).
222. Fan, S. *et al.* Self-oriented regular arrays of carbon nanotubes and their field emission properties. *Science*. ISSN: 00368075 (1999).
223. Su, C. Y. *et al.* Large-scale synthesis of boron nitride nanotubes with iron-supported catalysts. *Journal of Physical Chemistry C*. ISSN: 19327447 (2009).
224. Obraztsov, A. N. Making graphene on a large scale. *Nature Nanotechnology*. ISSN: 1748-3395 (2009).
225. Kim, K. S. K. S. *et al.* Large-scale pattern growth of graphene films for stretchable transparent electrodes. *Nature*. ISSN: 00280836 (2009).
226. Ma, X. *et al.* Capillary-Force-Assisted Clean-Stamp Transfer of Two-Dimensional Materials. *Nano Letters* **17**, 6961–6967. ISSN: 15306992 (2017).
227. Garcia, A. *et al.* Analysis of electron beam damage of exfoliated MoS₂ sheets and quantitative HAADF-STEM imaging. *Ultramicroscopy*. ISSN: 18792723 (2014).
228. Zan, R. *et al.* Control of radiation damage in MoS₂ by graphene encapsulation. *ACS Nano*. ISSN: 19360851 (2013).
229. Barreiro, A. *et al.* Understanding the catalyst-free transformation of amorphous carbon into graphene by current-induced annealing. *Scientific Reports*. ISSN: 20452322 (2013).
230. Xu, T. *et al.* Size-dependent evolution of graphene nanopores under thermal excitation. *Small*. ISSN: 16136810 (2012).

231. Xiao, F. *et al.* A general strategy to simulate osmotic energy conversion in multi-pore nanofluidic systems. *Materials Chemistry Frontiers* **2**, 935–941. ISSN: 2052-1537. <http://xlink.rsc.org/?DOI=C8QM00031J> (2018).
232. Gadaleta, A. *et al.* Sub-additive ionic transport across arrays of solid-state nanopores. *Physics of Fluids* **26**, 1–11. ISSN: 10897666 (2014).
233. Hayashi, T. *et al.* Nanopore Fabrication to Two-Dimensional Materials on SiO₂ Membranes Using He Ion Microscopy. *IEEE Transactions on Nanotechnology*. ISSN: 1536125X (2018).
234. Su, J. *et al.* Anomalous Pore-Density Dependence in Nanofluidic Osmotic Power Generation. *Chinese Journal of Chemistry*. ISSN: 16147065 (2018).
235. Lin, C. Y., Hsu, J. P. & Yeh, L. H. Rectification of ionic current in nanopores functionalized with bipolar polyelectrolyte brushes. *Sensors and Actuators, B: Chemical* **258**, 1223–1229. ISSN: 09254005. <http://dx.doi.org/10.1016/j.snb.2017.11.172> (2018).
236. Wang, X. *et al.* How the geometric configuration and the surface charge distribution influence the ionic current rectification in nanopores. *Journal of Physics D: Applied Physics*. ISSN: 00223727 (2007).
237. Sint, K., Wang, B. & Krüger, P. Selective ion passage through functionalized graphene nanopores. *Journal of the American Chemical Society*. ISSN: 00027863 (2008).
238. Zhao, S., Xue, J. & Kang, W. Ion selection of charge-modified large nanopores in a graphene sheet. *Journal of Chemical Physics* **139**. ISSN: 00219606 (2013).
239. Kiriya, D., Tosun, M., Zhao, P., Kang, J. S. & Javey, A. Air-stable surface charge transfer doping of MoS by benzyl viologen. *Journal of the American Chemical Society* **136**, 7853–6. ISSN: 1520-5126. <http://www.ncbi.nlm.nih.gov/pubmed/24836497> (2014).
240. Cheng, P. *et al.* Transparent Glass with the Growth of Pyramid-Type MoS₂ for Highly Efficient Water Disinfection under Visible-Light Irradiation. *ACS Applied Materials and Interfaces*. ISSN: 19448252 (2018).
241. Pandit, S., Karunakaran, S., Boda, S. K., Basu, B. & De, M. High antibacterial activity of functionalized chemically exfoliated MoS₂. *ACS Applied Materials and Interfaces*. ISSN: 19448252 (2016).
242. Schaetzle, O. & Buisman, C. J. Salinity Gradient Energy: Current State and New Trends. *Engineering*. ISSN: 20958099 (2015).
243. Mounet, N. *et al.* Two-dimensional materials from high-throughput computational exfoliation of experimentally known compounds. *Nature Nanotechnology*. ISSN: 17483395 (2018).
244. Zhu, Y. *et al.* Monolayer Molybdenum Disulfide Transistors with Single-Atom-Thick Gates. *Nano Letters* **18**, 3807–3813 (June 2018).
245. Wang, F. *et al.* *2D library beyond graphene and transition metal dichalcogenides: A focus on photodetection* 2018.

246. Haastrup, S. *et al.* *The Computational 2D Materials Database: High-throughput modeling and discovery of atomically thin crystals* 2018.
247. Duong, D. L., Yun, S. J. & Lee, Y. H. *Van der Waals Layered Materials: Opportunities and Challenges* 2017.
248. Roth, W. J., Nachtigall, P., Morris, R. E. & Čejka, J. *Two-dimensional zeolites: Current status and perspectives* 2014.
249. Kobayashi, K. & Yamauchi, J. Electronic structure and scanning-tunneling-microscopy image of molybdenum dichalcogenide surfaces. *Physical Review B* **51**, 17085. ISSN: 01631829. <https://journals.aps.org/prb/abstract/10.1103/PhysRevB.51.17085> (June 1995).
250. Splendiani, A. *et al.* Emerging Photoluminescence in Monolayer MoS₂. *Nano Letters* **10**, 1271–1275. <https://pubs.acs.org/doi/full/10.1021/nl903868w> (Apr. 2010).
251. B Radisavljevic, A. K. Mobility engineering and a metal–insulator transition in monolayer MoS₂. *Nature Mater.* **12**, 815–820 (2013).
252. Jayabal, S., Wu, J., Chen, J., Geng, D. & Meng, X. Metallic 1T-MoS₂ nanosheets and their composite materials: Preparation, properties and emerging applications. *Materials Today Energy* **10**, 264–279. ISSN: 2468-6069 (Dec. 2018).
253. Wang, H. *et al.* Microwave-assisted 1T to 2H phase reversion of MoS₂ in solution: a fast route to processable dispersions of 2H-MoS₂ nanosheets and nanocomposites. *Nanotechnology* **27**, 385604. ISSN: 0957-4484. <https://iopscience.iop.org/article/10.1088/0957-4484/27/38/385604> <https://iopscience.iop.org/article/10.1088/0957-4484/27/38/385604/meta> (Aug. 2016).
254. Gupta, D., Chauhan, V. & Kumar, R. A comprehensive review on synthesis and applications of molybdenum disulfide (MoS₂) material: Past and recent developments. *Inorganic Chemistry Communications* **121** (Nov. 2020).
255. Wang, S. *et al.* Shape evolution of monolayer MoS₂ crystals grown by chemical vapor deposition. *Chemistry of Materials* **26**, 6371–6379. ISSN: 15205002. <https://pubs.acs.org/doi/full/10.1021/cm5025662> (Nov. 2014).
256. Dumcenco, D. *et al.* Large-area epitaxial monolayer MoS₂. *ACS Nano*. ISSN: 1936086X (2015).
257. Choudhury, T. H., Zhang, X., Al Balushi, Z. Y., Chubarov, M. & Redwing, J. M. Epitaxial Growth of Two-Dimensional Layered Transition Metal Dichalcogenides. <https://doi.org/10.1146/annurev-matsci-090519-113456> **50**, 155–177. ISSN: 15317331. <https://www.annualreviews.org/doi/abs/10.1146/annurev-matsci-090519-113456> (July 2020).
258. Li, H., Li, Y., Aljarb, A., Shi, Y. & Li, L. J. Epitaxial Growth of Two-Dimensional Layered Transition-Metal Dichalcogenides: Growth Mechanism, Controllability, and Scalability. *Chemical Reviews* **118**, 6134–6150. ISSN: 15206890. <https://pubs.acs.org/doi/full/10.1021/acs.chemrev.7b00212> (July 2017).

259. Kim, H. *et al.* Role of alkali metal promoter in enhancing lateral growth of monolayer transition metal dichalcogenides. *Nanotechnology* **28**, 36LT01. ISSN: 0957-4484. <https://iopscience.iop.org/article/10.1088/1361-6528/aa7e5e> <https://iopscience.iop.org/article/10.1088/1361-6528/aa7e5e/meta> (Aug. 2017).
260. Wang, P. *et al.* Mechanism of Alkali Metal Compound-Promoted Growth of Monolayer MoS₂ : Eutectic Intermediates. <https://pubs.acs.org/sharingguidelines> (2019).
261. Ling, X. *et al.* Role of the seeding promoter in MoS₂ growth by chemical vapor deposition. *Nano Letters* **14**, 464–472. ISSN: 15306984. <https://pubs.acs.org/doi/full/10.1021/nl4033704> (Feb. 2014).
262. Young, J. R. *et al.* Uniform large-area growth of nanotemplated high-quality monolayer MoS₂. *Applied Physics Letters* **110**, 263103. ISSN: 0003-6951. <https://aip.scitation.org/doi/abs/10.1063/1.4989851> (June 2017).
263. Wang, X., Kang, K., Chen, S., Du, R. & Yang, E. H. Location-specific growth and transfer of arrayed MoS₂ monolayers with controllable size. *2D Materials* **4**, 025093. ISSN: 2053-1583. <https://iopscience.iop.org/article/10.1088/2053-1583/aa6e69> <https://iopscience.iop.org/article/10.1088/2053-1583/aa6e69/meta> (May 2017).
264. Sun, D. *et al.* Chemical vapor deposition growth of a periodic array of single-layer MoS₂ islands via lithographic patterning of an SiO₂/Si substrate. *2D Materials* **2**, 045014. ISSN: 2053-1583. <https://iopscience.iop.org/article/10.1088/2053-1583/2/4/045014> <https://iopscience.iop.org/article/10.1088/2053-1583/2/4/045014/meta> (Dec. 2015).
265. Fang, M. *et al.* Controlled Growth of Bilayer-MoS₂ Films and MoS₂-Based Field-Effect Transistor (FET) Performance Optimization. *Advanced Electronic Materials* **4**, 1700524. ISSN: 2199-160X. <https://onlinelibrary.wiley.com/doi/full/10.1002/aelm.201700524> <https://onlinelibrary.wiley.com/doi/abs/10.1002/aelm.201700524> <https://onlinelibrary.wiley.com/doi/10.1002/aelm.201700524> (Apr. 2018).
266. Chen, W. *et al.* Oxygen-Assisted Chemical Vapor Deposition Growth of Large Single-Crystal and High-Quality Monolayer MoS₂. *Journal of the American Chemical Society* **137**, 15632–15635. ISSN: 15205126. <https://pubs.acs.org/doi/full/10.1021/jacs.5b10519> (Dec. 2015).
267. Tai, G. *et al.* Fast and large-area growth of uniform MoS₂ monolayers on molybdenum foils. *Nanoscale* **8**, 2234–2241. ISSN: 20403372. <https://pubs.rsc.org/en/content/articlehtml/2016/nr/c5nr07226c> <https://pubs.rsc.org/en/content/articlelanding/2016/nr/c5nr07226c> (Jan. 2016).
268. Kim, Y., Bark, H., Ryu, G. H., Lee, Z. & Lee, C. Wafer-scale monolayer MoS₂ grown by chemical vapor deposition using a reaction of MoO₃ and H₂S. *Journal of Physics: Condensed Matter* **28**, 184002. ISSN: 0953-8984. <https://iopscience.iop.org/article/10.1088/0953-8984/28/18/184002> <https://iopscience.iop.org/article/10.1088/0953-8984/28/18/184002/meta> (Apr. 2016).

269. Tao, L. *et al.* Centimeter-Scale CVD Growth of Highly Crystalline Single-Layer MoS₂ Film with Spatial Homogeneity and the Visualization of Grain Boundaries. *ACS Applied Materials and Interfaces* **9**, 12073–12081. ISSN: 19448252. <https://pubs.acs.org/doi/abs/10.1021/acsami.7b00420> (Apr. 2017).
270. Lin, Z. *et al.* Controllable Growth of Large-Size Crystalline MoS₂ and Resist-Free Transfer Assisted with a Cu Thin Film. *Scientific Reports* **2015 5:1** **5**, 1–10. ISSN: 2045-2322. <https://www.nature.com/articles/srep18596> (Dec. 2015).
271. Ozden, A., Ay, F., Sevik, C. & Perkgöz, N. K. CVD growth of monolayer MoS₂: Role of growth zone configuration and precursors ratio. *Japanese Journal of Applied Physics* **56**, 06GG05. ISSN: 13474065. <https://iopscience.iop.org/article/10.7567/JJAP.56.06GG05%20https://iopscience.iop.org/article/10.7567/JJAP.56.06GG05/meta> (June 2017).
272. Thiruraman, J. P. *et al.* Gas flow through atomic-scale apertures. *Science Advances* **6**, 7927–7945. ISSN: 23752548. <https://www.science.org/doi/abs/10.1126/sciadv.abc7927> (Dec. 2020).
273. Thakur, M. *et al.* Wafer-Scale Fabrication of Nanopore Devices for Single-Molecule DNA Biosensing using MoS₂. *Small Methods* **4**, 2000072. ISSN: 2366-9608. <https://onlinelibrary.wiley.com/doi/full/10.1002/smt.202000072%20https://onlinelibrary.wiley.com/doi/abs/10.1002/smt.202000072%20https://onlinelibrary.wiley.com/doi/10.1002/smt.202000072> (Nov. 2020).
274. Beckstein, O., Tai, K. & Sansom, M. S. Not ions alone: Barriers to ion permeation in nanopores and channels. *Journal of the American Chemical Society* **126**, 14694–14695. ISSN: 00027863. <https://pubs.acs.org/doi/pdf/10.1021/ja045271e> (Nov. 2004).
275. Zhang, Y. J., Oka, T., Suzuki, R., Ye, J. T. & Iwasa, Y. Electrically switchable chiral light-emitting transistor. *Science* **344**, 725–728. ISSN: 10959203 (2014).
276. Baugher, B. W., Churchill, H. O., Yang, Y. & Jarillo-Herrero, P. Optoelectronic devices based on electrically tunable p-n diodes in a monolayer dichalcogenide. *Nat. Nanotechnol.* **9**, 262–267. ISSN: 17483395 (2014).
277. Radisavljevic, B., Radenovic, A., Brivio, J., Giacometti, V. & Kis, A. Single-layer MoS₂ transistors. *Nature Nanotechnology*. ISSN: 1748-3387. arXiv: 0402594v3 [cond-mat] (2011).
278. Lopez-Sanchez, O., Lembke, D., Kayci, M., Radenovic, A. & Kis, A. Ultrasensitive photodetectors based on monolayer MoS₂. *Nat. Nanotechnol.* **8**, 497–501. ISSN: 17483395 (2013).
279. Mak, K. F., McGill, K. L., Park, J. & McEuen, P. L. The valley Hall effect in MoS₂ transistors. *Science* **344**, 1489–1492. ISSN: 10959203 (2014).
280. Li, Y. *et al.* MoS₂ nanoparticles grown on graphene: An advanced catalyst for the hydrogen evolution reaction. *J. Am. Chem. Soc.* **133**, 7296–7299. ISSN: 00027863 (May 2011).

281. Voiry, D. *et al.* The role of electronic coupling between substrate and 2D MoS₂ nanosheets in electrocatalytic production of hydrogen. *Nat. Mater.* **15**, 1003–1009. ISSN: 14764660 (Sept. 2016).
282. Wu, W. Piezoelectricity of single-atomic-layer MoS₂ for energy conversion and piezotronics. *Nature* **514**, 470–474 (Oct. 2014).
283. Liu, K. K. *et al.* Growth of large-area and highly crystalline MoS₂ thin layers on insulating substrates. *Nano Lett.* **12**, 1538–1544. ISSN: 15306984 (Mar. 2012).
284. Heyne, M. H. *et al.* Multilayer MoS₂ growth by metal and metal oxide sulfurization. *J. Mater. Chem. C* **4**, 1295–1304. ISSN: 20507526 (2016).
285. Van Der Zande, A. M. *et al.* Grains and grain boundaries in highly crystalline monolayer molybdenum disulphide. *Nat. Mater.* **12**, 554–561. ISSN: 14761122 (June 2013).
286. Lee, Y. H. *et al.* Synthesis of large-area MoS₂ atomic layers with chemical vapor deposition. *Advanced Materials* **24**, 2320–2325. ISSN: 09359648 (May 2012).
287. Li, S. *et al.* Vapour-liquid-solid growth of monolayer MoS₂ nanoribbons. *Nat. Mater.* **17**, 535–542. ISSN: 14764660 (June 2018).
288. Kumar, V. K., Dhar, S., Choudhury, T. H., Shivashankar, S. A. & Raghavan, S. A predictive approach to CVD of crystalline layers of TMDs: the case of MoS₂. *Nanoscale* **7**, 7802–7810. ISSN: 2040-3372. <https://pubs.rsc.org/en/content/articlehtml/2015/nr/c4nr07080a> <https://pubs.rsc.org/en/content/articlelanding/2015/nr/c4nr07080a> (Apr. 2015).
289. Kim, H., Ovchinnikov, D., Deiana, D., Unuchek, D. & Kis, A. Suppressing nucleation in metal-organic chemical vapor deposition of MoS₂ monolayers by alkali metal halides. *Nano Lett.* **17**, 5056–5063. ISSN: 15306992 (Aug. 2017).
290. Song, J.-G. *et al.* Catalytic chemical vapor deposition of large-area uniform two-dimensional molybdenum disulfide using sodium chloride. *Nanotechnology* **28**, 465103. ISSN: 0957-4484. <https://iopscience.iop.org/article/10.1088/1361-6528/aa8f15> <https://iopscience.iop.org/article/10.1088/1361-6528/aa8f15/meta> (Oct. 2017).
291. Yang, P. *et al.* Batch production of 6-inch uniform monolayer molybdenum disulfide catalyzed by sodium in glass. *Nature Communications* **2018 9:1** **9**, 1–10. ISSN: 2041-1723. <https://www.nature.com/articles/s41467-018-03388-5> (Mar. 2018).
292. Chou, C.-H. S. J., Bitter, P. & Longstreth, J. *Toxicological Profile for Hydrogen Sulfide* 2006.
293. Li, X. *et al.* Role of hydrogen in the chemical vapor deposition growth of MoS₂ atomic layers. *Nanoscale* **7**, 8398–8404. ISSN: 20403372 (May 2015).
294. Lee, C. *et al.* Anomalous lattice vibrations of single- and few-layer MoS₂. *ACS Nano* **4**, 2695–2700. ISSN: 19360851 (May 2010).
295. Mak, K. F., Lee, C., Hone, J., Shan, J. & Heinz, T. F. Atomically thin MoS₂: A new direct-gap semiconductor. *Physical Review Letters*. ISSN: 00319007 (2010).

296. Baker, M. A., Gilmore, R., Lenardi, C. & Gissler, W. XPS investigation of preferential sputtering of S from MoS₂ and determination of MoS_x stoichiometry from Mo and S peak positions. *Appl. Surf. Sci.* **150**, 255–262. ISSN: 01694332 (Aug. 1999).
297. Wang, H. W., Skeldon, P. & Thompson, G. E. XPS studies of MoS₂ formation from ammonium tetrathiomolybdate solutions. *Surf. Coat. Technol.* **91**, 200–207. ISSN: 02578972 (May 1997).
298. Richter, B., Kühlenbeck, H., Freund, H. J. & Bagus, P. S. cluster core-level binding-energy shifts: The role of lattice strain. *Phys. Rev. Lett.* **93**, 026805. ISSN: 00319007 (July 2004).
299. Dumcenco, D. *et al.* Large-Area Epitaxial Monolayer MoS₂. *ACS Nano* **9**, 4611–4620. <https://pubs.acs.org/doi/full/10.1021/acsnano.5b01281> (Apr. 2015).
300. Dumcenco, D. *et al.* Large-area MoS₂ grown using H₂S as the sulphur source. *2D Mater* **2**, 044005. ISSN: 20531583 (Nov. 2015).
301. Close, R., Chen, Z., Shibata, N. & Findlay, S. D. Towards quantitative, atomic-resolution reconstruction of the electrostatic potential via differential phase contrast using electrons. *Ultramicroscopy* **159**, 124–137. ISSN: 18792723 (Dec. 2015).
302. Lazić, I., Bosch, E. G. & Lazar, S. Phase contrast STEM for thin samples: Integrated differential phase contrast. *Ultramicroscopy* **160**, 265–280. ISSN: 18792723 (Jan. 2016).
303. Haque, F., Li, J., Wu, H. C., Liang, X. J. & Guo, P. Solid-state and biological nanopore for real-time sensing of single chemical and sequencing of DNA. *Nano Today* **8**, 56–74. ISSN: 1748-0132 (Feb. 2013).
304. Dekker, C. *Solid-state nanopores* 2007.
305. Hernández-Ainsa, S. & Keyser, U. F. DNA origami nanopores: an emerging tool in biomedicine. <https://doi.org/10.2217/nnm.13.145> **8**, 1551–1554. ISSN: 17486963. <https://www.futuremedicine.com/doi/abs/10.2217/nnm.13.145> (Sept. 2013).
306. Butler, T. Z., Pavlenok, M., Derrington, I. M., Niederweis, M. & Gundlach, J. H. Single-molecule DNA detection with an engineered MspA protein nanopore. *Proceedings of the National Academy of Sciences* **105**, 20647–20652. ISSN: 0027-8424. <https://www.pnas.org/content/105/52/20647%20https://www.pnas.org/content/105/52/20647.abstract> (Dec. 2008).
307. Lu, H., Giordano, F. & Ning, Z. Oxford Nanopore MinION Sequencing and Genome Assembly. *Genomics, Proteomics & Bioinformatics* **14**, 265–279. ISSN: 1672-0229 (Oct. 2016).
308. Liu, K. *et al.* Geometrical Effect in 2D Nanopores. *Nano Letters* **17**, 4223–4230. ISSN: 15306992. <https://pubs.acs.org/doi/full/10.1021/acsnanolett.7b01091> (July 2017).
309. Liu, K., Feng, J., Kis, A. & Radenovic, A. Atomically thin molybdenum disulfide nanopores with high sensitivity for dna translocation. *ACS Nano* **8**, 2504–2511. ISSN: 1936086X. <https://pubs.acs.org/doi/full/10.1021/nn406102h> (Mar. 2014).

310. Graf, M., Lihter, M., Altus, D., Marion, S. & Radenovic, A. Transverse Detection of DNA Using a MoS₂ Nanopore. *Nano Letters* **19**, 9075–9083. ISSN: 15306992. <https://pubs.acs.org/doi/full/10.1021/acs.nanolett.9b04180> (Dec. 2019).
311. Kozubek, R. *et al.* Perforating Freestanding Molybdenum Disulfide Monolayers with Highly Charged Ions. *Journal of Physical Chemistry Letters* **10**, 904–910. ISSN: 19487185. <https://pubs.acs.org/doi/full/10.1021/acs.jpcllett.8b03666> (Mar. 2019).
312. Thiruraman, J. P., Masih Das, P. & Drndić, M. Irradiation of Transition Metal Dichalcogenides Using a Focused Ion Beam: Controlled Single-Atom Defect Creation. *Advanced Functional Materials* **29**. ISSN: 16163028 (Dec. 2019).
313. Ke, J. A., Garaj, S. & Gradečak, S. Nanopores in 2D MoS₂: Defect-Mediated Formation and Density Modulation. *ACS Applied Materials and Interfaces* **11**, 26228–26234. ISSN: 19448252. <https://pubs.acs.org/doi/full/10.1021/acsami.9b03531> (July 2019).
314. Castellanos-Gomez, A. *et al.* Deterministic transfer of two-dimensional materials by all-dry viscoelastic stamping. *2D Materials* **1**, 011002. ISSN: 2053-1583. <https://iopscience.iop.org/article/10.1088/2053-1583/1/1/011002> <https://iopscience.iop.org/article/10.1088/2053-1583/1/1/011002/meta> (Apr. 2014).
315. Frisenda, R. *et al.* Recent progress in the assembly of nanodevices and van der Waals heterostructures by deterministic placement of 2D materials. *Chemical Society Reviews* **47**, 53–68. ISSN: 1460-4744. <https://pubs.rsc.org/en/content/articlehtml/2018/cs/c7cs00556c> <https://pubs.rsc.org/en/content/articlelanding/2018/cs/c7cs00556c> (Jan. 2018).
316. Cun, H. *et al.* Wafer-scale MOCVD growth of monolayer MoS₂ on sapphire and SiO₂. *Nano Research* 2019 12:10 **12**, 2646–2652. ISSN: 1998-0000. <https://link.springer.com/article/10.1007/s12274-019-2502-9> (Aug. 2019).
317. Castellanos-Gomez, A. *et al.* Elastic Properties of Freely Suspended MoS₂ Nanosheets. *Advanced Materials* **24**, 772–775. ISSN: 1521-4095. <https://onlinelibrary.wiley.com/doi/full/10.1002/adma.201103965> <https://onlinelibrary.wiley.com/doi/abs/10.1002/adma.201103965> <https://onlinelibrary.wiley.com/doi/10.1002/adma.201103965> (Feb. 2012).
318. Lu, C., Liu, Y., Ying, Y. & Liu, J. Comparison of MoS₂, WS₂, and graphene oxide for DNA adsorption and sensing. *Langmuir* **33**, 630–637. ISSN: 15205827. <https://pubs.acs.org/doi/full/10.1021/acs.langmuir.6b04502> (Jan. 2017).
319. Li, H. *et al.* A universal, rapid method for clean transfer of nanostructures onto various substrates. *ACS Nano* **8**, 6563–6570. ISSN: 1936086X. <https://pubs.acs.org/doi/full/10.1021/nn501779y> (July 2014).
320. Yu, H. *et al.* Wafer-Scale Growth and Transfer of Highly-Oriented Monolayer MoS₂ Continuous Films. *ACS Nano* **11**, 12001–12007. <https://pubs.acs.org/doi/abs/10.1021/acsnano.7b03819> (Dec. 2017).

321. Meitl, M. A. *et al.* Transfer printing by kinetic control of adhesion to an elastomeric stamp. *Nature Materials* 2006 5:1 **5**, 33–38. ISSN: 1476-4660. <https://www.nature.com/articles/nmat1532> (Dec. 2005).
322. Ma, X. *et al.* Capillary-Force-Assisted Clean-Stamp Transfer of Two-Dimensional Materials. *Nano Letters* **17**, 6961–6967. ISSN: 15306992. <https://pubs.acs.org/doi/full/10.1021/acs.nanolett.7b03449> (Nov. 2017).
323. Thi, Q. H., Kim, H., Zhao, J. & Ly, T. H. Coating two-dimensional MoS₂ with polymer creates a corrosive non-uniform interface. *npj 2D Materials and Applications* 2018 2:1 **2**, 1–7. ISSN: 2397-7132. <https://www.nature.com/articles/s41699-018-0079-x> (Oct. 2018).
324. Zhang, K. *et al.* Considerations for Utilizing Sodium Chloride in Epitaxial Molybdenum Disulfide. *ACS Applied Materials & Interfaces* **10**, 40831–40837. <https://pubs.acs.org/doi/abs/10.1021/acsami.8b16374> (Nov. 2018).
325. Kwon, K. C. *et al.* Wafer-scale transferable molybdenum disulfide thin-film catalysts for photoelectrochemical hydrogen production. *Energy & Environmental Science* **9**, 2240–2248. ISSN: 1754-5706. <https://pubs.rsc.org/en/content/articlehtml/2016/ee/c6ee00144k> <https://pubs.rsc.org/en/content/articlelanding/2016/ee/c6ee00144k> (July 2016).
326. Mlack, J. T. *et al.* Transfer of monolayer TMD WS₂ and Raman study of substrate effects. *Scientific Reports* 2017 7:1 **7**, 1–8. ISSN: 2045-2322. <https://www.nature.com/articles/srep43037> (Feb. 2017).
327. Lee, J. U., Kim, K. & Cheong, H. Resonant Raman and photoluminescence spectra of suspended molybdenum disulfide. *2D Materials* **2**, 044003. ISSN: 2053-1583. <https://iopscience.iop.org/article/10.1088/2053-1583/2/4/044003> <https://iopscience.iop.org/article/10.1088/2053-1583/2/4/044003/meta> (Oct. 2015).
328. Chakraborty, B. *et al.* Symmetry-dependent phonon renormalization in monolayer MoS₂ transistor. *Physical Review B - Condensed Matter and Materials Physics* **85**, 161403. ISSN: 10980121. <https://journals.aps.org/prb/abstract/10.1103/PhysRevB.85.161403> (Apr. 2012).
329. Ma, D. *et al.* A universal etching-free transfer of MoS₂ films for applications in photodetectors. *Nano Research* 2015 8:11 **8**, 3662–3672. ISSN: 1998-0000. <https://link.springer.com/article/10.1007/s12274-015-0866-z> (Oct. 2015).
330. Krivanek, O. L. *et al.* Atom-by-atom structural and chemical analysis by annular dark-field electron microscopy. *Nature* 2010 464:7288 **464**, 571–574. ISSN: 1476-4687. <https://www.nature.com/articles/nature08879> (Mar. 2010).
331. Huang, P. Y. *et al.* Grains and grain boundaries in single-layer graphene atomic patchwork quilts. *Nature* 2010 469:7330 **469**, 389–392. ISSN: 1476-4687. <https://www.nature.com/articles/nature09718> (Jan. 2011).

332. Zhou, Z. *et al.* DNA Translocation through Hydrophilic Nanopore in Hexagonal Boron Nitride. *Scientific Reports* 2013 3:1 **3**, 1–5. ISSN: 2045-2322. <https://www.nature.com/articles/srep03287> (Nov. 2013).
333. Komsa, H.-P. & Krasheninnikov, A. V. Effects of confinement and environment on the electronic structure and exciton binding energy of MoS₂ class. *Physical Review B* **86**, 241201. <https://journals.aps.org/prb/abstract/10.1103/PhysRevB.86.241201> (Dec. 2012).
334. Holroyd, C., Horn, A. B., Casiraghi, C. & Koehler, S. P. Vibrational fingerprints of residual polymer on transferred CVD-graphene. *Carbon* **117**, 473–475. ISSN: 0008-6223 (June 2017).
335. Puster, M., Rodríguez-Manzo, J. A., Balan, A. & Drndić, M. Toward sensitive graphene nanoribbon-nanopore devices by preventing electron beam-induced damage. *ACS Nano* **7**, 11283–11289. ISSN: 19360851. <https://pubs.acs.org/doi/full/10.1021/nn405112m> (Dec. 2013).
336. Manzeli, S., Ovchinnikov, D., Pasquier, D., Yazyev, O. V. & Kis, A. 2D transition metal dichalcogenides. *Nature Reviews Materials* 2017 2:8 **2**, 1–15. ISSN: 2058-8437. <https://www.nature.com/articles/natrevmats201733> (June 2017).
337. Jiang, J.-W., Park, H. S. & Rabczuk, T. Molecular dynamics simulations of single-layer molybdenum disulphide (MoS₂): Stillinger-Weber parametrization, mechanical properties, and thermal conductivity. *Journal of Applied Physics* **114**, 064307. ISSN: 0021-8979. <https://aip.scitation.org/doi/abs/10.1063/1.4818414> (Aug. 2013).
338. Singh, E., Singh, P., Kim, K. S., Yeom, G. Y. & Nalwa, H. S. Flexible Molybdenum Disulfide (MoS₂) Atomic Layers for Wearable Electronics and Optoelectronics. *ACS Applied Materials & Interfaces* **11**, 11061–11105. <https://pubs.acs.org/doi/full/10.1021/acsami.8b19859> (Mar. 2019).
339. Yoon, J. *et al.* Highly Flexible and Transparent Multilayer MoS₂ Transistors with Graphene Electrodes. *Small* **9**, 3295–3300. ISSN: 1613-6829. <https://onlinelibrary.wiley.com/doi/full/10.1002/sml.201300134> <https://onlinelibrary.wiley.com/doi/abs/10.1002/sml.201300134> (Oct. 2013).
340. Singh Nalwa, H. A review of molybdenum disulfide (MoS₂) based photodetectors: from ultra-broadband, self-powered to flexible devices. *RSC Advances* **10**, 30529–30602. <https://pubs.rsc.org/en/content/articlehtml/2020/ra/d0ra03183f> <https://pubs.rsc.org/en/content/articlelanding/2020/ra/d0ra03183f> (Aug. 2020).
341. JA Rogers T Someya, Y. H. Materials and mechanics for stretchable electronics. *Science* **327**, 1603–1607 (Mar. 2010).
342. Wachter, S., Polyushkin, D. K., Bethge, O. & Mueller, T. A microprocessor based on a two-dimensional semiconductor. *Nature Communications* 2017 8:1 **8**, 1–6. ISSN: 2041-1723. <https://www.nature.com/articles/ncomms14948> (Apr. 2017).

343. Cho, B. *et al.* Chemical Sensing of 2D Graphene/MoS₂ Heterostructure device. *ACS Applied Materials and Interfaces* **7**, 16775–16780. <https://pubs.acs.org/doi/abs/10.1021/acsami.5b04541> (Aug. 2015).
344. Rathi, S. *et al.* Tunable Electrical and Optical Characteristics in Monolayer Graphene and Few-Layer MoS₂ Heterostructure Devices. *Nano Letters* **15**, 5017–5024. <https://pubs.acs.org/doi/abs/10.1021/acs.nanolett.5b01030> (Aug. 2015).
345. Schulman, D. S., Arnold, A. J., Razavieh, A., Nasr, J. & Das, S. The Prospect of Two-Dimensional Heterostructures: A Review of Recent Breakthroughs. *IEEE Nanotechnology Magazine* **11**, 6–17 (June 2017).
346. Gayatri Swain, Sabiha Sultana & Kulamani Parida. A review on vertical and lateral heterostructures of semiconducting 2D-MoS₂ with other 2D materials: a feasible perspective for energy conversion. *Nanoscale* **13**, 9908–9944. <https://pubs.rsc.org/en/content/articlehtml/2021/nr/d1nr00931a> <https://pubs.rsc.org/en/content/articlelanding/2021/nr/d1nr00931a> (June 2021).
347. Cai, Z., Liu, B., Zou, X. & Cheng, H.-M. Chemical Vapor Deposition Growth and Applications of Two-Dimensional Materials and Their Heterostructures. *Chemical Reviews* **118**, 6091–6133. <https://pubs.acs.org/doi/full/10.1021/acs.chemrev.7b00536> (July 2018).
348. Eda, G. *et al.* Coherent Atomic and Electronic Heterostructures of Single-Layer MoS₂. *ACS Nano* **6**, 7311–7317. <https://pubs.acs.org/doi/abs/10.1021/nn302422x> (Aug. 2012).
349. Liu, Y. *et al.* Van der Waals heterostructures and devices. *Nature Reviews Materials* **2016** *1*:9 **1**, 1–17. ISSN: 2058-8437. <https://www.nature.com/articles/natrevmats201642> (July 2016).
350. AK Geim, I. G. Van der Waals heterostructures. *Nature* **499**, 419–425 (2013).
351. Sitek, J. *et al.* Substrate-Induced Variances in Morphological and Structural Properties of MoS₂ Grown by Chemical Vapor Deposition on Epitaxial Graphene and SiO₂. *Cite This: ACS Appl. Mater. Interfaces* **12**, 45110. <https://dx.doi.org/10.1021/acsami.0c06173> (2020).
352. Shrivastava, M. & Rao, V. R. A Roadmap for Disruptive Applications and Heterogeneous Integration Using Two-Dimensional Materials: State-of-the-Art and Technological Challenges. *Nano Letters* **21**, 6359–6381. <https://pubs.acs.org/doi/abs/10.1021/acs.nanolett.1c00729> (Aug. 2021).
353. Kim, S.-Y., Kwak, J., Ciobanu, C. V. & Kwon, S.-Y. Recent Developments in Controlled Vapor-Phase Growth of 2D Group 6 Transition Metal Dichalcogenides. *Advanced Materials* **31**, 1804939. ISSN: 1521-4095. <https://onlinelibrary.wiley.com/doi/full/10.1002/adma.201804939> <https://onlinelibrary.wiley.com/doi/abs/10.1002/adma.201804939> <https://onlinelibrary.wiley.com/doi/10.1002/adma.201804939> (May 2019).
354. Wang, P., Yang, D. & Pi, X. Toward Wafer-Scale Production of 2D Transition Metal Chalcogenides. *Advanced Electronic Materials* **7** (Aug. 2021).

355. Boandoh, S. *et al.* A Novel and Facile Route to Synthesize Atomic-Layered MoS₂ Film for Large-Area Electronics. *Small* **13**, 1701306. ISSN: 1613-6829. <https://onlinelibrary.wiley.com/doi/full/10.1002/sml.201701306><https://onlinelibrary.wiley.com/doi/abs/10.1002/sml.201701306> (Oct. 2017).
356. Boandoh, S. *et al.* Wafer-Scale van der Waals Heterostructures with Ultraclean Interfaces via the Aid of Viscoelastic Polymer. *ACS Applied Materials and Interfaces* **11**, 1579–1586 (Jan. 2019).
357. Wang, Q. *et al.* Wafer-Scale Highly Oriented Monolayer MoS₂ with Large Domain Sizes. *Nano Letters* **20**, 7193–7199. <https://pubs.acs.org/doi/abs/10.1021/acs.nanolett.0c02531> (Oct. 2020).
358. He, T. *et al.* Synthesis of large-area uniform MoS₂ films by substrate-moving atmospheric pressure chemical vapor deposition: From monolayer to multilayer. *2D Materials* **6** (Mar. 2019).
359. Kim, T. *et al.* Wafer-scale production of highly uniform two-dimensional MoS₂ by metal-organic chemical vapor deposition. *Nanotechnology* **28**, 18LT01. ISSN: 0957-4484. <https://iopscience.iop.org/article/10.1088/1361-6528/aa6958><https://iopscience.iop.org/article/10.1088/1361-6528/aa6958/meta> (Apr. 2017).
360. Sun, J. *et al.* Synthesis Methods of Two-Dimensional MoS₂: A Brief Review. *Crystals* **2017**, Vol. 7, Page 198 **7**, 198. ISSN: 20734352. <https://www.mdpi.com/2073-4352/7/7/198/htm><https://www.mdpi.com/2073-4352/7/7/198> (July 2017).
361. Lin, Y.-C. Wafer-scale MoS₂ thin layers prepared by MoO₃ sulfurization. *Nanoscale* **4**, 6637–6641 (Oct. 2012).
362. Dhar, S., Kumar, V. K., Choudhury, T. H., Shivashankar, S. A. & Raghavan, S. Chemical vapor deposition of MoS₂ layers from Mo–S–C–O–H system: thermodynamic modeling and validation. *Physical Chemistry Chemical Physics* **18**, 14918–14926. ISSN: 1463-9084. <https://pubs.rsc.org/en/content/articlehtml/2016/cp/c6cp01617k><https://pubs.rsc.org/en/content/articlelanding/2016/cp/c6cp01617k> (June 2016).
363. Feng, Z. C. III-Nitride Semiconductor Materials. *III-Nitride Semiconductor Materials*. https://books.google.com/books/about/Iii_nitride_Semiconductor_Materials.html?id=GL0uDQAAQBAJ (Mar. 2006).
364. Jang, Y., Yeo, S., Lee, H. B. R., Kim, H. & Kim, S. H. Wafer-scale, conformal and direct growth of MoS₂ thin films by atomic layer deposition. *Applied Surface Science* **365**, 160–165. ISSN: 0169-4332 (Mar. 2016).
365. Lin, J. *et al.* Large-area growth of MoS₂ at temperatures compatible with integrating back-end-of-line functionality. *2D Materials* **8**, 025008. ISSN: 2053-1583. <https://iopscience.iop.org/article/10.1088/2053-1583/abc460><https://iopscience.iop.org/article/10.1088/2053-1583/abc460/meta> (Dec. 2020).

366. Mortelmans, W. *et al.* Epitaxial registry and crystallinity of MoS₂ via molecular beam and metalorganic vapor phase van der Waals epitaxy. *Applied Physics Letters* **117**, 033101. ISSN: 0003-6951. <https://aip.scitation.org/doi/abs/10.1063/5.0013391> (July 2020).
367. Kazzi, S. E. *et al.* MoS₂ synthesis by gas source MBE for transition metal dichalcogenides integration on large scale substrates. *Journal of Applied Physics* **123**, 135702. ISSN: 0021-8979. <https://aip.scitation.org/doi/abs/10.1063/1.5008933> (Apr. 2018).
368. Chiappe, D. *et al.* Layer-controlled epitaxy of 2D semiconductors: bridging nanoscale phenomena to wafer-scale uniformity. *Nanotechnology* **29**, 425602. ISSN: 0957-4484. <https://iopscience.iop.org/article/10.1088/1361-6528/aad798%20https://iopscience.iop.org/article/10.1088/1361-6528/aad798/meta> (Aug. 2018).
369. Schaefer, C. M. *et al.* Carbon Incorporation in MOCVD of MoS₂ Thin Films Grown from an Organosulfide Precursor. *Chemistry of Materials* **33**, 4474–4487. <https://pubs.acs.org/doi/full/10.1021/acs.chemmater.1c00646> (June 2021).
370. Mun, J. *et al.* Low-temperature growth of layered molybdenum disulphide with controlled clusters. *Scientific Reports* 2016 6:1 **6**, 1–7. ISSN: 2045-2322. <https://www.nature.com/articles/srep21854> (Feb. 2016).
371. Choi, S. H. *et al.* Water-Assisted Synthesis of Molybdenum Disulfide Film with Single Organic Liquid Precursor. *Scientific Reports* 2017 7:1 **7**, 1–8. ISSN: 2045-2322. <https://www.nature.com/articles/s41598-017-02228-8> (May 2017).
372. Li, H. From bulk to monolayer MoS₂: evolution of Raman scattering. *Adv. Funct. Mater.* **22**, 1385–1390 (Apr. 2012).
373. Shree, S. *et al.* High optical quality of MoS₂ monolayers grown by chemical vapor deposition. *2D Materials* **7**, 015011. ISSN: 2053-1583. <https://iopscience.iop.org/article/10.1088/2053-1583/ab4f1f%20https://iopscience.iop.org/article/10.1088/2053-1583/ab4f1f/meta> (Nov. 2019).
374. Komsa, H. P. *et al.* Two-dimensional transition metal dichalcogenides under electron irradiation: Defect production and doping. *Physical Review Letters* **109**, 035503. ISSN: 00319007. <https://journals.aps.org/prl/abstract/10.1103/PhysRevLett.109.035503> (July 2012).
375. Giannuzzi, L. A. & Stevie, F. A. A review of focused ion beam milling techniques for TEM specimen preparation. *Micron* **30**, 197–204. ISSN: 0968-4328 (June 1999).
376. Burnett, T. L. *et al.* Large volume serial section tomography by Xe Plasma FIB dual beam microscopy. *Ultramicroscopy* **161**, 119–129. ISSN: 0304-3991 (Feb. 2016).
377. Jiang, J., Xu, T., Lu, J., Sun, L. & Ni, Z. Defect Engineering in 2D Materials: Precise Manipulation and Improved Functionalities. *Research* **2019**, 1–14. ISSN: 26395274 (Dec. 2019).
378. Ahn, E. C. 2D materials for spintronic devices. *npj 2D Materials and Applications* 2020 4:1 **4**, 1–14. ISSN: 2397-7132. <https://www.nature.com/articles/s41699-020-0152-0> (June 2020).

379. Zhang, M. *et al.* Super-resolved Optical Mapping of Reactive Sulfur-Vacancies in Two-Dimensional Transition Metal Dichalcogenides. *ACS Nano* **15**, 7168–7178. ISSN: 1936086X. <https://pubs.acs.org/doi/full/10.1021/acsnano.1c00373> (Apr. 2021).
380. Caldwell, J. D. *et al.* Photonics with hexagonal boron nitride. *Nature Reviews Materials* **2019 4:8 4**, 552–567. ISSN: 2058-8437. <https://www.nature.com/articles/s41578-019-0124-1> (July 2019).
381. Glushkov, E. *et al.* Engineering optically active defects in hexagonal boron nitride using focused ion beam and water. <https://arxiv.org/abs/2107.02254v1> (July 2021).
382. Tuller, H. L. & Bishop, S. R. Point Defects in Oxides: Tailoring Materials Through Defect Engineering. <http://dx.doi.org/10.1146/annurev-matsci-062910-100442> **41**, 369–398. ISSN: 15317331. <https://www.annualreviews.org/doi/abs/10.1146/annurev-matsci-062910-100442> (July 2011).
383. Zhong, K., Bu, R., Jiao, F., Liu, G. & Zhang, C. Toward the defect engineering of energetic materials: A review of the effect of crystal defects on the sensitivity. *Chemical Engineering Journal* **429**, 132310. ISSN: 1385-8947 (Feb. 2022).
384. Lin, Z. *et al.* Defect engineering of two-dimensional transition metal dichalcogenides. *2D Materials* **3**, 022002. ISSN: 2053-1583. <https://iopscience.iop.org/article/10.1088/2053-1583/3/2/022002> %20https://iopscience.iop.org/article/10.1088/2053-1583/3/2/022002/meta (Apr. 2016).
385. Thiruraman, J. P., Masih Das, P. & Drndić, M. Ions and Water Dancing through Atom-Scale Holes: A Perspective toward “Size Zero”. *ACS Nano*. ISSN: 1936086X. <https://pubs.acs.org/doi/full/10.1021/acsnano.0c01625> (2020).
386. Xue, L. *et al.* Solid-state nanopore sensors. *Nature Reviews Materials* **2020 5:12 5**, 931–951. ISSN: 2058-8437. <https://www.nature.com/articles/s41578-020-0229-6> (Sept. 2020).
387. Drndić, M. Sequencing with graphene pores. *Nature Nanotechnology* **2014 9:10 9**, 743–743. ISSN: 1748-3395. <https://www.nature.com/articles/nnano.2014.232> (Oct. 2014).
388. Fang, A., Kroenlein, K., Riccardi, D. & Smolyanitsky, A. Highly mechanosensitive ion channels from graphene-embedded crown ethers. *Nature Materials* **2018 18:1 18**, 76–81. ISSN: 1476-4660. <https://www.nature.com/articles/s41563-018-0220-4> (Nov. 2018).
389. Fang, A., Kroenlein, K. & Smolyanitsky, A. Mechanosensitive Ion Permeation across Subnanoporous MoS₂ Monolayers. *Journal of Physical Chemistry C* **123**, 3588–3593. ISSN: 19327455. <https://pubs.acs.org/doi/full/10.1021/acs.jpcc.8b11224> (Feb. 2019).
390. Danda, G. & Drndić, M. Two-dimensional nanopores and nanoporous membranes for ion and molecule transport. *Current Opinion in Biotechnology* **55**, 124–133. ISSN: 0958-1669 (Feb. 2019).

391. Fried, J. P. *et al.* In situ solid-state nanopore fabrication. *Chemical Society Reviews* **50**, 4974–4992. ISSN: 1460-4744. <https://pubs.rsc.org/en/content/articlehtml/2021/cs/d0cs00924e> <https://pubs.rsc.org/en/content/articlelanding/2021/cs/d0cs00924e> (Apr. 2021).
392. Chen, J., Balan, A., Masih Das, P., Thiruraman, J. P. & Drndić, M. Computer vision AC-STEM automated image analysis for 2D nanopore applications. *Ultramicroscopy* **231**, 113249. ISSN: 0304-3991 (Dec. 2021).
393. Berg, S. *et al.* ilastik: interactive machine learning for (bio)image analysis. *Nature Methods* **16**, 1226–1232. ISSN: 1548-7105. <https://www.nature.com/articles/s41592-019-0582-9> (Sept. 2019).
394. Bradski, G. The OpenCV Library. *Dr. Dobbs's Journal of Software Tools* (2000).
395. Der Walt, S. *et al.* scikit-image: image processing in Python. *PeerJ* **2**, e453 (2014).
396. Otsu, N. THRESHOLD SELECTION METHOD FROM GRAY-LEVEL HISTOGRAMS. *IEEE Trans Syst Man Cybern* **SMC-9**, 62–66. ISSN: 00189472 (1979).
397. Govind Rajan, A. *et al.* Addressing the isomer cataloguing problem for nanopores in two-dimensional materials. *Nature Materials* **18**, 129–135. ISSN: 1476-4660. <https://www.nature.com/articles/s41563-018-0258-3> (Jan. 2019).
398. Davis, S. J. *et al.* Pressure-Induced Enlargement and Ionic Current Rectification in Symmetric Nanopores. *Nano Letters*. ISSN: 15306992. <https://pubs.acs.org/doi/abs/10.1021/acs.nanolett.0c03083> (2020).
399. Li, H., Huang, J. K., Shi, Y. & Li, L. J. Toward the Growth of High Mobility 2D Transition Metal Dichalcogenide Semiconductors. *Advanced Materials Interfaces* **6**, 1900220. ISSN: 2196-7350. <https://onlinelibrary.wiley.com/doi/full/10.1002/admi.201900220> <https://onlinelibrary.wiley.com/doi/abs/10.1002/admi.201900220> <https://onlinelibrary.wiley.com/doi/10.1002/admi.201900220> (Dec. 2019).
400. Hu, Z. *et al.* Two-dimensional transition metal dichalcogenides: interface and defect engineering. *Chemical Society Reviews* **47**, 3100–3128. ISSN: 1460-4744. <https://pubs.rsc.org/en/content/articlehtml/2018/cs/c8cs00024g> <https://pubs.rsc.org/en/content/articlelanding/2018/cs/c8cs00024g> (May 2018).
401. He, Y. M. *et al.* Single quantum emitters in monolayer semiconductors. *Nature Nanotechnology* **10**, 497–502. ISSN: 17483395 (June 2015).
402. Tran, T. T., Bray, K., Ford, M. J., Toth, M. & Aharonovich, I. Quantum emission from hexagonal boron nitride monolayers. *Nature Nanotechnology* **11**, 37–41. ISSN: 17483395 (Jan. 2016).
403. Sangwan, V. K. *et al.* Multi-terminal memtransistors from polycrystalline monolayer molybdenum disulfide. *Nature* **554**, 500–504. ISSN: 14764687 (Feb. 2018).
404. Sangwan, V. K. *et al.* Gate-tunable memristive phenomena mediated by grain boundaries in single-layer MoS₂. *Nature Nanotechnology* **10**, 403–406. ISSN: 17483395 (May 2015).

405. Avsar, A. *et al.* Defect induced, layer-modulated magnetism in ultrathin metallic PtSe₂. *Nature Nanotechnology* **14**, 674–678. ISSN: 17483395 (July 2019).
406. Ye, G. *et al.* Defects Engineered Monolayer MoS₂ for Improved Hydrogen Evolution Reaction. *Nano Letters* **16**, 1097–1103. ISSN: 15306992 (Feb. 2016).
407. Mitterreiter, E. *et al.* In-situ visualization of hydrogen evolution sites on helium ion treated molybdenum dichalcogenides under reaction conditions. *npj 2D Materials and Applications* **3**. ISSN: 23977132 (Dec. 2019).
408. Förster, A., Gemming, S., Seifert, G. & Tománek, D. Chemical and Electronic Repair Mechanism of Defects in MoS₂ Monolayers. *ACS Nano* **11**, 9989–9996. ISSN: 1936086X (Oct. 2017).
409. Makarova, M., Okawa, Y. & Aono, M. Selective adsorption of thiol molecules at sulfur vacancies on MoS₂ (0001), followed by vacancy repair via S-C dissociation. *Journal of Physical Chemistry C* **116**, 22411–22416. ISSN: 19327447 (Oct. 2012).
410. Yu, Z. *et al.* Towards intrinsic charge transport in monolayer molybdenum disulfide by defect and interface engineering. *Nature Communications* **5**. ISSN: 20411723 (Oct. 2014).
411. Ding, Q. *et al.* Basal-Plane Ligand Functionalization on Semiconducting 2H-MoS₂ Monolayers. *ACS Applied Materials and Interfaces* **9**, 12734–12742. ISSN: 19448252 (Apr. 2017).
412. Chou, S. S. *et al.* Ligand conjugation of chemically exfoliated MoS₂. *Journal of the American Chemical Society* **135**, 4584–4587. ISSN: 00027863 (Mar. 2013).
413. Ghorbani-Asl, M., Kretschmer, S., Spearot, D. E. & Krasheninnikov, A. V. Two-dimensional MoS₂ under ion irradiation: From controlled defect production to electronic structure engineering. *2D Materials* **4**. ISSN: 20531583 (June 2017).
414. Mignuzzi, S. *et al.* Effect of disorder on Raman scattering of single-layer Mo S₂. *Physical Review B - Condensed Matter and Materials Physics* **91**. ISSN: 1550235X (May 2015).
415. Kang, N., Paudel, H. P., Leuenberger, M. N., Tetard, L. & Khondaker, S. I. Photoluminescence quenching in single-layer MoS₂ via oxygen plasma treatment. *Journal of Physical Chemistry C* **118**, 21258–21263. ISSN: 19327455 (Sept. 2014).
416. Parkin, W. M. *et al.* Raman Shifts in Electron-Irradiated Monolayer MoS₂. *ACS Nano* **10**, 4134–4142. ISSN: 1936086X (Apr. 2016).
417. Novoselov, K. S., Mishchenko, A., Carvalho, A. & Castro Neto, A. H. *2D materials and van der Waals heterostructures* 2016.
418. Atatüre, M., Englund, D., Vamivakas, N., Lee, S. Y. & Wrachtrup, J. Material platforms for spin-based photonic quantum technologies. *Nature Reviews Materials* **3**, 38–51. ISSN: 20588437. <http://dx.doi.org/10.1038/s41578-018-0008-9> (2018).
419. Radha, B. *et al.* Molecular transport through capillaries made with atomic-scale precision. *Nature* **538**, 222–225. ISSN: 14764687 (2016).

420. Fumagalli, L. *et al.* Anomalously low dielectric constant of confined water. *Science* **360**, 1339–1342. ISSN: 10959203 (2018).
421. Kim, S. *et al.* Integrated on Chip Platform with Quantum Emitters in Layered Materials. *Advanced Optical Materials*, 1901132. ISSN: 2195-1071. <http://arxiv.org/abs/1907.04546> (2019).
422. Kianinia, M. *et al.* All-optical control and super-resolution imaging of quantum emitters in layered materials. *Nature Communications* **9**. ISSN: 20411723. <http://dx.doi.org/10.1038/s41467-018-03290-0> (2018).
423. Feng, J. *et al.* Imaging of Optically Active Defects with Nanometer Resolution. *Nano Letters* **18**, 1739–1744. ISSN: 15306992 (Mar. 2018).
424. Comtet, J. *et al.* Wide-Field Spectral Super-Resolution Mapping of Optically Active Defects in Hexagonal Boron Nitride. *Nano Letters* **19**, 2516–2523. ISSN: 15306992 (Apr. 2019).
425. Glushkov, E. *et al.* Waveguide-Based Platform for Large-FOV Imaging of Optically Active Defects in 2D Materials. *ACS Photonics* **6**, 3100–3107. ISSN: 23304022 (2019).
426. Malein, R. N. E., Khatri, P., Ramsay, A. J. & Luxmoore, I. J. Stimulated Emission Depletion Spectroscopy of Color Centers in Hexagonal Boron Nitride. *ACS Photonics* **8**, 1007–1012. ISSN: 23304022 (2021).
427. Khatri, P., Malein, R. N. E., Ramsay, A. J. & Luxmoore, I. J. Stimulated Emission Depletion Microscopy with Color Centers in Hexagonal Boron Nitride. *arXiv preprint arXiv:2103.01718* (2021).
428. Comtet, J. *et al.* Direct observation of water-mediated single-proton transport between hBN surface defects. *Nature Nanotechnology* **15**, 598–604. ISSN: 17483395 (July 2020).
429. Comtet, J. *et al.* Anomalous interfacial dynamics of single proton charges in binary aqueous solutions. *Science Advances* **7**, eabg8568. <https://www.science.org/doi/abs/10.1126/sciadv.abg8568> (2021).
430. Chejanovsky, N. *et al.* Single-spin resonance in a van der Waals embedded paramagnetic defect. *Nature Materials*. ISSN: 1476-4660. <https://doi.org/10.1038/s41563-021-00979-4> <http://arxiv.org/abs/1906.05903> (2021).
431. Gottscholl, A. *et al.* Initialization and read-out of intrinsic spin defects in a van der Waals crystal at room temperature. *Nature Materials* **19**, 540–545. ISSN: 14764660. <http://dx.doi.org/10.1038/s41563-020-0619-6> (2020).
432. Kianinia, M., White, S., Fröch, J. E., Bradac, C. & Aharonovich, I. Generation of Spin Defects in Hexagonal Boron Nitride. *ACS Photonics* **7**, 2147–2152. ISSN: 23304022 (2020).
433. Stern, H. L. *et al.* Room-temperature optically detected magnetic resonance of single defects in hexagonal boron nitride. *arXiv*, 1–25. <http://arxiv.org/abs/2103.16494> (2021).
434. Gottscholl, A. *et al.* Room temperature coherent control of spin defects in hexagonal boron nitride. *Science Advances* **7** (2021).

435. Caneva, S. *et al.* Nucleation control for large, single crystalline domains of monolayer hexagonal boron nitride via Si-doped Fe catalysts. *Nano Letters* **15**, 1867–1875. ISSN: 15306992 (2015).
436. Koperski, M. *et al.* Midgap radiative centers in carbon-enriched hexagonal boron nitride. *Proceedings of the National Academy of Sciences of the United States of America* **117**, 13214–13219. ISSN: 10916490 (2020).
437. Choi, S. *et al.* Engineering and Localization of Quantum Emitters in Large Hexagonal Boron Nitride Layers. *ACS Applied Materials & Interfaces* **8**, 29642–29648. ISSN: 1944-8244. <https://doi.org/10.1021/acsami.6b09875> (Nov. 2016).
438. Yim, D., Yu, M., Noh, G., Lee, J. & Seo, H. Polarization and Localization of Single-Photon Emitters in Hexagonal Boron Nitride Wrinkles. *ACS Applied Materials and Interfaces* **12**, 36362–36369. ISSN: 19448252 (2020).
439. Vogl, T., Buchler, B. C., Lu, Y. & Lam, P. K. Fabrication and Deterministic Transfer of High-Quality Quantum Emitters in Hexagonal Boron Nitride. *ACS Photonics* **5**, 2305–2312 (2018).
440. Fischer, M. *et al.* Controlled generation of luminescent centers in hexagonal boron nitride by irradiation engineering. *Science Advances* **7**, eabe7138. ISSN: 2375-2548. <https://advances.sciencemag.org/lookup/doi/10.1126/sciadv.abe7138> (2021).
441. Toledo, J. R. *et al.* Electron paramagnetic resonance signature of point defects in neutron-irradiated hexagonal boron nitride. *Physical Review B* **98**, 1–6. ISSN: 24699969 (2018).
442. Hayee, F. *et al.* Revealing multiple classes of stable quantum emitters in hexagonal boron nitride with correlated optical and electron microscopy. *Nature Materials*. ISSN: 14764660 (2020).
443. Proscia, N. V. *et al.* Near-deterministic activation of room-temperature quantum emitters in hexagonal boron nitride. *Optica* **5**, 1128–1134. <https://doi.org/10.1364/OPTICA.5.001128> <http://www.osapublishing.org/optica/abstract.cfm?URI=optica-5-9-1128> (Sept. 2018).
444. Li, C. *et al.* Scalable and Deterministic Fabrication of Quantum Emitter Arrays from Hexagonal Boron Nitride. *Nano Letters* **21**, 3626–3632. ISSN: 1530-6984. <http://arxiv.org/abs/2103.02875> (2021).
445. Hou, S. *et al.* Localized emission from laser-irradiated defects in 2D hexagonal boron nitride. *2D Materials* **5**. ISSN: 20531583 (2018).
446. Gao, X. *et al.* Femtosecond Laser Writing of Spin Defects in Hexagonal Boron Nitride. *ACS Photonics* **8**, 994–1000. ISSN: 23318422. <https://doi.org/10.1021/acsp Photonics.0c01847> (Apr. 2021).
447. Fournier, C. *et al.* Position-controlled quantum emitters with reproducible emission wavelength in hexagonal boron nitride. *Nature Communications* **12**. ISSN: 23318422. <http://arxiv.org/abs/2011.12224> (2021).

448. Ziegler, J. *et al.* Deterministic Quantum Emitter Formation in Hexagonal Boron Nitride via Controlled Edge Creation. *Nano Letters* **19**, 2121–2127. ISSN: 15306992 (2019).
449. Fox, D. S. *et al.* Nanopatterning and Electrical Tuning of MoS₂ Layers with a Subnanometer Helium Ion Beam. *Nano Letters* **15**, 5307–5313 (2015).
450. Mupparapu, R. *et al.* Facile Resist-Free Nanopatterning of Monolayers of MoS₂ by Focused Ion-Beam Milling. *Advanced Materials Interfaces* **7**. ISSN: 21967350 (2020).
451. Giannuzzi, L. & Smith, N. TEM Specimen Preparation with Plasma FIB Xe + Ions. *Microscopy and Microanalysis* **17**, 646–647. ISSN: 1431-9276 (2011).
452. Zhong, X. *et al.* Comparing Xe+pFIB and Ga+FIB for TEM sample preparation of Al alloys: Minimising FIB-induced artefacts. *Journal of Microscopy* **282**, 101–112. ISSN: 0022-2720. <https://doi.org/10.1111/jmi.12983> (May 2021).
453. Schué, L., Stenger, I., Fossard, F., Loiseau, A. & Barjon, J. Characterization methods dedicated to nanometer-thick hBN layers. *2D Materials* **4**, 15028 (2016).
454. Taniguchi, T. & Watanabe, K. Synthesis of high-purity boron nitride single crystals under high pressure by using Ba–BN solvent. *Journal of crystal growth* **303**, 525–529 (2007).
455. Ovesný, M., Křížek, P., Borkovec, J., Švindrych, Z. & Hagen, G. M. ThunderSTORM: A comprehensive ImageJ plug-in for PALM and STORM data analysis and super-resolution imaging. *Bioinformatics* **30**, 2389–2390. ISSN: 14602059 (Aug. 2014).
456. Turiansky, M. E., Alkauskas, A., Bassett, L. C. & Van De Walle, C. G. Dangling Bonds in Hexagonal Boron Nitride as Single-Photon Emitters. *Physical Review Letters* **123**. ISSN: 10797114 (2019).
457. Streletsii, A. N., Permenov, D. G., Bokhonov, B. B., Leonov, A. V. & Mudretsova, S. N. Mechanochemistry of hexagonal boron nitride. 2. Reactivity upon interaction with water. *Colloid Journal* **72**, 553–558. ISSN: 1061933X (2010).
458. Speiser, A. *et al.* Deep learning enables fast and dense single-molecule localization with high accuracy. *Nature Methods* **18**, 1082–1090. ISSN: 1548-7105. <https://doi.org/10.1038/s41592-021-01236-x> (2021).
459. Kalhor, N., Boden, S. A. & Mizuta, H. Microelectronic Engineering Sub-10 nm patterning by focused He-ion beam milling for fabrication of downscaled graphene nano devices. *MICROELECTRONIC ENGINEERING* **114**, 70–77. ISSN: 0167-9317. <http://dx.doi.org/10.1016/j.mee.2013.09.018> (2014).
460. Buchheim, J., Wyss, R. M., Shorubalko, I. & Park, H. G. Understanding the interaction between energetic ions and freestanding graphene towards practical 2D perforation. *Nanoscale* **8**, 8345–8354. ISSN: 20403372 (2016).
461. Shorubalko, I., Choi, K., Stiefel, M. & Park, H. G. Ion beam profiling from the interaction with a freestanding 2D layer. *Beilstein Journal of Nanotechnology* **8**, 682–687. ISSN: 21904286 (2017).

462. Odermatt, P. D. *et al.* High-Resolution Correlative Microscopy: Bridging the Gap between Single Molecule Localization Microscopy and Atomic Force Microscopy. *Nano Letters* **15**, 4896–4904. ISSN: 15306992 (Aug. 2015).
463. Pereiro, I., Fomitcheva Khartchenko, A., Petrini, L. & Kaigala, G. V. Nip the bubble in the bud: A guide to avoid gas nucleation in microfluidics. *Lab on a Chip* **19**, 2296–2314. ISSN: 14730189 (July 2019).
464. Dimitrov, V. *et al.* Nanopores in solid-state membranes engineered for single molecule detection. *Nanotechnology* **21**, 065502. ISSN: 0957-4484 (Feb. 2010).
465. Uram, J. D., Ke, K. & Mayer, M. L. Noise and bandwidth of current recordings from submicrometer pores and nanopores. *ACS Nano* **2**, 857–872. ISSN: 19360851 (May 2008).
466. Tabard-Cossa, V., Trivedi, D., Wiggin, M., Jetha, N. N. & Marziali, A. Noise analysis and reduction in solid-state nanopores. *Nanotechnology* **18**. ISSN: 09574484 (Aug. 2007).
467. Gravelle, S., Joly, L., Ybert, C. & Bocquet, L. Large permeabilities of hourglass nanopores: From hydrodynamics to single file transport. *Journal of Chemical Physics* **141**. ISSN: 10897690 (Nov. 2014).
468. Fragasso, A., Pud, S. & Dekker, C. 1/f noise in solid-state nanopores is governed by access and surface regions. *Nanotechnology* **30**. ISSN: 13616528 (July 2019).
469. Beamish, E., Kwok, H., Tabard-Cossa, V. & Godin, M. Precise control of the size and noise of solid-state nanopores using high electric fields. *Nanotechnology* **23**. ISSN: 09574484 (Oct. 2012).
470. Lohse, D. & Zhang, X. Surface nanobubbles and nanodroplets. *Reviews of Modern Physics* **87**. ISSN: 15390756 (Aug. 2015).
471. Cantley, L. *et al.* Voltage gated inter-cation selective ion channels from graphene nanopores. *Nanoscale* **11**, 9856–9861. ISSN: 20403372 (May 2019).
472. Li, Y. *et al.* Photoresistance switching of plasmonic nanopores. *Nano Letters* **15**, 776–782. ISSN: 15306992 (Jan. 2015).
473. Lloyd, D. *et al.* Adhesion, Stiffness, and Instability in Atomically Thin MoS₂ Bubbles. *Nano Letters* **17**, 5329–5334. ISSN: 15306992 (Sept. 2017).
474. Gaur, A. P. *et al.* Surface energy engineering for tunable wettability through controlled synthesis of MoS₂. *Nano Letters* **14**, 4314–4321. ISSN: 15306992 (Aug. 2014).
475. Chow, P. K. *et al.* Wetting of mono and few-layered WS₂ and MoS₂ films supported on Si/SiO₂ substrates. *ACS Nano* **9**, 3023–3031. ISSN: 1936086X (Mar. 2015).
476. Annamalai, M. *et al.* Surface energy and wettability of van der Waals structures. *Nanoscale* **8**, 5764–5770. ISSN: 20403372 (Mar. 2016).
477. Taherian, F., Marcon, V., Van Der Vegt, N. F. & Leroy, F. What is the contact angle of water on graphene? *Langmuir* **29**, 1457–1465. ISSN: 07437463 (Feb. 2013).

478. Zomer, P. J., Dash, S. P., Tombros, N. & Van Wees, B. J. A transfer technique for high mobility graphene devices on commercially available hexagonal boron nitride. *Applied Physics Letters* **99**. ISSN: 00036951 (Dec. 2011).
479. Agrawal, A. *et al.* Controlling the location and spatial extent of nanobubbles using hydrophobically nanopatterned surfaces. *Nano Letters* **5**, 1751–1756. ISSN: 15306984 (Sept. 2005).
480. Seddon, J. R., Kooij, E. S., Poelsema, B., Zandvliet, H. J. & Lohse, D. Surface bubble nucleation stability. *Physical Review Letters* **106**. ISSN: 00319007 (Feb. 2011).
481. Guo, Z., Liu, Y., Xiao, Q. & Zhang, X. Hidden Nanobubbles in Undersaturated Liquids. *Langmuir* **32**, 11328–11334. ISSN: 15205827 (Nov. 2016).
482. Wang, Y. *et al.* Entrapment of interfacial nanobubbles on nano-structured surfaces. *Soft Matter* **13**, 5381–5388. ISSN: 17446848 (2017).
483. Virtanen, P. *et al.* SciPy 1.0: fundamental algorithms for scientific computing in Python. *Nature Methods* **17**, 261–272. ISSN: 15487105 (Mar. 2020).
484. Waduge, P. *et al.* Nanopore-Based Measurements of Protein Size, Fluctuations, and Conformational Changes. *ACS Nano* **11**, 5706–5716. ISSN: 1936086X (June 2017).
485. Smirnov, S. N., Vlassiuk, I. V. & Lavrik, N. V. Voltage-gated hydrophobic nanopores. *ACS Nano* **5**, 7453–7461. ISSN: 19360851 (Sept. 2011).
486. Wu, J., Lewis, A. H. & Grandl, J. Touch, Tension, and Transduction – The Function and Regulation of Piezo Ion Channels. *Trends in Biochemical Sciences* **42**, 57–71. ISSN: 0968-0004 (Jan. 2017).
487. Brohawn, S. G., Su, Z. & MacKinnon, R. Mechanosensitivity is mediated directly by the lipid membrane in TRAAK and TREK1 K⁺ channels. *Proceedings of the National Academy of Sciences of the United States of America* **111**, 3614–3619. ISSN: 00278424. <https://www.pnas.org/content/111/9/3614%20https://www.pnas.org/content/111/9/3614.abstract> (Mar. 2014).
488. Marcotte, A., Mousterde, T., Niguès, A., Siria, A. & Bocquet, L. Mechanically activated ionic transport across single-digit carbon nanotubes. *Nature Materials* **2020 19:10 19**, 1057–1061. ISSN: 1476-4660. <https://www.nature.com/articles/s41563-020-0726-4> (July 2020).
489. Fang, A., Kroenlein, K. & Smolyanitsky, A. Mechanosensitive Ion Permeation across Sub-Nanoporous MoS₂ Monolayers.
490. Bertolazzi, S., Brivio, J. & Kis, A. Stretching and breaking of ultrathin MoS₂. *ACS Nano* **5**, 9703–9709. ISSN: 19360851. <https://pubs.acs.org/doi/full/10.1021/nn203879f> (Dec. 2011).
491. Lewis, A. H. & Grandl, J. Mechanical sensitivity of Piezo1 ion channels can be tuned by cellular membrane tension. *eLife* **4**. ISSN: 2050084X (Dec. 2015).
492. Cox, C. D., Bavi, N. & Martinac, B. Biophysical Principles of Ion-Channel-Mediated Mechanosensory Transduction. *Cell Reports* **29**, 1–12. ISSN: 2211-1247 (Oct. 2019).

493. Marion, S., Macha, M., Davis, S. J., Chernev, A. & Radenovic, A. Wetting of nanopores probed with pressure. *Physical Chemistry Chemical Physics* **23**, 4975–4987. ISSN: 14639076. <https://pubs.rsc.org/en/content/articlehtml/2021/cp/d1cp00253h> <https://pubs.rsc.org/en/content/articlelanding/2021/cp/d1cp00253h> (Mar. 2021).
494. Siwy, Z., Kosińska, I. D., Fuliński, A. & Martin, C. R. Asymmetric Diffusion through Synthetic Nanopores. *Physical Review Letters* **94**, 048102. ISSN: 0031-9007 (Feb. 2005).
495. Naumis, G. G. Electronic properties of two-dimensional materials. *Synthesis, Modeling, and Characterization of 2D Materials, and Their Heterostructures*, 77–109 (Jan. 2020).
496. Akinwande, D. *et al.* A review on mechanics and mechanical properties of 2D materials—Graphene and beyond. *Extreme Mechanics Letters* **13**, 42–77. ISSN: 2352-4316 (May 2017).
497. Alam, S., Asaduzzaman Chowdhury, M., Shahid, A., Alam, R. & Rahim, A. Synthesis of emerging two-dimensional (2D) materials – Advances, challenges and prospects. *FlatChem* **30**, 100305. ISSN: 2452-2627 (Nov. 2021).
498. Yu, J., Li, J., Zhang, W. & Chang, H. Synthesis of high quality two-dimensional materials via chemical vapor deposition. *Chemical Science* **6**, 6705–6716. ISSN: 2041-6539. <https://pubs.rsc.org/en/content/articlehtml/2015/sc/c5sc01941a> <https://pubs.rsc.org/en/content/articlelanding/2015/sc/c5sc01941a> (Nov. 2015).
499. He, Y., Tsutsui, M., Zhou, Y. & Miao, X. S. Solid-state nanopore systems: from materials to applications. *NPG Asia Materials* *2021 13:1* **13**, 1–26. ISSN: 1884-4057. <https://www.nature.com/articles/s41427-021-00313-z> (June 2021).
500. Haywood, D. G., Saha-Shah, A., Baker, L. A. & Jacobson, S. C. Fundamental Studies of Nanofluidics: Nanopores, Nanochannels, and Nanopipets. *Analytical Chemistry* **87**, 172–187. ISSN: 15206882. <https://pubs.acs.org/doi/full/10.1021/ac504180h> (Jan. 2014).
501. Loessberg-Zahl, J. *et al.* Exploring Voltage Mediated Delamination of Suspended 2D Materials as a Cause of Commonly Observed Breakdown. *Journal of Physical Chemistry C* **124**, 430–435. ISSN: 19327455. <https://pubs.acs.org/doi/full/10.1021/acs.jpcc.9b08500> (Jan. 2020).
502. Verguts, K., Coroa, J., Huyghebaert, C., De Gendt, S. & Brems, S. Graphene delamination using ‘electrochemical methods’: an ion intercalation effect. *Nanoscale* **10**, 5515–5521. ISSN: 2040-3372. <https://pubs.rsc.org/en/content/articlehtml/2018/nr/c8nr00335a> <https://pubs.rsc.org/en/content/articlelanding/2018/nr/c8nr00335a> (Mar. 2018).
503. Feng, J. *et al.* Observation of ionic Coulomb blockade in nanopores. *Nature Materials* **15**, 850–855. ISSN: 14764660 (Aug. 2016).
504. Kuan, A. T., Lu, B., Xie, P., Szalay, T. & Golovchenko, J. A. Electrical pulse fabrication of graphene nanopores in electrolyte solution. *Applied Physics Letters* **106**. ISSN: 00036951 (May 2015).

505. Levine, E. V., Burns, M. M. & Golovchenko, J. A. Nanoscale dynamics of Joule heating and bubble nucleation in a solid-state nanopore. *Physical Review E* **93**. ISSN: 24700053 (Jan. 2016).
506. Nagashima, G., Levine, E. V., Hoogerheide, D. P., Burns, M. M. & Golovchenko, J. A. Superheating and homogeneous single bubble nucleation in a solid-state nanopore. *Physical Review Letters* **113**. ISSN: 10797114 (July 2014).
507. Leung, C. *et al.* Mechanisms of solid-state nanopore enlargement under electrical stress. *Nanotechnology* **31**. ISSN: 1361-6528. <https://pubmed.ncbi.nlm.nih.gov/32698174/> (Oct. 2020).
508. Deng, S., Gao, E., Xu, Z. & Berry, V. Adhesion Energy of MoS₂ Thin Films on Silicon-Based Substrates Determined via the Attributes of a Single MoS₂ Wrinkle. *ACS Applied Materials and Interfaces* **9**, 7812–7818. ISSN: 19448252. <https://pubs.acs.org/doi/abs/10.1021/acsami.6b16175> (Mar. 2017).
509. Liu, K. *et al.* Elastic properties of chemical-vapor-deposited monolayer MoS₂, WS₂, and their bilayer heterostructures. *Nano Letters* **14**, 5097–5103. ISSN: 15306992 (Sept. 2014).
510. Boddeti, N. G. *et al.* Graphene blisters with switchable shapes controlled by pressure and adhesion. *Nano Letters* **13**, 6216–6221. ISSN: 15306984. <https://pubs.acs.org/doi/full/10.1021/nl4036324> (Dec. 2013).
511. Boddeti, N. G. *et al.* Mechanics of adhered, pressurized graphene blisters. *Journal of Applied Mechanics, Transactions ASME* **80**. ISSN: 15289036. <https://asmedigitalcollection.asme.org/appliedmechanics/article/80/4/040909/370651/Mechanics-of-Adhered-Pressurized-Graphene-Blisters> (July 2013).
512. Koenig, S. P., Boddeti, N. G., Dunn, M. L. & Bunch, J. S. Ultrastrong adhesion of graphene membranes. *Nature Nanotechnology* **2011** 6:96, 543–546. ISSN: 1748-3395. <https://www.nature.com/articles/nnano.2011.123> (Aug. 2011).
513. Vella, D., Bico, J., Boudaoud, A., Roman, B. & Reis, P. M. The macroscopic delamination of thin films from elastic substrates. *Proceedings of the National Academy of Sciences* **106**, 10901–10906. ISSN: 0027-8424. <https://www.pnas.org/content/early/2009/06/24/0902160106%20https://www.pnas.org/content/early/2009/06/24/0902160106.abstract> (June 2009).
514. Androulidakis, C., Koukaras, E. N., Pastore Carbone, M. G., Hadjinicolaou, M. & Galiotis, C. Wrinkling formation in simply-supported graphenes under tension and compression loadings. *Nanoscale* **9**, 18180–18188. ISSN: 2040-3372. <https://pubs.rsc.org/en/content/articlehtml/2017/nr/c7nr06463b%20https://pubs.rsc.org/en/content/articlelanding/2017/nr/c7nr06463b> (Nov. 2017).
515. Brennan, C. J. *et al.* Interface Adhesion between 2D Materials and Elastomers Measured by Buckle Delaminations. *Advanced Materials Interfaces* **2**, 1500176. ISSN: 2196-7350. <https://onlinelibrary.wiley.com/doi/full/10.1002/admi.201500176%20https://onlinelibrary.wiley.com/doi/abs/10.1002/admi.201500176%20https://onlinelibrary.wiley.com/doi/10.1002/admi.201500176> (Nov. 2015).

516. Delgado, A. V., González-Caballero, F., Hunter, R. J., Koopal, L. K. & Lyklema, J. Measurement and interpretation of electrokinetic phenomena. *Journal of Colloid and Interface Science* **309**, 194–224. ISSN: 0021-9797 (May 2007).
517. Xu, Y., Yazbeck, R. & Duan, C. Anomalous mechanosensitive ion transport in nanoparticle-blocked nanopores. *The Journal of Chemical Physics* **154**, 224702. ISSN: 0021-9606. <https://aip.scitation.org/doi/abs/10.1063/5.0046086> (June 2021).
518. Chernev, A., Marion, S. & Radenovic, A. Prospects of Observing Ionic Coulomb Blockade in Artificial Ion Confinements. *Entropy 2020, Vol. 22, Page 1430* **22**, 1430. ISSN: 1099-4300. <https://www.mdpi.com/1099-4300/22/12/1430/htm%20https://www.mdpi.com/1099-4300/22/12/1430> (Dec. 2020).



Michal Macha

Nanotechnology Specialist and Researcher

✉ the.michal.macha@gmail.com

☎ +41 78 73 10 401

📍 Renens, Switzerland

in [linkedin.com/in/michalmacha](https://www.linkedin.com/in/michalmacha)

KEY COMPETENCES

- Finding elegant solutions to complex problems
- Management and Leadership in a Multi-cultural Environment
- Critical approach towards Data and Market Analysis
- 2D Materials Synthesis and Nanotechnology Applications

EDUCATION

Ecole Polytechnique Fédérale de Lausanne (EPFL)

Lausanne, Switzerland

PhD in Materials Science and Engineering

04.2017 – Present

Thesis: Synthesis of 2D materials with CVD and MOCVD, large-area engineering and study of atomically thin membranes and nanofluidic devices

University of Silesia / Université du Maine

Katowice, Poland / Le Mans, France

MSc in Physics

09.2013 – 09.2015

Thesis: Modification of graphene and carbon nanotubes by D-elemental nanoparticles

Silesian University of Technology

Gliwice, Poland

MSc in Materials Science and Engineering

09.2012 – 09.2014

Thesis: CVD synthesis of atomically thin graphene

CORE EXPERIENCE

Laboratory of Nanoscale Biology (LBEN)

Lausanne, Switzerland

Doctoral Assistant

12.2016 – Present

- Developed and upscaled a novel synthesis method of atomically thin nanomaterials,
- Managed cleanroom fabrication and design of membrane-based biosensing devices,
- Supervised and lead installation, maintenance and development of experimental and industrial MOCVD and nanofluidic research setups,
- Led project to scientific breakthrough and major new insights in the academic field,
- Managed, supervised and trained students and interns on advanced experimental processes and protocols,
- Performed exhausting materials characterization using AFM, SEM, TEM, XPS, Raman and PL spectroscopy,
- Fabricated nano- and microdevices with e-beam lithography and photolithography,
- Performed complex data analysis (Python, Origin, MS Office, Image-J) and visualization through graphics design (posters, science-popularization publishing, scientific manuscripts figures),
- Led in-depth analysis of nanotech state-of-art and study ending in series of high-impact publications.

NeWave Technologies

Katowice, Poland

CEO and co-founder

03.2017 – 03.2019

- Managed the strategic development of the start-up,
- Created and revised business plan,
- Lead the team of scientists to develop a novel, nanotechnology-based products to the market,
- Co-developed a patent on a graphene flake synthesis.

Plasma System SA

Siemianowice Slaskie, Poland

Deputy Head of Materials Laboratory

08.2015 – 06.2016

- Managed and supervised an accredited materials lab,
- Engaged in client consulting and process engineering,
- Analyzed, designed and maintain surface processes for laser cladding, HVOF, flame and arc spraying,
- Created protocols, documents and tools for materials handling and customer communication.

ADDITIONAL EXPERIENCE

Ecole Polytechnique Fédérale de Lausanne (EPFL)

Lausanne, Switzerland

Safety correspondants (CoSEC)

06.2017 – Present

- Responsible for the laboratory safety management (chemical and gas hazard),
- Providing and managing safety procedures and first emergency contact

Student Representative

10.2017 – 10.2019

- Representing the voice of students as a liaison person,
- Annual doctoral school seminar event organization (100+ participants for oral and poster presentations),
- Advising on study plans, program regulations, ECTS credits, candidacy exam conditions etc.,
- Discussing and advising on student-life and well-being topics with Doctoral School Direction

The Foundation of Nanoscience and Nanotechnology Support NANONET

Katowice, Poland

Vice president, project manager

06.2014 – Present

- Responsible for strategic organization, planning and leading science outreach events,
- Providing analysis and consulting on emerging and innovative technologies,
- Organized over 10 educational workshops and experts' meetings for students and teachers,
- Managed the team of 20 volunteers during events, projects and daily activities,
- Co-wrote 4 EU H2020 project proposals with international consortia,
- Published popular-science articles on advanced academic topics

InterNanoPoland Conference

Katowice, Poland

Main organizer and co-initiator

01.2016 – Present

- Responsible for planning, team management, coordination and international affairs,
- Led the team of 10 to successfully organize an annual networking conference hosting 100-200 participants,
- Attracted over 10 sponsors from business and academia to fund the event,
- Initiated the Business-Science networking activities which led to project consortia and co-joint ventures,
- Organized panel sessions, public debates and outreach activities for nanotech stakeholders,

SKILLS

- | | | |
|--|--|--|
| <ul style="list-style-type: none">▪ Technical:▪ CAD design▪ SEM, FIB, TEM▪ Spectroscopy▪ 2D Materials Synthesis▪ Thin Film Fabrication▪ Nanoengineering▪ Nanofabrication▪ Cleanroom Processing▪ Programming (Python)▪ Data Analysis, Presentation | <ul style="list-style-type: none">▪ Managerial:▪ Project Management▪ Event Organization▪ Decision-Making▪ Strategy Planning▪ Business Plan creation▪ Coaching▪ Analytical Skills▪ Communication | <ul style="list-style-type: none">▪ Soft Skills:▪ Leadership▪ Science Communication▪ Teaching▪ Public Speaking▪ Professional Writing▪ Intercultural Fluency▪ Critical Thinking▪ Empathy and Awareness▪ Impeccable Sense of Humor |
|--|--|--|

LANGUAGES

English (Fluent, CPE certified),

Polish (Native),

French (A1, learning)

German (A1, learning)

INTERESTS

CROSSFIT AND FITNESS

GAMING

HISTORICAL REENACTMENT

SPECIALITY COFFEE

GUITAR PLAYING

CRYPTOCURRENCIES

ROLEPLAYING

BOARDGAMES

CINEMATOGRAPHY

ASTROPHYSICS

GRAPHICS DESIGN

PITCH PRESENTATION

1. **2D materials as an emerging platform for nanopore-based power generation.**
M Macha, S Marion, VVR Nandigana, A Radenovic.
Nature Reviews Materials, 2019.
2. **Wafer-scale MoS₂ with water-vapor assisted showerhead MOCVD.**
M Macha, HG Ji, M Tripathi, Y Zhao, M Thakur, J Zhang, A Kis, A Radenovic,
in preparation.
3. **Mass nanopore FIB drilling and automated pore-edging analysis.**
M Macha, S Marion, A Smolyanitsky, M Tripathi, M Thakur, M Lihter, A Kis, A Radenovic.
In preparation.
4. **Wafer-scale MOCVD growth of monolayer MoS₂ on sapphire and SiO₂.**
H Cun, M Macha, HK Kim, K Liu, Y Zhao, T LaGrange, A Kis, A Radenovic.
Nano Research, 2019
5. **Superconducting 2D NbS₂ Grown Epitaxially by Chemical Vapor Deposition,**
Z Wang, CY Cheon, M Tripathi, GM Marega, Y Zhao, HG Ji, M Macha, A Radenovic, A Kis.
ACS nano, 2021.
6. **Wafer-Scale Fabrication of Nanopore Devices for Single-Molecule DNA Biosensing using MoS₂.**
M Thakur, M Macha, A Chernev, M Graf, M Lihter, J Deen, M Tripathi, A Kis, A Radenovic.
Small Methods, 2020.
7. **Delamination and wrinkling phenomena of nanoporous 2D MoS₂ under pressure.**
M Macha, S Marion, M Thakur, A Radenovic.
In preparation.
8. **Wetting of nanopores probed with pressure.**
S Marion, M Macha, SJ Davis, A Chernev, A Radenovic.
Physical Chemistry Chemical, 2021.
9. **Pressure-induced enlargement and ionic current rectification in symmetric nanopores.**
SJ Davis, M Macha, A Chernev, DM Huang, A Radenovic, S Marion.
Nano Letters. 2020.
10. **Electrochemical Functionalization of Selectively Addressed MoS₂ Nanoribbons for Sensor Device Fabrication.**
M Lihter, M Graf, D Ivekovic, M Zhang, TH Shen, Y Zhao, M Macha, V Tileli, A Radenovic.
ACS Applied Nano Materials, 2021.
11. **Electrochemical Functionalization of Selectively Addressed MoS₂ Nanoribbons for Sensor Device Fabrication.**
M Lihter, M Graf, D Ivekovic, M Zhang, TH Shen, Y Zhao, M Macha, V Tileli, A Radenovic.
ACS Applied Nano Materials, 2021.
12. **Super-resolved Optical Mapping of Reactive Sulfur-Vacancies in Two-Dimensional Transition Metal Dichalcogenides.**
M Zhang, M Lihter, TH Chen, M Macha, A Rayabharam, K Banjac, Y Zhao, Z Wang, J Zhang, J Comtet, NR Aluru, M
Lingenfelder, A Kis, A Radenovic.
ACS nano, 2021.
13. **Engineering optically active defects in hexagonal boron nitride using focused ion beam and water.**
E Glushkov, M Macha, E Rath, V Navikas, N Ronceray, CY Cheon, A Aqeel, A Avsar, K Watanabe, T Taniguchi, I
Shorubalko, A Kis, G Fantner, A Radenovic.
ACS nano, under revision.



Google Scholar

[HTTPS://SCHOLAR.GOOGLE.COM/CITATIONS?USER=U56PIJYAAAAJ&HL=EN](https://scholar.google.com/citations?user=U56PIJYAAAAJ&hl=en)



Researchgate

[HTTPS://WWW.RESEARCHGATE.NET/PROFILE/MICHAL-MACHA-2](https://www.researchgate.net/profile/Michal-Macha-2)